Galaxy clustering and dynamics from redshift surveys

Hale-Sutton, Duncan

Galaxy Clustering and Dynamics from Redshift Surveys

by

Duncan Hale-Sutton

November 1990

Being an account of the work undertaken at the Department of Physics and submitted to the University of Durham in accordance with the regulations for admission to the degree of Doctor of Philosophy.

To Jackie and our future

"As large telescopes probe further and further into space, more and more galaxies are discovered. Far from being the only one, the Milky Way is one of millions, which fill space out to some ten thousand million light-years, the farthest distance which our present-day telescopes can reach.

The galaxies form the bricks out of which the large-scale universe is built, and they are separated by distances of a few million light-years. But the distances are not fixed. The galaxies all seem to move apart, outwards from each other, as if the whole universe were stretching like a balloon which is being inflated.

Why do they spread out in this way? Did they all start in one great huddle some thousands of millions of years ago, before being blown apart and scattering as we now see them? Or is there another explanation for the 'expansion of the universe', as it is called? We do not know. This remains one of the great mysteries of the universe."

A Ladybird Book of the Night Sky, 1965.

Preface

The work described in this thesis has not been submitted for any degree, diploma or other qualification at any other university. The work has been carried out in collaboration with Drs. R. Fong and T. Shanks at Durham but the majority is the author's own work.

The following results have been published elsewhere:-

Shanks, T., Hale-Sutton, D., & Boyle, B.J., 1988. "Observations of galaxy and QSO clustering." In: Large-Scale Structures in the Universe, IAU Symposium No. 130, p371, eds. Audouze, J. et al., Reidel, Dordrecht.

Hale-Sutton, D., Fong, R., Metcalfe, N., & Shanks, T., 1989. "An extended galaxy redshift survey - II. Virial constraints on Ω_0 ." Mon. Not. R. astr. Soc., 237, 569.

Shanks, T., Hale-Sutton, D., Fong, R., & Metcalfe, N., 1989. "An extended galaxy redshift survey - III. Constraints on large-scale structure." Mon. Not. R. astr. Soc., 237, 589.

Acknowledgments

I would firstly like to thank Dick Fong and Tom Shanks for their supervision of this thesis and for many helpful discussions over the years. I would particularly like to thank Tom for his recent 'Mac. support' in the latter stages of the production of this thesis.

I would also like to offer my thanks to my colleagues who have provided me with help in one way or another. I would like to mention Nigel Metcalfe for his help on matters of photometry, John Lucey for his discussions and his support of DUSDERS, Paddy Oates and Fred Watson for their help with the observations at the UKST, and Harvey MacGillivray for providing me the COSMOS data presented in this thesis. My thanks also go to the staff at the UKST and UKSTU, and Alan Lotts for keeping the VAX going so well.

I would like to acknowledge the receipt of an SERC studentship for the period in which this research was carried out.

My special thanks and love goes to Jackie, who has been so supportive over the past months as this work was drawing to its completion. I would also like to thank her for all that typing, cutting and sticking!

Abstract

Duncan Hale-Sutton

Galaxy Clustering and Dynamics from Redshift Surveys

The clustering and dynamical properties of the 368 galaxies in the redshift surveys of Metcalfe et al. (1989) and Parker et al. (1986) are investigated. These galaxies were selected from ten high galactic latitude fields complete to a magnitude limit of $m(b_J) \leq 17^m$. These complement the five similarly selected fields in the survey of Peterson et al. (1986) and so the overall clustering and dynamical properties of all three samples are discussed.

Initial studies of the distribution of galaxies in the survey of Peterson et al. were carried out by Bean (1983). This thesis extends that earlier work by examining the conclusions of Bean in the larger volume of the new surveys considered here. It is found that, whilst the combined estimate of the line-of-sight peculiar motions in the three samples together is in reasonable accord with that found previously, the range of peculiar motions in the individual samples is larger than previously anticipated. The rms pair-wise velocity $\langle \omega^2 \rangle^{1/2}$ is found to be $\langle \omega^2 \rangle^{1/2} = (600 \pm 140) \text{kms}^{-1}$ in the Metcalfe et al. survey as compared to $\langle \omega^2 \rangle^{1/2} = (0 \pm 240) \text{kms}^{-1}$ and $\langle \omega^2 \rangle^{1/2} = (190 \pm 90) \text{kms}^{-1}$ in the Parker et al. and Peterson et al. samples, respectively. These estimates of the motions of galaxies at spatial scales of $\sim 1h^{-1}$ Mpc ($H_o = 100 \text{kms}^{-1}$ Mpc^{-1}) together with measures of the clustering provide constraints on the mean mass density of the Universe through the Cosmic Virial Theorem. It is found that the mean mass density parameter for the three samples considered as a whole is $\Omega_o = 0.18 \pm 0.09$, on the assumption that galaxies trace the mass distribution, and this constraint is similar to that obtained previously mainly because of the larger range of peculiar motions found.

The clustering distribution of the galaxies in the new samples was investigated on spatial scales ranging from a few up to $\sim 100h^{-1}$ Mpc. It was found from the number-redshift and number-magnitude counts that these

samples were fairly homogeneous at the largest scales and in good agreement with previous results from the Peterson et al. catalogue. Thus using these samples to estimate the mean clustering properties of galaxies, it was found, from the two-point correlation function $\xi_s(s)$, that the galaxies in the new samples appear to exhibit a preferred clustering length at $\sim 2h^{-1}$ Mpc and this confirms the 'shoulder ' detected in the correlation function of the Peterson et al. data by Bean (1983). On the basis that this shoulder is a real spatial feature (and not caused by peculiar motions) the mean clustering length of galaxies in the three samples is $r_o=(6.6\pm0.5)h^{-1}$ Mpc in the range $2\lesssim s\lesssim 7h^{-1}$ Mpc and this is significantly larger than the $r_o=5h^{-1}$ Mpc that was previously thought to apply to galaxies in this region of separation.

At scales larger than $\sim 7h^{-1}$ Mpc the correlation function in the combined sample of the three surveys indicates that the galaxy distribution rapidly approaches homogeneity. Although there are some tentatively detected spatial scale lengths in the galaxy distibution at these larger scales, the main conclusion from the correlation function for these galaxies is that there is no evidence of large-scale clustering at the 2 sigma statistical significance level from separations of ~ 10 to $100h^{-1}$ Mpc. Thus on the assumption that these galaxies trace the mass distribution this implies that the Universe is homogeneous to $\sim 15\%$ at these scales.

Finally, some new redshifts of galaxies were presented that were observed with the FLAIR spectrograph on the UK Schmidt telescope. These observations indicate that this instrument is capable of performing systematic redshift surveys of $m(b_J)\lesssim 17^m$ galaxies with a completeness of $\sim 80\%$ and with an accuracy in redshift velocity of $\pm 150 kms^{-1}$ rms. This will then pave the way for future large area redshift surveys in the southern hemisphere.

Contents

Chapter 1

Introduction

Homogeneous and isotropic models for the description of the matter distribution on the largest spatial scales have become a common feature in studies of cosmology. These models, coupled with the dynamical equations of General Relativity, have had a remarkable success in helping to predict a wide range of phenomena from the abundance of the light chemical elements (Wagoner 1973, Olive et al. 1981, Yang et al. 1984) to the observation of the 3K Cosmic Microwave Background radiation (Penzias and Wilson 1965). Whilst the homogeneity and isotropy may be demonstrable on these scales (for example, fluctuations in the observed microwave background temperature imply isotropy of the matter distribution to better than one part in 10^4 on a wide range of angular scales; see, for example, Wilkinson 1988 for a review), the Universe appears to be very inhomogeneous at much smaller separations as is illustrated by objects such as galaxies which are clearly strong enhancements in the matter distribution. The questions that naturally come to mind are then, what are the perturbations in the matter distribution which gave rise to objects such as galaxies and at what spatial scale do these fluctuations approach homogeneity?

Knowledge of how the mass is distributed in the Universe is of prime importance in understanding the evolution of the matter fluctuations since gravity is the predominant force acting on large scales. However, as the visible parts of galaxies may only contain a small fraction of the total mass (see, for example, Faber and Gallagher 1979) the question then arises as to the relationship between the visible and non-visible components of the matter distribution; for example, it is not a trivial assumption that galaxies should trace an underlying mass component. In spite of this, any evolutionary model for an underlying mass distribution must eventually describe the formation of galaxies and galaxies themselves will in a dynamical sense act as test particles that move in the gravitational potentials of the mass fluctuations. Thus, observations of the spatial and dynamical distributions of galaxies (which are the most numerous and easily detectable objects at redshifts $z \lesssim 0.5$) will provide significant information on the present day form and

evolution of the matter fluctuations in the Universe.

As reviewed by Peebles (1980), there have been two general approaches to the study of large-scale structure from the two- or three-dimensional galaxy distributions. In the 'morphological' or 'botanical' approach various specific large-scale structures have been studied either individually (as, for example, in the 3-d map of the Perseus-Pisces filament; see Haynes and Giovanelli 1988 and the references therein, or in the Boötes void; Kirshner et al. 1981, 1987) or collectively (as, for example, in the catalogue of rich clusters by Abell, 1958). Although such inspections of the galaxy distribution have been very fruitful in contributing to our understanding of such structures (see, for example, Oort 1983) there has always been the uncertainty over the subjective choice as to what constitutes an important structure. For example, it is possible that under the random processes involved in galaxy clustering there may be a considerable number of possibly 'important' objects to observe and catalogue in this morphological way.

The alternative approach to this 'botanical' method is to treat the galaxy distribution in an objective statistical fashion and measure the mean properties which apply to the whole distribution. This has the distinct advantage that, in the case where galaxies trace (in some sense) or dynamically follow the underlying mass distribution, these mean properties will also be directly important in constraining models for the evolution of the overall mass perturbations. Clearly, it is not, at present, feasible to collect the 3-d positions of all the galaxies and so it is generally assumed that, like other global properties, galaxy clustering is a statistically homogeneous process. Thus, under this assumption, it may be possible to examine independent subsets of the global distribution that reflect the mean overall properties but differ from these in a random way. This so-called 'fair' sample hypothesis is central to such statistical studies of large-scale structure.

Hence, to effectively characterise aspects of the mass distribution, the spatial positions of galaxies are required in a region of space that samples all the relevant clustering processes that are seen in the Universe. In this work statistical analyses of galaxy clustering and dynamics are performed on two new, relatively deep ($z \leq 0.1$), redshift catalogues (Metcalfe et al. 1989, hereafter the Durham/SAAO Survey, and Parker et al. 1986) in ten random areas of the sky sampled from lists of galaxies complete to an apparent

magnitude of $b_J \approx 16^m.8$ ($16^m.5$ in the Parker et al. sample). This extends and complements the earlier work of Bean (1983) on the redshift survey of Peterson et al. (1986, hereafter the Durham/AAT Survey) in five similar fields to an equivalent depth.

Thus, in Chapter 2 the basic statistical methods used in this work are reviewed and the uncertainties of the statistical properties described. In Chapter 3 the new redshift samples are introduced and some aspects of the homogeneity of their 3-d distributions presented. The basic statistical results for these new samples is given in Chapters 4 and 5, with Chapter 4 describing the clustering and peculiar motions of galaxies at small ($\leq 1h^{-1}$ Mpc [1]) spatial scales. Using the virial methods described in Chapter 2 these observations can be used to constrain the mean mass density of the Universe. In Chapter 5 measurements of the clustering of galaxies at large scales ($\geq 1h^{-1}$ Mpc) are presented and the constraints on the evolutionary models of the mass distribution are discussed. In both Chapters 4 and 5 detailed comparisons are made between the results for these two samples and those from other redshift surveys (particularly the Durham/AAT Survey). Finally, Chapter 6 describes some preliminary observations of galaxies with a new spectrographic system on the UK Schmidt telescope which may pave the way for future redshift surveys covering a large area of the southern sky to a limit of $b_J \approx 17^m$. Some conclusions on the questions addressed in this thesis are given in Chapter 7.

---

[1] Throughout this work Hubble's constant is given as $H_0 = 100 \, h \, kms^{-1} Mpc^{-1}$.

Chapter 2

Review of the methods of clustering and dynamical analyses

In Chapter 1 it was briefly indicated that important constraints on the present day form of the mass perturbations in the Universe may come from a study of the spatial and dynamical distributions of galaxies. In this chapter simple statistical measures are described (Section 2.1) which can be applied easily and directly to the new redshift catalogues of galaxies that form the basis of this work. Since the observed redshift of a galaxy can contain both a Hubble recession velocity and a dynamical peculiar velocity, these measures applied in 'redshift space' provide information jointly on both the spatial and dynamical distributions of galaxies (Section 2.1.2.2). Thus, in Section 2.2 models for these peculiar motions are described and the important information concerning the mean mass density of the Universe that can, in principle, be obtained, is discussed.

2.1 Statistical measures of galaxy clustering

As was discussed in Chapter 1 the aim of this statistical approach is to attempt to analyse the galaxy distribution objectively as a complete entity, rather than rely on a subjective division into its component 'morphological' parts. However, as was seen, general features of the galaxy clustering may be obtained from subsamples of the overall distribution provided that these approximate independent realisations of the same clustering process. Thus, the aim of this work is to utilise what are believed to be fair samples of the galaxy clustering to obtain estimates of quantities that may describe the distribution as a whole.

On the other hand not all statistical measures will be useful. It is easy to think up statistical tests which have little relevance to the evolution of the galaxy distribution, and so, this objectivity needs to be directed by the observations and the underlying physical processes. A statistical measure should, therefore, give reproducible results for independent galaxy samples and be governed, in some sense, by an underlying physical mechanism.

Importantly, it must be able to effectively distinguish between different classes of evolutionary model.

Historically, the most popular statistic has been based on variants of the autocorrelation function and its related quantity the count of galaxies in cells (see Peebles 1980, Section 29). There have been many others; some of which are more specific to particular features in the observed galaxy distribution, such as the minimal spanning tree analysis for filaments (see, for example, Bhavsar and Ling 1988), while others are less specific (see, for example, the mutifractal analysis of Jones et al. 1988). However, the more complicated the statistical test the more difficult it is to express its physical evolution and the more demanding it is of the data. As pointed out by White (1979) some measures, in any case, have a strong dependence on the autocorrelation function and so may not provide much new information. A careful appraisal of the test and its relation to the autocorrelation function may thus prove a useful guide to its worth.

Why is the autocorrelation function of such value? As Peebles notes this statistic has been successfully applied in other fields of study and so there is little reason why it should not be useful here. Initially, it was of particular interest in the analysis of 2-d galaxy catalogues, as estimates of the angular correlation function could be used to deduce the form of the spatial correlation function using a simple linear integral relation and, as seen below, (Section 2.1.2.4) this is still a useful way of constraining observations of either function. The scaling of the angular form with the depth of the galaxy catalogue also enabled tests to be made of the homogeneity assumptions discussed in Chapter 1 and possible systematic errors in the catalogues, such as induced by Galactic obscuration.

Thus, although the statistic does contain limited information, it is, nevertheless, an easy one to estimate and it does provide data against which models of the galaxy distribution can be tested in detail. For example, the scale-free nature of the form estimated from galaxy catalogues directly motivated the suggestion that galaxies cluster hierarchically, i.e. by clumping in a self-similar way (Peebles 1974). Further, as the mass autocorrelation function appears directly in the equations of motion of matter in the Universe (Section 2.2) observations of galaxy correlations may directly constrain the evolution of large-scale structures. For example, in the regime where these

mass correlations are small and gravity is the predominant force acting on large scales, then this function is expected to evolve in a simple linear way and this implies that the initial structure of the mass distribution may be inferred directly from the observations of galaxy correlations in this clustering regime under the assumption that these objects trace the mass.

In the following sections the concept of the n-point correlation functions is introduced together with the methods for the estimation of low orders from redshift surveys. Simple models for their form are considered and interrelations between their properties described. The uncertainties of estimation, derived from models, from the data and from the simulations are discussed.

2.1.1 Introduction to the n-point correlation functions

The two- and three-point correlation functions are defined in Sections 2.1.2 and 2.1.3 below, but to illustrate their importance consider the count of galaxies in a cell (see Peebles 1980, Section 36). Imagine placing a cell, of volume V, at random within the galaxy distribution and counting the number, N, of galaxies that lie within its boundary. It is assumed that V is much larger than the typical volume of a galaxy. Repeating this procedure many times allows a discrete frequency histogram to be drawn up for the observed count N; the frequency with which N is recorded is plotted against the value of N. In the case where galaxies are randomly and homogeneously distributed in space the histogram would be Poisson, with a mean

$$\langle N \rangle = nV \qquad (2\text{-}1)$$

and the second moment, or variance,

$$\langle (N-\langle N \rangle)^2 \rangle = \langle N \rangle \qquad (2\text{-}2)$$

Here n is the mean homogeneous space density and, as usual, the dispersion is the square root of the variance, i.e. $\langle N \rangle^{1/2}$. If $\langle N \rangle$ is small (≤ 1) the frequency histogram is skew to low N but as $\langle N \rangle$ tends to large values the shape tends to that of a Gaussian.

Now consider the situation in which galaxies are clustered or, equivalently, correlated. It is easy to see that, for the case where the clustered and unclustered distributions have the same $\langle N \rangle$, the variation in the count N for the clustered galaxies will generally be different. This relative difference in the variance is directly related to the form of the two-point autocorrelation function.

As an example, consider the model in which galaxies are clustered into tight clumps (of volume $v \ll V$) and each clump contains exactly m members. Consider, also, that the **clumps**, rather than the galaxies are randomly and homogeneously distributed in space, with the number counted in V being N_c. Thus, the mean of the count of N galaxies in V is,

$$\langle N \rangle = m \langle N_c \rangle \tag{2-3}$$

(as $N \approx m N_c$) but unlike the previous unclustered distribution, the dispersion in this number is **not** $\langle N \rangle^{1/2}$, as it is the **clumps** that are randomly distributed. For this model the dispersion in the number of clumps in V is $\langle N_c \rangle^{1/2}$ and that of the galaxies is $m \langle N_c \rangle^{1/2}$, i.e. $(m \langle N \rangle)^{1/2}$. Therefore, in this clustered model the variance in the count of galaxies is increased by a factor m over the random distribution with the same $\langle N \rangle$, viz;

$$\langle (N - \langle N \rangle)^2 \rangle = m \langle N \rangle \tag{2-4}$$

In general, the nth moment for the count N of galaxies is directly related to the n-point correlation function and this illustrates, that, although the two-point correlation function is limited in its information about clustering, higher order functions are more difficult to estimate because of their strong dependence on N (N^n).

2.1.1.1 The mean homogeneous number density, n.

The mean homogeneous number density, n, plays an important rôle in quantifying galaxy clustering and since it is related to the first moment of the galaxy distribution it seems logical to discuss this in advance of the n-point correlation functions. The significance of determining the mean density lies in its use as a baseline for comparing densities at different points in space; clearly a clustered (or anticlustered) distribution will be over (or under) dense with respect to the mean. However, in order to make the measurement of n meaningful, the galaxy distribution must approach homogeneity at the largest scales as is already implicit in models for the evolution of the overall mass density.

To illustrate the difficulty in estimating n, consider the clustered model for the distribution of galaxies described above in the introduction to Section 2.1.1. A random placement of the cell leads to an estimate of the density $n_e=N/V$ where N is the count of galaxies observed in volume V. Since the galaxies are distributed in clumps of exactly m members, N has roughly a 70% chance of lying within $\pm(m\langle N\rangle)^{1/2}$ of the mean count . Expressing this dispersion as a fraction of $\langle N\rangle$, this is $(m/\langle N\rangle)^{1/2}$ which is small provided $\langle N\rangle \gg m$, i.e. provided that the cell, on average, contains many independent clumps. If, on the other hand, the clumps are themselves clustered, the dispersion in N will increase and so the measurement of n becomes more uncertain. Coupled with this there will also be a tendency for cells that are closely placed to be correlated and this may lead to a further systematic error in the estimate of n. Thus, in order to obtain a fair estimate of $\langle N\rangle$, this simple model would suggest that the largest **mean** clustering length must be much smaller than a typical dimension of the sample volume. This problem of fair sampling is persistent in clustering studies (see, for example, de Lapparent et al., 1988) and is discussed further in Chapter 5.

As well as the statistical uncertainties described above, there are also the practical difficulties with obtaining and using estimates of the mean density. It is clear from an observational point of view that it is necessary to select galaxies according to some specific criteria and so it is important to discuss the use and limitations of such samples in the current context. In particular, in the 17^m redshift surveys described in this work, galaxies are selected in a blue photographic passband by total apparent magnitude m, so

that each galaxy in the sample is brighter than some limit m_{lim}, i.e. $m \leq m_{lim}$. Thus, at a given distance only a limited range of absolute magnitudes, M, will be visible to the observer and, hence, the apparent density is a function of redshift

$$n_{app} = n(z) \qquad (2\text{-}5)$$

In a Friedmann[2] Universe, the relation between the apparent and absolute magnitudes for a galaxy selected in a narrow wavelength band is given by

$$m\text{-}M = 5\log_{10}(cz/H_o)+25+[1.086(1\text{-}q_o)+K]z = DM(z) \qquad (2\text{-}6)$$

in which the apparent brightness is proportional to the absolute brightness divided by the square of the luminosity distance. DM(z) is the usual distance modulus of the galaxy. This equation is to first order in the observed redshift z with q_o being the deceleration parameter (related to Ω_o, the density parameter, by $q_o = \Omega_o/2$ for a zero Cosmological Constant) and H_o is the Hubble constant. The units of distance have been expressed in Mpc and the K-correction[3] has been represented as a polynomial in z. For a mean value of[4] K=3.0 for blue selected galaxies, the ratio of the K-correction to curvature term is 3.1 for $q_o=0.1$ and 5.5 for $q_o=0.5$ and so the curvature can be neglected for reasonable values of q_o. With the selection criterion that $m \leq m_{lim}$, equation 2-6 implies that at redshift z only galaxies with absolute magnitudes brighter than

$$M_{max} = m_{lim}\text{-}DM(z) \qquad (2\text{-}7)$$

are within the sample. Clearly then, to estimate n(z) it is necessary to know the frequency distribution of absolute magnitudes (or luminosities) for galaxies.

---

[2] More correctly this is a Friedmann-Lemaitre world model with a Robertson-Walker space-time metric.

[3] If (λ_1,λ_2) is the effective wavelength range observed, then at the source this corresponds to $(\lambda_1,\lambda_2)/(1+z)$ and so the K-correction takes into account the difference in the bandwidth between the source and observer, as well as the shift in the source spectrum.

[4] This value is the weighted mean K-correction for galaxies of different morphological types in the J-photographic band (see Shanks et al. 1984).

To model this frequency distribution, the differential luminosity function, $\phi(M)dMdV$, is defined as the mean number of galaxies expected in volume dV in an absolute magnitude range M to $M+dM$ and, like the mean density, is an ensemble average property over fair samples of galaxies. Observations indicate that for bright galaxies (see, for example, Efstathiou et al. 1988) the distribution is well approximated by a Schechter (1976) function, which in luminosity, L, has the form

$$\phi(L)dL = \phi^*(L/L^*)^\alpha e^{-L/L^*}d(L/L^*) \tag{2-8}$$

The characteristic luminosity L^* divides the two asymptotic forms of this function; at $L \ll L^*$, $\phi(L)$ behaves like a power law $\phi(L) \approx (L/L^*)^\alpha$, whereas, after the knee at L^*, $\phi(L)$ tends to an exponential, rapidly declining to small values. The parameter ϕ^* is a number per unit volume which can be adjusted to give the correct density for a given L^* and α. Assuming that L is the B-band luminosity, then, L/L^* can be written as

$$L/L^* = y = 10^{0.4(M^*-M)} \tag{2-9}$$

and so the luminosity distribution as a function of absolute magnitude for a Schechter function becomes

$$\phi(M)dM = 0.4(\ln 10)\phi^* y^{(\alpha+1)} e^{-y} dM \tag{2-10}$$

With the condition given in equation 2-7, a simple model for the apparent density is thus

$$n(z) = \int_{-\infty}^{M_{max}(z)} \phi(M)dM \tag{2-11}$$

which for the Schechter model in equation 2-10 becomes

$$n(z) = \phi^* \int_{y_{min}(z)}^{\infty} y^\alpha e^{-y} dy = \phi^* \Gamma(\alpha+1, y_{min}(z)) \tag{2-12}$$

The lower limit on the luminosity is obtained from equation 2-9 with $M=M_{max}(z)$ and $\Gamma(a,x)$ is the incomplete Gamma function.

Since the observations indicate that the value of α lies in the range $-1.25 \leq \alpha \leq -1$ (see, for example, the review by Binggeli et al. 1988) certain care should be taken in using this model for n(z) since Γ diverges as $z \rightarrow 0$ for $\alpha \leq -1$. However, as the volume in which the intrinsically faint galaxies can be observed behaves like $10^{-0.6M}$ and $\phi(M) \approx 10^{-0.4(\alpha+1)M}$, the number of low luminosity objects tends to zero provided $\alpha > -2.5$.

In the application of the above model for the mean density in equation 2-11 to a galaxy sample it is important to use a self-consistent estimate of the galaxy luminosity function since errors in the estimate of $\phi(M)dM$ may percolate through as errors in the correlation functions. Further, it is also important that this self-consistent estimate be measured in a way which is independent of the observed clustering within the sample, i.e. that the density-independent **shape** of $\phi(M)dM$ is obtained as a function of position. In the Schechter model for n(z) in equation 2-12 the parameters M^* and α control the shape of $\phi(M)$ while ϕ^* can be adjusted to give the appropriate normalisation. As was indicated earlier, an estimate of the density can be obtained from the total number of galaxies in a sample and this will be a fair estimate provided that the volume contains many of the largest mean clustering elements. Although, in a realistic situation there is uncertainty over whether a sample does approach this ideal, there are some reasons for using this form of self-consistent normalisation. One of these being that the measured density is appropriate to the selection procedures adopted, whether these are explicitly known or not and so this may help to avoid spurious detections of clustering. The question of the normalisation of n(z) will be returned to in Section 2.1.2.3. below where uncertainties in the estimate of the correlation function are discussed.

So far in this section no consideration has been given to how the selection method may affect estimates of, say, the clustering in a sample of galaxies. Obviously, if there is a connection between the selection quantity and the property to be estimated, then the results may depend on the selection method adopted. For example, in the model for n(z) in equation 2-11 above, intrinsically brighter galaxies are found at larger redshifts and, thus, a correlation between clustering and luminosity may lead to different clustering results being obtained from a sample selected by apparent magnitude, than

one, say, selected by volume, since each sample weights galaxies in a different way. Such considerations are obviously important for obtaining a clear picture of galaxy clustering and this will be borne in mind in succeeding chapters. In particular, in Chapter 3 the selection criteria for the 17^m redshift surveys discussed in this work will be described in more detail and in Chapter 5 estimates of dependencies, such as clustering on luminosity, will be presented.

2.1.1.2 Galaxy counts and the normalisation of n(z).

In the introduction to Section 2.1.1, it was shown how the counts of galaxies in a cell could be used to estimate the clustering properties of a sample of galaxies. In what follows now, the model for n(z) in equation 2-11 is used to predict the form of the mean counts for galaxies that are distributed uniformly within the sample volumes. This then not only allows for tests of homogeneity and fairness of the sample but also provides estimates of the form of clustering on various scales. As well as discussing the form of the models for these mean counts, some discussion of the uncertainties based on simple models will also be given. This then leads to a method for normalisation of the models.

It has been seen how the apparent density depends on redshift through the selection of galaxies via apparent magnitude. A simple one-dimensional count of galaxies is obtained from binning galaxies in redshift such that $\Delta N(z)$ is the count of galaxies in redshift interval z to $z+\Delta z$. In order to model this for the expected count $\Delta \langle N(z) \rangle$, the volume of the sample is needed as a function of redshift. In a Friedmann world model, to 4th order in z, this is

$$V(z) = (\Omega/3)(cz/H_o)^3[1-1.5(1+q_o)z] \qquad (2\text{-}13)$$

where Ω is the solid angle of the survey.

Thus, with the mean density in equation 2-11 the mean count of galaxies in an interval of redshift from z to z+dz is

$$d\langle N(z) \rangle = n(z)(dV(z)/dz)dz \qquad (2\text{-}14)$$

and this model for $d\langle N(z)\rangle$ using the Schechter model for $\phi(M)$ ($\alpha=-1$ in equation 2-12) is shown in Figure 2.1. In this figure the dashed line is for the spatially flat Universe with $q_o=0.5$ and $K=3.0$ whereas the solid line is the Euclidean count which ignores K- and curvature corrections. In this latter case $y_{min}(z)$ in equation 2-12 is

$$y_{min} = \beta^2 \qquad \beta = z/z^* \qquad z^* = H_oD^*/c \qquad (2\text{-}15)$$

where the characteristic depth D^* is given by

$$D^* = 10^{0.2(m_{lim}-M^*-25)} \qquad (2\text{-}16)$$

and so, $d\langle N(z)\rangle$ scaled as a function of D^* can be simply written as

$$d\langle N(\beta)\rangle = \Omega D^{*3}\phi^*\Gamma(\alpha+1,\beta^2)\beta^2 d\beta \qquad (2\text{-}17)$$

As the characteristic depth $z^*\approx0.076$ is typical of the 17^m surveys described in this work, the dashed line figure indicates that K- and curvature corrections to the luminosity and volume element are important at redshifts $z\gtrsim0.03$ and so the simple model in equation 2-17 must be modified to take account of this. However, the q_0 dependence in the luminosity relation and the volume element only has a small effect on the form of the dashed model (for example, the dotted line is the model which neglects the q_0 terms in equations 2-6 and 2-13) and so the K-correction will be generally kept whereas the curvature terms (involving q_0) will be omitted.

The characteristic depth D^* is a somewhat misleading term. It gives the distance to which an M^* galaxy can be seen and yet still be a part of the survey. A more appropriate measure for the distribution $d\langle N(z)\rangle$ is the peak depth which lies close to the mean or median. In the model in equation 2-17 ($\alpha=-1$) the peak lies at $0.66D^*$ ($0.59D^*$ in the dotted model in Figure 2.1) and this is a much more useful way to gauge a survey's mean depth.

As well as the differential counts $\Delta N(z)$, one can also measure the integral counts as a function of apparent limiting magnitude which for homogeneously distributed galaxies takes the form

13
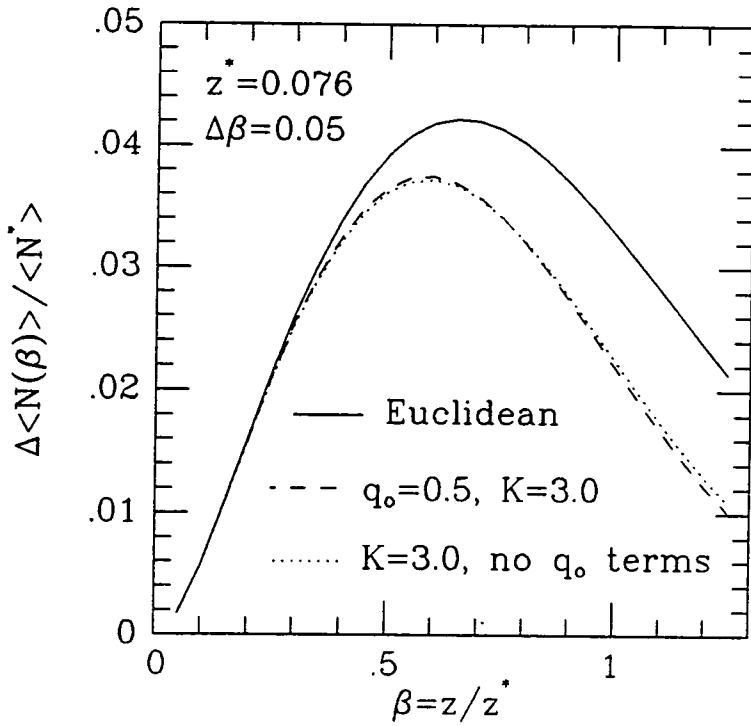
Figure 2.1. The preditions for the mean count $d\langle N(z)\rangle$ from the Schechter model (α=-1) for $n(z)$. The solid line is the Euclidean model count which neglects K- and curvature corrections to the luminosity and volume element. The dashed line is the predicted count for q_0=0.5 and K=3.0, whereas the dotted line is the count for K=3.0 but no q_0 terms. The predicted numbers are normalised to $\langle N*\rangle = \phi*\Omega D*^3/3$; the number of galaxies within the volume z<z* with density $\phi*$ (in the Euclidean limit).

$$\langle N(\leq m_{lim})\rangle = \int_0^\infty d\langle N(z)\rangle = \int_0^\infty n(z)(dV(z)/dz)dz \qquad (2\text{-}18)$$

The model in equation 2-18 neglecting K- and curvature corrections leads to the well-known result that the expected $\langle N(\leq m_{lim})\rangle$ and differential $d\langle N(m)\rangle$ number-apparent magnitude counts scale as $10^{0.6m}$. Given these models for the galaxy counts as a function of apparent magnitude and as a function of redshift one can examine how the counts behave for a galaxy sample. Deviations of the observed counts from the model can then be used to estimate the degree of homogeneity of the sample as well as testing the assumptions inherent in the model.

So what sort of variations from homogeneity are expected given a clustered distribution? Consider again the model described in the introduction to Section 2.1.1 above in which galaxies are clustered into tight clumps of m members. Unlike the situation there the count of galaxies seen in a volume will depend on redshift. The probability that a galaxy at redshift z will be in the sample is given by the selection function

$$\varphi(z) = n(z)/n \qquad (2\text{-}19)$$

where n is the density expected in the absence of a selection by apparent magnitude (according to equation 2-12 this is obtained as $z \to 0$, in which case n diverges in the Schechter model without a faint-end cut-off if $\alpha \leq -1$). Thus, in a volume V_i ($\gg v$, the volume of a clump) at redshift z_i where the selection function is approximately constant, the observed count of galaxies is roughly, for large m ($\gg 1$)

$$N_i \approx \varphi_i m N_c^i \qquad (2\text{-}20)$$

where N_c^i is the observed count of clumps in V_i. The expected number over many independent volumes is thus

$$\langle N_i\rangle = \varphi_i m \langle N_c^i\rangle \qquad (2\text{-}21)$$

at redshift z_i and so the expected variance in the galaxy count is

$$\langle (N_i - \langle N_i\rangle)^2\rangle = (\varphi_i m)^2 \langle N_c^i\rangle = \varphi_i m \langle N_i\rangle \qquad (2\text{-}22)$$

since the clumps are randomly distributed in V_i.

Thus, where the volumes V_i are much larger than the clustering length this model predicts that the percentage rms error $\langle(N_i-\langle N_i\rangle)^2\rangle^{1/2}/\langle N_i\rangle=1/\langle N_c\rangle^{1/2}$ is independent of the number of galaxies observed in each cluster, at least until φ_i (extrapolated) approaches unity whence a single galaxy, on average, is observed in each cluster ($\langle N_i\rangle=\langle N_c\rangle$) and the fluctuation again behaves like a Poisson distribution for the count of clusters. This again may be expected since it is the independent clusters which are causing the variance in N_i. As will be seen in the next section similar features to this model will also be seen when considering uncertainties in the estimates of the two-point correlation function.

One aspect of this model is that the expected variance on the count N_i depends on the product $\varphi_i\langle N_i\rangle$ and so the fluctuations will peak at a slightly different position from the peak in $d\langle N(z)\rangle$. Figure 2.2 shows the product of $n(z)d\langle N(z)\rangle$ for a model (solid line) in which $n(z)$ is given by equation 2-12 with $\alpha=-1$ and $d\langle N(z)\rangle$ by equation 2-14. The parameters for this model are the same as those for the dotted $d\langle N(z)\rangle$ model in Figure 2.1 ($z^*=0.076$, K=3.0, and no q_0 terms) and that model is reproduced in Figure 2.2 for comparison (dotted line). This latter figure shows that the peak in $n(z)d\langle N(z)\rangle$ occurs at ~50% of the peak in $d\langle N(z)\rangle$.

In the previous section the normalisation of $n(z)$ was briefly discussed and it was suggested that there may be reasons for normalising to the total count of galaxies in the sample. Given the differential $\Delta N(z)$ and integral $N(\leq m_{lim})$ counts there are several ways to achieve this. One method (the minimum variance method, see Davis and Huchra 1982) would be to weight the contribution from the galaxies observed in volume V_i by the inverse square of the error, i.e. by $1/\varphi_i m\langle N_i\rangle$ (each galaxy by $1/\varphi_i m$). Another would be to normalise just to the total number $N(\leq m_{lim})$. Since this latter count is dominated by the peak of the distribution of $d\langle N(z)\rangle$, the variance in $N(\leq m_{lim})$ is $\approx \varphi_i^{peak} m\langle N_i^{peak}\rangle$ whereas the minimum variance method gives more weight to larger volumes. However, the simple approach is to normalise to $N(\leq m_{lim})$ since this does not require a prior knowledge of the clustering within the sample (given by m) nor a knowledge of which model to assume (which may be affected by considerations of field shape, selection function etc.). In the following analysis the simple approach is adopted and this will be returned
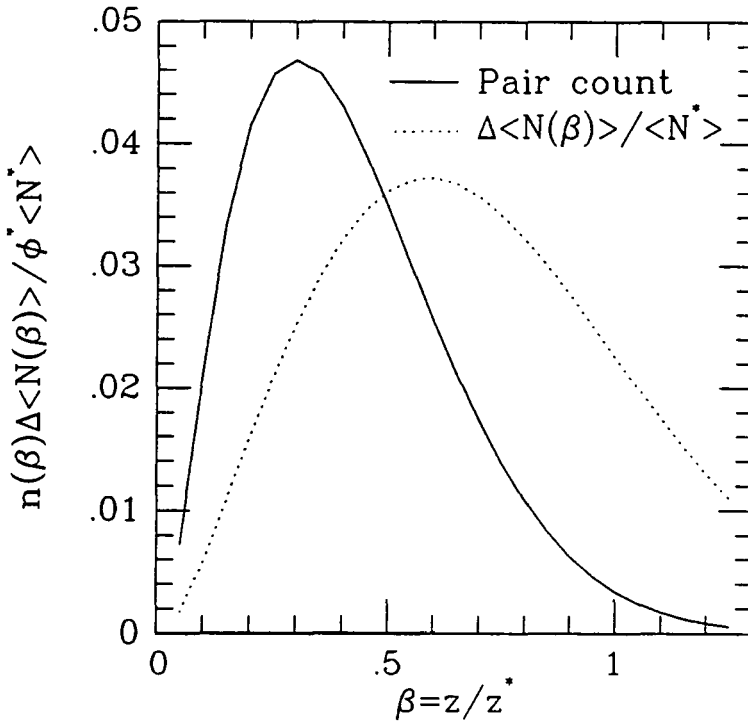
Figure 2.2. The Schechter model (α=-1) prediction for the form of the variance in the number count as a function of redshift. The solid line is the model $n(z)d\langle N(z)\rangle$ for the form of the variance which neglects the q_0 terms in equations 2-12 and 2-13 but has a K-correction of K=3.0. As will be seen below this model also describes the distribution of the count of galaxy pairs (see Section 2.1.2.2 below). The dotted line is the count $d\langle N(z)\rangle$ as in Figure 2.1 (also dotted).

to in Chapter 3.

2.1.2 The two-point correlation functions

2.1.2.1 The spatial two-point correlation function $\xi(r)$

The two-point correlation function was introduced at the beginning of Section 2.1.1 via the count of galaxies in a randomly placed cell; there it was seen to be related to the width of the frequency distribution of the count N. Although, this provides a useful way of illustrating the importance of the function, it is not necessarily the easiest way to define its measurement. A more direct method is via the count around a randomly chosen galaxy (see Peebles 1980)

$$dP = n(1+\xi(r))dV \qquad (2\text{-}23)$$

In this model, dP measures the conditional probability that a galaxy will be found in the elemental volume dV at a separation r from a galaxy randomly chosen from the global distribution. The two-point function $\xi(r)$ thus measures the excess probability of finding a galaxy in dV over a distribution which is randomly and homogeneously distributed (given by dP=ndV where n is, as usual, the homogeneous number density). As intimated in Section 2.1.1.1 $\xi > 0$ (<0) implies a clustered (or anticlustered) distribution, whereas $\xi = 0$ is homogeneous. The two-point function has been written explicitly as a function of r only in keeping with the assumption of homogeneity and isotropy of the general distribution. Thus, although this makes this statistic an easy one to measure it also limits the information ξ can provide, since any estimate will average the distribution over spherical shells around typical galaxies.

To estimate the correlation function from a sample of galaxies equation 2-23 must be manipulated into a form which is more suitable for measurement. If galaxies are selected by apparent magnitude then the mean number of galaxies expected in volume ΔV_{ij} at redshift z_j at a separation r from a randomly chosen galaxy i is (in which clustering is independent of luminosity)

$$\langle N_{ij}(r)\rangle = n(z_j)(1+\xi(r))\Delta V_{ij} \qquad (2\text{-}24)$$

where it is assumed that ξ and n are approximately constant over ΔV_{ij}.

16

Summing over all volumes ΔV_{ij} lying within the sample volume at separation r from i, and all contributions from randomly chosen galaxies i, the expected pair count is

$$\langle DD(r)\rangle = \left\{ \sum_i \sum_j n(z_j)\Delta V_{ij} \right\}(1+\xi(r)) \qquad (2\text{-}25)$$

The expression in curly brackets is the expectation value for the count of randomly distributed galaxies around the data

$$\langle DR(r)\rangle = \sum_i \sum_j n(z_j)\Delta V_{ij} \qquad (2\text{-}26)$$

and thus $\xi(r)$ can be written as

$$\xi(r) = \frac{\langle DD(r)\rangle}{\langle DR(r)\rangle} - 1 \qquad (2\text{-}27)$$

Thus, an estimate of $\xi(r)$ can be obtained from the sample by counting pairs DD(r) and DR(r) for all galaxies i in the sample and utilising equation 2-27. However, it should be emphasised that the measurement of the two-point function from a sample of galaxies will lead to an estimate of the correlation function that will differ in some random or systematic way from the global form for the whole distribution given by equation 2-23 and different estimators from equation 2-27 will lead to varying results for ξ (see, for example, Sharp 1979 and Hewett 1982).

2.1.2.2 The redshift two-point correlation functions $\xi_v(\sigma,\pi)$ and $\xi_s(s)$

In a sample of galaxies selected by redshift, the Hubble distance v_H/H_o cannot be inferred directly from the observed velocity since there will, in general, be a component of peculiar velocity;

$$v_{obs} = v_H + (\underline{v}_p.\hat{\underline{z}}) \qquad (2\text{-}28)$$

where $\hat{z}$ is a unit vector along the line-of-sight and $\underline{v}_p$ is the peculiar velocity vector of the observed galaxy. The form of these additional velocities generated in excess of the Hubble flow are either random motions or coherent (or streaming) flows and both of these can distort the form of the spatial map in redshift space (obtained by assuming that $v_H = v_{obs}$, see Kaiser 1987, White et al. 1987). In this case the redshift distance s between two galaxies with observed velocities v_1 and v_2 separated by an angle θ on the sky is given by

$$s = (v_1{}^2 + v_2{}^2 - 2v_1 v_2 \cos\theta)^{1/2}/H_o \qquad (2\text{-}29)$$

and this makes s a poor estimator of the true spatial separation r when the line-of-sight relative peculiar velocity ω [5] between the two galaxies is $\sim H_o s$. The distortion along the line-of-sight at $s \ll v_H/H_o$ will be approximately symmetrical about that direction, suggesting that the correlation function ξ_v estimated in redshift space will be a function of the variables (Peebles 1979)

$$\sigma \approx \theta(v_1 + v_2)/2H_o \quad \text{and} \qquad \pi \approx (v_1 - v_2)/H_o \qquad (2\text{-}30)$$

which are the perpendicular and parallel redshift separations between the two galaxies ($s^2 \approx \sigma^2 + \pi^2$).

Although the Hubble distance v_H cannot be separated directly from the peculiar velocity $\underline{v}_p.\hat{z}$ without a reliable independent estimate of the distance, $\xi(r)$ can, in principle, be obtained from $\xi_v(\sigma,\pi)$ by inversion (see, for example, Davis and Peebles 1983). However, in this case $\xi_v(\sigma,\pi)$ needs to be known accurately at all separations for the inversion to provide an accurate estimate of $\xi(r)$ and this is often difficult to achieve where ξ_v is small and uncertain. Thus, there will again be some dependence of the estimate of $\xi(r)$ on the form of the peculiar motions present in the galaxy distribution (and vice versa) and this tends to be a feature of the analysis of $\xi_v(\sigma,\pi)$.

A well known form of peculiar motions in redshift maps is the so-called 'Finger of God' effect caused by random velocities associated with virialised clustering. In its simplest form, the frequency distribution of such random velocities between galaxy pairs is expected to be isotropic and only slowly

<hr>

[5] For a Gaussian distribution of line-of-sight velocities with zero mean, the rms relative velocity $\langle \omega^2 \rangle^{1/2} = \sqrt{2} \langle (\underline{v}_p.\hat{z})^2 \rangle^{1/2}$

dependent on the separation between galaxies (Peebles 1976a). Thus if $f(\omega)$ is the normalised frequency distribution of ω then $\xi_v(\sigma,\pi)$ can be modelled as a convolution of f and ξ;

$$\xi_v(\sigma,\pi) = \int_{-\infty}^{\infty} \xi\{[\sigma^2+(\pi-\omega/H_0)^2]^{1/2}\}f(\omega)d\omega \qquad (2\text{-}31)$$

and this accounts for the smearing effect seen in redshift maps. Note that this assumes that the observed separation π is partly made up by a Hubble separation and partly by ω/H_0. In clusters that have separated from the Hubble flow this assumption may not be valid. Instead, the whole part will be made up by the relative peculiar motion ω.

In a clustering model that develops by gravitational growth, virialised motions must be important at small scales where the galaxies have had sufficient time to interact and randomise their velocities. Estimates of the rms relative peculiar velocity $\langle\omega^2\rangle^{1/2}$ put this scale at $\leq 3h^{-1}$ Mpc ($\langle\omega^2\rangle^{1/2}\approx 300$kms^{-1}, see Chapter 4 Section 4.3.3). At larger separations where the density contrasts are small, galaxies, on the other hand, are still expected to be falling into regions of denser clustering. These larger scale coherent flows also influence estimates of the redshift correlation function causing a flattening of ξ_v in the redshift direction. Models for this infall and a further discussion of virialised motions is given in Section 2.2.1 of this chapter.

To estimate $\xi_v(\sigma,\pi)$ from a sample of galaxies, a similar method is used to that described for $\xi(r)$ (equation 2-24). Instead, here, the mean number expected in volume ΔV_{ij} at redshift z_j from a randomly chosen galaxy i at coordinates (σ,π) is

$$\langle N_{ij}(\sigma,\pi)\rangle = n(z_j)(1+\xi_v(\sigma,\pi))\Delta V_{ij} \qquad (2\text{-}32)$$

As before, the observed counts $DD(\sigma,\pi)$ and $DR(\sigma,\pi)$ are formed by summing the contributions of all volume elements j lying in the sample volume V at separation (σ,π) from galaxy i (the sum over j of ΔV_{ij} is just $\Delta\pi\Delta A_i(\sigma)$ where $\Delta A_i(\sigma)$ is the area of the annulus in V) and all contributions from galaxies i in the sample. Since from isotropy $f(\omega)$ in equation 2-31 is symmetric in ω this makes $\xi_v(\sigma,\pi)$ symmetric in π and so the counts at (σ,π) can be combined with counts at $(\sigma,-\pi)$.

In the redshift surveys used in this work, samples of galaxies are obtained from fields with a small solid angle on the sky and this limits the information about $\xi_v(\sigma,\pi)$ in the perpendicular direction to the line-of-sight. In particular the expected count $\langle DD(\sigma,\pi)\rangle$ for a single field behaves like

$$\langle DD(\sigma,\pi)\rangle \approx (1+\xi_v(\sigma,\pi))\Delta\pi\Delta\sigma \int_0^\infty \bar{c}(z,\sigma)n(z)d\langle N(z)\rangle \qquad (2\text{-}33)$$

where $\bar{c}(z,\sigma)$ is the average circumference of the annulii within the field volume at redshift z. This assumes that π is smaller than the decrement in z over which n(z) changes significantly. It can be seen that at $\sigma \ll \theta_f cz/H_o$ (where θ_f is the maximum angular extent, in radians, of the solid angle of the field) $\bar{c}(z,\sigma) \approx 2\pi\sigma$ whereas for $\sigma \geq \theta_f cz/H_o$ then $\bar{c}(z,\sigma)=0$. From Figure 2.2 in Section 2.1.1.2 the peak of $n(z)d\langle N(z)\rangle$ occurs at $z\approx 0.023$ for the surveys used in this work and so $DD(\sigma,\pi)$ will provide useful information up to around the equivalent separation in σ, i.e. for $\sigma \lesssim 70\theta_f h^{-1}$ Mpc ($\sim 5h^{-1}$ Mpc for $\theta_f \approx 4°$). This limitation in the σ direction, which is a result of the narrow field shape used, is an important consideration for such surveys.

As the estimator $\xi_v(\sigma,\pi)$ attempts to describe a function of two variables, a complementary and less noisy estimator of the two-point function is the direction-averaged redshift correlation function $\xi_s(s)$. This is estimated from a galaxy sample in exactly the same way as for $\xi(r)$ indicated above in equation 2-27, except that s, instead of r, is held constant making $\xi_s(s)$ an average of $\xi_v(\sigma,\pi)$ over a spherical shell at s. This function can be modelled as

$$\xi_s(s) = \int_0^1 \xi_v{'}(s,\mu)d\mu \qquad (2\text{-}34)$$

where μ is the cosine of the angle between the line-of-sight and the line joining the two galaxies. $\xi_v{'}(s,\mu)$ is the function $\xi_v(\sigma,\pi)$ with the substitutions

$$\pi = s\mu \qquad \text{and} \qquad \sigma = s(1-\mu^2)^{1/2} \qquad (2\text{-}35)$$

However, in reality, as was seen with the estimation of $\xi_v(\sigma,\pi)$, not all of the spherical shell will be available for this average in fields which are narrow in shape. In particular $\xi_s(s)$ in this case will be more dominated by

pairs of galaxies that lie parallel rather than perpendicular to the line-of-sight and this, together with the effects of the selection function, makes this estimate more difficult to model directly. A more indirect numerical approach, and one which is favoured more by the author, is to use Monte Carlo simulations of the galaxy distribution for which the input form of $\xi(r)$ is known and then to estimate $\xi_s(s)$ using the selection functions, field shapes and random peculiar motions which are typical for the data. This then integrates the form of the model $\xi(r)$ indirectly to output a form for $\xi_s(s)$. This approach is discussed more fully in Section 2.1.4 below.

So far, the estimation of $\xi_s(s)$ has been discussed for scales of separation up to $\sim 10h^{-1}$ Mpc where peculiar motions are thought to cause deviations of $\xi_s(s)$ from $\xi(s)$ but at larger scales $\xi_s(s) \rightarrow \xi(s) \rightarrow \xi(r)$. For a survey of galaxies which contains several fields scattered over the sky it is possible, at these larger separations, to obtain an estimate of $\xi_s(s)$ that comes from between fields as well as one that is estimated from within the volumes. According to equation 2-24 this interfield $\xi_s(s)$ is measured by counting $\langle N_{ij}(s)\rangle$ for pairs of galaxies i and j that lie between two fields whereas the within-field estimate comes from i and j in the same field. A discussion of the interfield correlation function is given in Chapter 5.

2.1.2.3 The two-point correlation functions; errors in the estimates.

The most important consideration in the estimation of any quantity is the careful appraisal of the systematic and random errors associated with its measurement. In this section, the form of the errors in the measurement of the two-point function are described and, based on the methods outlined above, appropriate models for the errors are given. However, to facilitate the discussion of these errors, the relationship between ξ and the variance in the count of galaxies in a cell ($\langle (N-\langle N\rangle)^2\rangle$, see the introduction to Section 2.1.1) of volume V is explicitly derived as in Section 36 of Peebles (1980).

Imagine that the randomly placed volume V is divided up into elements of volume ΔV_i where i labels the position of ΔV in V. If N_i is the count of galaxies in volume ΔV_i, and ΔV_i is such that N_i is either 0 or 1 (with the probability of obtaining more than one galaxy in ΔV_i being an infinitessimal of higher order), then, over many such volumes V the expected count is

$$\langle N_i \rangle = \langle N_i^2 \rangle = \langle N_i^3 \rangle \ldots = n\Delta V_i \tag{2-36}$$

since $N_i{}^n = N_i$. The count in V is thus

$$N = \sum_i N_i \tag{2-37}$$

and its expectation value is

$$\langle N \rangle = \sum_i \langle N_i \rangle = \sum_i n\Delta V_i = nV \tag{2-38}$$

as before. To find the variance in the count N the relation

$$\langle (N - \langle N \rangle)^2 \rangle = \langle N^2 \rangle - \langle N \rangle^2 \tag{2-39}$$

can be used where the first term on the RHS can be split up into joint and disjoint volumes

$$\sum_i \sum_j \langle N_i N_j \rangle = \sum_i \langle N_i^2 \rangle + \sum_{i \, i \neq j} \sum_j \langle N_i N_j \rangle \tag{2-40}$$

the expectation value $\langle N_i N_j \rangle$ ($i \neq j$) is the joint probability of finding a galaxy in ΔV_i and in ΔV_j and hence, using equation 2-23, this is given by

$$\langle N_i N_j \rangle = n^2 (1 + \xi(r_{ij})) \Delta V_i \Delta V_j \tag{2-41}$$

Thus the variance takes the form

$$\langle (N - \langle N \rangle)^2 \rangle = \langle N \rangle + n^2 \sum_{i \, i \neq j} \sum_j \xi(r_{ij}) \Delta V_i \Delta V_j \tag{2-42}$$

which can be usefully expressed as

$$\frac{\langle (N - \langle N \rangle)^2 \rangle}{\langle N \rangle} = 1 + \frac{n}{V} \sum_{i \, i \neq j} \sum_j \xi(r_{ij}) \Delta V_i \Delta V_j \tag{2-43}$$

22

With the model given in the introduction to Section 2.1.1 where galaxies are clustered into tight clumps (volume $v \ll V$) of exactly m members

$$\sum_i \Delta V_i \{ \sum_j \xi(r_{ij}) \Delta V_j \} \approx V \int_V \xi(r) dV \qquad (2\text{-}44)$$

and so on comparison of equation 2-43 with equation 2-4

$$m \approx 1 + 4\pi n J_3(r) \qquad r \gg \sqrt[3]{v} \qquad (2\text{-}45)$$

where $J_3(r)$ is the integral

$$J_3(r) = \int_0^r r'^2 \xi(r') dr' \qquad (2\text{-}46)$$

This is an important relation for estimating errors in counts where the volume V is much larger than the volume occupied by typical clusters. However, where this assumption is not valid an effective value of m can be taken from equation 2-43.

To illustrate the importance of this model for determining the significance of the two-point function consider the estimate in V (no selection by apparent magnitude) of $\xi(r)$ at large scales (where ξ is small) for a bin between separations r_1 and r_2. As seen above this estimate is obtained from equation 2-27

$$\xi_e = \frac{DD(\bar{r})}{DR(\bar{r})} - 1 \qquad \bar{r} \approx \frac{r_1 + r_2}{2} \qquad (2\text{-}47)$$

with $DD(\bar{r})$ and $DR(\bar{r})$ being the observed data-data and data-random pair counts respectively. Thus, fluctuations in ξ_e come from not only DD but also DR since this contains an uncertain number of centres 'D' and an uncertain normalisation for 'R'. With many estimates of ξ_e from random placing of V, the expected rms fluctuation is

$$\langle (\xi_e - \xi_g)^2 \rangle^{1/2} = \langle [(DD/DR) - (\langle DD \rangle / \langle DR \rangle)]^2 \rangle^{1/2} \qquad (2\text{-}48)$$

where ξ_g is the global estimate of the correlation function as given by

equation 2-23. It may be expected in certain circumstances (where, for example, an estimate of the global density is used to normalise the mean density n) that fluctuations in the count DD will dominate this error and so taking that $DR \approx \langle DR \rangle$

$$\langle (\xi_e - \xi_g)^2 \rangle^{1/2} \approx \frac{\langle (DD - \langle DD \rangle)^2 \rangle^{1/2}}{\langle DR \rangle} \qquad (2\text{-}49)$$

If N_p is the number of distinct pairs contributing to $DD(\bar{r})$ ($DD(\bar{r})$ counts galaxies twice according to the method outlined in Section 2.1.2.1 and so $DD(\bar{r})=2N_p$) and the volume occupied by the shell between r_1 and r_2 is large compared to the clump size then

$$\langle (DD - \langle DD \rangle)^2 \rangle^{1/2} \approx 2m \langle N_p \rangle^{1/2} \qquad (2\text{-}50)$$

since, like the variance in the number counts (equations 2-4 and 2-43), the variance in the pair count is expected to be random in the number of clump pairs (N_p/m^2, Peebles 1973). Thus, from equation 2-49 the rms fluctuation in ξ is (Kaiser 1986a)

$$\delta\xi = \langle (\xi_e - \xi_g)^2 \rangle^{1/2} = \frac{2m \langle N_p \rangle^{1/2}}{\langle DR \rangle} \approx \frac{m}{\langle N_p \rangle^{1/2}} \qquad (2\text{-}51)$$

since for this model $\langle DR(\bar{r}) \rangle \approx \langle DD(\bar{r}) \rangle$. Thus, the observed form of the large-scale ξ can be compared with fluctuations from zero derived from a model where galaxies are clustered into clumps of m members.

In reality, equation 2-51 is only useful to a limited extent as there are other considerations to be taken into account in the model. As was seen above for $\xi_s(s)$ field shape and selection function in a magnitude limited sample will modify the form of the error and make $\delta\xi_e$ given above unreliable. For example, m given in equation 2-51, will depend on redshift not only through n(z) but also through the fact that the width of the bin in the direction perpendicular to the line-of-sight will be limited by the width of the field at redshift z. Further, the assumption that the volume of the bin is large compared to the clump size is likely to break down at smaller scales making equation 2-43 a more appropriate measure of the effective value of m. In any case, at smaller scales the form of $\delta\xi_e$ will depend on a different combination

of effects including the possible inclusion of higher order moments and peculiar motions.

At this point it is worth discussing possible weighting schemes for galaxy pairs that might reduce the rms error in ξ_e at large scales in this model. If each distinct galaxy pair contributes an independent amount δ_p to δDD in equation 2-49 then $(\delta DD(r))^2 = 4N_p\delta_p^2$, and so, from equation 2-50, $\delta_p = 1/m$. As the minimum variance in ξ_e is obtained by weighting according to the inverse square of the error, each pair should get a weight (Efstathiou 1988)

$$w_p = \frac{1}{m^2} \qquad (2\text{-}52)$$

This can be achieved by giving each galaxy in the survey a weight $1/m$ which again depends on redshift as previously described above. Note that this is like weighting according to the selection function for $4\pi n(z)J_3 \gg 1$ i.e. for $m \gg 1$ (Bean 1983), however, with equation 2-52 there is a natural cut-off to Poisson weight, i.e. $m \rightarrow 1$, as z becomes large.

As seen in Section 2.1.1.2 the advantage of this form of scheme over one which gives equal weight to each galaxy ($w_p = 1$, as in equation 2-47) is that equal volumes are given equal weight. However, the main difficulty with this method is that both the form of the correlation function and the appropriate model error for the sample is required in advance of the estimation of ξ. This and the fact that a stronger reliance is made on fewer pairs, which may or may not provide a more reliable estimate of ξ, may make this sort of weighting scheme unstable and difficult to implement. There is also the problem that at smaller scales m should be modified in some fashion, as in equation 2-43, to take account of the smaller bin sizes, otherwise the weight in equation 2-45 will make the error at small scales larger rather than smaller (Davis and Peebles 1983). Thus, in general, in the analysis described in this work w_p is set to unity for samples selected in the same fashion and Monte Carlo simulations (see Section 2.1.4) are used to calculate the model errors; this then deals with the volume dependencies (which would in an analytical model be otherwise difficult to calculate) indirectly .

So far in this section only random errors in the estimate of the correlation function have been discussed. As was seen in Section 2.1.1.1 the

mean homogeneous density n is a variable and the measurement of this quantity can lead to further systematic uncertainties in the estimate of $\xi(r)$. For a volume V, where N galaxies are observed (where again there is no magnitude selection), an estimate of the density would be $n_e=N/V$. Similarly, an estimate of the correlation function in V, using equation 2-27, would give, at a particular bin,

$$\xi_e = \frac{DD}{DR} - 1 \qquad (2\text{-}53)$$

(c.f. equation 2-47) where in the data-random pair count, DR, the estimate of the density n_e is used. Suppose now that the observed value for n_e was in error due to an unspecified cause and that a different value n_e' was measured where n_e' is not too dissimilar from n_e. In this case, the estimate of the correlation function at the same bin becomes

$$\xi_e' = \frac{DD}{DR'} - 1 \qquad (2\text{-}54)$$

where the superscript on R of DR' indicates that a different density estimate n_e' has been used for the random pair count. From equation 2-26, it is clear that the ratio of DR to DR' is just given by

$$\frac{DR}{DR'} = \frac{n_e}{n_e'} \qquad (2\text{-}55)$$

and so by equations 2-53, 2-54 and 2-55 the two estimates of the correlation function are related by

$$\xi_e' = \frac{n_e}{n_e'} (1+\xi_e) - 1 \qquad (2\text{-}56)$$

Thus, where the original estimate of the correlation function ξ_e was either much greater or much less than unity, the erroneous estimate divides into two regimes:-

$$\xi_e' \approx \frac{n_e}{n_e'} \xi_e \qquad |\xi_e| \gg 1$$

$$(2\text{-}57)$$

$$\xi_e{}' \approx \frac{n_e}{n_e{}'} - 1 \qquad |\xi_e| \ll 1$$

In the first instance it can be seen that, where the original correlation function is large, the erroneous estimate $\xi_e{}'$ differs by a factor of $n_e/n_e{}'$, whereas where ξ_e is small $\xi_e{}'$ has a constant positive (or negative) offset for when $n_e > n_e{}'$ (or $n_e < n_e{}'$). Thus, an error in the density estimate n_e of, say, ~10% can lead to a ~10% systematic amplitude difference at small scales and a systematic offset of ±0.1 at large scales. As will be seen in Chapter 5 it is important to bear in mind such possible variations in the estimates of the correlation function, especially at large scales where ξ is small.

The source of uncertainty in the estimate of the density, n_e, can either be random or systematic in origin. As was seen in Section 2.1.1.1 random errors in n_e can arise through sampling fluctuations where the observed number, N, of galaxies in V is randomly drawn from a distribution. This is the case if the volumes V are well separated so that their mean separation is much greater than the largest correlation length between galaxies. However, estimates of the density n_e are closely related to those of ξ_e and it is not a trivial matter to separate out the variations of one upon the other. For example, in equation 2-53, if there is a large fluctuation in the count N of galaxies in V then this will also tend to be reflected in a larger pair count DD and a larger number of centres D and so fluctuations in n_e caused by variations in the sampled N are likely to be smoothed out, to some extent, in the ratio DD/DR (Davis and Peebles 1983).

To obtain a handle on the expected variations in the estimate of the correlation function caused by fluctuations in the estimated density, the model above for an erroneous density estimate in the pair count DR will be expanded in more detail. In this case let the error in n_e be assumed to be a process that is independent of the clustering in V, and, further, let the volume V be large enough so that ξ_e and n_e approach their global forms; i.e. $\xi_e \approx \xi_g$ and $n_e \approx n_g$. Repeated observations of the correlation function $\xi_e{}'$ (obtained with density measurement $n_e{}'$) in different volumes V leads to an expected rms variation of (see equation 2-56)

$$\langle(\xi_e{}' - \xi_g)^2\rangle^{1/2} = (1 + \xi_g)\langle(\frac{n_g}{n_e{}'} - 1)^2\rangle^{1/2} \qquad (2\text{-}58)$$

Thus, with the assumption that $n_e{}'$ is a small random fluctuation from n_g

$$n_e' = n_g(1+\varepsilon) \qquad |\varepsilon| \ll 1 \tag{2-59}$$

then equation 2-58 becomes

$$\langle (\xi_e' - \xi_g)^2 \rangle^{1/2} \approx (1+\xi_g)\langle -\varepsilon + \varepsilon^2 \rangle^{1/2} \tag{2-60}$$

to second order in ε. For a random fluctuation about n_g, $\langle \varepsilon \rangle = 0$ leading to the result that

$$\langle (\xi_e' - \xi_g)^2 \rangle^{1/2} \approx (1+\xi_g)\langle \varepsilon^2 \rangle^{1/2} \qquad \varepsilon = \frac{n_e' - n_g}{n_g} \tag{2-61}$$

and so at small scales (where $\xi_g \gg 1$) this is the expected rms variation in the observed density n_e' about n_g scaled up by the correlation function whereas at large scales (where $\xi_g \ll 1$) this is just the rms variation.

Magnitude errors are an example of the type of error that can lead to fluctuations in the observed density. For instance, suppose that galaxies catalogued in V each have a small magnitude error Δm which is the same for all objects in V, and that repeated observations of different volumes leads to a fluctuation in Δm. For a given observed volume, which is not very deep

$$n_e' \approx 10^{-0.6\Delta m}n_g \qquad V \gg (D^*)^3 \tag{2-62}$$

which follows from equation 2-18 in the presence of a constant luminosity function. As before it is assumed that V is large enough so that $n_e \approx n_g$. Thus provided $0.6\Delta m$ is small then

$$n_e' \approx n_g(1-0.6\ln(10)\Delta m) \tag{2-63}$$

and so

$$\langle (\frac{n_e' - n_g}{n_g})^2 \rangle^{1/2} = 0.6\ln(10)\langle \Delta m^2 \rangle^{1/2} \tag{2-64}$$

i.e. the rms fluctuation on the density is directly related to the expected rms fluctuation on the magnitudes from volume to volume (note that $\langle \Delta m \rangle$ is assumed to be zero in keeping with equation 2-59).

In general it should be noted that the expected value of $\xi_e{}'$ over many volumes V does not equal that of the global function ξ_g. In this case

$$\langle\xi_e{}'\rangle = \langle\frac{n_g}{n_e}\rangle(1+\xi_g)-1 \qquad (2\text{-}65)$$

with the assumptions above that the volume V is large enough that $\xi_e \approx \xi_g$ and $n_e \approx n_g$. Further from equation 2-59

$$\langle\xi_e{}'\rangle \approx (1+\langle\varepsilon^2\rangle)(1+\xi_g)-1 \qquad (2\text{-}66)$$

again to second order in ε. Note the dependence on ε here is $\sim\langle\varepsilon^2\rangle$ whereas the rms fluctuation depended on $\langle\varepsilon^2\rangle^{1/2}$. This makes deviations of $\langle\xi_e{}'\rangle$ from ξ_g of the order $\sim 1/\langle\varepsilon^2\rangle^{1/2}$ smaller in this case. Thus again, like in equation 2-56, there is a systematic difference between $\langle\xi_e{}'\rangle$ and ξ_g. Here where the true correlation function is much greater than or less than unity it is found that

$$\langle\xi_e{}'\rangle \approx (1+\langle\varepsilon^2\rangle)\xi_g \qquad |\xi_g|\gg 1$$

$$\langle\xi_e{}'\rangle \approx \langle\varepsilon^2\rangle \qquad |\xi_g|\ll\langle\varepsilon^2\rangle\ll 1 \qquad (2\text{-}67)$$

and this is similar to the findings of Groth and Peebles (1977, equation 31) and Maddox et al. (1990a). The enhanced correlation function is understandable since the random errors in the estimation of the density mimics large-scale clustering in the volumes V and this shows up here. Note that the source of the increased correlation function comes from equations 2-56 and 2-59; symmetric variations in $n_e{}'$ do not lead to symmetric variations in $\xi_e{}'$, with the bias being to positive correlations.

So far sampling variations in the density n_e due to clustering have not been discussed because of the interconnection between the estimated correlation function and n_e in this case. However, as was noted above, the estimator for ξ_e in equation 2-53 is expected to be quite stable to clustering induced density fluctuations because of the cancelling effect in the ratio of DD/DR (see above). Suppose now that in volumes V, ξ_e approximates the global function ξ_g but the estimator $\xi_e{}'$ is measured using the global density. From equation 2-56 it is seen that the rms fluctuation in $\xi_e{}'$ expected in this case is

$$\langle(\xi_e{}'-\xi_g)^2\rangle^{1/2} \approx (1+\xi_g)\langle(\frac{n_e-n_g}{n_g})^2\rangle^{1/2} \qquad (2\text{-}68)$$

which is very similar to equation 2-58. The rms fluctuation on the density for volumes of the same size is just

$$\langle(\frac{n_e-n_g}{n_g})^2\rangle^{1/2} = \frac{\langle(N-\langle N\rangle)^2\rangle^{1/2}}{\langle N\rangle} \qquad (2\text{-}69)$$

where N and $\langle N\rangle$ are the observed and expected count of galaxies in V respectively. According to the model for the clustering described in the introduction to Section 2.1.1 in which galaxies are gathered into tight clumps (v«V) of exactly m members, the variance on the observed count is given by equation 2-4 and thus,

$$\langle(\xi_e{}'-\xi_g)^2\rangle^{1/2} \approx (1+\xi_g)(\frac{m}{\langle N\rangle})^{1/2} \qquad (2\text{-}70)$$

which implies $\delta\xi/\xi \approx (m/\langle N\rangle)^{1/2}$ at scales where $\xi_g \gg 1$ and $\delta\xi \approx (m/\langle N\rangle)^{1/2}$ where $\xi_g \ll 1$. In this case the expected value of $\xi_e{}'$ is just $\langle\xi_e{}'\rangle = \xi_g$ as may be anticipated since the expectation of n_e, $\langle n_e\rangle = n_g$.

As stressed above such models for the uncertainty in $\xi(r)$ arising from clustering induced fluctuations must be treated with caution and are only a guide to the likely size of the errors. In a magnitude limited sample the variation in the count N observed to a limit m_{lim} can be obtained from the appropriate (for the limit) two-point angular correlation function $\omega(\theta)$ defined in a similar fashion to $\xi(r)$ (see Section 2.1.2.4 below). In this case

$$\frac{\langle(N-\langle N\rangle)^2\rangle}{\langle N\rangle} = 1+\frac{\langle N\rangle}{\Omega^2}\int\int_\Omega d\Omega_1 d\Omega_2 \omega(\theta_{12}) \qquad (2\text{-}71)$$

(Peebles 1980, equation 45.6) where $\omega(\theta)$ is integrated over the solid angle Ω of the survey. As will be seen in Chapter 5 this is a useful way of predicting the rms variance in the counts if a model for $\xi(r)$ and the luminosity function for the sample is assumed.

Finally, there is a further systematic uncertainty in the observed

correlation function arising from the use of the observed numbers of galaxies in a sample to normalise the mean background density n. This so called integral constraint (Peebles 1980, Section 32) can be illustrated with a simple heuristic description again based on the model with galaxies distributed in tight clumps of m objects per clump (see the introduction to Section 2.1.1). Thus, at a separation r much larger than the size of the clumps but much smaller than the volume of the sample the observed number of data-data pairs for a sample of N galaxies is

$$DD \approx N\Delta V(n_e - \frac{m}{V}) \qquad n_e = \frac{N}{V} \qquad\qquad (2-72)$$

since siting the centre of the shell of volume ΔV on a galaxy (and thus a clump) has biassed the mean density for this pair count low by $n_e - m/V$. As the data-random count is just

$$DR \approx Nn_e\Delta V \qquad\qquad (2-73)$$

this implies ξ_e will be biassed low by a constant of order (see equation 2-53)

$$C = -\frac{m}{N} \qquad\qquad (2-74)$$

and this is small if the number of galaxies in the sample is large with respect to the mean number of galaxies per cluster.

This simple heuristic model is difficult to apply to the magnitude limited surveys discussed in this work because of the necessary inclusion in this model of the field shape and selection function appropriate to these samples. In this case it is simpler to refer directly to the constraint on the estimate ξ_e in such a sample, viz;

$$\int\int_V n_e(R_1)n_e(R_2)(1+\xi_e(r_{12}))dV_1dV_2 \quad = N(N-1) \qquad\qquad (2-75)$$

which relates the integral number of pairs (LHS) observed in a volume V ($\approx D^{*3}$) to the total number available (RHS). Here $n_e(R)$ is the estimate of the density at distance R ($=cz/H_o$) and since this is normalised to the observed number of galaxies in the sample (brighter than some limit), this can be

written as

$$n_e(R) = \frac{N}{\langle N \rangle} n_g(R) \qquad (2\text{-}76)$$

Here $n_g(R)$ is the global estimate of the mean density and it is assumed that the luminosity function variations are small from sample-to-sample. Thus equations 2-75 and 2-76 give directly that

$$\int \int_V n_g(R_1)n_g(R_2)\xi_e(r_{12})dV_1dV_2 \ = -\frac{\langle N \rangle^2}{N} \qquad (2\text{-}77)$$

and, assuming that ξ_e differs from ξ_g by some constant C (as suggested above) this implies

$$C \approx -\frac{1}{N} - \frac{1}{\langle N \rangle^2}\int \int_V n_g(R_1)n_g(R_2)\xi_g(r_{12})dV_1dV_2 \qquad \xi_e \approx \xi_g + C \qquad (2\text{-}78)$$

As will be seen in the following section (equation 2-85) the integral on the RHS over the volume V is related to the integral of the global angular correlation function $\omega(\theta_{12})$ over the solid angle Ω of the sample so that

$$\frac{\langle N \rangle^2}{\Omega^2}\int \int_\Omega d\Omega_1 d\Omega_2 \omega_g(\theta_{12}) \ = \int \int_V n_g(R_1)n_g(R_2)\xi_g(r_{12})dV_1dV_2 \qquad (2\text{-}79)$$

and together with equation 2-71 this gives

$$C \approx -(\frac{1}{N} - \frac{1}{\langle N \rangle}) - \frac{\langle (N-\langle N \rangle)^2 \rangle}{\langle N \rangle^2} \qquad (2\text{-}80)$$

and this relates C to the expected variation in the count of objects in the sample brighter than the apparent limit. Taking the expectation value of C over many independent samples and expanding 1/N as a function of $\langle N \rangle$ it can be shown that, to second order,

$$\langle C \rangle \approx -\frac{m'}{\langle N \rangle} \qquad (2\text{-}81)$$

similar to equation 2-74 above except that m´ is defined like equation 2-4 with

N refering to the count of galaxies brighter than the limit of the sample. This again is a particularly useful way to predict this effect on the estimated correlation function.

2.1.2.4 The projected two-point correlation functions $\omega(\theta)$ and $\omega_v(\sigma)$

Prior to the advent of systematic redshift surveys objective studies of large-scale structure in the Universe were confined to 2-d catalogues of magnitudes and positions. Studies of the large-area (~half sky) maps such as those of Zwicky et al. (1961-68) and Shane and Wirtanen (1967, the Lick Catalogue), by Peebles and his collaborators (see Peebles 1980 and references therein) led to a first-order analysis of the galaxy distribution which motivated much of the present day work into the formation of galaxies and galaxy structures. With the construction of more homogeneous galaxy catalogues in the southern galactic cap from objective machine measurements (Heydon-Dumbleton et al. 1989, Collins et al. 1988b, Maddox et al. 1988, Maddox et al. 1990b, Maddox et al. 1990c) of deep UK Schmidt plates there arises the opportunity to obtain a more consistent picture of galaxy clustering from both the 2-d and 3-d distributions. However, because of the loss of signal-to-noise of the clustering in projection, the 2-d data is more prone to systematic errors such as non-uniformities in plate-to-plate detection and this makes the observation of structure at large angular (and spatial) scales still somewhat uncertain.

The two-point angular correlation function is defined in a similar way to that of the spatial function (see equation 2-23);

$$dP = N(1+\omega(\theta))d\Omega \qquad (2\text{-}82)$$

Here dP measures the conditional probability that a galaxy will be found in an elemental solid angle $d\Omega$ at an angular separation θ from a randomly chosen galaxy. N is the mean density of objects per unit solid angle at the limit of the catalogue, i.e. $N = \langle N(\leq m_{lim})\rangle/\Omega$ in equation 2-18.

As stated in the introduction to Section 2.1 the distinct advantage of the two-point correlation function is that there exists a simple linear integral relation between its spatial and angular forms (Limber 1953). In the Euclidean

limit and in the absence of a correlation between luminosity and clustering, this relation can simply be obtained as follows. From equation 2-23 (see also equation 2-41) the probability of observing a galaxy in volumes dV_1 and in dV_2 at distances R_1 (=cz_1/H_0) and R_2 respectively is

$$dP = n(R_1)n(R_2)(1+\xi(r_{12}))R_1^2 dR_1 d\Omega_1 R_2^2 dR_2 d\Omega_2 \qquad (2\text{-}83)$$

where n(R) is the apparent mean homogeneous density at distance R and dV has been written as $R^2 dR d\Omega$. The probability dP' that a galaxy lies in $d\Omega_1$ and in $d\Omega_2$ comes from summing all contributions from volume elements along the line-of-sight

$$dP' = \int_0^\infty dR_1 \int_0^\infty dR_2 n(R_1)n(R_2)R_1^2 R_2^2 (1+\xi(r_{12})) d\Omega_1 d\Omega_2 \qquad (2\text{-}84)$$

Thus, from equation 2-82 it follows that

$$\omega(\theta_{12}) = \frac{1}{N^2} \int_0^\infty dR_1 \int_0^\infty dR_2 n(R_1)n(R_2)R_1^2 R_2^2 \xi(r_{12}) \qquad (2\text{-}85)$$

with

$$r_{12}^2 = R_1^2 + R_2^2 - 2R_1 R_2 \cos\theta_{12} \qquad (2\text{-}86)$$

For the case where the correlation length between galaxies is much less than both the width of the distribution $n(R)R^2 dR$ (which is $d\langle N(R)\rangle$, see equation 2-14 and Figure 2.1) and the distance to its peak, then equation 2-85 becomes

$$\omega(\theta_{12}) = \frac{1}{N^2} \int_0^\infty dR_1 n(R_1)^2 R_1^4 \int_{-\infty}^\infty dr_\| \xi\{[r_\|^2 + (R_1\theta_{12})^2]^{1/2}\} \qquad (2\text{-}87)$$

This is the small angle approximation in which the separation r_{12}^2 is written as a sum of the parallel ($r_\|^2$) and perpendicular [($R_1\theta_{12})^2$] distances. From this it is clear that $\xi(r)$ is smoothed in projection by both the integration over the separations $r_\|$ and R_1 and this makes $\omega(\theta)$ a poor discriminator of true spatial features in $\xi(r)$ (Fall and Tremaine 1977, Peebles 1980).

With the scaling for the distance R as in equation 2-15 (R=βD*) $\omega(\theta)$

for a Schechter function (equation 2-8) takes the useful form (equation 2-87 with equations 2-12 and 2-15)

$$\omega(\theta) = \frac{1}{D^*} \frac{\int_0^\infty d\beta \Gamma(\alpha+1,\beta^2)^2\beta^4 \int_{-\infty}^\infty dr_{\shortparallel}\xi\{[r_{\shortparallel}^2+(\beta D^*\theta)^2]^{1/2}\}}{[\int_0^\infty d\beta \Gamma(\alpha+1,\beta^2)\beta^2]^2}$$

$$= \frac{1}{D^*} W(\theta D^*)$$

(2-88)

and this can be numerically integrated for any function $\xi(r)$ to output the corresponding function $\omega(\theta)$. Peebles (1980, Section 52) has shown that this approximation is reasonably accurate out to scales of ~30°.

In Figure 2.3 the original observations of $\omega(\theta)$ from the $m_B\le19^m.0$ Lick (Groth and Peebles 1977) and the $m_B\le15^m.0$ Zwicky Catalogues (Peebles and Hauser 1974) are presented together with the results from a small objective machine-measured catalogue to $b_J\le21^m$ by Stevenson et al. (1985). Although these samples have been selected at different magnitude limits the scaling relation for $\omega(\theta)$ (similar to equation 2-88 but incorporating curvature and K-correction terms) allows the deeper catalogues to be compared at the same depth as the Zwicky Catalogue. These results show that $\omega(\theta)$ is quite a good power law in the range $0.04°\le\theta\le6°$ with

$$\omega(\theta) \approx 0.65 \; \theta^{-0.8}$$

(2-89)

and this is shown as a dashed line in the figure. However, at scales larger than ~6° there appears to be a break away from this small-angle behaviour although the position and existence of this feature is somewhat uncertain. From the peak in the $\Delta N(z)$ distribution in the CfA $m_B\le14^m.5$ sample (Davis and Huchra 1982) the peak in the Zwicky $m_B\le15^m.0$ $d\langle N(R)\rangle$ sample is predicted to occur at $D_{peak}\approx50h^{-1}$ Mpc corresponding to a D^* of ~76h^{-1} Mpc and on a naive basis this would imply a break in the spatial correlation function at roughly ~$D_{peak}\theta_{break} \approx 5h^{-1}$ Mpc ($d\langle N(R)\rangle$ is peaked around D_{peak}; see Figure 2.1 of Section 2.1.1.2).

The evidence for a pure power law in $\omega(\theta)$ over such a large angular scale was taken as evidence that $\xi(r)$ also exhibits a scale-free form (Peebles
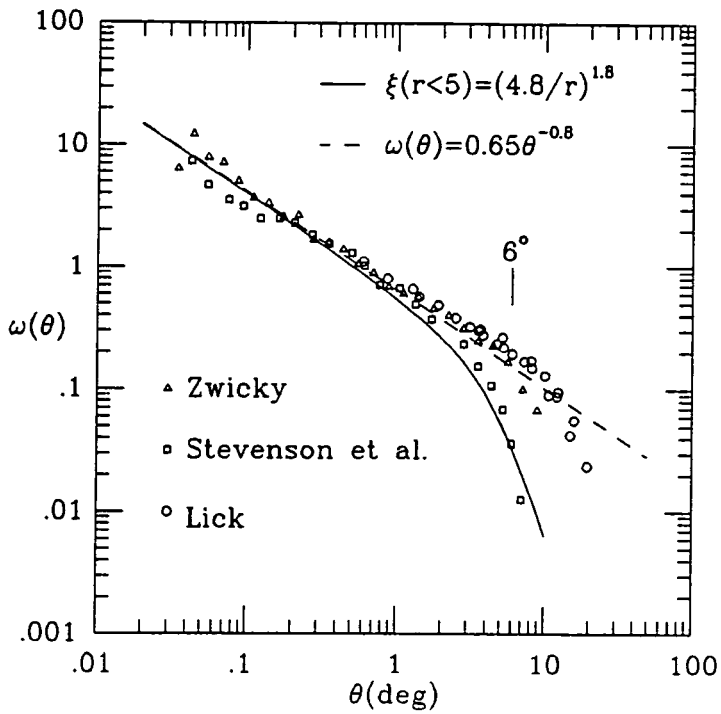
Figure 2.3. Observations of the angular correlation function $\omega(\theta)$ at the depth of the Zwicky Catalogue. The dashed line the power law which describes the observations in the range $0.04°{\le}\theta{\le}6°$. The solid line is the model for $\omega(\theta)$ (equation 2-88) in which $\xi(r)$ is the power law $\xi(r){=}(4.8/r)^{1.8}$ for $r{\le}5h^{-1}$ Mpc and $\xi(r){=}0$ at larger scales. In this model $\alpha{=}{-}1$ and $D^{*}{=}76h^{-1}$ Mpc.

1974, see also the introduction to Section 2.1). With the assumption that $\xi(r)$ is represented as

$$\xi(r) = (r_0/r)^\gamma \qquad (2\text{-}90)$$

with r_0 as a clustering scale length and γ the power-law index, $\xi(r)$ can be integrated via equation 2-88 to give

$$\omega(\theta) = A\theta^{1-\gamma} \qquad (2\text{-}91)$$

The amplitude A for θ in degrees is

$$A = (\frac{r_0}{D^*})^\gamma (\frac{\pi}{180})^{1-\gamma} 2H_\gamma \frac{\int_0^\infty d\beta\, \Gamma(\alpha+1,\beta^2)^2\beta^{5-\gamma}}{[\int_0^\infty d\beta\, \Gamma(\alpha+1,\beta^2)\beta^2]^2} \qquad (2\text{-}92)$$

and H_γ, given by

$$H_\gamma = \int_0^\infty dx(1+x^2)^{-\gamma/2} \qquad (2\text{-}93)$$

converges to a product of Gamma functions for $\gamma > 1$

$$H_\gamma = \frac{\Gamma(1/2)\Gamma[(\gamma-1)/2]}{2\Gamma(\gamma/2)} \qquad (2\text{-}94)$$

Thus, from the observed result for $\omega(\theta)$ summarised in equation 2-89, $\gamma \approx 1.8$ and $r_0 \approx 4.8h^{-1}$ Mpc with the above D^* (since for $\alpha = -1$ $A \approx 93(r_0/D^*)^{1.8}$) which is close to the results in Groth and Peebles (1977).

The discovery that a possible break scale in $\xi(r)$ occurs roughly at where $\xi(r) \approx 1$ is of strong physical interest since, on the assumption that galaxies trace the mass distribution, this separation is approximately where there is expected to be a transition between linear ($\xi < 1$) and non-linear ($\xi > 1$) clustering (Davis et al. 1977). However, such inferences from the data need careful inspection in the light of the smoothing properties of $\omega(\theta)$ (equation 2-87). In Figure 2.3, the solid line is a direct integration, via equation 2-88, of a two-component model for $\xi(r)$; $\xi(r) = (4.8/r)^{1.8}$ for $r \leq 5h^{-1}$ Mpc and $\xi(r) = 0$ at

36

larger scales. As can be seen at angles less than ~1° there is close agreement between the model and data as might be expected and, further, at much larger separations the shape in the turnover of $\omega(\theta)$ is also well matched. However, as noted by Bean (1983) the break in the model appears to occur at a much smaller angle than predicted above ($\theta_{break}=6°$ is marked) and this is a result of the small-scale (<5h^{-1} Mpc) form of $\xi(r)$ smoothing out with the break in projection.

As pointed out by Soneira and Peebles (1978) these observations would seem to imply there is more large-scale power in $\xi(r)$ than the above model seems to suggest. However, because of the projection properties of $\omega(\theta)$ this does **not** necessarily imply a simple continuation of the spatial power-law to larger scales (see Chapter 5), although this is a possibility. A careful analysis of the 2-d and 3-d distributions, as said above, may lead to a more consistent picture for the clustering.

As seen in Section 2.1.2.2, in a redshift catalogue the correlation function $\xi_v(\sigma,\pi)$ differs from the spatial correlation function $\xi(r)$ at small separations due to the peculiar motions between galaxy pairs. However, as this distortion is confined to the line-of-sight, it is, as in $\omega(\theta)$, possible to infer information concerning the form of $\xi(r)$ from a projection of $\xi_v(\sigma,\pi)$ along the π direction (Peebles 1979, 1980, Bean 1983, Bean et al. 1983). This makes use of pair conservation

$$\omega_v(\sigma) = \int_0^{\pi_{cut}} \xi_v(\sigma,\pi)d\pi \qquad (2\text{-}95)$$

(where the limit π_{cut} is introduced for the observational reasons discussed below)
which becomes

$$\omega_v(\sigma) \approx \int_0^{\pi_{cut}} \xi[(\sigma^2+\pi^2)^{1/2}]d\pi \qquad (2\text{-}96)$$

in the limit where π_{cut} is large enough to include the majority of pairs that are smeared by peculiar motions. For example, in the random motion model for $\xi_v(\sigma,\pi)$ in equation 2-31, this will occur when $\pi_{cut} \gg \langle\omega^2\rangle^{1/2}/H_o$.

The function $\omega_v(\sigma)$ is then, in this limit, similar to the $r_{\parallel}$ integral in equation 2-87, but differs from $\omega(\theta)$ in that the redshift information can be used to increase the signal-to-noise of the observations by excluding possibly

37

uncorrelated pairs at separations $\pi > \pi_{cut}$ (in equation 2-87 the projected function is further smoothed with the distribution $[d(N(R))/dR]^2$). Further, by reducing π_{cut} to where the galaxy signal-to-noise in $\xi_v(\sigma,\pi)$ is significant, the inclusion of systematic offsets in ξ caused by background normalisation errors (see Section 2.1.2.3) can be avoided. However, as with $\omega(\theta)$, the projection inherent in $\omega_v(\sigma)$ makes the interpretation of the data ambiguous, and a careful treatment by direct modelling (i.e. numerical integration of equation 2-96) is required, to understand the effects.

Firstly, with a power-law correlation function for $\xi(r)$ as in equation 2-90, $\omega_v(\sigma)$ (equation 2-96) becomes

$$\omega_v(\sigma) = H_\gamma(\pi_{cut}/\sigma)r_o{}^\gamma\sigma^{(1-\gamma)} \qquad (2\text{-}97)$$

Here, $H_\gamma(\pi_{cut}/\sigma)$ is the integral

$$H_\gamma(\pi_{cut}/\sigma) = \int_0^{\pi_{cut}/\sigma} (1+x^2)^{-\gamma/2}dx \qquad (2\text{-}98)$$

which asymptotes to H_γ (equation 2-94) when $\pi_{cut}/\sigma \gg 1$ and $\gamma>1$. In Figure 2.4 the solid line with $\pi_{cut}=10h^{-1}$ Mpc, $\gamma=1.8$ and $r_o=5h^{-1}$ Mpc is compared to the asymptotic model, $\pi_{cut} \gg \sigma$, (dashed line) with the same parameters. As may be expected, at small σ ($\lesssim 1h^{-1}$ Mpc) the dependence on π_{cut} is relatively weak, but at larger separations the solid model decreases more rapidly than the power law of $\sigma^{-0.8}$, in spite of integrating the power-law $\xi(r)$ to a larger separation r (for example, at $\sigma=10h^{-1}$ Mpc, $r \approx 14h^{-1}$ Mpc). To make this more apparent, the dotted line in Figure 2.4 is a direct integration of equation 2-96 in which the correlation function is given by $\xi(r)=(5/r)^{1.8}$ for $r \leq 10h^{-1}$ Mpc and $\xi(r)=0$ at larger scales; this decreases even more rapidly than the above models at the largest separations.

This fall below a single power law in the model $\omega_v(\sigma)$ at $\sigma \geq 1h^{-1}$ Mpc is similar to that seen in $\omega(\theta)$; the finite cut-off in equation 2-95 acts like a break in $\xi(r)$ and so the correlation function ξ at $r \leq 10h^{-1}$ Mpc is effectively smoothed with $\xi=0$ at larger scales (Bean 1983). The uncertain nature of $\xi(r)$ at $r \geq 10h^{-1}$ Mpc makes $\omega_v(\sigma)$ at $\sigma \geq 1h^{-1}$ Mpc difficult to interpret and sensitive to the choice of π_{cut}. In this light it is inadvisable to fit a $\sigma^{-0.8}$ power law to the entire range of data up to $\sigma=10h^{-1}$ Mpc, as did Bean et al. (1983) for the

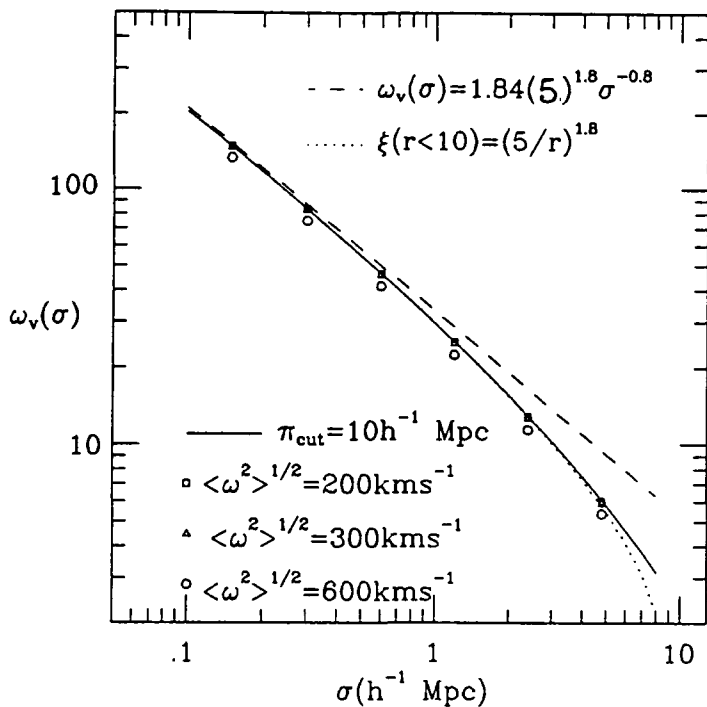**Figure 2.4.** Model predictions for the projected two-point correlation function $\omega_v(\sigma)$. The solid line is the model in equation 2-97 with $\xi(r)=(5.0/r)^{1.8}$ integrated up to a π_{cut} of $10h^{-1}$ Mpc. The dashed line is the power-law asymptotic form of this equation (same parameters) with $\pi_{cut}\gg\sigma$. The dotted line model is a direct integration of equation 2-96 in which $\xi(r)$ is $\xi(r)=(5/r)^{1.8}$ for $r\leq 10h^{-1}$ Mpc and $\xi(r)=0$ at larger scales. The open symbols in this figure illustrate the effects of random peculiar motions; here equation 2-95 is integrated directly using a model for $\xi_v(\sigma,\pi)$ from equation 2-31.

Durham/AAT Survey. A more consistent estimate of the correlation function at small scales may come from $\sigma \leq 1h^{-1}$ Mpc.

To assess the importance of the assumption of a finite π_{cut} for inclusion of the majority of pairs smeared by peculiar motions, Figure 2.4 also shows (at various values of σ) a direct numerical integration of equation 2-95 with a range of pair-wise rms velocities $\langle \omega^2 \rangle^{1/2}$ (the model for $\xi_v(\sigma,\pi)$ comes from equation 2-31). Here the spatial correlation function is again $\xi(r)=(5/r)^{1.8}$ to a π_{cut} of $10h^{-1}$ Mpc and the figure shows that even with $\langle \omega^2 \rangle^{1/2}=600kms^{-1}$ this limit in π leads to an underestimate of $\omega_v(\sigma)$ of only ~6% in r_0. However, this is a model for random motions; there is also a possibility that infall may be present in the data and this is discussed later in Chapters 4 and 5.

2.1.3 The three-point correlation function

The three-point correlation function is related to the third moment of the distribution of counts in a cell (see Section 2.1.1) and, as such, is more difficult to estimate than the two-point function $\xi(r)$. A more practical definition of this function is through the probability of obtaining triplets of galaxies (Peebles 1980, Section 34)

$$dP = n^3[1+\xi(r_1)+\xi(r_2)+\xi(r_3)+\zeta(r_1,r_2,r_3)]dV_1dV_2dV_3 \qquad (2-99)$$

in which dP is the probability of finding a galaxy in each of the elemental volumes dV_1, dV_2 and dV_3 at the vertices of a triangle of sides r_1, r_2 and r_3. $\zeta(r_1,r_2,r_3)$ is the reduced part of the 3-point function and, under the assumption of homogeneity and isotropy of the general galaxy distribution, is written as a symmetric function of r_1, r_2 and r_3. Note that equation 2-99 describes the distribution of galaxies around randomly chosen pairs, and so, if galaxies are tracers of the mass distribution, the three-point function provides the form of the gravitational potential well for such galaxies. As will be seen in Section 2.2.2.1 below, this is an essential part of the Cosmic Virial Theorem (Peebles 1976a) applied to the distribution.

To estimate $\zeta(r_1,r_2,r_3)$, consider the mean count of triplets of galaxies $\langle DDD \rangle$ in some small but finite volumes ΔV_2 and ΔV_3 given that a galaxy has already been identified in ΔV_1 (Peebles and Groth 1975)

$$\langle DDD \rangle = \langle DRR \rangle (1 + \xi(r_1) + \xi(r_2) + \xi(r_3) + \zeta(r_1,r_2,r_3)) \qquad (2\text{-}100)$$

in which $\langle DRR \rangle = n^2 \Delta V_2 \Delta V_3$, is the count of randomly distributed pairs around the data. The count of data pairs in ΔV_2 and ΔV_3 for a randomly distributed galaxy identified in ΔV_1 is

$$\langle RDD \rangle_1 = \langle DRR \rangle_1 (1 + \xi(r_1)) \qquad (2\text{-}101)$$

where r_1 is opposite the vertex for volume ΔV_1. Likewise, similar expressions can be written for each vertex, and so the total data pair count around a randomly placed galaxy is

$$\langle DDR \rangle = \langle RDD \rangle_1 + \langle DRD \rangle_2 + \langle DDR \rangle_3 \qquad (2\text{-}102)$$

Thus it is easy to see that in equation 2-100, for $\Delta V_1 = \Delta V_2 = \Delta V_3$

$$1 + \xi(r_1) + \xi(r_2) + \xi(r_3) = \frac{\langle DDR \rangle}{\langle DRR \rangle} - 2 \qquad (2\text{-}103)$$

and so

$$\zeta(r_1,r_2,r_3) = \frac{\langle DDD \rangle - \langle DDR \rangle}{\langle DRR \rangle} + 2 \qquad (2\text{-}104)$$

It follows that an estimate of $\zeta(r_1,r_2,r_3)$ can be obtained from counting triplets DDD, DDR and DRR observed in the data for fixed triangles of sides r_1, r_2 and r_3 and utilising the above equation.

In redshift surveys of galaxies, as with the two-point function, the redshift form of the 3-point function is distorted by peculiar motions for scales where $H_0 r \approx |\underline{v}_p|$. Thus, in order to reduce the effects of these velocities, a projected form of the three-point function $z_v(\sigma_1,\sigma_2,\sigma_3)$ can be measured in a similar way in which $\omega_v(\sigma)$ was defined for $\xi_v(\sigma,\pi)$ (see Section 2.1.2.4). The projected 3-point function z_v can be obtained from counting triplets DDD, DDR and DRR for fixed triangles of projected sides σ_1, σ_2 and σ_3 within all π separations up to a maximum π_{cut}. The expectation value of z_v is then identical to ζ in equation 2-104 above in terms of these triplet counts.

In the surveys discussed in this work, the narrow fields again limit information about $z_v(\sigma_1,\sigma_2,\sigma_3)$ to separations $\sigma \approx 5h^{-1}$ Mpc (where galaxies have been given equal weight in the triplet counts). Thus unlike the two-point function, which can be derived from ξ_s to large s, the three-point function information gathered from such surveys is quite restricted. From the analysis of galaxy catalogues, Groth and Peebles (1977) showed that $\zeta(r_1,r_2,r_3)$ may be reasonably approximated by

$$\zeta(r_1,r_2,r_3) = Q\{\xi(r_1)\xi(r_2)+\xi(r_2)\xi(r_3)+\xi(r_1)\xi(r_3)\} \qquad (2\text{-}105)$$

and so z_v looks like

$$z_v = Q\{\omega_v(\sigma_1)\omega_v(\sigma_2)+\omega_v(\sigma_2)\omega_v(\sigma_3)+\omega_v(\sigma_1)\omega_v(\sigma_3)\} \qquad (2\text{-}106)$$

where $\omega_v(\sigma)$ is formed from the mean data-data and data-random counts to π_{cut}

$$\omega_v(\sigma) = \frac{\langle DD \rangle}{\langle DR \rangle} - 1 \qquad (2\text{-}107)$$

Hence, for the Cosmic Virial Theorem studies in this work, this form is assumed and so Q, the amplitude of the three-point function, is the single independent parameter to be estimated.

2.1.4 Simulations of the galaxy clustering

As suggested in Section 2.1.2.2, a convenient way to model the measurable quantities for a sample of galaxies, where the effects of field shape and selection function are important, is through static Monte Carlo simulations of the galaxy clustering. Soneira and Peebles (1978) devised a suitable model for the galaxy distribution based on hierarchical clustering and this gave results for the spatial two- and three-point functions which agreed in form with the results summarised in equations 2-90 and 2-105. Following this, Bean (1983) and Bean et al. (1983) used this model to simulate the distribution in the Durham/AAT redshift survey (Peterson et al. 1986, see Chapter 3). In this work the methods developed by these authors are continued but slightly different constructions and parameters are used which aim to reproduce the results for the studies in Chapters 4 and 5.

Each simulation is intended to represent an independent realisation of the model clustering process much in the same way that a fair galaxy sample is assumed to be an independent realisation of the overall galaxy distribution. This statistical model is achieved by randomly drawing a population from the probability distribution for each process (the Monte Carlo approach). With an accurate model for the clustering and selection properties of the galaxies in each sample it is then possible to form an ensemble of such simulations to derive statistical averages and standard errors for the observable quantities.

As it is necessary to obtain the errors in the estimate of the interfield correlation function (described in Section 2.1.2.2) an important consideration for the model was the requirement for each simulation to represent a single clustering process over the exact positions of the field volumes in the 17^m surveys considered in this work. In view of this, the method for constructing the simulations was as follows. The hierarchical clump is a tree-like distribution constructed from pairs of points placed at random within spherical volumes of decreasing radii. The first two points, initially placed at random within a sphere of radius R_1, become centres for the spheres, radii R_1/λ of the second level. The procedure is repeated up to the ninth level where eventually the $2^9=512$ points in spheres of radii R_1/λ^8 are taken to represent the positions of galaxies. Such clumps randomly distributed in a volume reproduce the form of the two- and three-point spatial correlation functions in equations 2-90 and 2-105, over separation r from $R_1/\lambda^8 \leq r \leq R_1$. In the catalogues in this work $R_1=6h^{-1}$ Mpc and $\lambda=1.8$, thus giving $\xi(r)\approx(r_o/r)^{1.82}$ and $\zeta(r)\propto Q\xi(r)^2$ with $Q\approx0.5$ (Peebles 1980, Section 61) over the range $0.05\leq r\leq6h^{-1}$ Mpc. At separations $r\gtrsim6h^{-1}$ Mpc, $\xi(r)$ breaks away from this small-scale behaviour and tends to zero at $r_{max}\approx26.8h^{-1}$ Mpc (the maximum correlation length between two galaxies).

In view of the selection of galaxies by apparent magnitude, centres for the clumps were placed randomly within a spherical volume defined by $z\leq z_{max}$. Clumps that lay beyond the boundary of any field by more than $r_{max}/2$ were rejected. For each clump that intersected a field, a new hierarchy was constructed as described above, but, to match the amplitude $B=r_o^{1.82}$ of the observed small-scale ($r\leq R_1$) correlation function, m points were chosen at random from the 512 available. Following this, each of these points was assigned an absolute magnitude in the range $-21.5\leq M\leq-17.5$ from a

Schechter (1976) function with M^*=-20 and α=-1 (H_o=100). Apparent magnitudes for the 'galaxies' were then calculated according to equation 2-6 with a K-correction of K=3.0 (and no curvature correction) and those fainter than m_{lim} were rejected. The remaining galaxies were then assigned a line-of-sight peculiar velocity from a frequency distribution $f(v) \propto \exp(-C|v|^{3/2})$ that approximates the observations of such one dimensional random motions in the simulations of Efstathiou and Eastwood (1981). The dispersion $\langle v^2 \rangle^{1/2}$ of this distribution was adjusted to give a pair-wise rms peculiar velocity of $\langle \omega^2 \rangle^{1/2} \approx 350 \text{kms}^{-1}$.

The simulation is terminated when the number of galaxies in the catalogue matches the number $N(\leq m_{lim})$ observed to that depth. According to Soneira and Peebles (1978) the mean density within clusters at resolution r at redshift z in this hierarchical model is

$$n_r(z) \propto \varphi(z) m r^{-\gamma} \qquad (2\text{-}108)$$

where $\varphi(z)$ is the selection function (equation 2-19). As the observed correlation function is $\xi_e(r)=Br^{-\gamma}$ at 0.05 $\leq r \leq 6h^{-1}$ Mpc and since

$$\xi_e(r) \approx \frac{n_r(\bar{z})}{n(\bar{z})} \propto \frac{m r^{-\gamma}}{n} \qquad (2\text{-}109)$$

with $\bar{z}$ approximately at the peak of $n(z) \propto \langle N(z) \rangle$, this implies

$$B \propto \frac{m}{n} \qquad (2\text{-}110)$$

Therefore, for an n fixed by $N(\leq m_{lim})$, the amplitude B can be altered by varying m proportionately.

For a match to the Durham/AAT and Durham/SAAO surveys 20 catalogues of simulations were created with $m_{lim}=16^m.8$ ($z^* \approx 0.076$, see equation 2-16 and Figure 2.1) and z_{max}=0.1. With the observed number of galaxies per square degree at this depth being $N \approx 5.8 \text{deg.}^{-2}$ ($N(\leq m_{lim})$=1141 for the 14 fields, see Chapter 3) a small-scale amplitude of B$\approx$21 was obtained for m=38 and this gives a reasonable representation of the observations (see Chapters 4 and 5). To match the sampling in the Durham/SAAO Survey the galaxies in the simulated fields of this catalogue

were ranked in order of increasing apparent magnitude and every third object chosen for subsequent analysis. Figure 2.5 shows the observed mean spatial function $\xi(r)$ (solid line) for all the galaxies in the 20 simulations together with the errors of estimation. The dashed line is the model $\xi(r)=21r^{-1.8}$ fitted to the power law below $3h^{-1}$ Mpc and as can be seen there is some indication that the estimates fall below this model between $3<r<6h^{-1}$ Mpc suggesting that the break in $\xi(r)$ is somewhat smoother than suggested above.

Finally, 20 catalogues of simulations were also generated for the Parker et al. Survey and the parameters chosen here were $m_{lim}=16.25$ ($z^*\approx0.059$) and $z_{max}=0.07$. In this case 5 fields similar in construction to the Parker et al. field were generated in each catalogue and a similar amplitude of $B\approx21$ was obtained with $N\approx2.9$deg.$^{-2}$ ($N(\leq m_{lim})=415$ over 5 fields) and m=38 (as before). A single field from each catalogue was used in the subsequent analysis.

2.2 Measures of peculiar motions and their relation to the clustering of mass in the Universe

The motions of galaxies that are observed as a distortion of the radial Hubble flow of the Universe have been well documented over the years and have been seen to occur in a wide variety of structures; from orbital motions in individual pairs of galaxies (Turner 1976), through to the dispersions in groups (Huchra and Geller 1982, Nolthenius and White 1987), clusters (Kent and Gunn 1982, Lucey et al. 1986) and even, possibly, superclusters (Bahcall et al. 1986). Recently, the observed dipole in the Cosmic Microwave Background (Fixsen et al. 1983, Lubin et al. 1985) has also led to a concerted study of peculiar motions of galaxies in the local ($\leq100h^{-1}$ Mpc) neighbourhood (Burstein et al. 1986, Dressler et al. 1987). In its simple interpretation this dipole implies the Sun is moving in the cosmic frame with a velocity of 377kms^{-1} towards $l^{II}=267°$, $b^{II}=50°$. However, the Sun is known to be moving with respect to the Local Group with a velocity of 300kms^{-1} towards $l^{II}=90°$, $b^{II}=0°$ and so the Local Group is, in the cosmic frame, estimated to have a velocity of 614kms^{-1} towards $l^{II}=269°$, $b^{II}=28°$ (Lynden-Bell 1987). Recently Rowan-Robinson et al. (1990) have claimed that mass distributed like IRAS galaxies may be responsible for this motion although this remains a matter for strong debate.

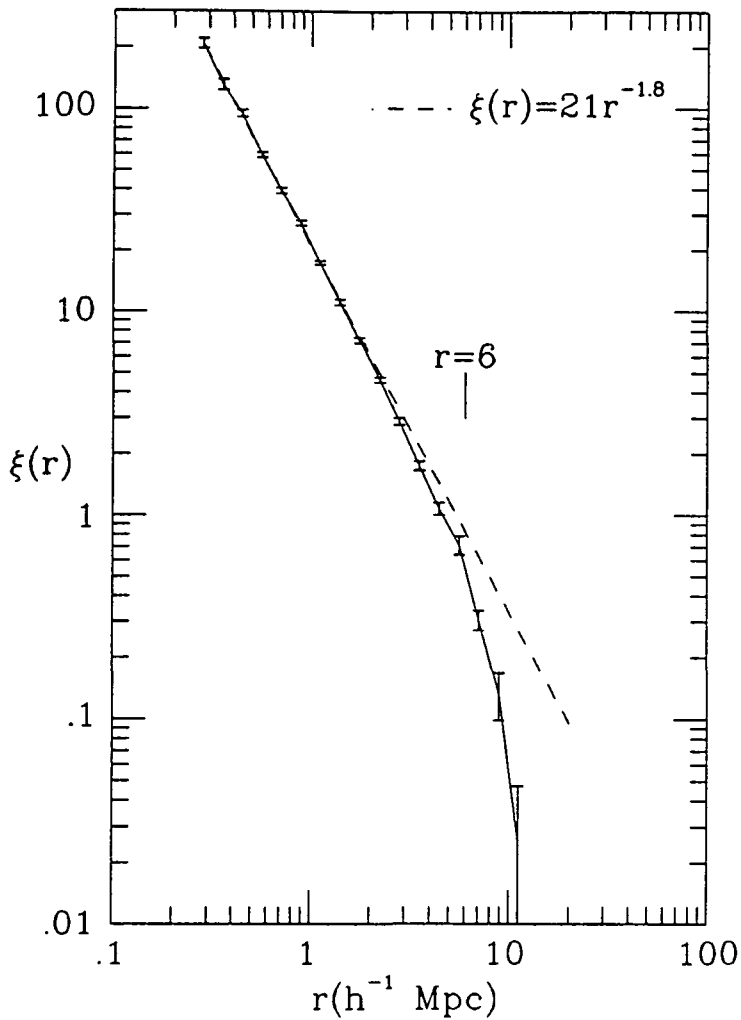As was suggested earlier in Section 2.1.2.2, it is worthwhile, at this

Figure 2.5. The mean spatial correlation function estimated from the 20 catalogues of simulations of the Durham/SAAO and Durham/AAT surveys. The mean estimate of $\xi(r)$ is shown as a solid line together with the errors of estimation. The dashed line is the power law $\xi(r)=21r^{-1.8}$ that fits the data at $r<3h^{-1}$ Mpc. The radius of the first hierarchical level is indicated at $r=6h^{-1}$ Mpc.

point, to make a clear distinction between two particular forms of peculiar motion (see Kaiser 1987, for example). To do this, suppose that in a small region of space it is possible to obtain all the peculiar velocity vectors $\underline{v}_p{}^i$ for all the galaxies i that lie within the region's boundary. If the average $\langle \underline{v}_p \rangle$ has a non-zero value that is unlikely to have arisen by chance then the interpretation is that this region of space is undergoing a coherent or streaming flow with velocity $\langle \underline{v}_p \rangle$ for the particular scale size of the region viewed. If the velocity coherence length is larger than or of the same order as the dimensions of this region, then nearby volumes will exhibit similar velocity vectors.

On the other hand, it is also possible that there is no coherent flow on this scale, in which case the average $\langle \underline{v}_p \rangle$ will be consistent with zero ($\underline{0}$), but the individual velocities $\underline{v}_p{}^i$ are non-zero (as shown by, say, the finite width of the frequency distribution in the magnitudes of $\underline{v}_p{}^i$). Here the galaxy velocities are described as incoherent or random over this scale size and velocity vectors observed in neighbouring volumes would not correlate.

Generally, both forms of motion will be present in the galaxy distribution but to varying degrees depending on the position and size of the region studied. Since gravity is the dominant force acting on large scales it may be expected that most peculiar motions have been generated by the growth of small perturbations in the uniform mass (or energy) density. This perturbation can be characterised at any position $\underline{x}$ by the density contrast,

$$\frac{\delta\rho(\underline{x})}{\rho_b} = \frac{\rho(\underline{x}) - \rho_b}{\rho_b} \qquad (2\text{-}111)$$

where ρ_b is the background mass density. There are two distinct regimes for the growth of structure in the Universe; in the regime where the density contrast is small, i.e. $\delta\rho/\rho_b \lesssim 1$, perturbations grow in a linear fashion such that, after decoupling of matter and radiation, $\delta\rho/\rho_b$ at time t is related to the fluctuation at an earlier epoch t_o by

$$(\delta\rho/\rho_b)_t = \frac{A(t)}{A(t_o)} (\delta\rho/\rho_b)_{t_o} \qquad (2\text{-}112)$$

where A(t) is an amplification factor depending on t. For example, in an $\Omega_o = 1$ Universe $A(t) \propto t^{2/3}$ for the growing mode of perturbations. However, where

$\delta\rho/\rho_b \gtrsim 1$ growth of structure is non-linear and, generally occurs at a faster rate.

For example, at small scales where the clustering eventually becomes strong ($\delta\rho/\rho_b \gg 1$) clumps of matter may separate from the Hubble flow and have sufficient time, within the age of the Universe, to interact and randomise their motions. In this case, it would be expected that the distribution becomes virialised, i.e. that velocities are stably bound by the gravitational potential of the excess matter associated with the clustering. For particles at a radius r from an overdensity

$$\langle \underline{v}_p{}^2 \rangle \approx \frac{GM(r)}{r} \qquad M(r) \approx \delta\rho r^3 \qquad (2\text{-}113)$$

where $\delta\rho$ is the magnitude of the fluctuation within r. Since $\rho_b = \rho^{\circ}{}_c \Omega_o$ ($\rho^{\circ}{}_c = 3H_o{}^2/8\pi G$, the critical density needed to close the Universe at the current epoch) this can be rewritten as

$$\langle \underline{v}_p{}^2 \rangle \approx \frac{\delta\rho}{\rho_b} \Omega_o (H_o r)^2 \qquad (2\text{-}114)$$

It is these virialised motions which are responsible for the dispersions in clusters and lead to the 'Finger of God' effects seen in redshift maps. A similar condition to equation 2-114 is used in the Cosmic Virial Theorem (Peebles 1976a) discussed below.

At larger scales where the mass clustering remains small ($\delta\rho/\rho_b \lesssim 1$) it would be expected that galaxies are still falling into (or streaming out of) denser (or less dense) regions. This is the form of motion that is likely to be the cause of the dipole in the Cosmic Microwave Background discussed above. Here, mass particles experience an acceleration of $\sim -GM(r)/r^2$ for approximately a Hubble time ($\sim 1/H_o$) and so their infall velocity, at the present epoch is

$$\langle \underline{v}_p \rangle \approx - \frac{GM(r)}{H_o r^3} \underline{r} \qquad (2\text{-}115)$$

which can be expressed as

$$\langle \underline{v}_p \rangle \approx -\Omega_o \frac{\delta\rho}{\rho_b} (H_o r) \, \hat{\underline{r}} \qquad\qquad (2\text{-}116)$$

Note that when $\delta\rho/\rho_b < 0$, as for a void, the streaming velocity is outward in direction (which is equivalent to a repulsive force). As will be seen below, this equation is the basis for a model for the peculiar motion due to infall.

In both these models for peculiar motions (equations 2-114 and 2-116) both the form of mass clustering (i.e. $\delta\rho/\rho_b$) and the underlying density of the homogeneous material (given by Ω_o) play an important rôle in determining the magnitude of $\underline{v}_p$. Further, as discussed in Chapter 1, there is also the question of the relation between the observed perturbation (defined by the visible galaxies) and the perturbation in the mass (which is $\delta\rho/\rho_b$). Clearly, the assumption that $\delta\rho/\rho_b = \delta n/n_b$ (the fluctuation in the number density of galaxies) is not trivial, and, indeed, several mechanisms have been suggested for the formation of galaxies which will lead to a bias with respect to the mass distribution (Dekel and Rees 1987, Kaiser 1986b). One model (Kaiser 1984, Politzer and Wise 1984) is to introduce a bias parameter b of the form

$$\frac{\delta n}{n_b} = b \frac{\delta\rho}{\rho_b} \qquad\qquad (2\text{-}117)$$

where b is a constant. Thus, since galaxies are assumed to have peculiar motions similar to the mass (i.e. $\underline{v}_p^m \approx \underline{v}_p^g$) this implies directly from equations 2-114 and 2-116 that

$$\Omega_o^{eff} \approx \Omega_o/b \qquad\qquad (2\text{-}118)$$

where Ω_o^{eff} is Ω_o measured assuming that galaxies trace the mass. In the rest of this chapter possibilities for how the mass is clustered relative to the galaxies are discussed.

In the following study of Chapter 4, estimates of peculiar motions will be derived from their line-of-sight distortion of the two-point correlation function measured in redshift space. The advantage of this method is that using approximately fair samples of the galaxy distribution mean estimates of pair-wise peculiar velocities can be obtained in a statistical average and this

circumvents the need for specifying the type and form of structures which are to be analysed (as is required, for example, in the measurement of dispersions in groups or clusters). However, it should be noted that this average is pair weighted and this may make the results more dominated by richer areas of clustering than a simple mean of peculiar motions would be, if they were known.

Thus, in the following sections models and methods of estimation will be given for both the random and coherent (infall) aspects of peculiar motions as deduced from the redshift two-point function $\xi_V(\sigma,\pi)$. After this, the virial theorems will be discussed as a means of constraining both Ω_0 and large-scale structure.

2.2.1 Peculiar motions; models and methods of estimation

2.2.1.1 Random motions; methods of estimation

In the above introduction to Section 2.2 virial motions within dense regions of clustering were described and in Section 2.1.2.2 a simple model for their effect on the two-point function $\xi_V(\sigma,\pi)$ measured in redshift space was given (equation 2-31). In this section methods for estimating pair-wise random peculiar motions from $\xi_V(\sigma,\pi)$ are now discussed as these can then be used to obtain a constraint on the density parameter Ω_0 through the Cosmic Virial Theorem.

Firstly, it is clear that if the model in equation 2-31 is to be used directly, it is necessary to obtain or, at least, assume a form for the distribution of pair-wise peculiar velocities $f(\omega)$ as this is not provided for by the virial theorems such as in equation 2-114. As was stated earlier, a general assumption is that in the virial limit motions of galaxies will be isotropic and only weakly correlated with position (as in equation 2-114 above with $\delta\rho/\rho_b \approx r^\gamma$ and $\gamma=1.8$). Thus a general constraint of $f(\omega)$ is then that it is symmetric i.e. $f(\omega)=f(-\omega)$ which implies

$$\int_{-\infty}^{\infty} f(\omega)\omega d\omega = \langle\omega\rangle = 0 \tag{2-119}$$

48

The constraint that

$$\int_{-\infty}^{\infty} f(\omega)d\omega = 1 \qquad (2\text{-}120)$$

is, of course, required for a probability function. A simple way to quantify $f(\omega)$ is to make it a function of only ω and its second moment $\langle\omega^2\rangle$ which is

$$\int_{-\infty}^{\infty} f(\omega)\omega^2 d\omega = \langle\omega^2\rangle \qquad (2\text{-}121)$$

and several forms have been considered. However, as dynamic simulations prefer a form of the type

$$f(\omega) = (c_1/\langle\omega^2\rangle^{1/2}) \exp\left[-c_2(|\omega|/\langle\omega^2\rangle^{1/2})^{3/2}\right] \qquad (2\text{-}122)$$

(Efstathiou and Eastwood 1981) this will be assumed in the future analyses. In this case the constraints in equations 2-120 and 2-121 give

$$c_1 = 0.75\Gamma(2/3)^{-3/2} \approx 0.476 \qquad c_2 = \Gamma(2/3)^{-3/4} \approx 0.797 \qquad (2\text{-}123)$$

Thus, using equations 2-31, 2-122 and 2-123 and a function for $\xi(r)$, a model $\xi_v(\sigma,\pi)$ can be fitted directly to the estimates of $\xi_v(\sigma,\pi)$ using, say, least squares. If the form for $\xi(r)$ is known (or assumed) then the parameter $\langle\omega^2\rangle^{1/2}$ can be obtained directly. As will be seen below (Section 2.2.2.1) this pair-wise rms peculiar velocity is used in the Cosmic Virial Theorem (see also equation 2-114).

This method of modelling $\xi_v(\sigma,\pi)$ was preferred by Bean et al. (1983) but it is also possible to obtain $\langle\omega^2\rangle^{1/2}$ directly from the 'width' of $\xi_v(\sigma,\pi)$ without assuming a model for the peculiar velocity distribution $f(\omega)$. This uses the second moment of $\xi_v(\sigma,\pi)$ (Peebles 1980), namely

$$\int_{-\pi_{cut}}^{\pi_{cut}} \pi^2 \xi_v(\sigma,\pi)d\pi = M_2 \qquad (2\text{-}124)$$

which according to the random motion model for $\xi_v(\sigma,\pi)$ in equation 2-31 can be written as

$$M_2 = \int_{-\infty}^{\infty} [\int_{-\pi_{cut}}^{\pi_{cut}} \pi^2 \xi \{[\sigma^2+(\pi-\omega/H_o)^2]^{1/2}\} d\pi] f(\omega) d\omega \qquad (2\text{-}125)$$

With the substitution that $y = \pi - \omega/H_o$ in the inner integral and the assumption that $\pi_{cut} \gg \langle\omega^2\rangle^{1/2}/H_o$ this becomes

$$M_2 \approx \int_{-\infty}^{\infty} f(\omega) d\omega \int_{-\pi_{cut}}^{\pi_{cut}} y^2 \xi \{[\sigma^2+y^2]^{1/2}\} dy \;+$$

$$2 \int_{-\infty}^{\infty} f(\omega)(\omega/H_o) d\omega \int_{-\pi_{cut}}^{\pi_{cut}} y \xi \{[\sigma^2+y^2]^{1/2}\} dy \;+$$

$$\int_{-\infty}^{\infty} f(\omega)(\omega/H_o)^2 d\omega \int_{-\pi_{cut}}^{\pi_{cut}} \xi \{[\sigma^2+y^2]^{1/2}\} dy \qquad (2\text{-}126)$$

Thus according to equations 2-119, 2-120 and 2-121, an estimate for $\langle\omega^2\rangle$ is

$$\frac{\langle\omega^2\rangle}{H_o^2} = \frac{\int_0^{\pi_{cut}} \pi^2 \xi_v(\sigma,\pi) d\pi}{\int_0^{\pi_{cut}} \xi_v(\sigma,\pi) d\pi} - \frac{\int_0^{\pi_{cut}} \pi^2 \xi \{[\sigma^2+\pi^2]^{1/2}\} d\pi}{\int_0^{\pi_{cut}} \xi \{[\sigma^2+\pi^2]^{1/2}\} d\pi} \qquad (2\text{-}127)$$

where the symmetry in π of $\xi_v(\sigma,\pi)$ has been used. The advantage of this formulation of the estimator is that the first term on the RHS ($\langle\pi^2\rangle_{\xi_v}$) can be measured from the data whereas the second term ($\langle\pi^2\rangle_\xi$) can be modelled directly using a function for $\xi(r)$. Also, since both terms are stable to variations of the form $\xi \to A\xi$, this makes the estimator insensitive to amplitude fluctuations.

Equation 2-127 can easily be understood since $\langle\pi^2\rangle_{\xi_v}$ is the quadrature sum of the widths $\langle\pi^2\rangle_\xi^{1/2}$ and $\langle\omega^2\rangle_f^{1/2}$ (where the subscript denotes the appropriate weighting function). However, as stated previously for clustering which has separated from the Hubble flow (as required for virialisation, see above), or is infalling, the correction $\langle\pi^2\rangle_\xi$ is not strictly valid and so $\langle\pi^2\rangle_{\xi_v}^{1/2}$ is an upper limit to $\langle\omega^2\rangle^{1/2}$.

As Bean et al. (1983) have discussed, this estimator is very sensitive to the uncertain large-scale form of ξ_v since it is weighted by π^2 and for a power-law $\xi(r)$ of the form $\xi(r)=(r_o/r)^\gamma$ (equation 2-90), $\langle\pi^2\rangle_\xi$ becomes (see

also equation 2-98)

$$\langle\pi^2\rangle_\xi = \frac{\sigma^2[H_{\gamma-2}(\pi_{cut}/\sigma)-H_\gamma(\pi_{cut}/\sigma)]}{H_\gamma(\pi_{cut}/\sigma)}$$ (2-128)

which diverges for $\gamma<3$ as $\pi_{cut}/\sigma\to\infty$. As $\gamma\approx1.8$ it is apparent that as π_{cut} is increased equation 2-127 becomes the difference between two diverging terms and so small differences in the large-scale form of the observed ξ_v and model ξ will lead to a large, but discrepant, value of $\langle\omega^2\rangle^{1/2}$.

In Figure 2.6 (a) to (f), the $\langle\omega^2\rangle^{1/2}$ estimator in equation 2-127 is shown as a function of π_{cut} and σ for when $\langle\pi^2\rangle_{\xi_v}$ is obtained directly from the model for $\xi_v(\sigma,\pi)$ in equation 2-31 with $f(\omega)$ as in equation 2-122. In each of the model lines $\langle\pi^2\rangle_{\xi_v}$ has a $\xi(r)$ of the form $\xi(r)\propto r^{-\gamma}$ for $r\le10h^{-1}$ Mpc and $\xi(r)=0$ at larger separations. On the other hand, $\xi(r)$ for $\langle\pi^2\rangle_\xi$ is modelled as a straight power law; $\xi(r)\propto r^{-1.8}$ for all r (see equation 2-128). As can be seen in Figures 2.6 (a) and (b), the estimates of $\langle\omega^2\rangle^{1/2}$ at $\sigma<1.0h^{-1}$ Mpc peak near the true value of $\langle\omega^2\rangle^{1/2}=300kms^{-1}$ even though $\xi(r)$ in $\langle\pi^2\rangle_\xi$ differs from that in $\langle\pi^2\rangle_{\xi_v}$; the same also seems to be true in Figures 2.6 (d) and (e) where $\langle\omega^2\rangle^{1/2}=600kms^{-1}$. This shows that, at these separations, equation 2-127 converges sufficiently to contain all smeared pairs before the uncertain form of the large-scale correlation function begins to dominate the estimates of $\langle\omega^2\rangle^{1/2}$.
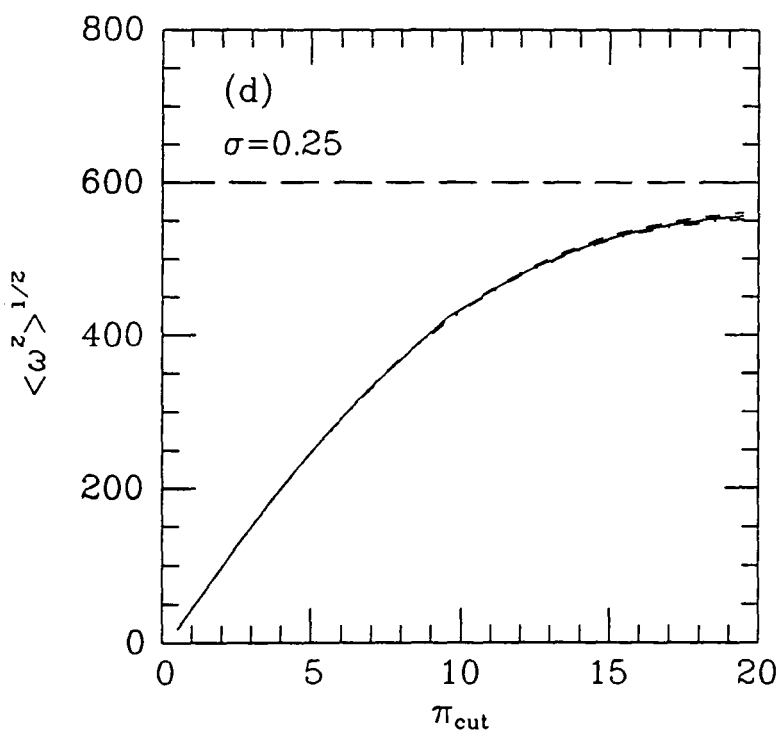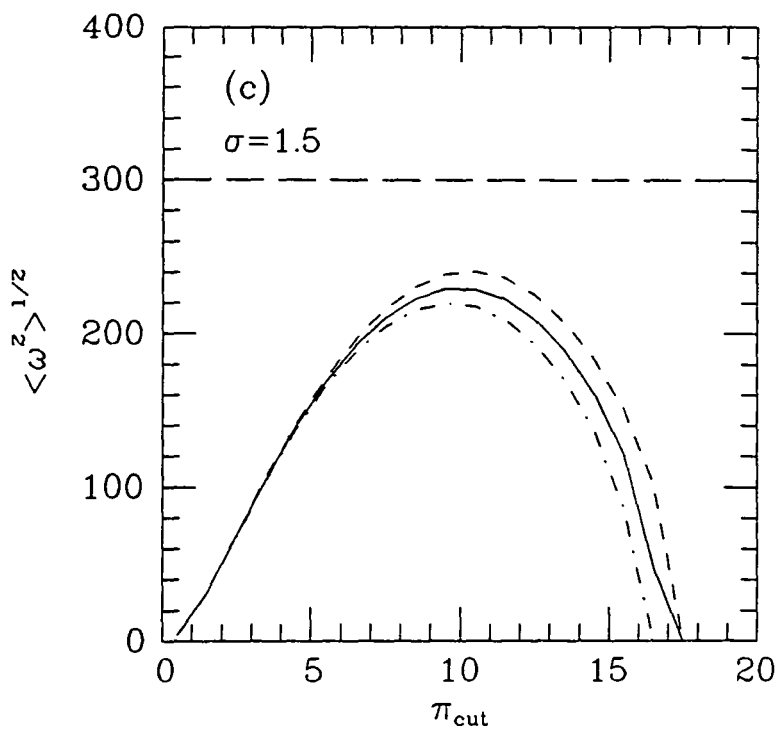
At larger σ values, the differences in the correlation functions for $\langle\pi^2\rangle_{\xi_v}$ and $\langle\pi^2\rangle_\xi$ cause larger variations in the estimates of $\langle\omega^2\rangle^{1/2}$ but would seem to be able to distinguish the $\langle\omega^2\rangle^{1/2}=600kms^{-1}$ from the $\langle\omega^2\rangle^{1/2}=300kms^{-1}$ models for $f(\omega)$. This estimator, then, provides a useful complementary approach to the direct model fits to $\xi_v(\sigma,\pi)$ and should not be overlooked in the analysis.
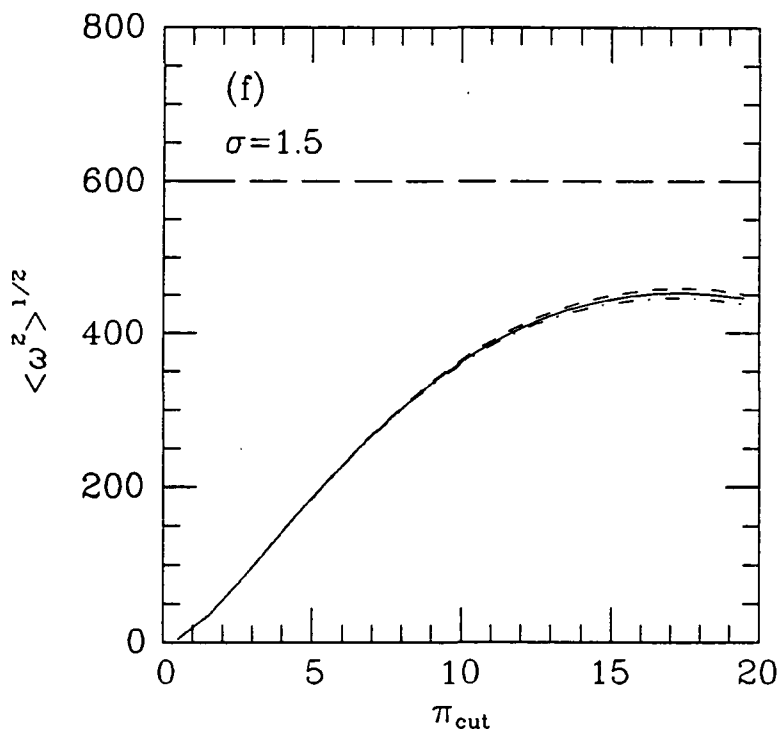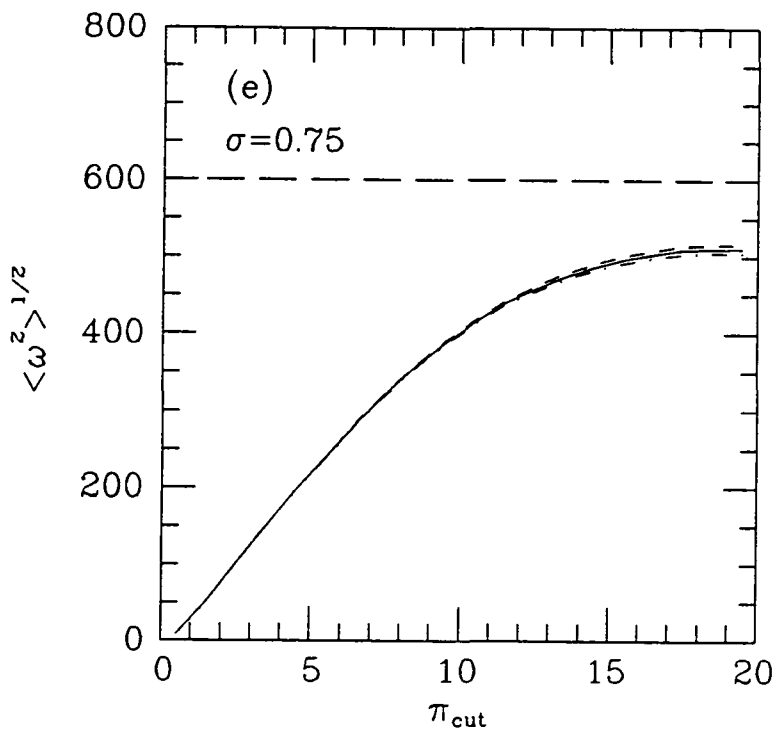
2.2.1.2 Infall models

In the introduction to Section 2.2 given above, the form of coherent infall into clusters at low density contrasts was described and a simple model for its form presented (equation 2-116). However, as peculiar motions are to be estimated from their distortion of the redshift correlation function $\xi_v(\sigma,\pi)$ (or $\xi_s(s)$), a pair-wise model for infall is required and so two simple pictures for such motions are discussed below.

Figure 2.6. Model predictions for the second moment estimate of $\langle\omega^2\rangle^{1/2}$ (in kms^{-1}) at various projected separations σ (in h^{-1} Mpc) and at various limits π_{cut} (in h^{-1} Mpc). The models are based on a direct integration of $\xi_v(\sigma,\pi)$ (equation 2-31) for $\langle\pi^2\rangle_{\xi_v}$ and a model for $\langle\pi^2\rangle_\xi$ from equation 2-128. In $\langle\pi^2\rangle_{\xi_v}$ the correlation function was of the form $\xi(r)\propto r^{-\gamma}$ for $r\le10$h^{-1} Mpc and $\xi(r)=0$ at larger scales with $\gamma=1.7$ (short dash line), 1.8 (solid line) and 1.9 (dot-dash line). In $\langle\pi^2\rangle_\xi$ the correlation function was a uniform power law with $\gamma=1.8$. In (a), (b) and (c) $\langle\omega^2\rangle^{1/2}=300$kms^{-1} whereas in (c), (d) and (e) $\langle\omega^2\rangle^{1/2}=600$kms^{-1} .

(a)
$\sigma = 0.25$

$\langle \omega^2 \rangle^{1/2}$

π_{cut}

(b)
$\sigma = 0.75$

$\langle \omega^2 \rangle^{1/2}$

π_{cut}

(e) $\sigma = 0.75$

(f) $\sigma = 1.5$
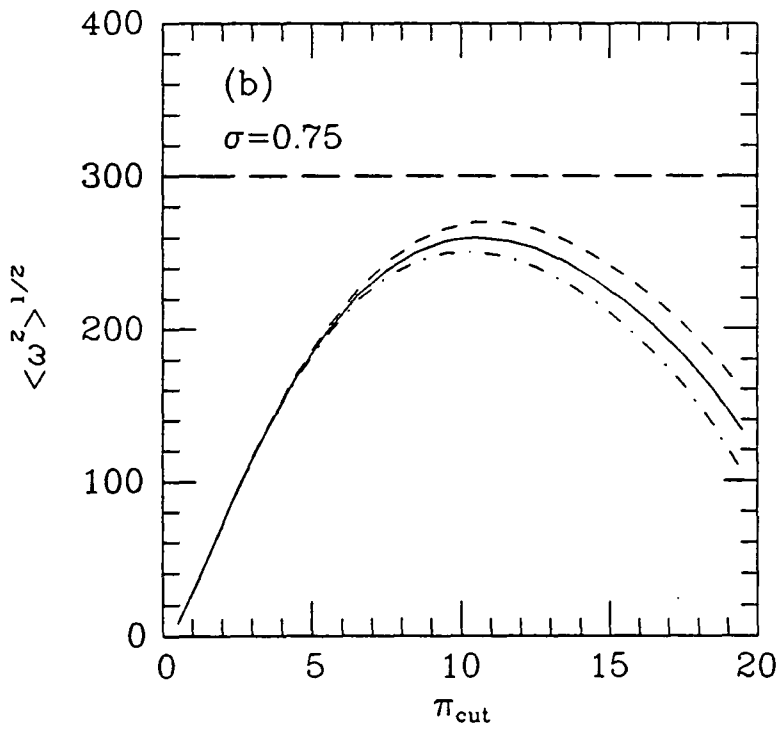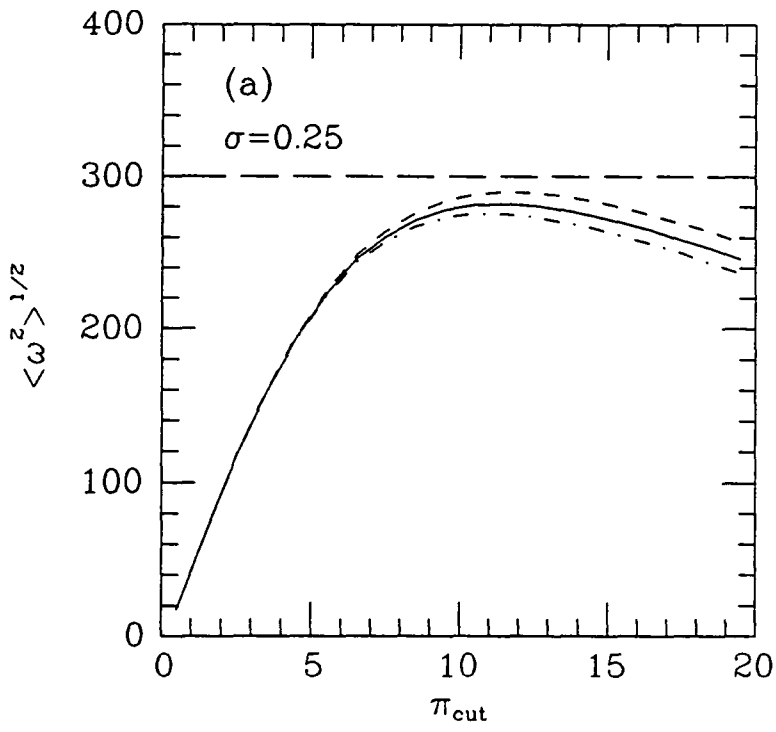
The first approach to the construction of a model for pair-wise infall is through the use of the second BBGKY (Bogoliubov-Born-Green-Kirkwood-Yvon) hierarchy equation which describes the dynamical conservation of particle pairs (see Peebles 1980, Section 71, p266). This can be written as (Peebles 1980, equation 71.6)

$$\frac{\partial}{\partial t} \int_0^x x'^2 \xi^m(x',t) dx' + \frac{1}{a(t)} x^2 (1+\xi^m(x,t)) v(x,t) = 0 \qquad (2\text{-}129)$$

and expresses the conservation of the mean number of neighbours within a fixed comoving radial separation x from a randomly chosen mass particle (here ξ^m refers to the matter correlation function). Here, $v(x,t)$ is the radial velocity of a neighbour at time t and position x and $a(t)$ is the expansion factor.

In the linear regime ($\xi^m \leq 1$) it may be expected that the mass correlation function $\xi^m \approx \overset{2}{A(t)} B(x)$ (see equation 2-112). Thus, for $B(x) \propto x^{-\gamma}$ ($\gamma < 3$) and $A(t)$ dominated by the growing mode of perturbations

$$\underline{v} = - \frac{2}{(3-\gamma)} \Omega_0^{0.6} \frac{\xi^m}{(1+\xi^m)} H_0 \underline{r} \qquad (2\text{-}130)$$

at the current epoch. This is similar to the model described above (equation 2-116) since $\xi^m \approx \langle (\delta\rho/\rho_b)^2 \rangle$ and $(1+\xi^m) \approx 1$ in the linear regime. Note that extrapolating this model to where $\xi^m \gg 1$ this equation has the property that $\underline{v} \approx -(2/(3-\gamma))\Omega_0^{0.6} H_0 \underline{r}$ and this cancels, to some extent, the Hubble expansion previously assumed in the form for $\xi_v(\sigma,\pi)$ (equation 2-31) as is required for the clustering to be stably bound. Previously several groups of workers have used this model in equation 2-130; Bean et al. (1983) considered infall with $\Omega_0=1$ with the factor $2/(3-\gamma)$ neglected while in Davis and Peebles (1983) γ was set to a value of 2 and the factor $F=2\Omega_0^{0.6}$ left variable.

Such streaming motions can be incorporated into the form for the galaxy correlation function $\xi_v(\sigma,\pi)$ in equation 2-31. If it is assumed that the galaxy correlation function $\xi(r)$ is related to that of the mass by

$$\xi(r) = b^2 \xi^m(r) \qquad (2\text{-}131)$$

as in equation 2-117 ($\xi \approx \langle(\delta n/n_b)^2\rangle$ and $\xi^m \approx \langle(\delta\rho/\rho_b)^2\rangle$), then the model for $\xi_v(\sigma,\pi)$ becomes

$$1+\xi_v(\sigma,\pi) = \int_{-\infty}^{\infty} [1+\xi(r)]f(\omega' + \frac{F\xi(r)H_o\hat{r}\cdot\hat{z}}{(b^2+\xi(r))})d\omega' \qquad (2\text{-}132)$$

where

$$r = [\sigma^2+(\pi-\omega'/H_o)^2]^{1/2} \qquad \hat{r}\cdot\hat{z} = \pi-\omega'/H_o \qquad (2\text{-}133)$$

and $\hat{z}$ is a unit vector along the line-of-sight. This model can then be used in direct fits to the observed data as described in Section 2.2.1.1 or it can be used to predict the form for the direction averaged correlation function $\xi_s(s)$ as in equation 2-34.

Kaiser (1986a) has also obtained linearised models for coherent infall from considering the power spectrum of low density contrasts in redshift space. Since the redshift two-point function is the Fourier transform of this power spectrum then equivalent expressions to equation 2-132 for the matter correlation functions $\xi^m_v(\sigma,\pi)$ and $\xi^m_s(s)$ can be found. In particular, for the direction averaged redshift correlation function, $\xi^m_s(s)$ Kaiser finds

$$\xi^m_s(s) = (1+\frac{2}{3}\Omega_o^{0.6}+\frac{1}{5}\Omega_o^{1.2})\xi^m(s) \qquad |\xi^m(s)| \ll 1 \qquad (2\text{-}134)$$

whereas for the above model at small $|\xi^m|$ (equation 2-132 with b=1) he obtains

$$\xi^m_s(s) = (1+\frac{2}{3}\Omega_o^{0.6})\xi^m(s) \qquad |\xi^m(s)| \ll 1 \qquad (2\text{-}135)$$

which lacks a term proportional to $\Omega_o^{1.2}$. Such infall clearly leads to quite a strong amplification of the correlation function; in the Kaiser description in equation 2-134 this amounts to a factor of 28/15 for $\Omega_o=1$ as compared to 5/3 in the BBGKY model (equation 2-135). However, if galaxies are biassed relative to the mass, but are infalling at the same rate, then equations 2-130 and 2-131 say that the effective value of Ω_o measured, on the assumption that galaxies trace the mass, is (c.f. equation 2-118)

$$\Omega_0{}^{\text{eff}} = \frac{\Omega_0}{b^\lambda} \qquad |\xi^m| \ll 1 \qquad\qquad (2\text{-}136)$$

where $\lambda = 10/3$ and $5/3$ for the BBGKY and Kaiser models, respectively. Clearly, this leads to a smaller amplification, via equations 2-134 and 2-135, for the galaxy correlation function $\xi_s(s)$ if $b > 1$.

2.2.2 Virial theorems and the relation to Ω_0

2.2.2.1 The Cosmic Virial Theorem

The balance between the kinetic energy of small-scale particle motions and the gravitational potential of their associated mass perturbations has been described in the introduction to Section 2.2 (see equation 2-114). As with the infall models discussed above, such a virial theorem needs to be extended to pair-wise peculiar motions and this has been provided for in the Cosmic Virial Theorem (CVT) of Peebles (1976a). Essentially, in this model, the spatial gradient of the 'pressure' of peculiar motions between particles of mean mass m is balanced in an equilibrium state by the attractive gravitational force of the surrounding excess matter. Under the assumption that peculiar motions are isotropic (i.e. that the radial component of the mean square pair-wise peculiar velocity $\langle v_r^2 \rangle$ is half the transverse component $\langle v_t^2 \rangle$) and that stability occurs where $\xi^m \gg 1$, then this is (Peebles 1976a, equation 24);

$$-\frac{\partial}{\partial r}(\rho(r)\langle v_r^2 \rangle) \approx \frac{2Gm\rho(r)}{r^2} + \frac{2G\rho(r)\rho_b}{\xi^m(r)} \int_V d^3z\, \hat{r} \cdot \hat{z} \frac{\zeta^m(r,z,|\underline{r}-\underline{z}|)}{z^3} \qquad (2\text{-}137)$$

where the correlation functions of the mass particles are described by ξ^m and ζ^m.

This equation deals with the equilibrium at separation $-\underline{r}$ from a randomly chosen mass particle m (see Figure 2.7). The observed mean fluid pressure at r is $\sim \rho(r)\langle v_r^2 \rangle$ directed along $-\underline{r}$ (where the mass density $\rho(r)$ at r is $\sim \xi^m(r)\rho_b$) and its (radial) gradient is $\partial(\rho(r)\langle v_r^2 \rangle)/\partial r$ (LHS of equation 2-137). To balance this gradient at r, there are two sources of Newtonian gravitational interaction; the first is the 'binary interaction' between the matter at r and the mass particle m (amounting to a force of $2Gm\rho(r)/r^2$ directed along $\underline{\dot{r}}$; this is
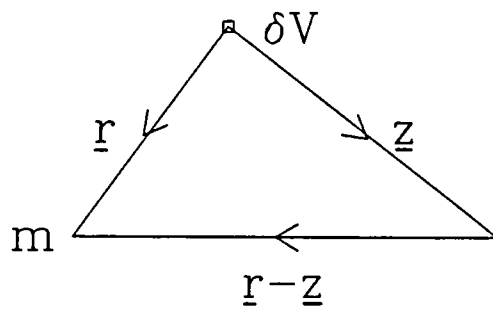
Figure 2.7. The spatial relationship between the mass particle m, the volume δv, and the surrounding matter. The balance between the pressure force and the gravitational interactions is carried out in volume δv.

the first term on the RHS of equation 2-137). The second is a 'collective interaction' between the matter at r and all the surrounding particles; at separation z from δv (see Figure 2.7) this amounts to a force of $2G\rho(r)\rho_b \; \hat{r} \cdot z \zeta^m(r,z,| r-z|)/\xi^m(r)z^3$ in the $\hat{r}$ direction, which integrated over all z gives the second term on the LHS of equation 2-137.

Generally it is assumed that the collective interaction term dominates equation 2-137 ($\zeta^m \gg \xi^m \gg 1$) and so, with equations 2-90 and 2-105 as a model for the two- and three-point matter functions, respectively, the equality can be integrated over r to give (c.f. equation 2-114)

$$\langle v_r^2(r) \rangle = C_\gamma H_o^2 Q^m \Omega_o (r_o{}^m)^\gamma r^{(2-\gamma)} \tag{2-138}$$

(Peebles 1976a, equation 29) where C_γ is a constant depending only on γ. This is the basic result which relates the peculiar motions of mass particles to the amplitudes of the two- and three-point matter correlations ($B^m = r_o{}^{m\gamma}$ and Q^m, respectively). This motion is only a slowly varying function of r if $\gamma \approx 1.8$ and supports the assumption of a nearly constant random peculiar velocity distribution as in equation 2-122. To obtain the one-dimensional motion as a function of the perpendicular separation σ as in $\langle \omega^2 \rangle^{1/2}$, $\langle v_r^2(r) \rangle$ must be averaged over separations r_3 parallel to the line-of-sight, viz;

$$\langle \omega^2 \rangle = \frac{\int_0^\infty \xi[(\sigma^2 + r_3^2)^{1/2}]\langle v_r^2[(\sigma^2 + r_3^2)^{1/2}]\rangle \, dr_3}{\int_0^\infty \xi[(\sigma^2 + r_3^2)^{1/2}] \, dr_3} \tag{2-139}$$

The assumptions that have been incorporated into the model in equation 2-138 are now briefly discussed. The assumption of stability requires that the matter distribution is not expanding or collapsing in proper coordinates and this is achieved if the peculiar motions dominate the expansion within the stability region of scale r, i.e.

$$\frac{\langle v_r^2(r) \rangle^{1/2}}{H_o r} \gg 1 \tag{2-140}$$

Dynamical simulations seem to indicate that stability can be maintained on scales of less than $\sim 0.5 h^{-1}$ Mpc (Efstathiou and Eastwood 1981, Davis et al. 1985).

As well as assuming that the matter particles move on isotropic orbits, it is also feasible that other orbits may be applicable (from radial to circular) as considered by Davis and Peebles (1983) and Bean et al. (1983). Figure 7 of Bean et al. (1983) shows an anisotropic model for the pair-wise peculiar motion $\langle \omega^2 \rangle^{1/2}$ and the effect is similar to that produced by a cut-off in the gravitational potential as discussed below.

The assumption of the power-law form for the three-point function ζ^m leads to an unacceptably large contribution to the small-scale velocity dispersion in equation 2-138 arising from the diverging concentration of matter around the point at $-\underline{r}$ from m (see Figure 2.7). This makes the integrated form (equation 2-137) of the third term in equation 2-105 divergent as $z \to 0$. There are various physically acceptable ways of avoiding this based on modifying the gravitational potential of the mass distribution. Davis and Peebles (1983) replaced the third term in equation 2-105 with the second, whilst Peebles (1976b) and Bean et al. (1983) modified the potential by having a cut-off in the mass distribution (obtained by replacing $r^{-\gamma}$ with $(r_c+r)^{-\gamma}$ in $\xi(r)$ in the first instance and by replacing z^3 in the third term in equation 2-137 with $(z_c+z)^3$ in the second) at the scale r_c typical of a galaxy.

Finally, there is also the uncertainty over how matter is distributed around galaxies. Davis and Peebles (1983) have argued that the observed slow dependence of the velocity dispersion on radius (see Chapter 4) supports the hierarchical picture (equations 2-90 and 2-105) and so the two- and three-point functions of the galaxies will be related to those of the mass by (c.f. equation 2-131)

$$\xi^g \approx b^2 \xi^m \qquad \zeta^g \approx c \zeta^m \qquad \qquad (2\text{-}141)$$

However, Bean (1983) has pointed out that if the velocity dispersion is dominated by relatively few bright galaxies the binary interaction term in equation 2-137 may dominate the collective force and so the velocity dispersion will, for a point mass, behave like

$$\langle v_r^2(r) \rangle \simeq r^{-1} \qquad \qquad (2\text{-}142)$$

Thus for a galaxy with a massive halo that has $m(r) \propto r$ that extends out to

several hundreds of kpc it is possible to achieve a velocity dispersion that has a very slow dependence on r (see, for example, Barnes 1987).

2.2.2.2 The Cosmic Energy Equation

Like the Cosmic Virial Theorem discussed in the previous section, the Cosmic Energy Equation (Fall 1979, Peebles 1980) relates the peculiar motions of particles to the gravitational potential of the underlying distribution of matter. However, unlike the previous virial theorem this cosmic energy equation connects all the rms peculiar motions at both small and large scales (not just where the distribution is stable) to the mass distribution. According to Fall (1979) the gravitational potential of the mass fluctuations written as

$$W = \frac{1}{2} \rho_b \int_{V \to \infty} d^3 \underline{r} \, (-G/r) \xi^m(r) \qquad (2\text{-}143)$$

can be related to the 'kinetic energy' written as

$$T = \frac{1}{2} \langle v_p^2 \rangle \qquad (\langle v_p^2 \rangle^{1/2} \text{ 3-d dispersion}) \qquad (2\text{-}144)$$

by

$$\frac{d}{dt}(T+W) + \frac{1}{a}\frac{da}{dt}(2T+W) = 0 \qquad (2\text{-}145)$$

at an epoch t (with an expansion factor a(t)). In the early Universe Ω lies close to unity and so T, W and a(t) are all proportional to $t^{2/3}$. From equation 2-145 this implies

$$T = -\frac{2}{3}W \qquad (2\text{-}146)$$

At much later times, after clusters have formed and collapsed, the virialised regions are expected to have (from the Cosmic Virial Theorem)

$$T = -\frac{1}{2}W \qquad (2\text{-}147)$$

and so

$$T \approx -KW \tag{2-148}$$

where K will lie in the range

$$\frac{1}{2} \leq K \leq \frac{2}{3} \tag{2-149}$$

Thus, with $\rho_b = 3H_o^2 \Omega_o / 8\pi G$ at the present epoch equations 2-143, 2-144 and 2-148 indicate that

$$\langle v_p^2 \rangle = \frac{3}{2} K \Omega_o H_o^2 J_2(\infty) \tag{2-150}$$

where $J_2(r)$ is the integral

$$J_2(r) = \int_0^r r' \xi^m(r') dr' \tag{2-151}$$

As will be seen in Chapter 5 this is a useful way in which to place an alternative constraint on large-scale structure from peculiar motions.

Chapter 3

The redshift surveys and their properties

In this chapter the form, construction and some general properties of the Durham/SAAO, Parker et al. and Durham/AAT surveys, which were briefly introduced in Chapter 1, are described in some detail in preparation for the spatial and velocity analyses given in Chapters 4 and 5. As was previously stated, the new information about such distributions is obtained from the first two of these catalogues, since Bean (1983) has studied the Durham/AAT Survey in detail. However, as these surveys are very compatible, comparisons, and, eventually, overall properties will be drawn from all three observations and this necessitates the inclusion of the Durham/AAT Survey in the description here.

Thus in Section 3.1 details of the Durham/SAAO, Parker et al. and Durham/AAT catalogues are given with a view to presenting the principal aims of the construction of such surveys. In Section 3.2 some preliminary aspects of the distribution of galaxies in these catalogues are discussed in order to assess the potential fairness of the samples chosen.

3.1 Introduction to the $b_J \leq 17^m$ Surveys

Traditionally, samples of the galaxy distribution have been taken from complete magnitude limited galaxy catalogues, and here, the major constraint on the compilation of a redshift survey is the telescope time required to obtain sufficient signal-to-noise spectra for determination of the redshifts (see Chapter 6). However, given that N galaxies are to be observed there is some degree of freedom as to how these objects are to be selected from different parts of the sky. From equation 2-16, 2-17 and 2-18 it is seen that $\langle N(\leq m_{lim}) \rangle \propto \Omega 10^{0.6 m_{lim}}$ and so, for a given N, either Ω can be small and m_{lim} faint, or Ω can be large and m_{lim} bright. Over recent years there has been a notable diversification in these two directions. Historically, the first complete catalogues of redshifts that covered a large area of the sky were based on the original Shapley-Ames (1932) Survey, which, recently revised (Sandage and

Tammann 1987), is an all sky map of 1200 galaxies approximately complete to a blue photographic magnitude of $m_B \approx 13^m$ and has a depth of $D_{peak} \approx 20h^{-1}$ Mpc. Following this, the Center for Astrophysics (CfA) Survey (Huchra et al. 1983) was the first systematic redshift survey which covered a large part of the north Galactic hemisphere ($b^{II} \geq 40°$, $\delta \geq 0°$) and some parts of the south ($b^{II} < -30°$, $\delta > -2.5°$). This survey, comprising of ~2000 galaxies from the Zwicky Catalogue (Zwicky et al. 1961-1968), is complete to $m_B \approx 14.5^m$ and has a corresponding depth of $D_{peak} \approx 40h^{-1}$ Mpc. More recently this work has been extended in the south ($b^{II} \leq -30°$, $\delta \leq -17.5°$) with the Southern Sky Redshift Survey (da Costa et al. 1988) which is selected from the ESO/Uppsala Catalogue of galaxies (Lauberts 1982) by apparent diameter and is complete to a similar depth.

However, although these surveys have the advantage of being complete to their magnitude limits and the time taken to obtain good quality spectra of these bright galaxies is relatively short, the shallow depth of these catalogues may lead to sampling problems because of certain large inhomogeneities, such as the Virgo and Coma clusters in the north and the Fornax and Eridanus in the south, that are seen locally. Clearly, following the discussion in the previous chapter, if D_{peak} is the same order of size as a typical fluctuation in the galaxy distribution, then these samples may not be globally representative, even though, at first sight, they contain many galaxies. This is because with the large solid angle of these surveys there is a tendency to observe complete clusters whereas in narrow angle surveys many more parts of independent structures are intersected. Further, these shallow samples are quite severely affected by the motion of the Local Group with respect to more distant galaxies and this makes the predicted n(z) distributions sensitive to the choice of the measured motion (such as into Virgo, Davis and Huchra 1982).

One way in which to avoid these problems is to probe deeper into the galaxy distribution and this has been the approach of de Lapparent et al. where the original CfA Survey has been extended to include Zwicky galaxies to $m_B \approx 15.5^m$ in, currently, two complete 6° slices through the NGP (de Lapparent et al. 1986a, 1988). However, even at this depth ($D_{peak} \approx 50h^{-1}$ Mpc) inhomogeneities may still be persistent and, furthermore, there is also the question of how reliable the Zwicky magnitudes are beyond $m_B = 15^m.0$

(see Chapter 5). By narrowing the solid angle further and splitting the survey up into many fields, which are then placed at random positions over the sky, much deeper redshift surveys can be achieved which may intersect many more of the typical clustering features. This was the aim of workers such as Kirshner, Oemler and Schechter (1978, the KOS Survey, see also Kirshner et al. 1983) and Peterson et al. (1986) who first used such surveys to constrain the form of the galaxy distribution on scales of up $100h^{-1}$ Mpc.

More recently, however, it has been realised that, in a complete redshift survey, some of the information about the galaxy distribution is redundant at separations much larger than the typical clustering scale length (given by r_0 in equation 2-90). Clearly, if there are m galaxies in an average cluster, all of these represent only one piece of independent information for the estimation of the clustering of clusters and so there is an m-fold redundancy. A simple way to reduce this over-sampling is to randomly select galaxies from the magnitude limited catalogue, thus increasing the volume surveyed whilst not increasing the telescope observation time drastically (see Kaiser 1986a). In this work such a survey is described (the Durham/SAAO Survey) which increases by a factor of ~3 the volume covered by the original Durham/AAT Survey. More recently still, other workers have also used such sparse sampling techniques as, for example, in the 1-in-6 survey of IRAS selected galaxies by Rowan-Robinson et al. (1990, the QDOT Survey) and the 1-in-20 survey of $b_J<17^m$ galaxies in the APM Galaxy Catalogue (Maddox et al. 1990b) by Loveday (1989). As will be seen in Chapter 6 this approach to systematic redshift surveys may provide a suitable method of mapping large volumes of space.

3.1.1 The Durham/SAAO Survey

As seen in the introduction to Section 3.1, the Durham/SAAO Survey (Metcalfe et al. 1989) is a large volume extension of the original Durham/AAT Survey (Peterson et al. 1986); whereas the latter catalogue contains 5 fields of ~3°.75x3°.75 area limited to $b_J \leq 16^m.8$, the new survey contains 9 such fields of similar dimensions and magnitude limit. The original aim of the Durham/AAT Survey was to obtain accurate redshift velocities ($\leq 50 kms^{-1}$ error) for all the galaxies in the 5 fields to the magnitude limit for the purposes of estimating the mean mass density of the Universe via the Cosmic Virial

Theorem (Peebles 1976a, see also Chapter 2, Section 2.2.2.1). However, preliminary results on the form of the spatial galaxy distribution on scales of 2 up to $100h^{-1}$ Mpc indicated several interesting features which needed to be investigated in a larger volume survey. Briefly, these were as follows; although the overall form of the two-point correlation function estimated from this survey at scales $\leq 10h^{-1}$ Mpc approximately followed a power law of the form $\xi(r) \approx (r_0/r)^{1.8}$ (equation 2-90) as deduced from the projected correlation function $\omega(\theta)$ (see Section 2.1.2.4), there were some indications that this simple picture needed to be modified. In particular, at $\sim 2h^{-1}$ Mpc $\xi_s(s)$ showed a pronounced rise above the power law with $r_0 \approx 4.5h^{-1}$ Mpc before breaking to smaller values at $\sim 5h^{-1}$ Mpc. At larger scales, the correlation function was consistent with homogeneity up to $\sim 100h^{-1}$ Mpc, but with some evidence for low signal-to-noise features such as anticorrelation at $s \approx 14h^{-1}$ Mpc and peaks at $s \approx 28$ and $56h^{-1}$ Mpc.

Clearly, this form for $\xi_s(s)$ and its interpretation for $\xi(r)$ needs to be examined in more detail in a larger volume of space. To achieve this, without increasing the observing time significantly, galaxies in the Durham/SAAO Survey were sampled on a 1-in-3 basis from the complete lists of galaxies for each field ranked in increasing order of apparent magnitude. However, although the within-field pair count DD(s) (c.f. equation 2-25), at any particular separation s, is down, on average, by a factor of $\sim 1/5$ relative to the Durham/AAT Survey (assuming that the same number of galaxies are observed in each field), not all of the pairs provide independent information in the estimates of $\xi_s(s)$ even at small scales ($\leq 10h^{-1}$ Mpc). Indeed, at a small separation r (where $\xi \gg 1$) it is expected that $\delta\xi/\xi \approx \delta DD/\langle DD \rangle \approx m(r)/\langle N_p(r) \rangle^{1/2}$ (Peebles 1973, see also equations 2-49 and 2-50), where m(r) is the mean number of galaxies per cluster at resolution r (see equation 2-45) and thus only at separations r where $m(r) \approx 1$ will the lower pair count in the Durham/SAAO Survey lead to a larger error in ξ.

In Figure 3.1 the 1σ error estimates in $\xi_s(s)$ from the simulations (Section 2.1.4) of both surveys are presented together (the third-sampling procedure being mimicked in the Durham/SAAO simulations) for separations ranging from 1 to $140h^{-1}$ Mpc. In Figure 3.2 and Figure 3.3 these estimates are compared to those from field-to-field fluctuations in these surveys (here, each field is treated separately as an independent sample) and this seems to show that the simulated errors are representative of the true fluctuations.
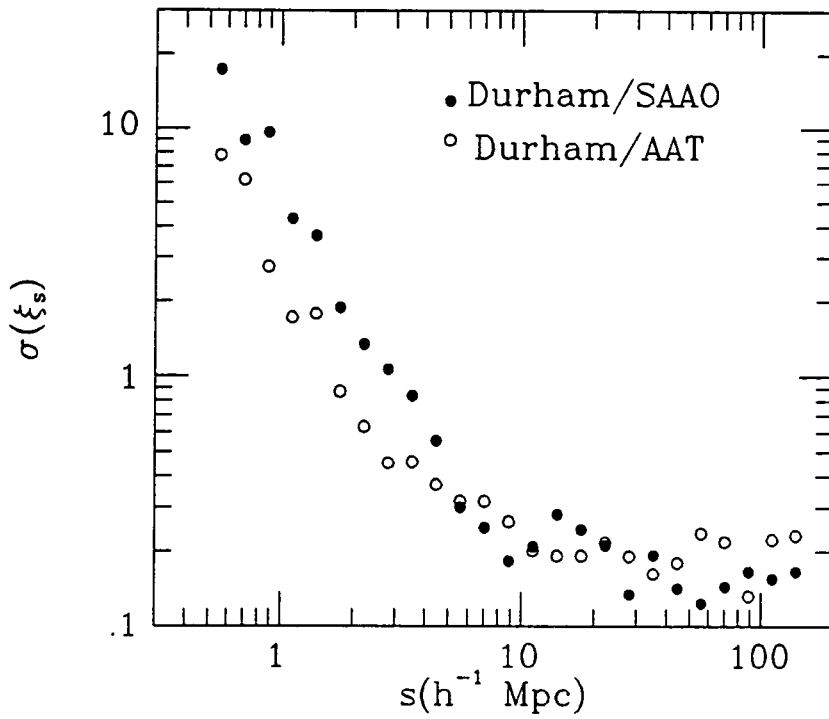
Figure 3.1. Error estimates $\sigma(\xi_s(s))$ on the two-point correlation function $\xi_s(s)$ obtained from the simulations of the Durham/SAAO and Durham/AAT surveys. The error is calculated in each bin from the rms variation in $\xi_s(s)$ estimated from the 20 catalogues of simulations of each survey.
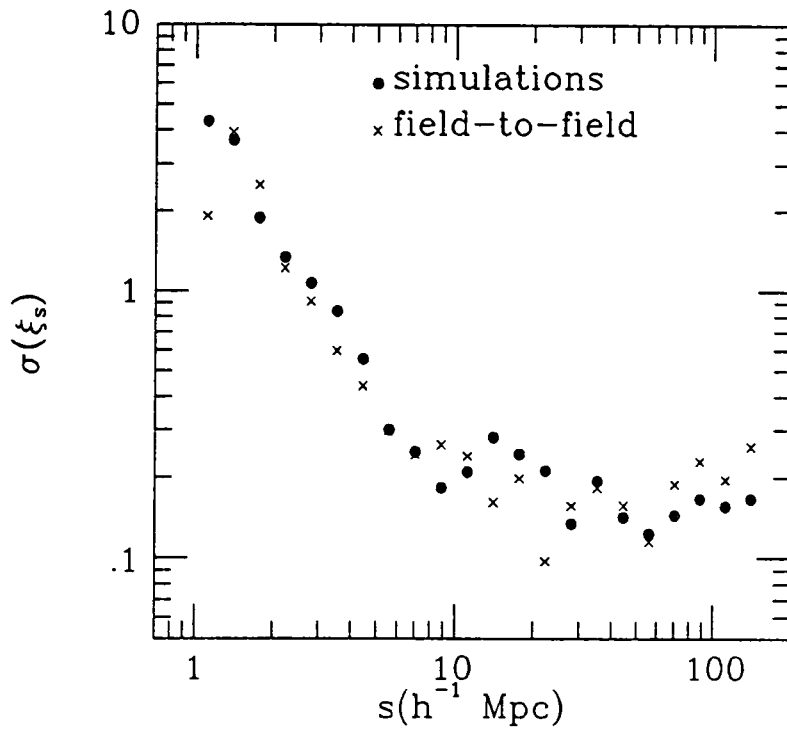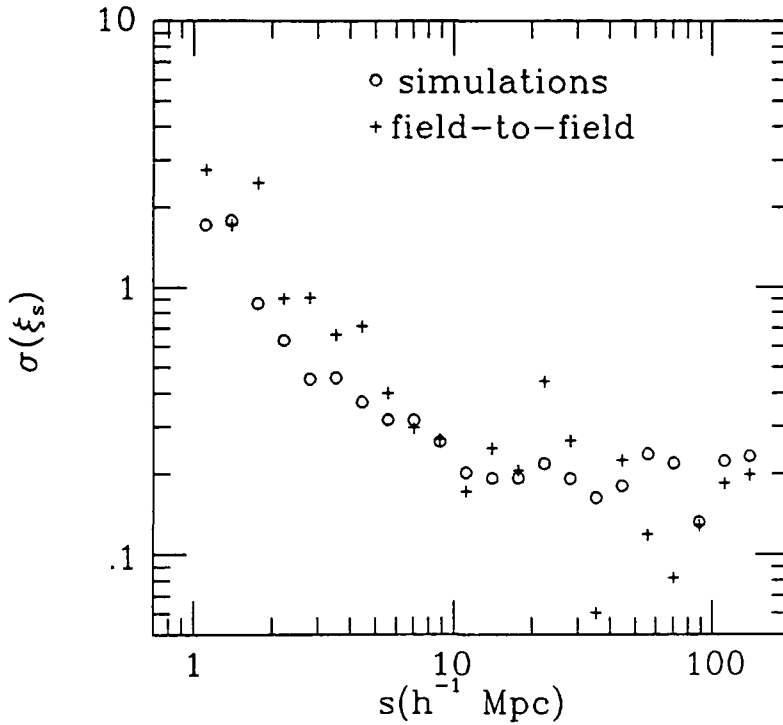
Figure 3.2. Measures of the error $\sigma(\xi_s(s))$ on the two-point correlation function $\xi_s(s)$ estimated from the Durham/SAAO Survey. The errors from the simulated catalogues are the same as those in Figure 3.1. The field-to-field errors come from the rms variation in $\xi_s(s)$ ($\xi_s(s)$ being calculated from each field individually). This rms error in each bin is then divided by $\sqrt{9}$ to give the error on the entire survey shown here.

Figure 3.3. Measures of the error σ(ξ$_s$(s)) on the two-point correlation function ξ$_s$(s) estimated from the Durham/AAT Survey. The errors from the simulated catalogues are the same as those in Figure 3.1. The field-to-field errors come from the rms variation in ξ$_s$(s) (ξ$_s$(s) being calculated from each field individually). This rms error in each bin is then divided by √5 to give the error on the entire survey shown here.

Figure 3.1 clearly indicates that the Durham/SAAO Survey is capable of providing well-determined results for $\xi_s(s)$ at small scales ($\leq 10h^{-1}$ Mpc) and somewhat better results than the Durham/AAT Survey at the larger scales, as anticipated.

Although the Durham/SAAO Survey was aimed at the determination of the large-scale clustering of galaxies, Metcalfe et al. (1989) suggest that the typical errors on the redshift velocities are $\sim\pm130$kms^{-1} rms and although this is much larger than the ±50kms^{-1} error for the Durham/AAT Survey, it leads to a 1-d pair-wise error of $\sim\pm180$kms^{-1} which is still smaller than the typical random motions of $\sim\pm300$kms^{-1} between galaxies (see Chapter 4). This suggests that the Durham/SAAO Survey can also provide a check on the line-of-sight pair-wise peculiar velocities seen in the Durham/AAT Survey and a further constraint on the mean mass density of the Universe. In Table 3.1 the errors on the line-of-sight rms peculiar velocity $\langle\omega^2\rangle^{1/2}$ estimated from $\xi_v(\sigma,\pi)$ for the simulations and for individual fields (again treated independently), are compared between the two surveys. Although the simulated error looks to be unrepresentative in both samples, both methods suggest that the uncertainties on $\langle\omega^2\rangle^{1/2}$ are comparable between the two surveys and so such studies for the Durham/SAAO Survey are worthwhile.

Full details of the Durham/SAAO Catalogue, its photometry and its spectroscopic observations are given in the paper by Metcalfe et al. (1989). As the methods are similar to those given in Chapter 6 only a summary is presented here of the overall features. Fields for the catalogue were chosen at random from the high Galactic latitude ($|b^{II}|\geq40°$), low extinction ($\leq0.1^m$), area of the UK Schmidt Telescope (UKST) photographic J (III-aJ emulsion plus a GG395 filter) survey of the southern sky. Photometric and positional information of galaxies were obtained from measurements of Atlas plates using the automated scanning machine COSMOS (MacGillivray and Stobie 1984) at the Royal Observatory, Edinburgh. By thresholding the intensity maps at a faint isophote $\sim25^m.0$ arcsec^{-2} approximately total magnitudes were obtained which were subsequently calibrated using CCD B and V photometry of on-plate galaxy sequences observed with the SAAO 1m telescope. These photographic magnitudes were shown to be approximately linear with the CCD magnitudes over the range $14^m\leq b_J\leq17^m$ with a dispersion of $\sim\pm0.3^m$ per galaxy, thus giving zero-point errors of $\pm0.1^m$ for an average of 5 calibrated galaxies. However, due to the limited dynamic range of

	Durham/SAAO		Durham/AAT	
	(1)	(2)	(3)	(4)
	sim	f-to-f	sim	f-to-f
$\sigma < 1h^{-1}$ Mpc	68	117	46	108

Table 3.1. Error estimates for the pair-wise rms peculiar velocity $\langle \omega^2 \rangle^{1/2}$ (in units of kms^{-1}) along the line-of-sight. Columns (1) and (2) are, respectively, the simulated and field-to-field errors for the Durham/SAAO Survey. Likewise, columns (3) and (4) are these quantities, respectively, for the Durham/AAT Survey.

COSMOS, some high surface brightness galaxies, such as E/S0 morphological types, may have underestimated magnitudes. Table 3.2 lists the 9 fields chosen, their centres, sizes, and magnitude limits which vary slightly from field-to-field due to the absolute calibration being obtained after the spectroscopic data was observed.

Redshifts for the 264 1-in-3 galaxies complete to $b_J \approx 16^m.8$ were obtained in 6 one-week runs from September 1983 to October 1984 at the SAAO 1.9m telescope. For all runs except the last, the Image-Tube Spectrograph and Reticon Photon Counting System were used with a grating of 210Å/mm to give spectra with a resolution of ~7Å FWHM. Using reduction methods similar to those given in Chapter 6 redshifts were measured from wavelength calibrated absorption and emission features in the range 3500-7600Å. Using the cross-correlation methods of Tonry and Davis (1979) to estimate the absorption redshifts and fitting the emission lines with Gaussian profiles, redshift velocities accurate to $\pm 130 kms^{-1}$ rms were obtained. Comparing with sources of velocities from other catalogues negligible zero-point error was observed. In this work the galaxies with high quality redshifts were used (codes 0, 1, 2, and 5 in the catalogue of Metcalfe et al. 1989) and the numbers of such objects available to the magnitude limit of each field is shown in Table 3.2.

3.1.2 The Durham/AAT and Parker et al. surveys

The Durham/AAT Survey contains redshifts for 329 galaxies in 5 high Galactic latitude fields to a magnitude limit of $b_J \approx 16^m.8$. Spectroscopic and photometric methods for this catalogue are described elsewhere (Bean 1983, Peterson et al. 1986) but are similar to those described in the previous section and in Chapter 6. The photometry was calibrated in a photoelectric B_J system (Couch and Newell 1980) and this is close to, but differs from, the b_J system in colour (see Shanks et al. 1984)

$$B_J \approx b_J + 0.1(B-V) \tag{3-1}$$

Further, b_J in the Durham/SAAO catalogue is close to a total magnitude whereas B_J in the Durham/AAT catalogue was measured at a higher isophote of $23^m.6$ arcsec^{-2} and this means that there is a galaxy profile dependent isophotal correction between the two systems. On average, however, this is

(1)	(2)	(3)	(4)	(5)	(6)	(7)	(8)
Field	RA	Dec	w	ht	m_{lim}	N_T	N_G
	h m	° ′	°	°	b_J		
GNX	11 00.8	- 10 01	3.75	3.75	16.70	90	25
GNY	12 30.4	+00 23	3.75	3.75	17.00	82	25
GNH	14 40.8	- 15 03	3.75	3.75	16.75	51	13
GNZ	15 19.4	+02 14	3.75	3.75	16.90	89	27
GSG	20 57.1	- 25 09	3.73	3.73	16.80	115	35
GSM	22 03.9	- 20 02	3.75	3.75	16.80	104	31
GSI	22 35.5	- 40 01	3.75	3.75	16.70	85	24
GSN	01 10.8	- 35 33	3.73	3.73	16.65	122	35
GSP	03 49.7	- 29 22	3.73	3.73	17.05	71	17

Table 3.2. The Durham/SAAO Survey fields. Column (1) gives the field names and columns (2) and (3) the Equatorial co-ordinates (1950.0) of their centres. The width and height of the fields is given in columns (4) and (5). The number of catalogue galaxies in each field brighter than the apparent magnitude limit (column (6)) is indicated in column (7). Column (8) gives the number of 1-in-3 galaxies with well-determined redshifts (codes 0, 1, 2, 5 of Metcalfe et al.)

approximately (Shanks priv. comm.)

$$b_J(23^m.6 \text{ arcsec}^{-2}) \approx b_J(25^m.0 \text{ arcsec}^{-2}) + 0.25 \qquad (3\text{-}2)$$

and so with a mean colour of $(B\text{-}V) \approx 1$ for the galaxies this gives

$$B_J(23^m.6 \text{ arcsec}^{-2}) \approx b_J(25^m.0 \text{ arcsec}^{-2}) + 0.35 \qquad (3\text{-}3)$$

Thus, as the mean magnitude limit for the Durham/AAT Survey fields is $B_J=17.11$, this corresponds to $b_J=16^m.76$, which is close to the $b_J=16^m.82$ for the Durham/SAAO Survey (see Table 3.2).

As stated before, the Durham/AAT Survey was measured at a higher spectroscopic resolution ($\sim1\text{Å}$ FWHM) than the Durham/SAAO catalogue giving velocity errors of $\leq 50 \text{kms}^{-1}$ rms. Comparison of the Durham/AAT Survey with other, overlapping redshift catalogues indicate that there are no serious velocity zero-point errors.

In the survey of Parker et al. (1986) redshifts are presented for 104 galaxies in a single field of area $5°.35 \times 5°.35$ sq. degrees centred at 00^h00^m, $-35°00'$. The catalogue is $\sim80\%$ complete to $b_J=16^m.5$ and velocity errors are claimed to be accurate to $\sim70 \text{kms}^{-1}$ rms. In Section 3.2.3 it is seen from the differential number counts as a function of apparent magnitude that the incompleteness of this catalogue seems to occur beyond $b_J=16^m.25$. Thus omitting objects fainter than this limit gives 80 galaxies in total for subsequent analysis. The field was previously chosen at random for a UKST objective-prism redshift survey and this data was to provide redshift information at the bright end of the catalogue. Since the photometric and spectroscopic methods used by Parker et al. were identical to those of Metcalfe et al., this sample of 80 galaxies is easily combined with the data sets already discussed above.

3.2 The observed spatial distribution and mean counts of galaxies

In the following two chapters, a considerable emphasis will be placed on obtaining mean statistical measures from the galaxy samples so far discussed. However, before such methods are applied it is worthwhile to inspect the data visually to anticipate some of the features that are likely to be present. It has been seen how redshift maps offer a wide variety of information both on galaxy clustering and on line-of-sight peculiar motions. In the following section both the angular and, more importantly, the 'spatial' positions of galaxies will be inspected for such effects and an awareness will be kept for features that may also be detected in the following statistical analysis.

As a further view of the overall properties of the catalogues, Sections 3.2.2 and 3.2.3 contain the observations of the counts of galaxies. In Section 3.2.2 the frequency distribution of absolute magnitudes is used to derive estimates of the luminosity function that aim to be independent of the clustering in the sample and, following this, in Section 3.2.3, models for the homogeneous number density are compared to counts of galaxies as a function of redshift and apparent magnitude. Such comparisons enable a study of the overall homogeneity and fairness of the samples and, again, such studies complement the objective analyses of the following chapters.

3.2.1 Angular and spatial positions

Perhaps the first clear pictorial view of the variety of forms of galaxy clustering came with the construction of the large-scale 2-d map of galaxy counts (Seldner et al. 1977) from the Lick Survey (Shane and Wirtanen 1967). This deep $m \leq 19^m$ map seem to indicate a hierarchy of clustering structures that appear to be interconnected by a network of filamentary chains and between these are regions apparently devoid of galaxies that hint at possible true spatial holes in the distribution. Although the overall properties of the map could be generated by simple numerical models (Soneira and Peebles 1978), certain features such as the 'filaments' or 'chains' were never reproduced satisfactorily in the simulations. However, in spite of these first few inspiring observations, there remained the difficulty of interpreting features from the map in view of the inherent projection difficulties and the possible systematic variations in the counts from plate-to-plate (Geller et al. 1984, de Lapparent et

al. 1986b).

As redshift catalogues became available, it became clear that visually galaxies do appear to be strongly clumped with large intervening underdense regions and this has led to a variety of descriptions of the distribution such as 'cellular' (Einasto et al. 1980), 'frothy' (Davis et al. 1981) and 'bubble-like' (de Lapparent et al. 1986a). Indeed, de Lapparent et al. (1988) have gone so far as to claim that the underdense regions or voids (of size, typically, ~30h^{-1} Mpc in diameter) are the main elements of the clustering distribution and that galaxies may fill the intervening spaces with uniform density. Clearly, this would inevitably imply that the clustering distribution has large-scale structure and this needs to be tested at some objective level.

However, before such tests are made, it should be emphasised that voids of such size are readily reproduced in numerical simulations in which there is no such large-scale power in the correlation functions. In Figure 3.4, their maps of the galaxy positions in their 2-d declination slices (a,b) (Huchra et al. 1988) are reproduced next to model maps (c,d) of similar proportions taken from a simulation of the Zwicky catalogue based on **random** clumps (but with hierarchical clustering within the clumps as described in Section 2.1.4 of Chapter 2). As can be seen, voids of similar dimensions to those in the slice data are visible in the simulated maps.

There are, however, some strong differences between the model and observed distributions, particularly in the lower CfA declination slice (a). In the centre of this map is the Coma Cluster; a large overdensity with a central core that displays a line-of-sight rms dispersion of ~1000kms^{-1} (Kent and. Gunn 1982). From this central region there appear to be several extensions (referred to as the 'stick man') which include a 'wall' that extends right across this map at a redshift velocity of ~10000kms^{-1}; the same feature also seems to appear at the same position in the upper declination slice (b). Given that clusters as rich as the Coma. Cluster ac rarely seen in the galaxy distribution (it is of richness class 2/3, Abell 1958) it is difficult to assess its affect on the overall appearance of these real maps. Certainly the clustering in the upper slice (b) is more like that in the simulated maps (c) and (d).

There are other differences between the observed and model maps too; the boundary between the voids and the galaxies appears more

Figure 3.4. Redshift maps for slices through the observed and simulated Zwicky catalogues of galaxies. In (a) and (b) are shown two adjacent declination slices of the Zwicky Catalogue ($m_B < 15^m.5$) reproduced from Huchra et al. (1988, Figures 3a and 3b). In (c) and (d) are shown two similarly defined adjacent slices from a simulation of the Zwicky Catalogue ($m_B < 15^m.0$) that is based on randomly distributed hierarchical clumps (see Section 2.1.4 of Chapter 2). The simulation parameters were chosen so as to match the mean density and amplitude of clustering in the $m_B < 15^m.0$ catalogue (see Section 2.1.2.4 of Chapter 2). In (a) and (b) the angular coordinate (R.A.) is in hours whereas in (c) and (d) it is in degrees. In all four maps the radial coordinate is the redshift velocity in kms^{-1}.

(a)

0.0 < m ≤ 21.4
26.5 ≤ δ < 32.5°

cz (km/s)

(b)

0.0 < m ≤ 21.0
32.5 ≤ δ < 38.5°

cz (km/s)

(c)

(d)
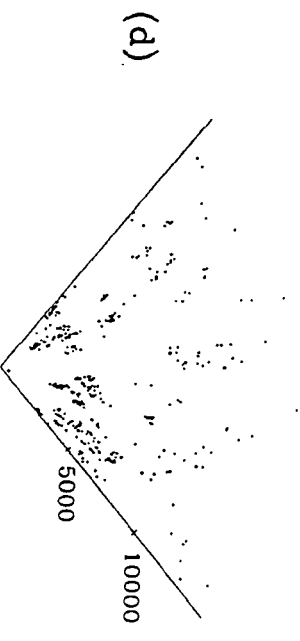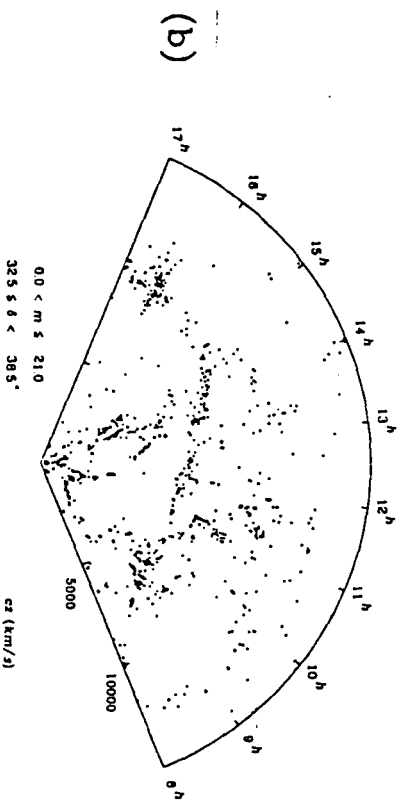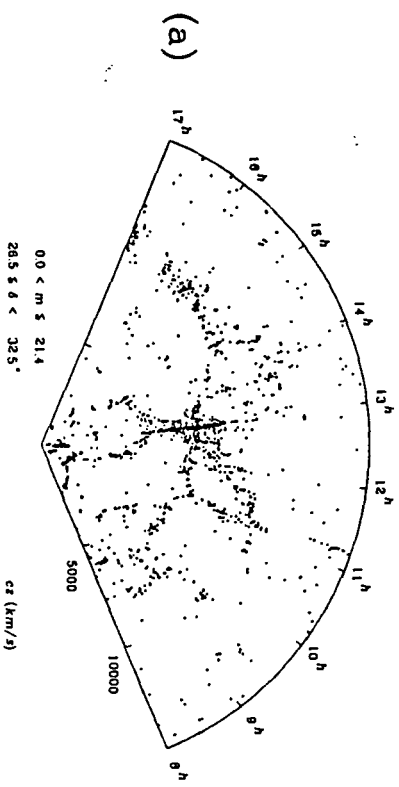
continuous in the observed map. Some of this may be real, or it may be due to peculiar motions in a way suggested by Kaiser (1987). Certainly, the general appearance of the void boundaries in both the real and simulated maps is enhanced by the 'Finger of God' effect arising from random motions in clusters and cases where the void boundary points towards the observer can be found in all four slices. On the other hand, other structures in the data may also be narrowed by some degree of infall; an effect which is not present in the model.

This shows that although visual inspections of the data can be profitable, they can also be misleading and care must be taken to understand some of the effects that can be present. With respect to the 2-d slices, it is difficult, in any case, to understand how de Lapparent et al. (1988) can draw such specific conclusions about voids when, at the same time, they clearly state that their samples are not fair representations of the overall distribution. The hierarchical simulations in this work and those of Soneira and Peebles (1978), are only rough models for comparison, but better, and more consistent models, come from the evolution of simulated particles as, for example, in those of White et al. (1987) which are based on Cold Dark Matter (see Chapter 5 below). The main point here is that visually acceptable maps of the galaxy distribution can be produced that have **no large-scale, i.e. $\geq 10h^{-1}$ Mpc, power in their low-order correlation functions** (see their Figure 10). Finally, to emphasise that these shallow depth surveys may be inhomogeneous, Figures 3.5 (a) and (b) (see also Figure 3.12 below) show some of the slice data for the SSRS Survey (da Costa et al. 1988). This seems to have a somewhat different texture to the NGP slices and appears to be a closer approximation to the simulated maps in Figure 3.4. This again emphasises the need for deeper redshift surveys.

With the above points borne in mind, the data for the deep redshift surveys are now discussed. In Figure 3.6 the positions of the Durham/SAAO and Parker et al. Survey fields (solid symbols) are plotted on a map of Equatorial coordinates with some of the delineating Galactic coordinates (l^{II},b^{II}) superimposed. For comparison, the positions of the Durham/AAT redshift survey fields and other survey boundaries are marked. As can be seen there is some overlap of these 17^m fields with the CfA ($m_B \leq 14^m.5$) Survey (CfA1) in the north and the SSRS Survey in the south.

Figure 3.5. Redshift maps for two declination slices through the SSRS Survey of galaxies. These two maps are reproduced from Figures 7a and 7b of da Costa et al. 1988. In each case the radial coordinate is in kms^{-1} and the angular coordinate (R.A.) is in hours
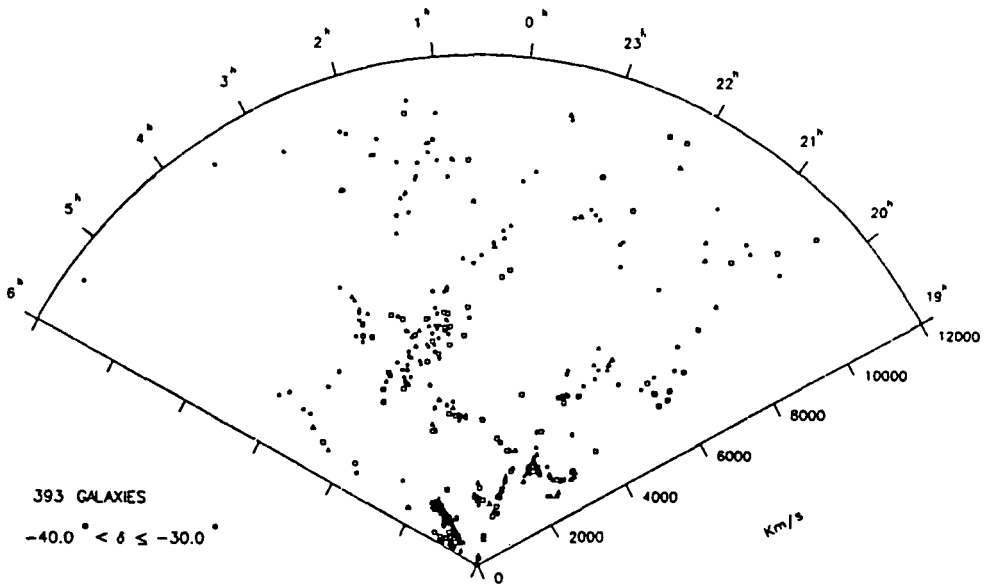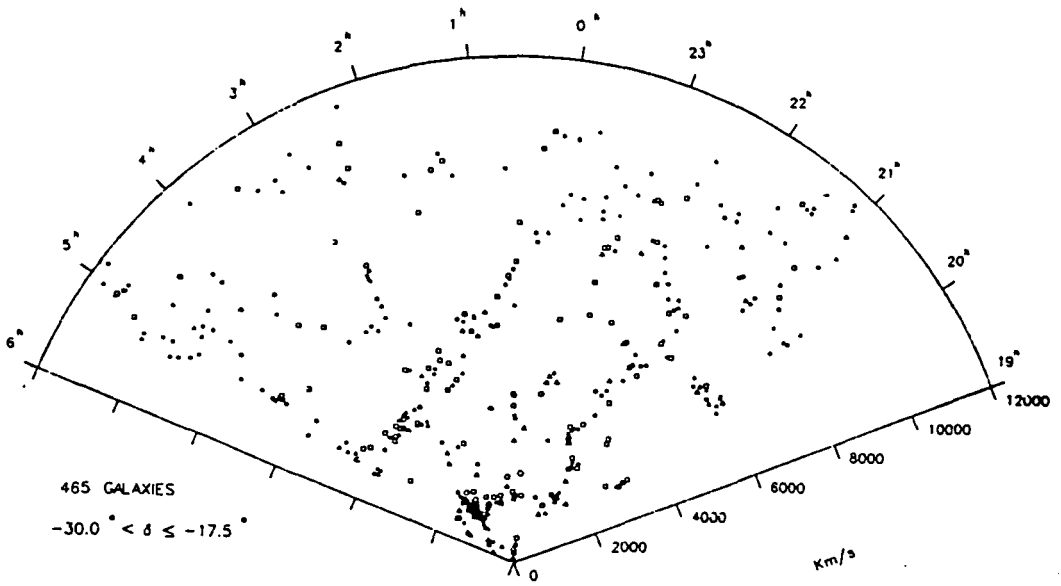
465 GALAXIES

$-30.0° < δ ≤ -17.5°$

393 GALAXIES

$-40.0° < δ ≤ -30.0°$

Figure 3.6. A cartesian map of the Equatorial coordinates R.A. and Dec. (1950.0) showing the positions of the Durham/SAAO, Parker et al. and other redshift survey boundaries. The solid symbols (of approximately proportionate area) are the positions of the Durham/SAAO and Parker et al. survey fields. Other fields with the prefix G are from the Durham/AAT Survey. Those fields with the prefix N or S are from Kirshner et al. (1978, the KOS Survey) and Kirshner et al. (1983). The areas delineated by a solid line are the $m_B < 14^m.5$ CfA Survey (CfA1, Huchra et al. 1983), the $m_B < 15^m.5$ CfA slices (CfA2, de Lapparent et al. 1988) and the SSRS Survey (SSRS, da Costa et al. 1988). The dashed lines are the Galactic coordinates $b^{ll} = \pm 20°$. The R.A. coordinate is in hours the Dec. coordinate in degrees.
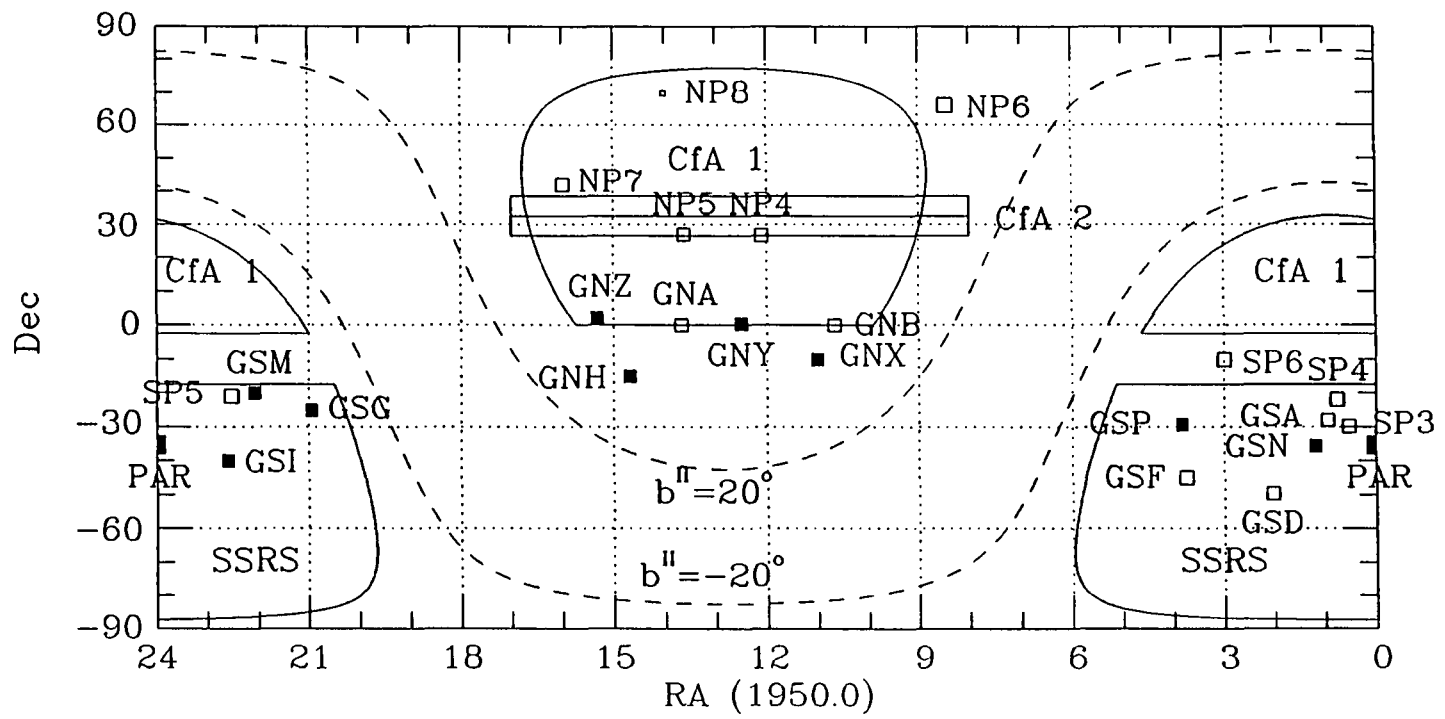
Since such a map distorts the relative separations between these 17^m fields, Figure 3.7 shows their positions on a polar projection of the north (a) and south (b) Galactic caps and Figure 3.8 shows the frequency histogram for their relative angular separations. Although the histogram in this latter figure is bimodal as a result of the fields being situated in both the north and south Galactic hemispheres ($|b^{II}|>40°$), both of these figures indicate that these surveys are likely to provide quite independent estimates of the galaxy distribution since the majority of fields lie more than 10° away ($23h^{-1}$ Mpc at the peak depth; see Figure 2.1 of Chapter 2, Section 2.1.1.2) from a nearest neighbour. The mean of the angular separations at $\theta_f<80°$ is 37° which corresponds to $87h^{-1}$ Mpc at the peak depth and this is much greater than the typical clustering length of galaxies ($r_o\approx5h^{-1}$ Mpc, see Section 2.1.2.4, Chapter 2).

Although much of the signal from a clustered distribution is lost in projection it is worthwhile presenting this information in the case of the Durham/SAAO Survey, as the redshift sample is a subset of the complete magnitude limited catalogue. In Figure 3.9 (a) to (i), the angular positions of those galaxies with redshifts (filled circles; codes 0, 1, 2, and 5 in Metcalfe et al. 1989) and those without (open circles) are presented for the 9 fields in this survey. As can be seen, the 1-in-3 sampling appears to be fairly uniform with no obvious biasses in the selection. From these figures it is evident that there are regions that are devoid of galaxies, even seen in projection, and this is not a result of noise introduced via the sampling for redshifts. Further, in GNX and GSG there are two clusters which merit more attention as they are, from these plots, fairly rich, if not very compact (likely members for these clusters are encompassed by a circle about their apparent centres).
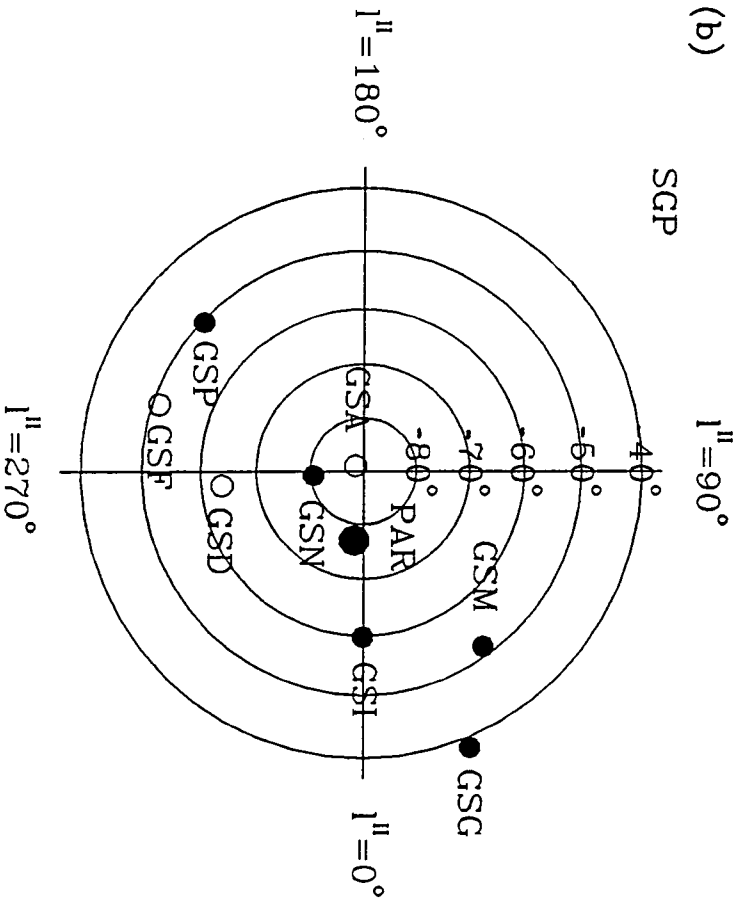
For comparison, similar 2-d plots of galaxy positions for the Durham/AAT Survey can be seen in Bean (1983) and for the Parker et al. Survey in Parker et al. (1986). As Bean points out, the former survey shows no evidence for any condensed structures which would, or have been classed, as of Abell (1958) richness. As will be seen below the GNX cluster lies at a distance of $82 h^{-1}$ Mpc and that in GSG at $115 h^{-1}$ Mpc. Bean states that 30 or so galaxies would be expected for an Abell cluster in a radius of 1 Mpc at this depth (from a consideration of the cluster-galaxy cross-correlation function of Seldner and Peebles 1977) and the cluster on GSG appears to have a membership that comes close to this level (the circles in Figures 3.9

Figure 3.7. The postions of the 17^m fields in a projection onto the north (a) and south (b) Galactic caps. The solid circles represent the position and approximate sizes of the Durham/SAAO and Parker et al. survey fields. The open circles represent those from the Durham/AAT Survey. The radial coordinate is the Galactic latitude b^{II} whilst the angular coordinate is the Galactic longitude l^{II}. Both coordinates are in degrees.
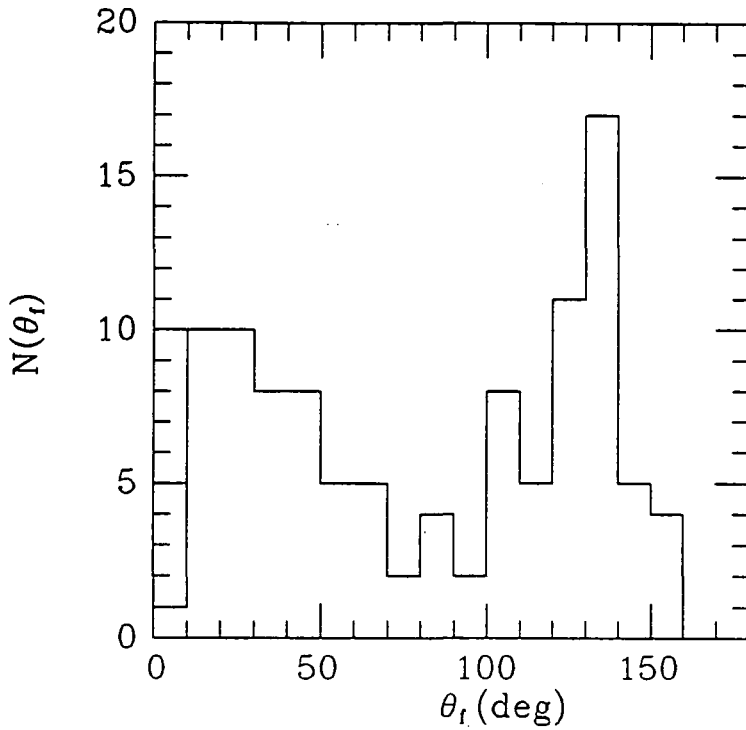
(a)

NGP

$l^{II}=0°$

$l^{II}=90°$

$l^{II}=270°$

$l^{II}=180°$

GNH
GNZ
◎GNA
GNY
80°
70°
60°
50°
40°
GNX
GNB

(b)

SGP

$l^{II}=180°$

$l^{II}=90°$

$l^{II}=270°$

$l^{II}=0°$

GSP
◎GSF
GSA
GSD
GSN
PAR
-80°
-70°
-60°
-50°
-40°
GSM
GSI
GSG
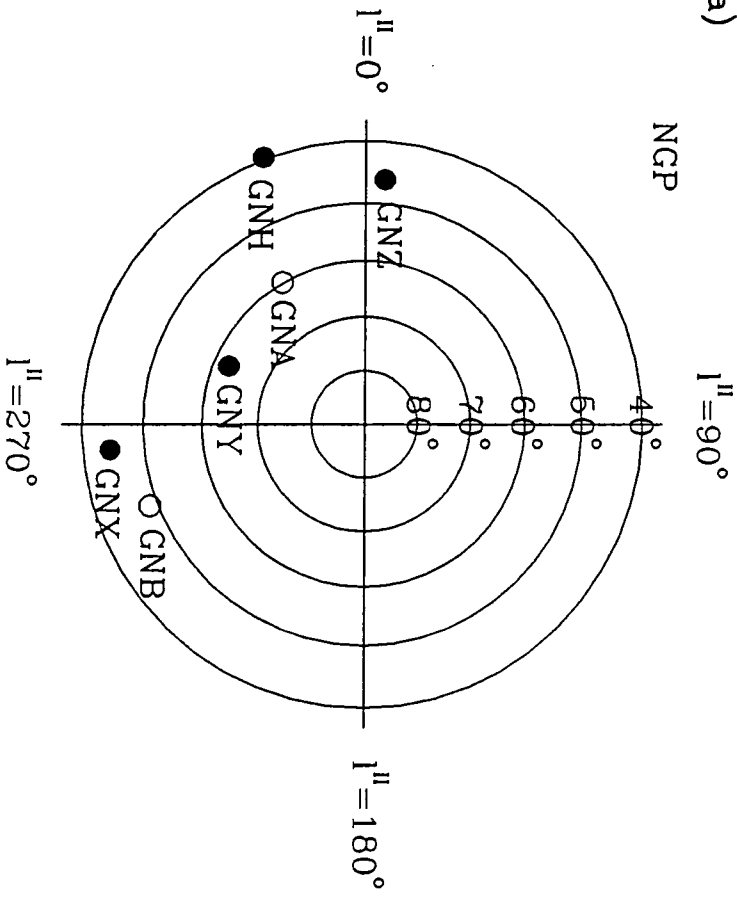
Figure 3.8. The frequency distribution for the angular separations between the fields in the Durham/SAAO, Durham/AAT and Parker et al. surveys. The number of angular separations $N(\theta_f)$ in bins of 10° is plotted against the angular separation θ_f (in degrees).

Figure 3.9. The distribution of galaxies on the sky in the Durham/SAAO Survey. In (a) to (i) the galaxy positions for each field are presented as they would appear on the sky; the orientation East and North is indicated. The open and filled circles are for galaxies with and without redshifts, respectively (the galaxies with redshifts have codes 0, 1, 2 and 5 in Metcalfe et al. 1989). In (a) and (e) two clusters are indicated by circles (these have a projected radius of $1h^{-1}$ Mpc). The membership for these clusters is 22 (14 corrected) and >30 (>25 corrected) for the clusters on GNX and GSG, respectively (the corrected values are obtained after subtracting a background count).
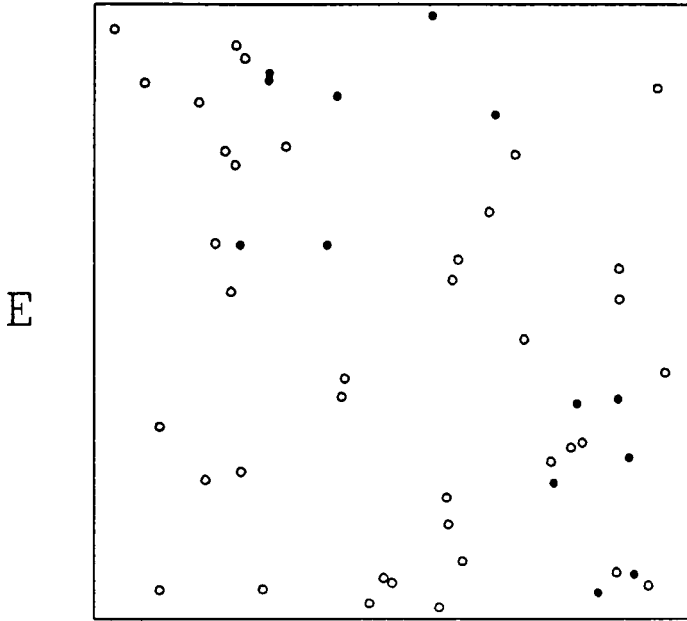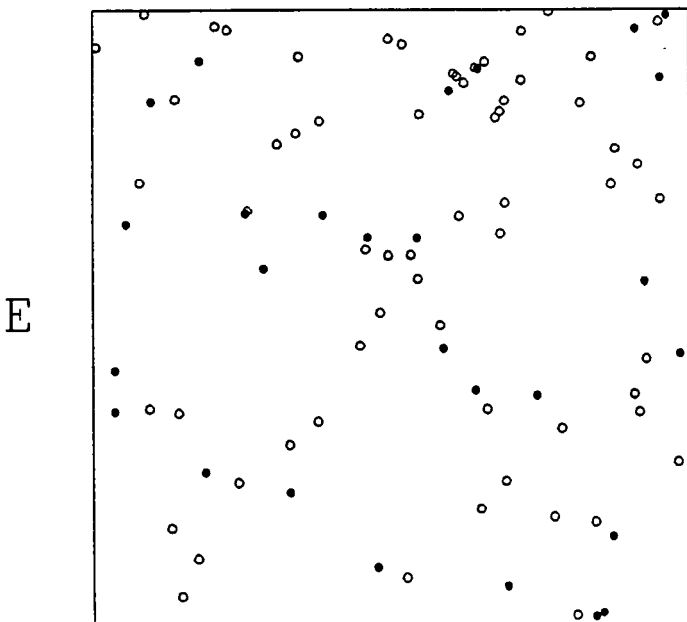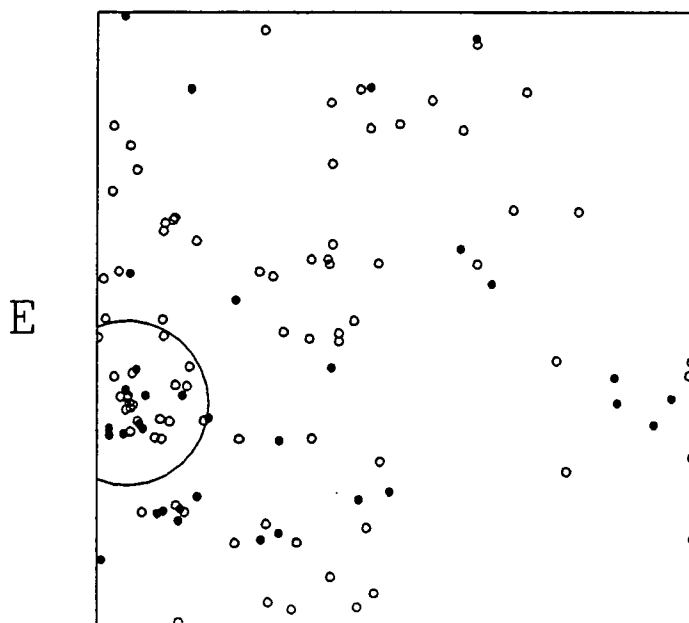
(a) GNX   N
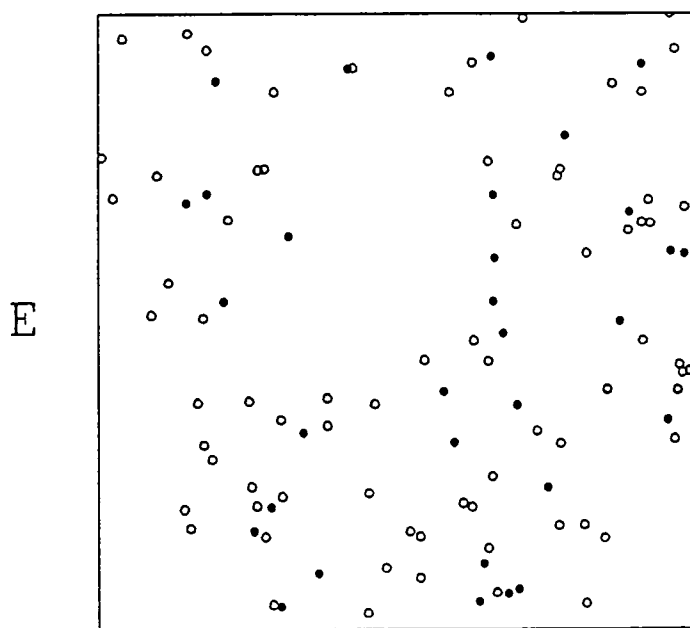
E

(b) GNY   N

E

(c) GNH N

E

(d) GNZ N

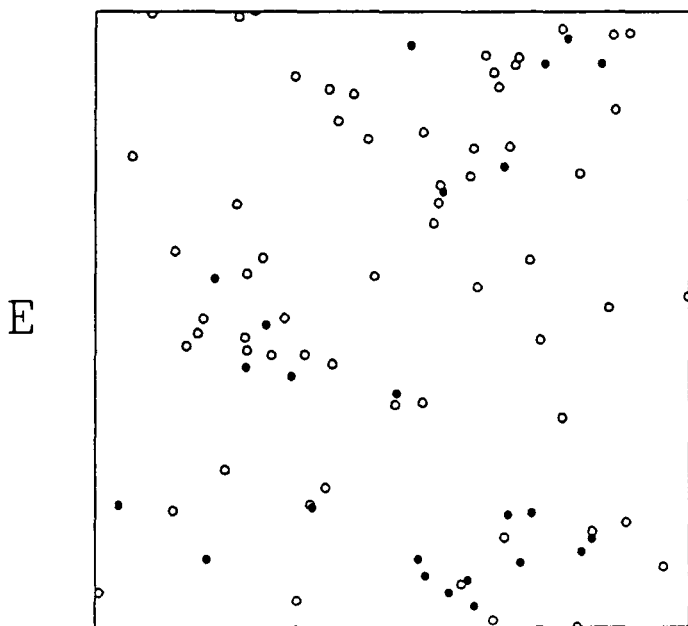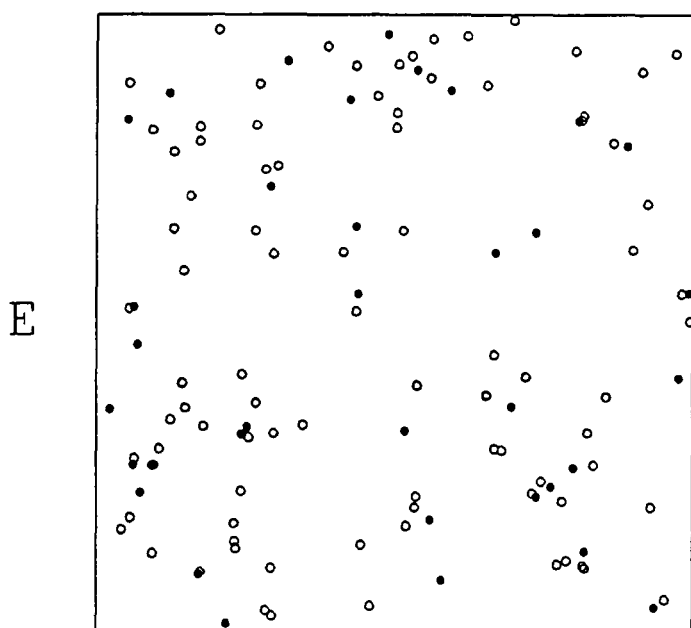E

(e) GSG   N
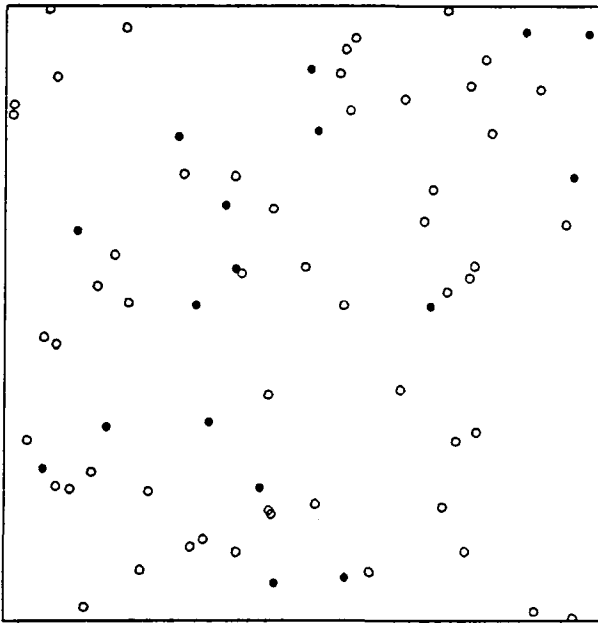
E

(f) GSM   N

E

(g) GSI   N

E

(h) GSN   N

E
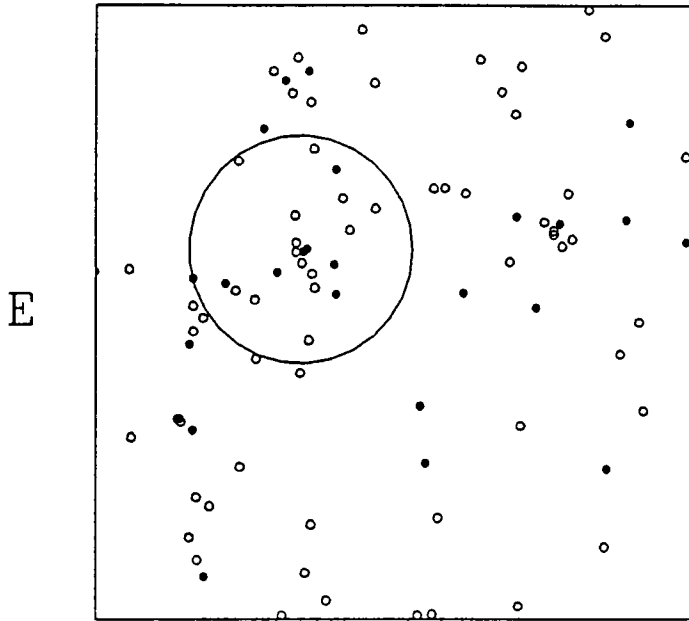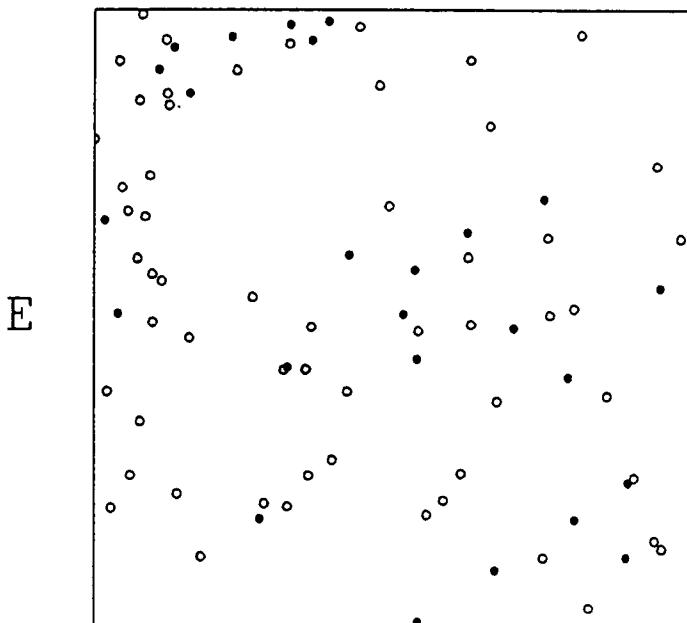
(i) GSP

(a) and (e) correspond to a radius of 1 Mpc at a depth of the clusters) although it has not been classed as such (Metcalfe et al. 1989). In fact, there are probably two Abell clusters (Abell 1564 in GNY and Abell 2412 in GSM) which contribute to the Durham/SAAO Survey but these are at a high redshift ($z \approx 0.077$) and so only a few (2 for the former and 4 for the latter) of the members are seen. This implies that the expected number of ~3 Abell clusters in these three surveys together is, perhaps, being obtained (based on a cluster density of 4.8×10^{-6} Mpc^{-3} from Peebles 1980) and this indicates that rich areas of clustering are not being avoided.
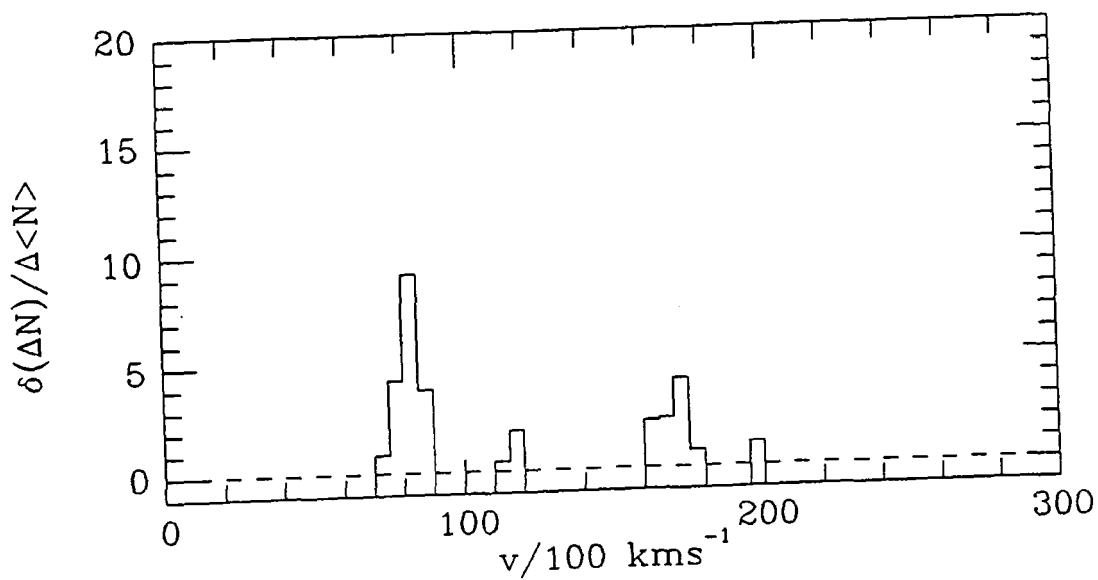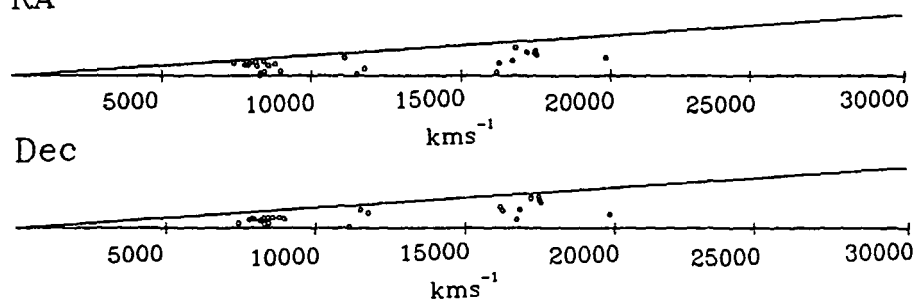
A better picture of the clustering distribution is obtained from the redshift maps. In Figure 3.10 (a) to (i), cone diagrams (plots of redshift velocity projected onto both the Right Ascension and Declination planes) for the Durham/SAAO Survey fields are presented, and below each is a histogram of the relative fluctuation in the count $\delta(\Delta N)/\langle \Delta N \rangle = (\Delta N - \langle \Delta N \rangle)/\langle \Delta N \rangle$ (see Section 2.1.1.2, of Chapter 2) in bins of $5h^{-1}$ Mpc in which the selection by apparent magnitude has been normalised out. The general view of these fields is that, similar to the Durham/AAT Survey, there is evidence for a distinct clumpiness down the redshift volumes (with prominent regions devoid of galaxies) but in contrast to that earlier work (see Bean 1983) the edges of the Durham/SAAO clusters generally exhibit less of the sharpness that was previously observed. To show that this is not necessarily a result of the sampling in the Durham/SAAO catalogue, in Figure 3.10 (j) to (n) equivalent 1-in-3 sampled versions of the Durham/AAT Survey are presented for comparison. As can be seen, in particular, in GSA and GSD there are clumps that appear to be quite tightly clustered along the line-of-sight (as shown by the values of $\delta(\Delta N)/\langle \Delta N \rangle$), whereas the Durham/SAAO fields more closely resemble GSF, in which this form of clustering is not so prominent.

It is tempting to speculate on the causes of these differences. The suggestion of flat structures perpendicular to the redshift direction evokes the picture of the redshift fields intersecting voids or sheets as suggested in the model by de Lapparent et al. (1988) and it is profitable to look for any likely structures that may extend between the redshift fields. In Figure 3.11, the relative counts $\delta(\Delta N)/\langle \Delta N \rangle$ are compared for 10 pairs of fields that lie within 18 degrees on the sky and as can be seen there is sometimes a good correlation between the counts (especially for fields GSP and GSF, for example). Using the overlap in the south at $v < 12000$ kms^{-1} between the Durham/SAAO,

Figure 3.10. Redshift cone plots of the galaxies in the Durham/SAAO, Durham/AAT and Parker et al. surveys. The cone plots and histograms of the relative fluctuations in the counts $\delta(\Delta N)/\langle\Delta N\rangle = (\Delta N - \langle\Delta N\rangle)/\langle\Delta N\rangle$ are shown in (a) to (i) for the Durham/SAAO Survey, (j) to (n) for the Durham/AAT Survey and in (o) for the Parker et al. Survey. The Durham/AAT plots and histograms were obtained from a 1-in-3 sampled version of that catalogue. In all the figures the cone plot marked R.A. is the projection on to the Right Ascension plane. Likewise the cone plot marked Dec. is the projection onto the Declination plane (R.A. and Dec. both increase up the page). The horizontal axis in all plots is the redshift velocity in units of kms^{-1}.

(a) GNX
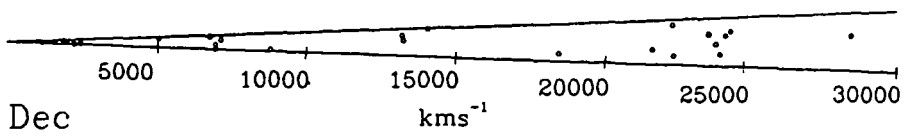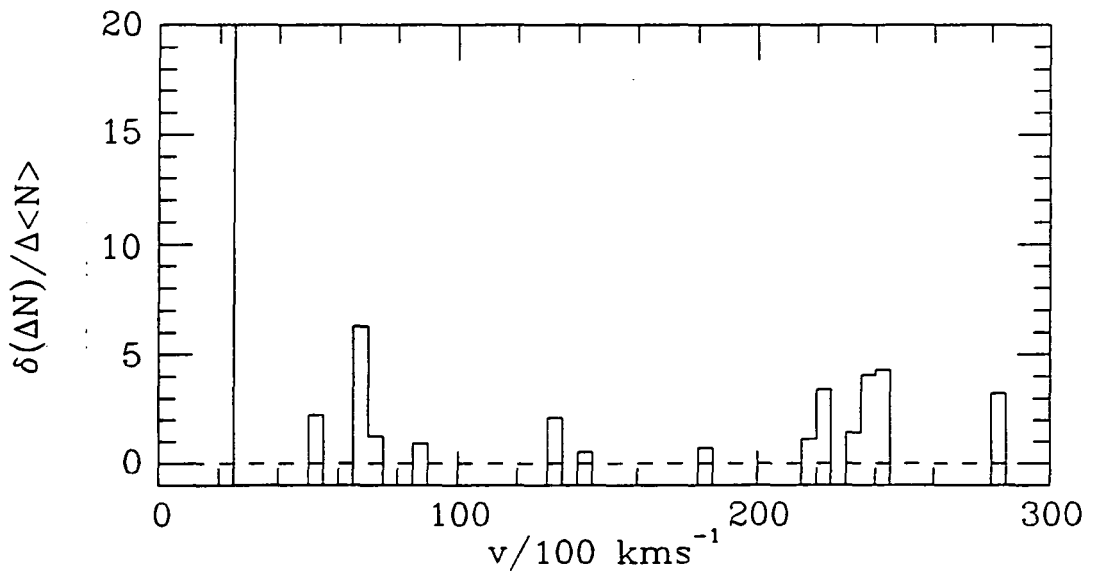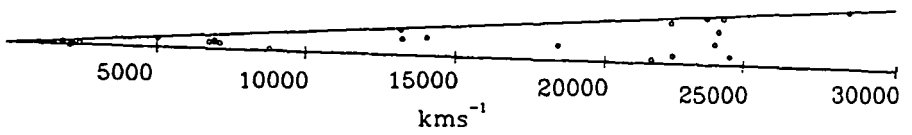
(b) GNY

RA

Dec

$\delta(\Delta N)/\Delta\langle N\rangle$

$v/100 \ \mathrm{kms}^{-1}$

(c) GNH

RA

Dec

(d) GNZ

(e) GSG

(f) GSM

RA

Dec

$\delta(\Delta N)/\Delta\langle N\rangle$

$v/100\ \mathrm{kms^{-1}}$

(g) GSI

RA

Dec

$\delta(\Delta N)/\Delta\langle N\rangle$

$v/100\ kms^{-1}$

(h) GSN

RA

Dec

$\delta(\Delta N)/\Delta\langle N\rangle$

v/100 kms^{-1}

(i) GSP

RA

Dec

(j) GSA

RA

Dec

(k) GSD

RA

Dec
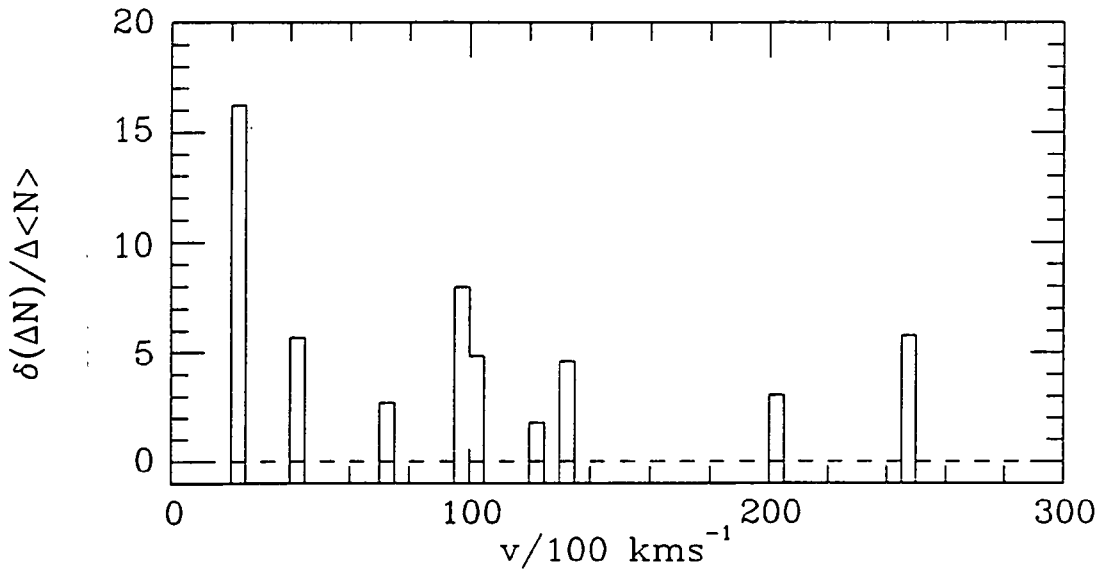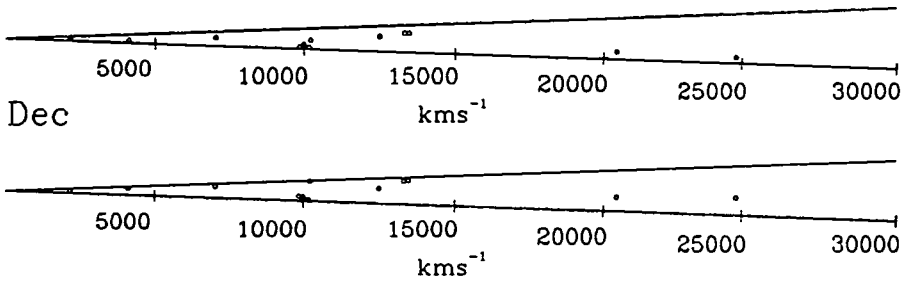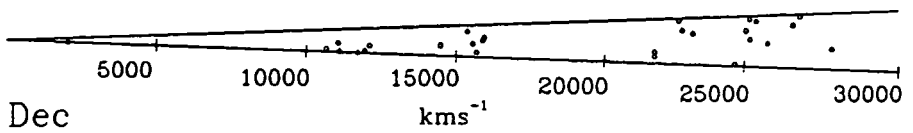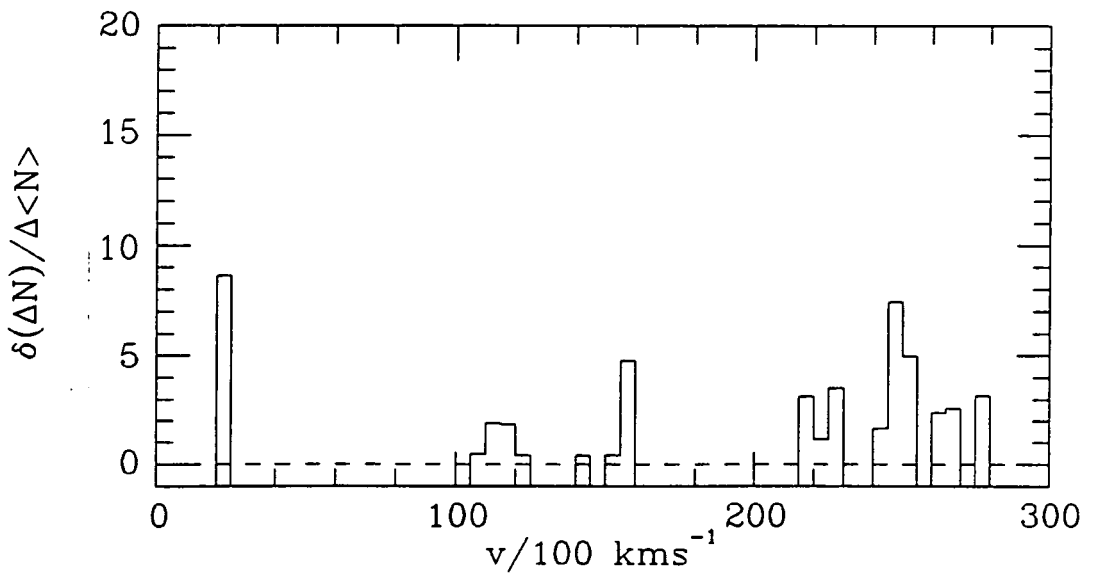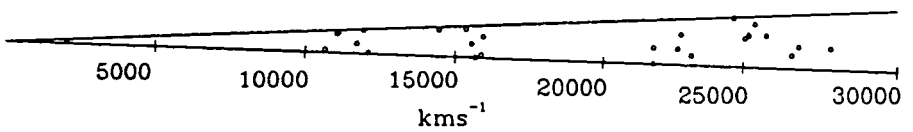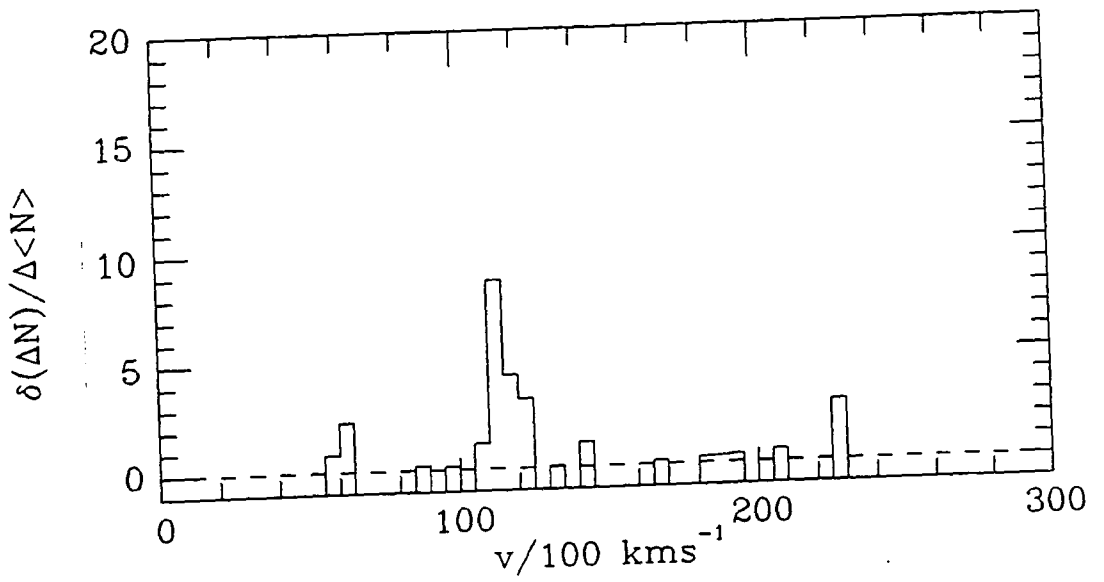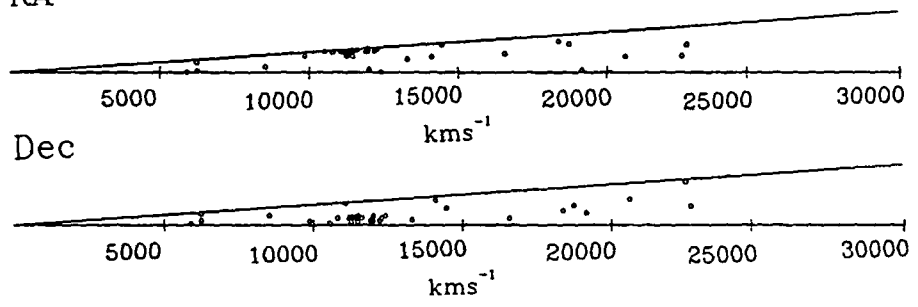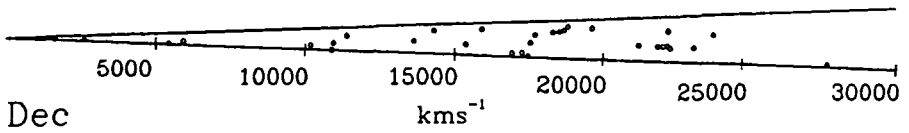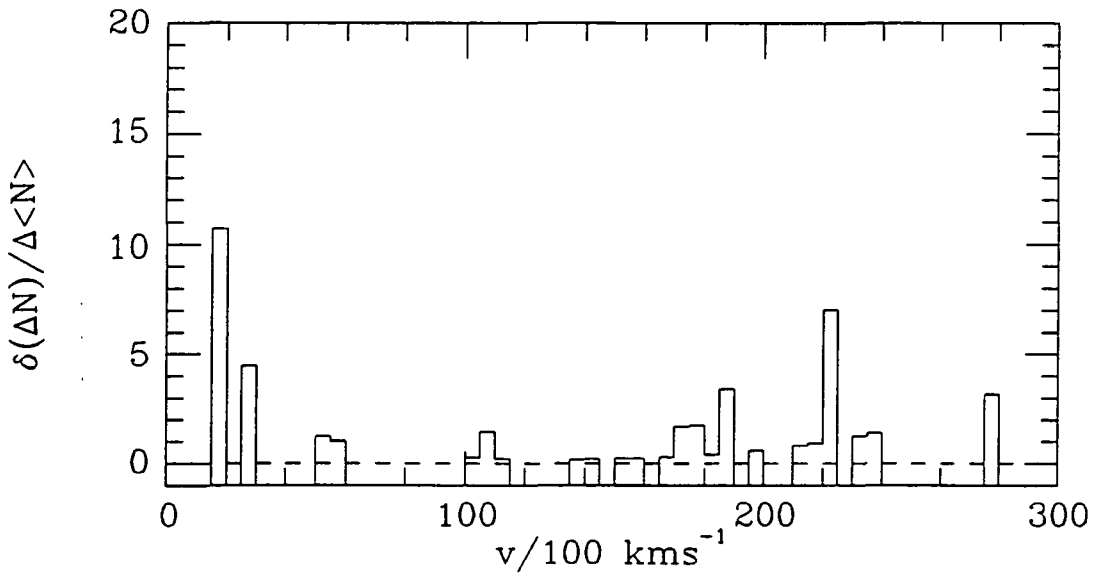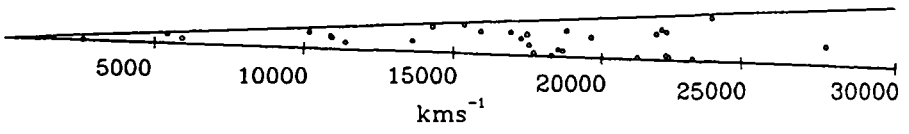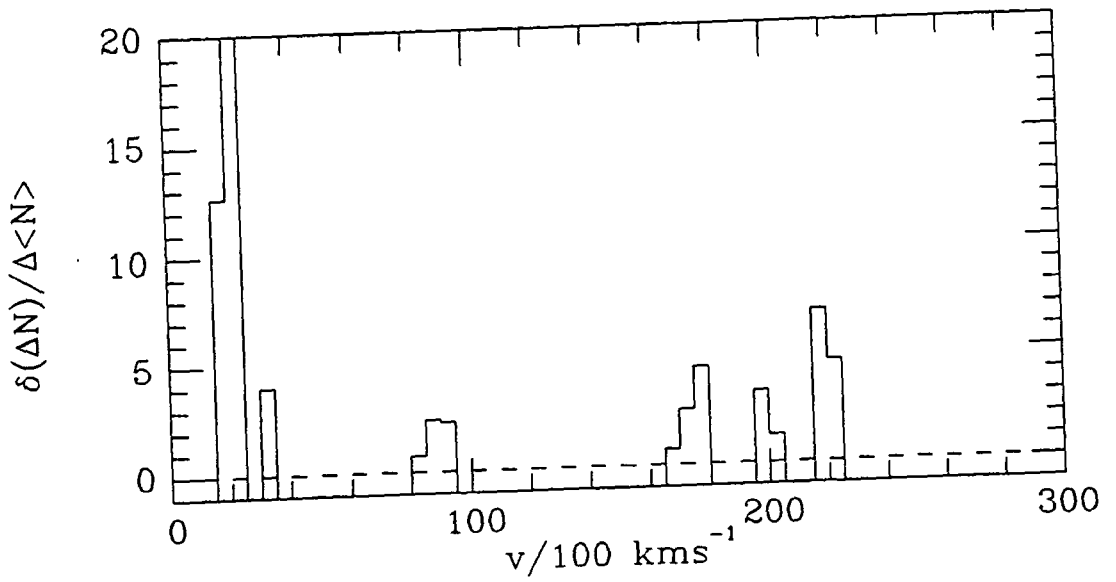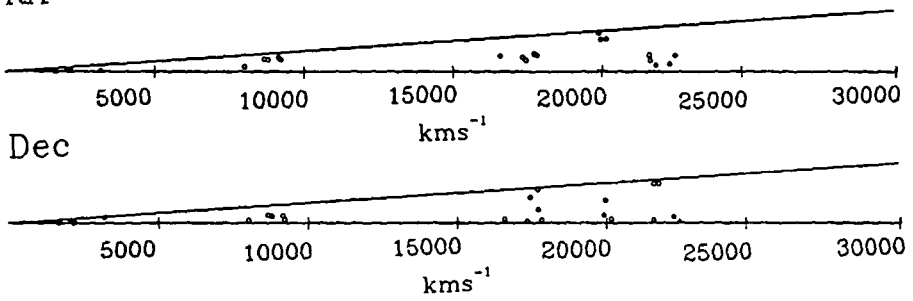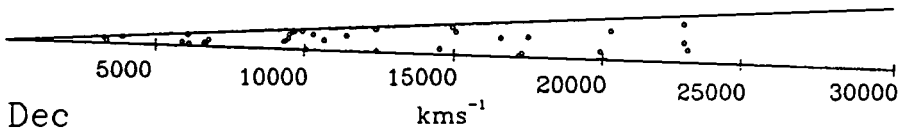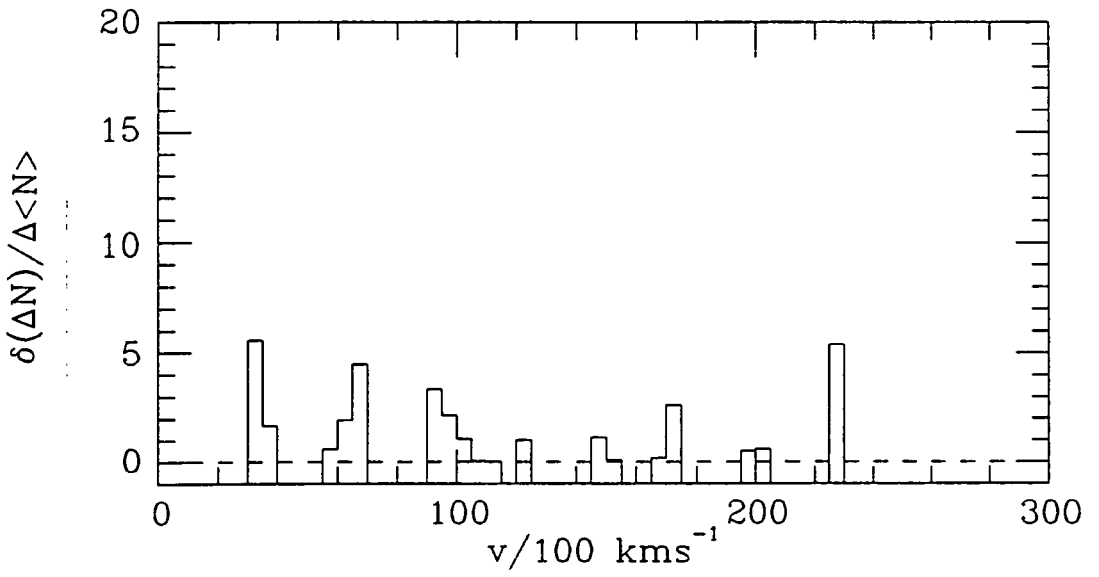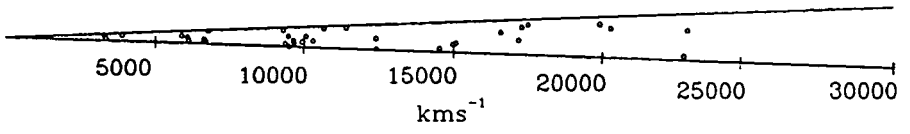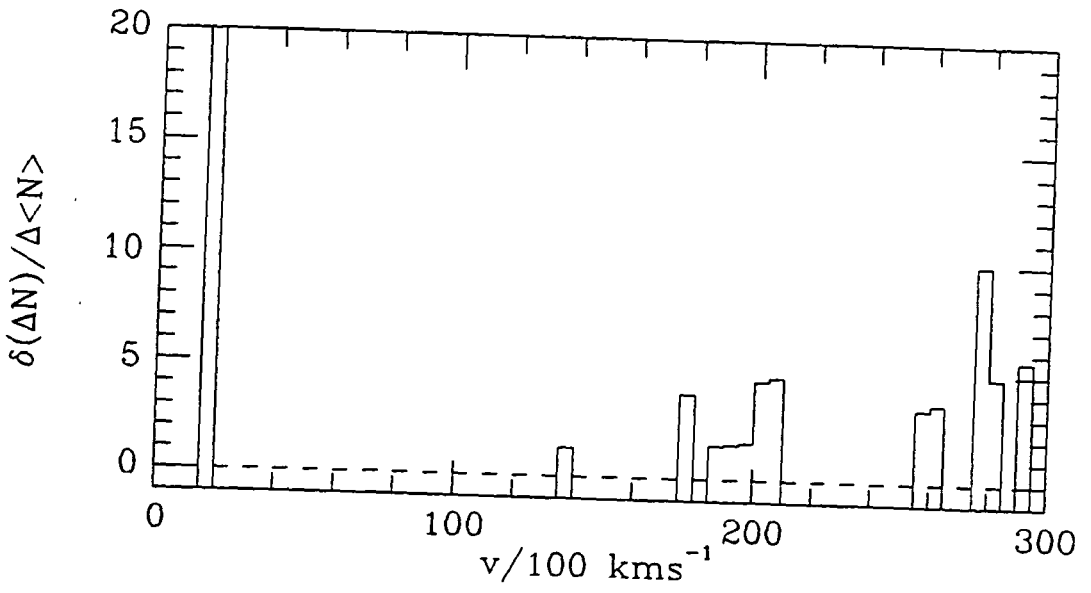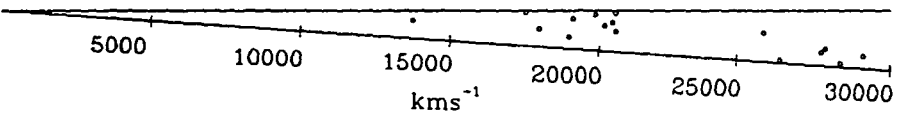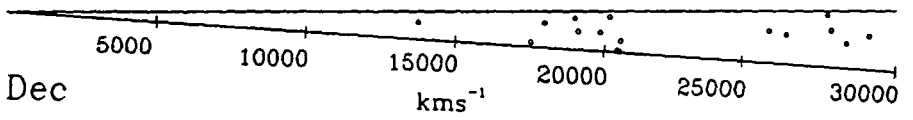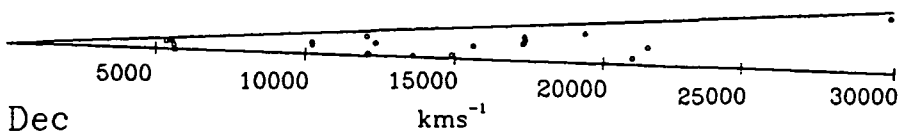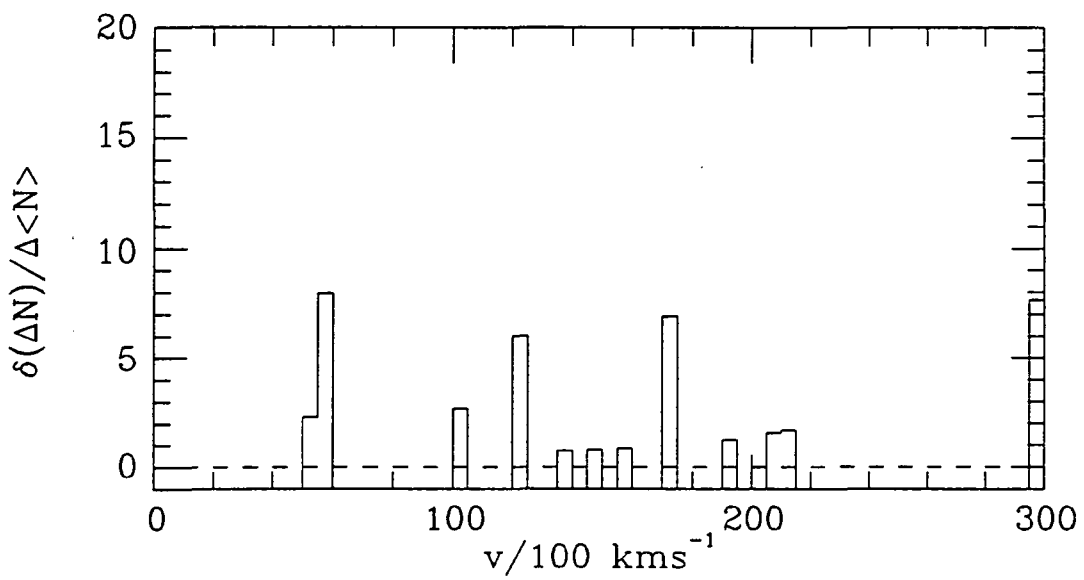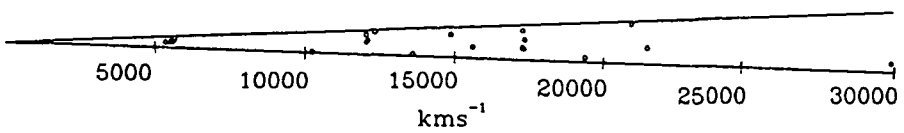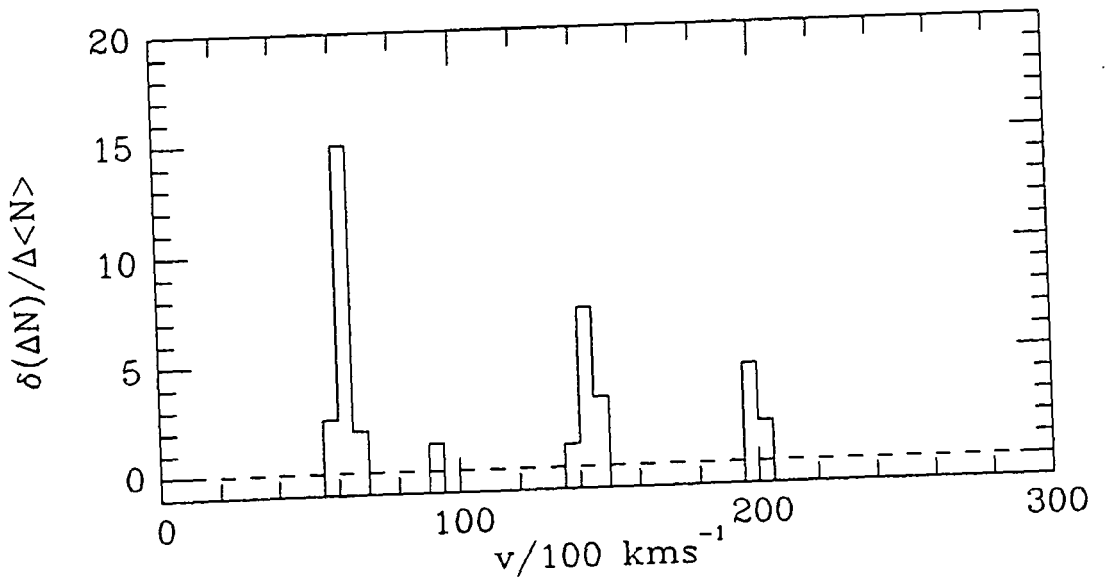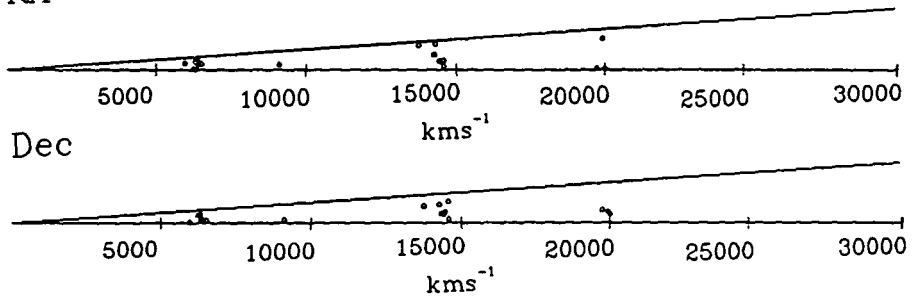
(1) GSF

RA

Dec

(m) GNA

RA

Dec

$\delta(\Delta N)/\Delta\langle N\rangle$

$v/100 \text{ kms}^{-1}$

(n) GNB

(o) PAR

RA

Dec
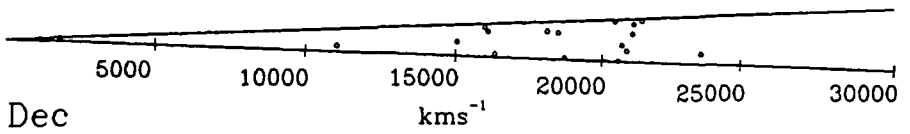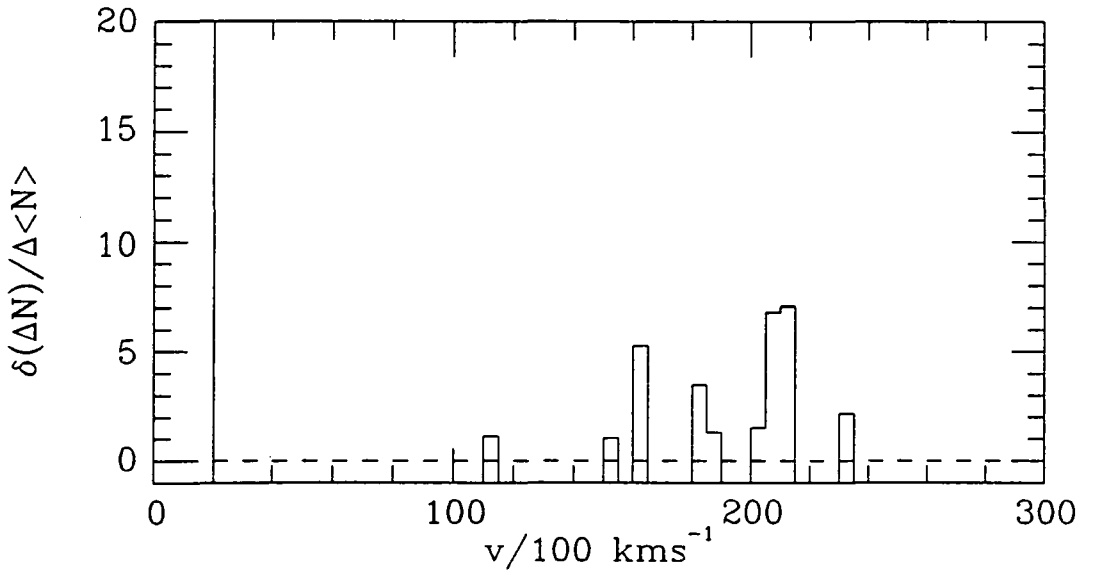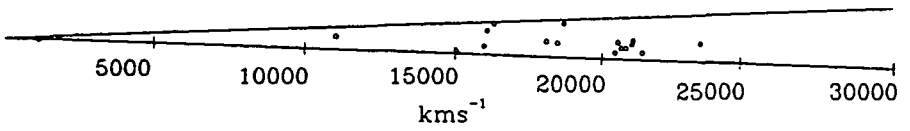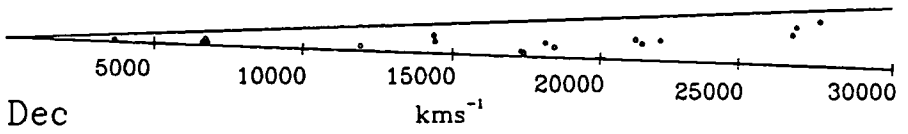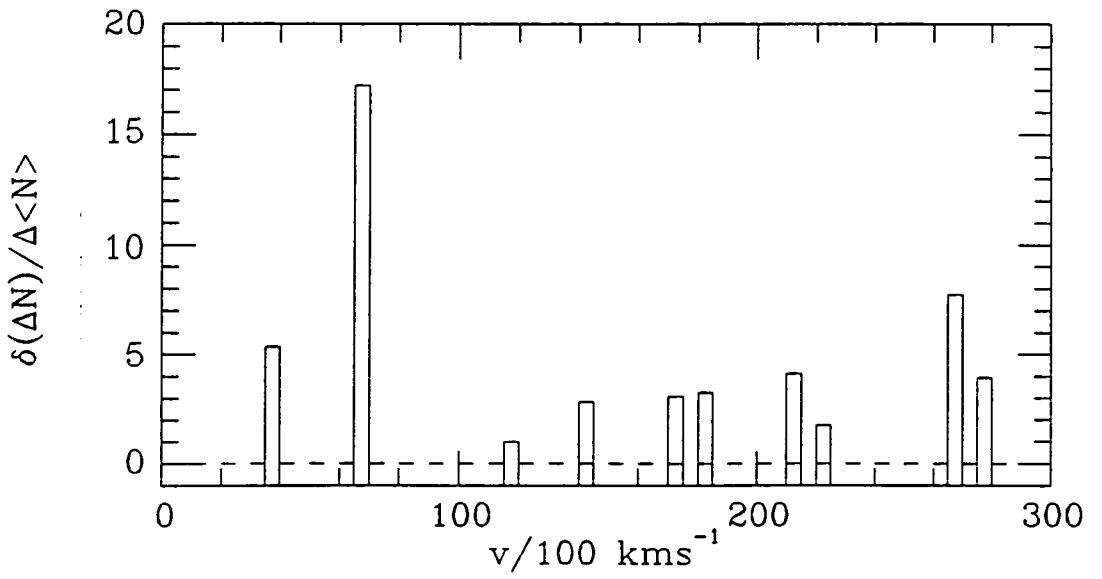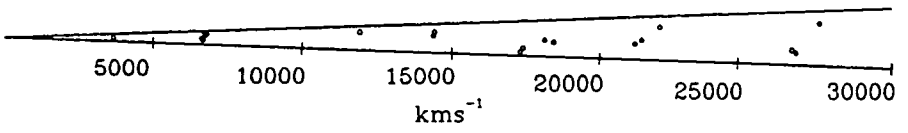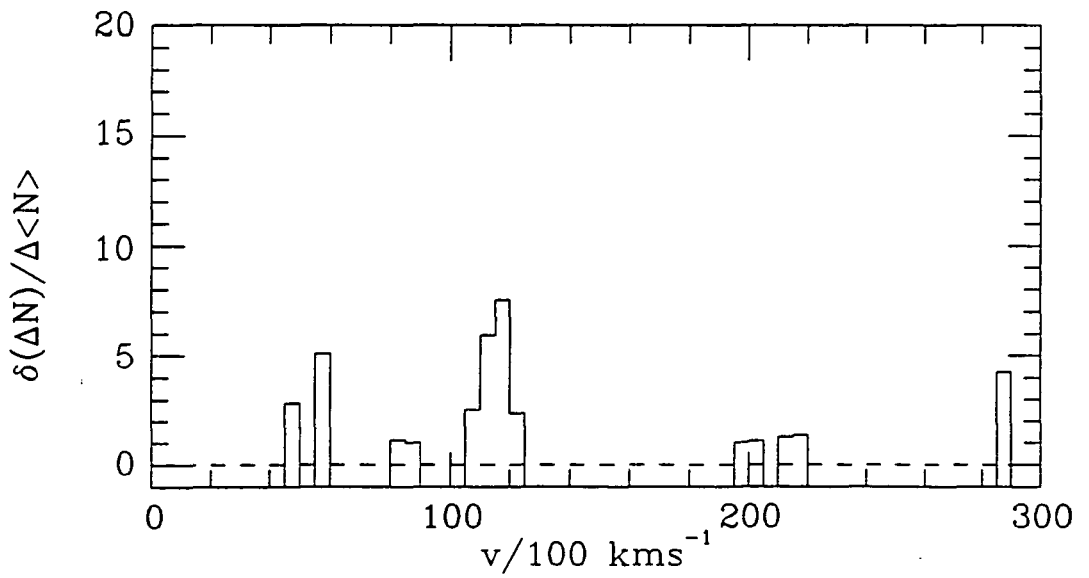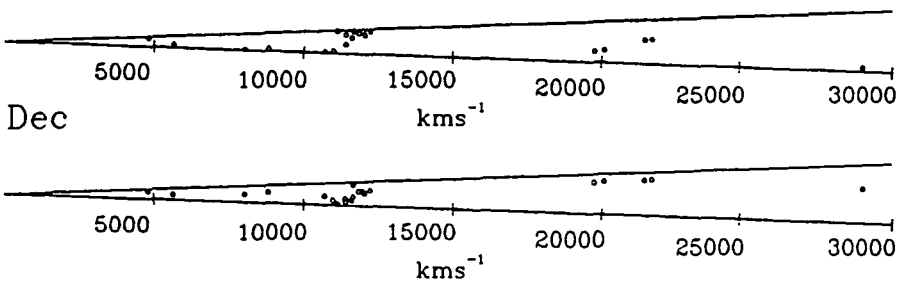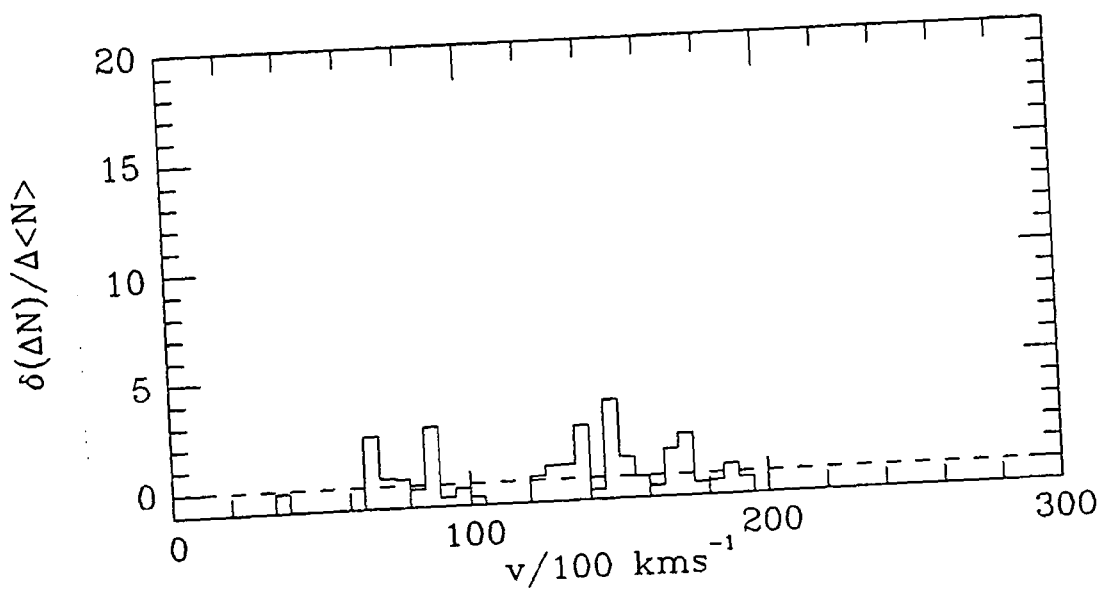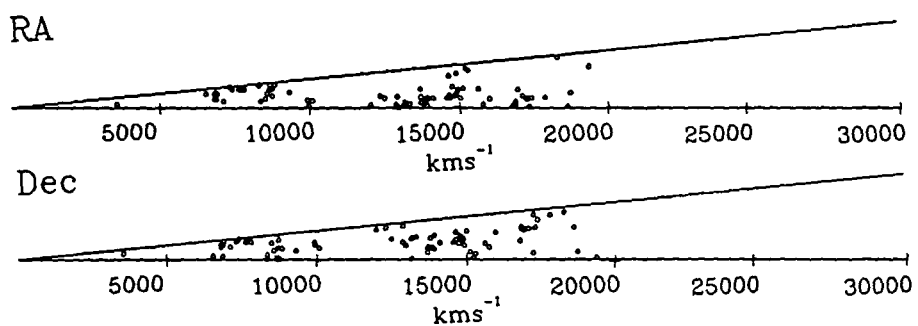
Figure 3.11. The distributions of the relative fluctuations in the counts $\delta(\Delta N)/\langle \Delta N \rangle$ for 10 pairs of fields in the Durham/SAAO, Durham/AAT and Parker et al. surveys that lie within 18° on the sky. The $\delta(\Delta N)/\langle \Delta N \rangle$ distributions are the same as those in Figure 3.10 (a) to (o); for clarity the upper field has been offset by +20 in $\delta(\Delta N)/\langle \Delta N \rangle$. The angular separation in degrees is marked.

(a)

GSP GSA GSM GSG

465 GALAXIES
-30.0° < δ ≤ -19.5°

Km/s

(b)

GSP GSN PAR GSI

393 GALAXIES
-40.0° < δ ≤ -30.0°

Km/s

(c)

GSF GSD GSI

295 GALAXIES
-50.0° < δ ≤ -40.0°

Km/s

(a)   8.09

(c) 14.05

(d) 14.34

(e)   15.67

GSP

GSF

(f)   16.23

GSM

GSG

(g)   16.91

GSN

GSD

$\delta(\Delta N)/\Delta\langle N\rangle$

$v/100 \ kms^{-1}$

(h)   17.36

GSI

PAR

$\delta(\Delta N)/\Delta\langle N\rangle$

$v/100 \ kms^{-1}$

(j)   17.90

(i)   17.58
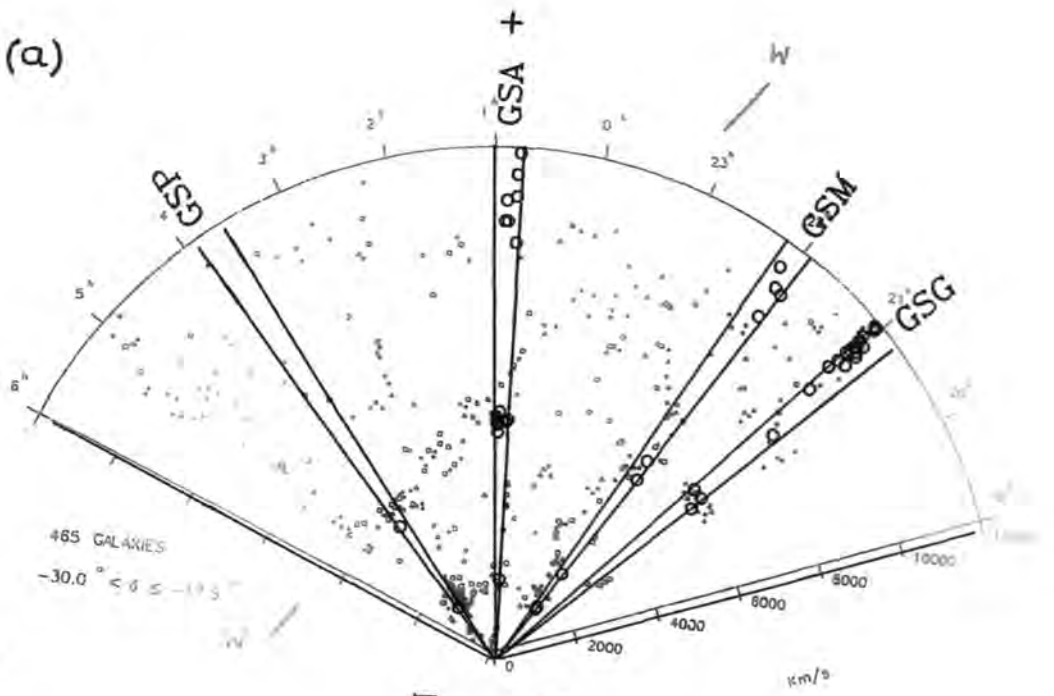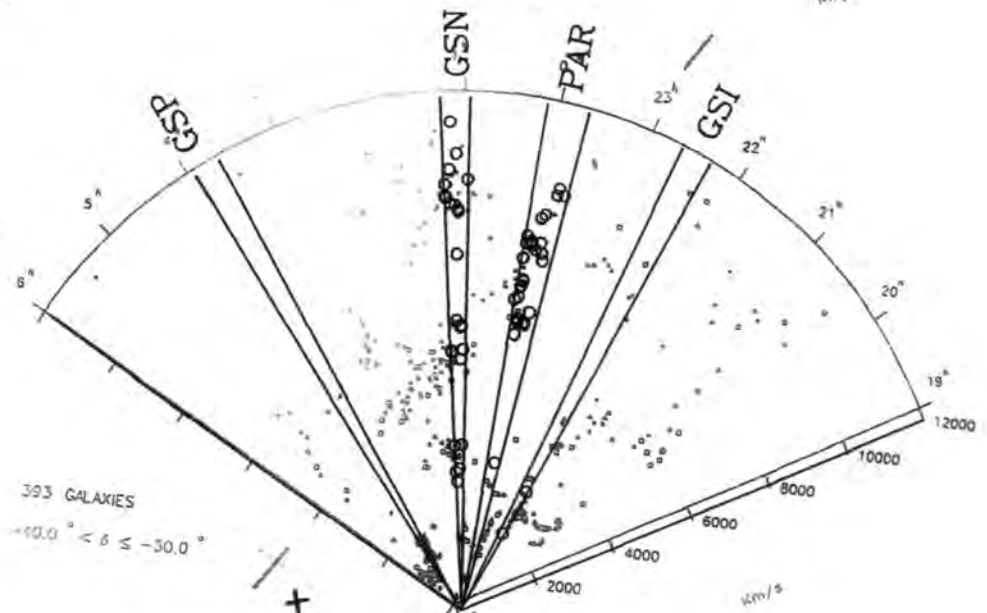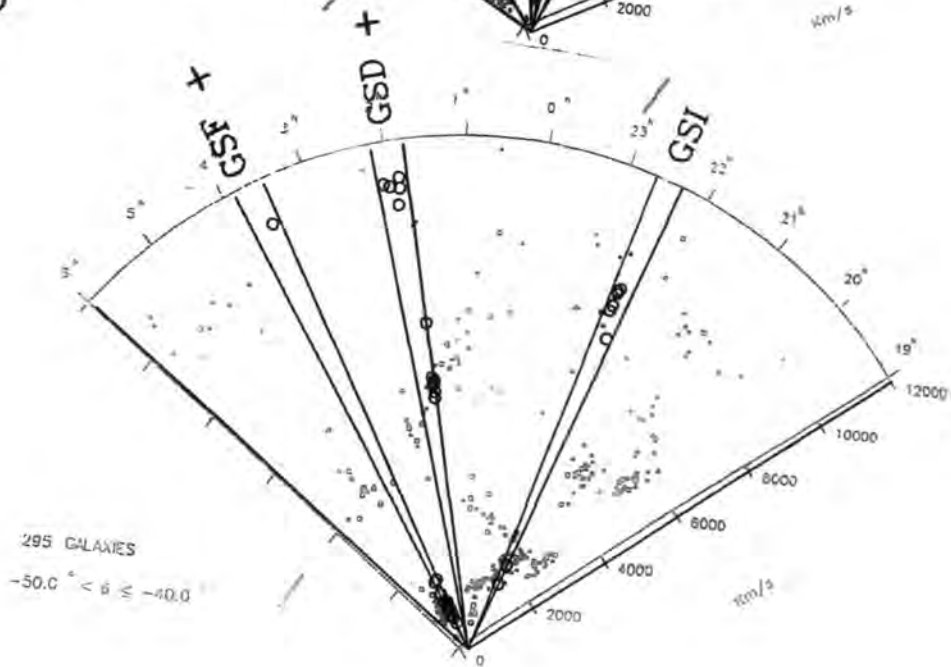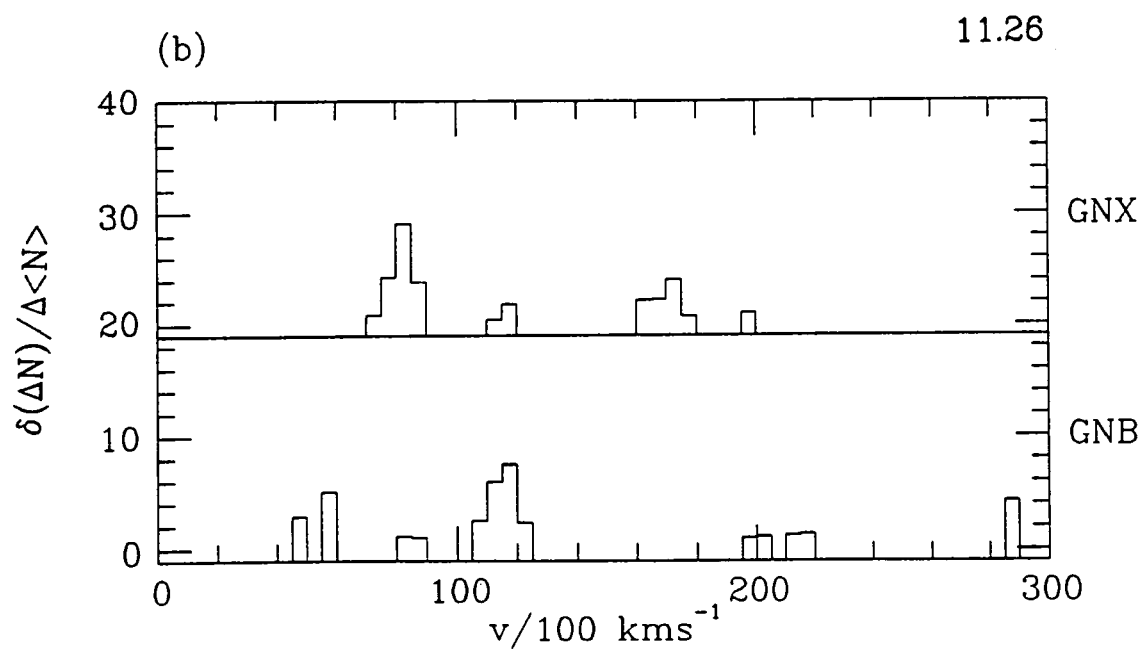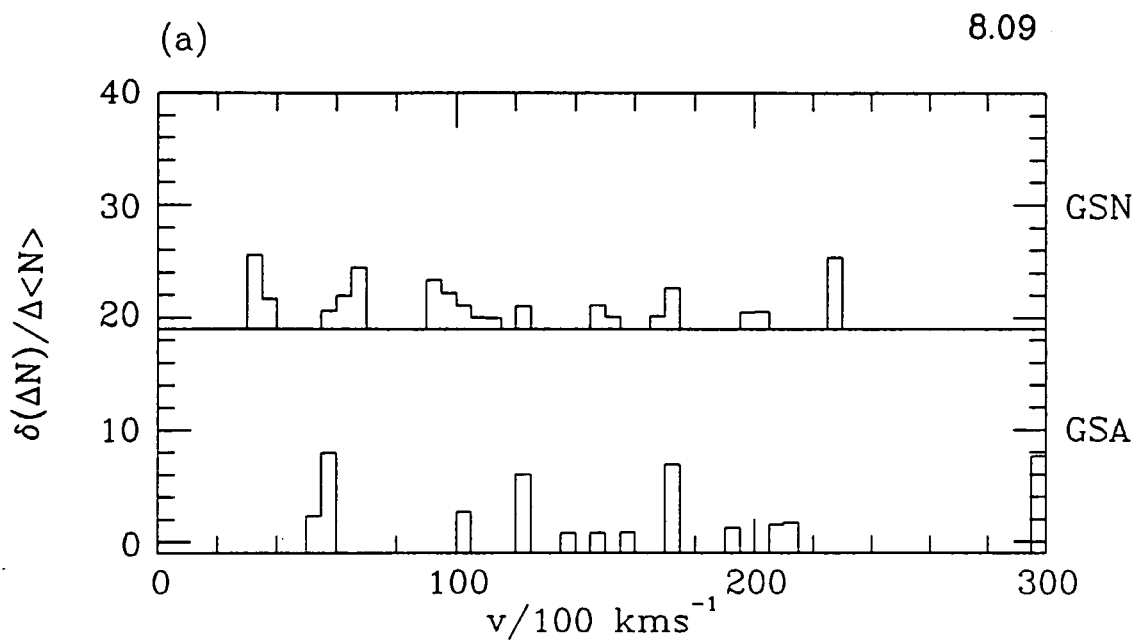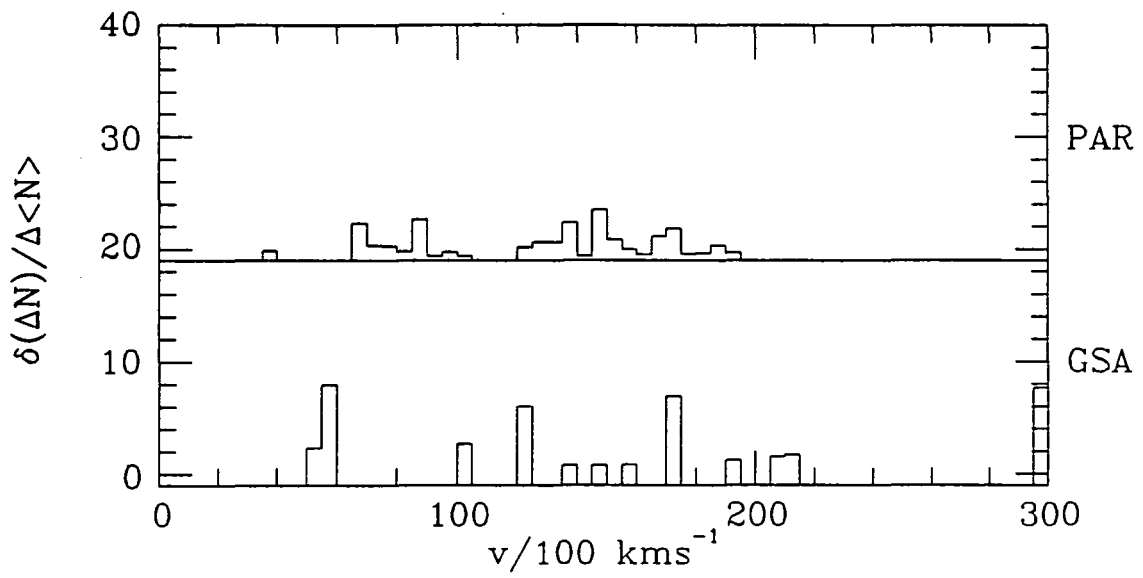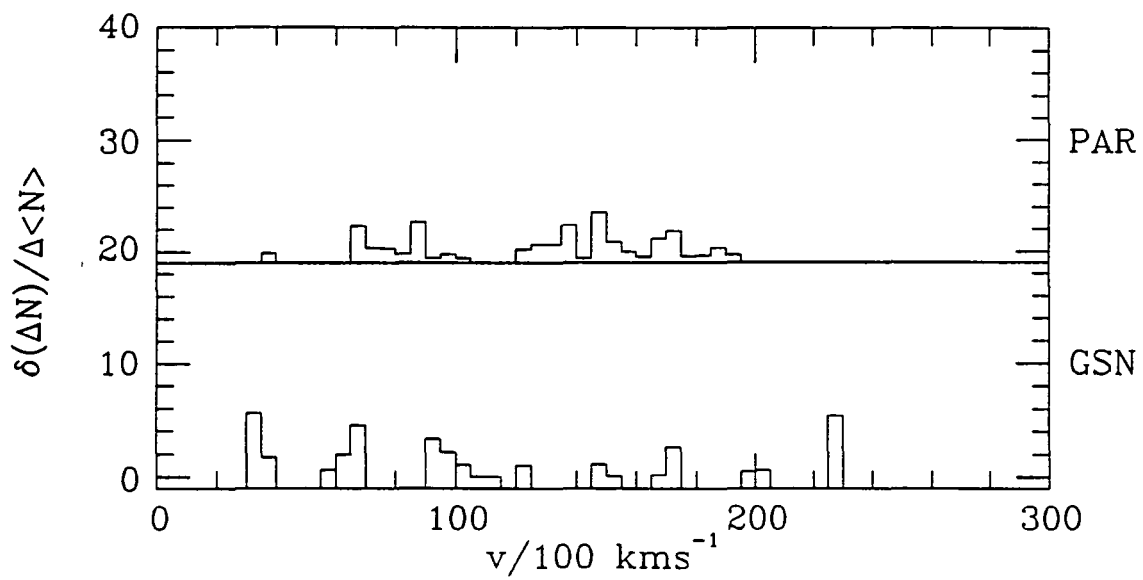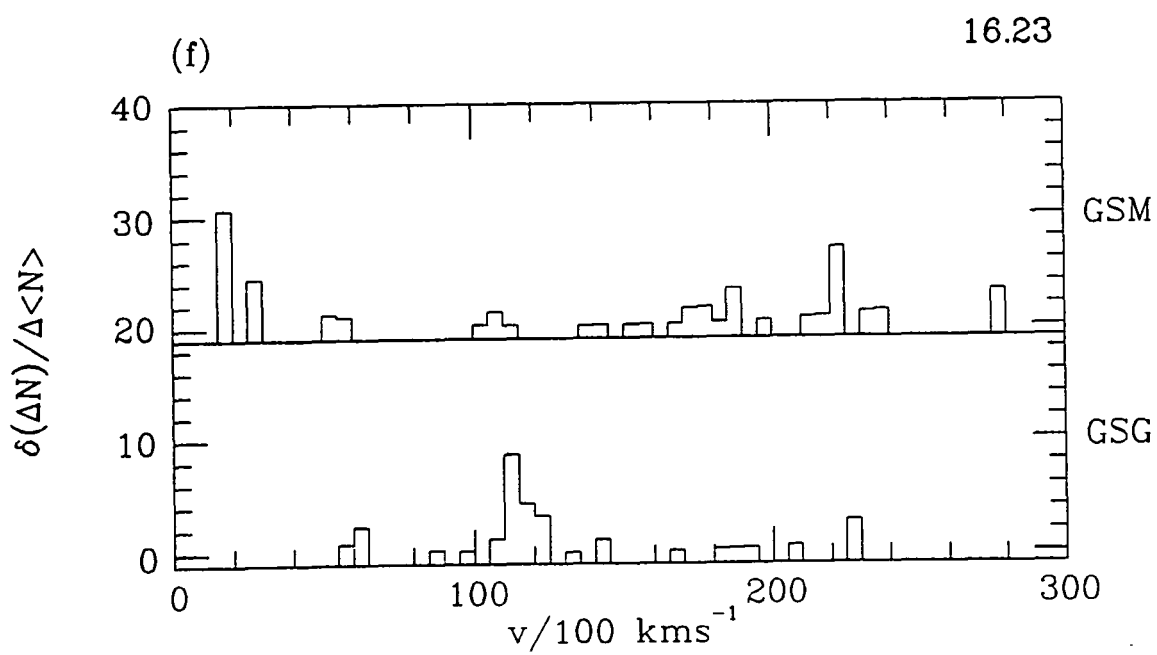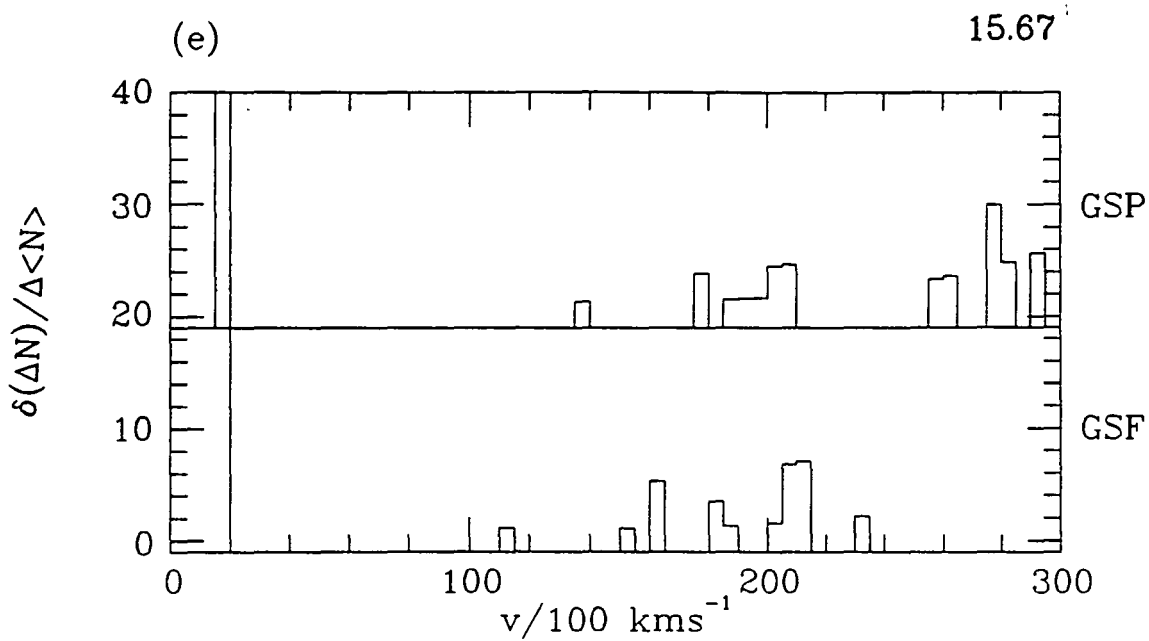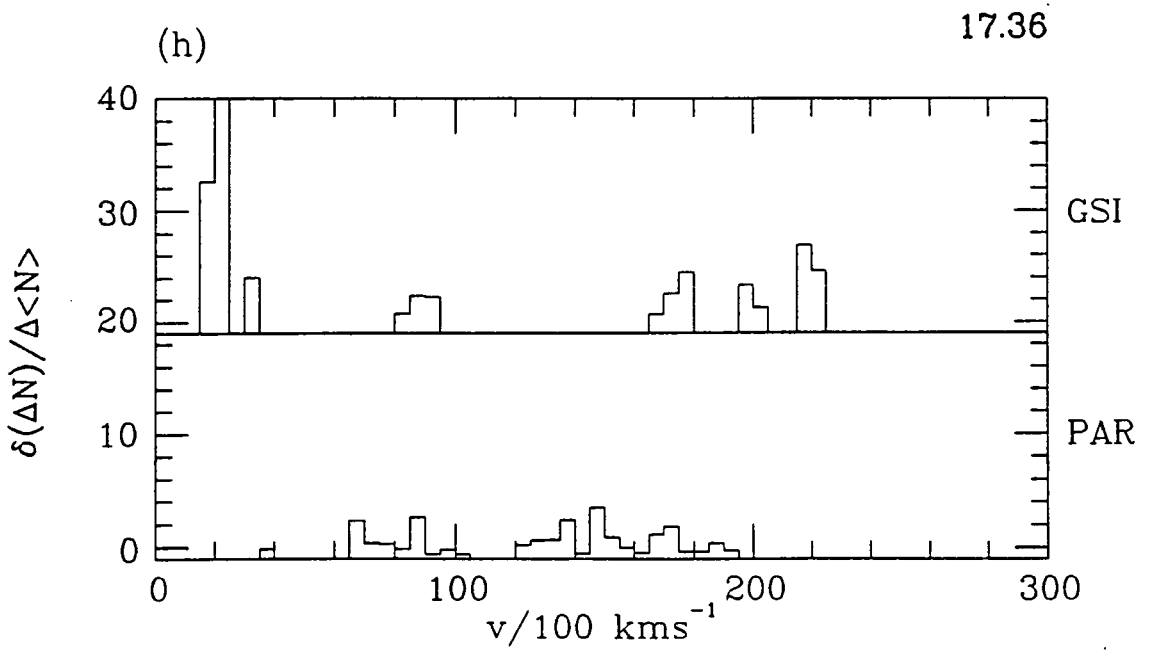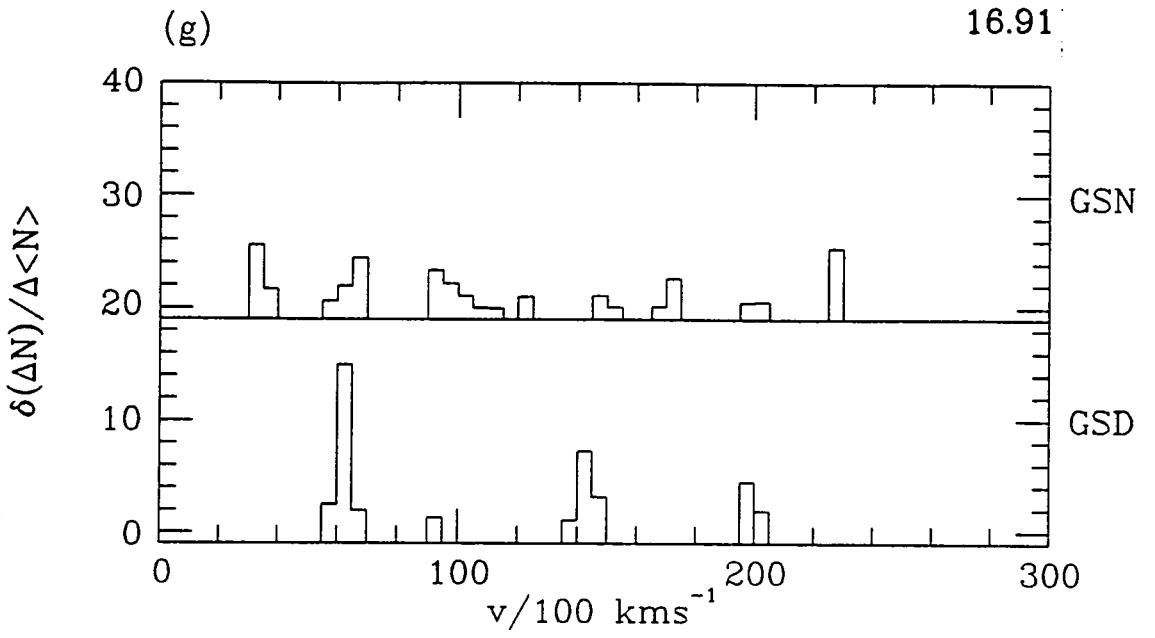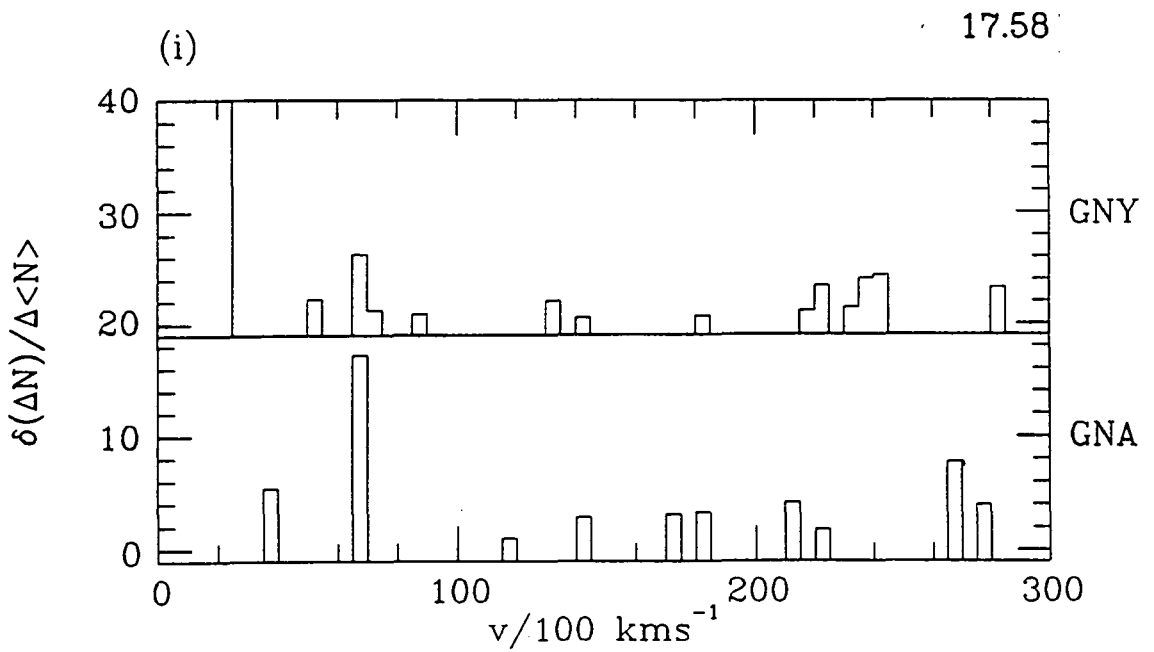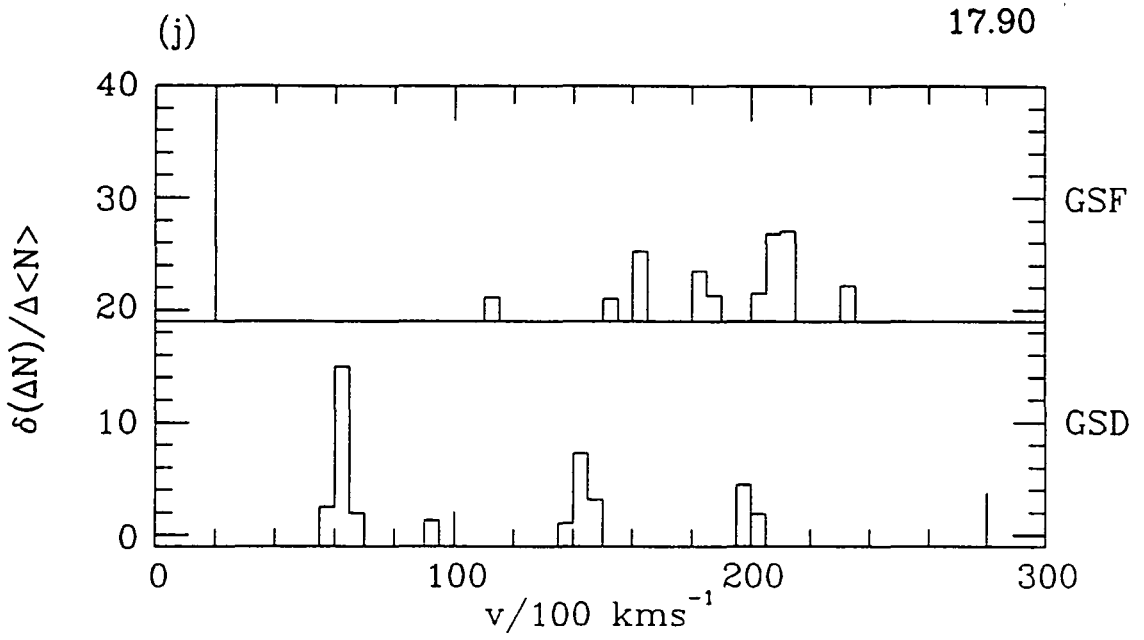
Durham/AAT and Parker et al. surveys and the SSRS sample (Da Costa et al. 1988), extended structure can be searched for in more detail. In Figure 3.12 (a) to (c) the $b_J \leq 17^m$ fields are reproduced on top of the appropriate slice of the SSRS sample and from this it can be seen that there appears to be some continuity in the clustering across the fields. For example, the 'wall' referred to in da Costa et al., and marked in Figure 3.11 (a), (b) and (c), can be seen to cut across 6 of the fields; GSA and GSP in (a), GSN and the Parker et al. field in (b) and GSD and GSF in (c). Further, the large underdensity in GSP and GSF is also seen as an underdensity of diameter ~50 h^{-1} Mpc in the SSRS Survey and this may make it comparable in size to the Boötes void of Kirshner et al. (1981, 1987). However, it should again be emphasised that although there do   appear to be extended voids and filaments (or sheets) in these maps this does not necessarily imply that there is, on average, large-scale structure in the overall galaxy distribution; as seen before (Figure 3.4 (c) and (d)) apparently extended structure can be caused by the overlap (or absence) of several randomly placed clumps of galaxies.

The difference in the morphology of the clumps in the Durham/AAT and Durham/SAAO surveys could be caused by differences in the observed peculiar motions. In the presence of large random velocities it would be expected that the sharp edges in the distribution would be blurred by the fingering effect discussed previously (Chapter 2, Section 2.1.2.2). In the Durham/AAT Survey this does not appear to be the case and this is backed up by the study of the pair-wise line-of-sight peculiar motions in this sample which are seen to be $\langle \omega^2 \rangle^{1/2} \approx 200 \text{kms}^{-1}$ (Bean 1983, Bean et al. 1983). Alternatively, distinct edges and increased correlations perpendicular to the line-of-sight can be caused by some degree of infall as has been noted by Bean et al. (1983) and Kaiser (1987). As will be seen in the following chapter such tests can be made from an analysis of $\xi_v(\sigma,\pi)$ which averages the various forms of clustering over the whole survey enabling a separation, to some extent, of the pair-wise velocities from the spatial clustering distribution.

The two clusters described above in GSG and GNX are clearly observable in the cone diagrams in Figure 3.10 (a) and (e) and are not just caused by the overlap of smaller clumps. Taking those members that lie within the projected circles in Figure 3.9 (a) and (e) with redshift velocities in the range 7200 to 9200 kms^{-1}, in the case of GNX, and 10500 to 12500 kms^{-1}, in the case of GSG, line-of-sight rms velocity dispersions of 409 and

Figure 3.12. Overlaps between the fields in the Durham/SAAO, Durham/AAT and Parker et al. surveys and the SSRS Survey. The $m(b_J) \leq 17^m$ redshift survey fields are overlayed on three of the declination slices of the SSRS Survey (see Figure 7a,b,c of da Costa et al. 1988). In the overlays (a), (b) and (c) the galaxies indicated (large open circles) are those that lie within the corresponding R.A. and Dec. range of the corresponding slice. All the galaxies with redshifts to the magnitude limit of the fields are shown and the positions of the galaxies indicated are exactly as they would appear in the underlying slice. The fields marked with a '+' are in the Durham/AAT Survey. The radial coordinate is the redshift velocity in kms^{-1} and the angular coordinate the R.A. in hours.

461 kms[-1] are found, respectively, for these clusters. These values agree well with typical velocities expected for such structures (Zabludoff et al. 1990) although the measurements are fairly uncertain because of the details of the cluster membership.

Finally, a brief comment is made on the Parker et al. Survey. This one field is twice the solid angle of a single Durham/SAAO or Durham/AAT field and shows some extended continuous structure separated by regions of quite low density. Like the Durham/AAT Survey, the edges of the underdense boundaries appear to be fairly sharp and there seems to be little evidence for any particularly remarkable clusters showing the fingering effect. However, the concentration at ~15000kms[-1] does appear to be fairly prominent when the field is seen in projection (see Parker et al. 1986, Figure 1). As will be seen below this field provides a fairly well-determined correlation function and augments the data presented here.

3.2.2 The galaxy luminosity function

As well as providing a model for the mean number density of galaxies in a magnitude selected sample (as seen in Chapter 2, Section 2.1.1.1), the luminosity function estimated from local fair samples (the so-called unevolved field luminosity function) also places constraints on a number of important processes, such as the local luminosity density of matter (e.g. Felten 1977), the evolution of galaxy counts (Ellis 1987) and, perhaps, the formation of galaxies themselves (Press and Schechter 1974). It has often been assumed that there is a universal luminosity function that is an ensemble average property over many fair samples (each sample providing an estimate of this function that differs in only a small random statistical way from the mean). However, it has become apparent that there may be dependencies of the luminosity function on properties such as galaxy colour or morphological type or environment (such as the local density; see Dressler 1980 for the density-morphology relation for galaxies in clusters). This may make the estimate of the luminosity function from a sample dependent on both its selection properties and the form of the inhomogeneities present within its volume, leading, inevitably, to larger errors (both systematic and random) in estimates of the clustering. However, provided these dependencies are small, and the samples are large enough, the estimated luminosity functions should

be, to first order, non-variant, and the correlation functions comparable (save for counting errors) from sample-to-sample.

In this work the luminosity function of the Durham/SAAO and Parker et al. surveys are measured as a means to obtain a model for the mean homogeneous number density $n(z)$. A more detailed analysis and comparison with the Durham/AAT Survey is given in Shanks (1990); there the B and V galaxy magnitudes in the Durham/AAT (Metcalfe et al. 1990a) and Kirshner et al. (KOS 1978) surveys are used to derive dependencies of the luminosity function on colour. Here, methods for obtaining a density independent form for $\phi(M)dMdV$ are briefly described and this is followed by the results for the Durham/SAAO and Parker et al. surveys. These are then compared with the results from a reanalysis of the Durham/AAT Survey.

The basic luminosity function estimator (the BE method of Bean 1983) for a flux-limited sample is obtained from dividing the observed counts of galaxies as a function of absolute magnitude, $\Delta N(M)$, by the appropriate volume $V_{max}(M)$ to which galaxies of magnitude M can be seen and, yet, still be part of the survey. If galaxies are truly homogeneously distributed within the field volumes or if $V_{max}(M)$ is much larger than the typical clustering length of galaxies then this method will give an unbiassed estimate of the sample luminosity function. The maximum redshift z_{max} a galaxy with magnitude M can be seen to comes from inverting equation 2-6 with $m=m_{lim}$ thus giving $V_{max}(M)=V(z_{max})$ (equation 2-13). However, where clustering is important the assumption that galaxies occupy the full volume $V_{max}(M)$ is inappropriate and a clustering insensitive estimator must be used.

Methods for deriving clustering independent luminosity functions have developed over recent years (see the reviews by Binggeli et al. 1988 and Efstathiou et al. 1988) but are generally of two types. The first are methods based on a position dependent separation of the density and shape of the luminosity function; in the case of the Maximum Likelihood Estimator, or MLE method, of Bean (1983, based on a private communication of Peebles) the mean number of galaxies observed in absolute magnitude range $M_i \pm \Delta M_i/2$ and in a distance modulus range $DM_j \pm DM_j/2$ is written as

$$\langle N_{ij} \rangle = \phi_i \rho_j \qquad (3\text{-}4)$$

in each field volume. Here, ϕ_i is the expected luminosity function for that magnitude interval and ρ_j is a density function that scales up ϕ_i to account for the clustering in that appropriate redshift range. By assuming that the probability of obtaining the observed count N_{ij} in bins (i,j) is given by a Poisson distribution (with a mean as in equation 3-1) a Likelihood function can be formed. By maximising this function, recurrence relations for ρ_j and ϕ_i can be obtained that give a non-parametric (though bin dependent) form for the luminosity function.

Other density independent methods for measuring the luminosity function rely on a quotient of functions of $\phi(M)$; in the method of Sandage et al. (1979, the Maximum Likelihood Fitting, or MLF, method of Bean, 1983) the probability that a galaxy i has an absolute magnitude M at redshift z_i is

$$P_i \propto \frac{\phi(M)}{\int_{-\infty}^{M_{max}(z_i)} \phi(M)dM} \qquad (3\text{-}5)$$

By multiplying together all the probabilities, a Likelihood function can be formed which can again be maximised, but in contrast to the above method, $\phi(M)$ needs to be specified and the Schechter function (equation 2-10) seems to provide the best fit to the data.

In Figure 3-13 (a) and (b), the luminosity functions from the BE and MLE estimators are presented for the Durham/SAAO and Parker et al. surveys, respectively. Here, 0.4 magnitude bins were used in the range $-22.2 \leq M(b_J) \leq -16.2$ and the arbitrary agreement between the two methods at $M(b_J)=-20.8$ is fixed by the need for normalisation of the MLE method. The errors are derived from Poisson fluctuations in the counts $\Delta N(M)$ (the observed values are shown as histograms in Figures 3-13 (a) and (b)) in each bin and, although these may be unrepresentative, the estimates from both methods agree reasonably well over the entire magnitude range indicating that the clustering is reasonably homogeneous within the sample volumes.

In Figure 3.14 (a) and (b), the BE and MLE estimates for these two surveys are compared with those for the Durham/AAT Survey (Figure 3.13(c)) using the correction for the magnitude system given in equation 3-3. Excellent agreement to within the errors is seen between all three of these surveys and this indicates that the luminosity functions in these samples are reasonably

Figure 3.13. BE and MLE estimates of the differential luminosity function $\phi(M)$ in the Durham/SAAO, Parker et al. and Durham/AAT surveys. The estimates of $\phi(M)$ in the upper section of all three figures were obtained in bins of 0.4 in M in the range $-22.2 \leq M(b_J) \leq -16.2$. The MLE estimates are arbitrarily normalised so that they agree with the BE method at M=-20.8. The 1σ errors shown for the BE estimates were obtained from Poisson fluctuation in $\Delta N(M)$. The solid line in each figure is the mean best fit to the luminosity function in each sample (in the range $-22.2 \leq M(b_J) \leq -17.4$) from the MLE and MLF methods ($\alpha=-1$, see equation 3-6). The lower section of each figure shows the observed counts $\Delta N(M)$.

(a) Durham/SAAO

MLE
BE

$M^* = -19.9$ $\alpha = -1.0$

$\phi(M)$ (h^3 Mpc^{-3} mag.$^{-1}$)

$\Delta N(M)$

M (+5 log$_{10}$ h)

(b) Parker et al.

● MLE
○ BE

.1
.01
.001
.0001
1

$\phi(M)$ (h^3 Mpc^{-3} mag.$^{-1}$)

$M^* = -20.0$ $\alpha = -1.0$

-22   -20   -18

30
20
10
0

$\Delta N(M)$

-22   -20   -18

M ($+5 \log_{10} h$)

(c) Durham/AAT

$\bullet$ MLE
$\circ$ BE

$M^{*}=-20.18$ $\alpha=-1.0$
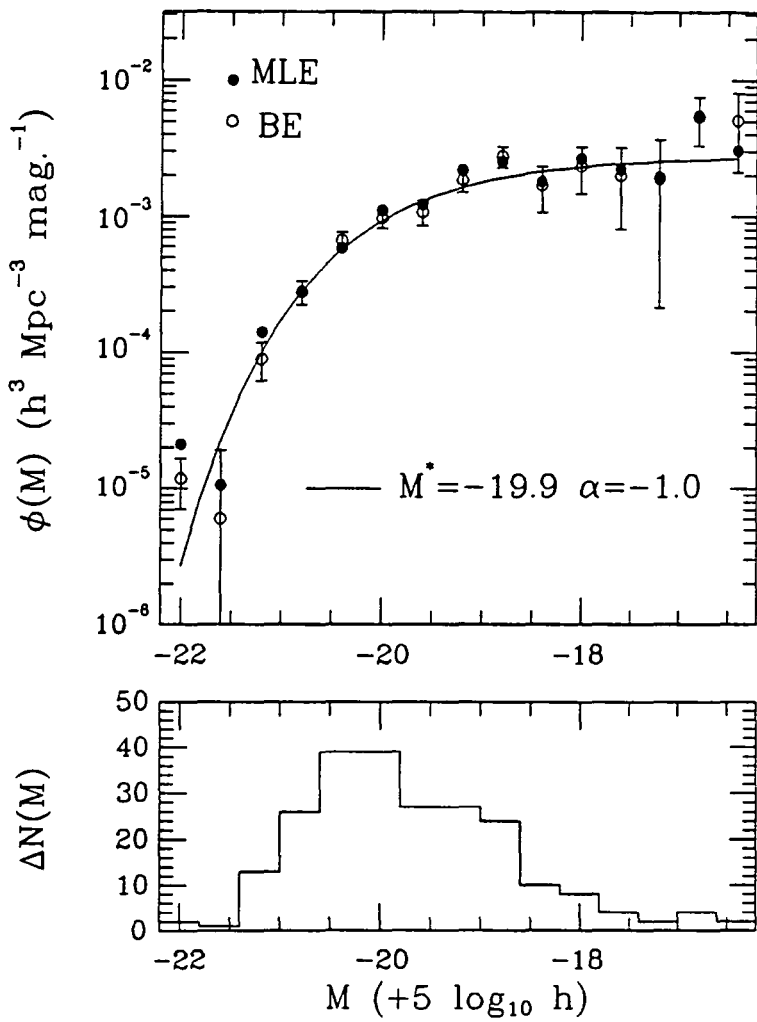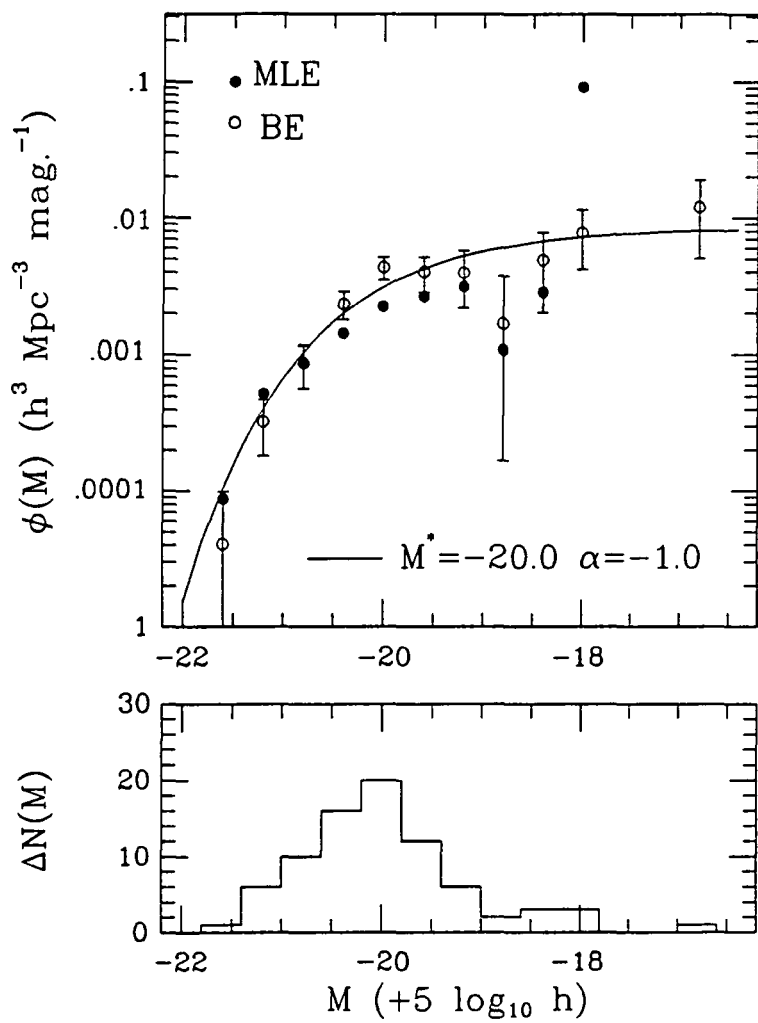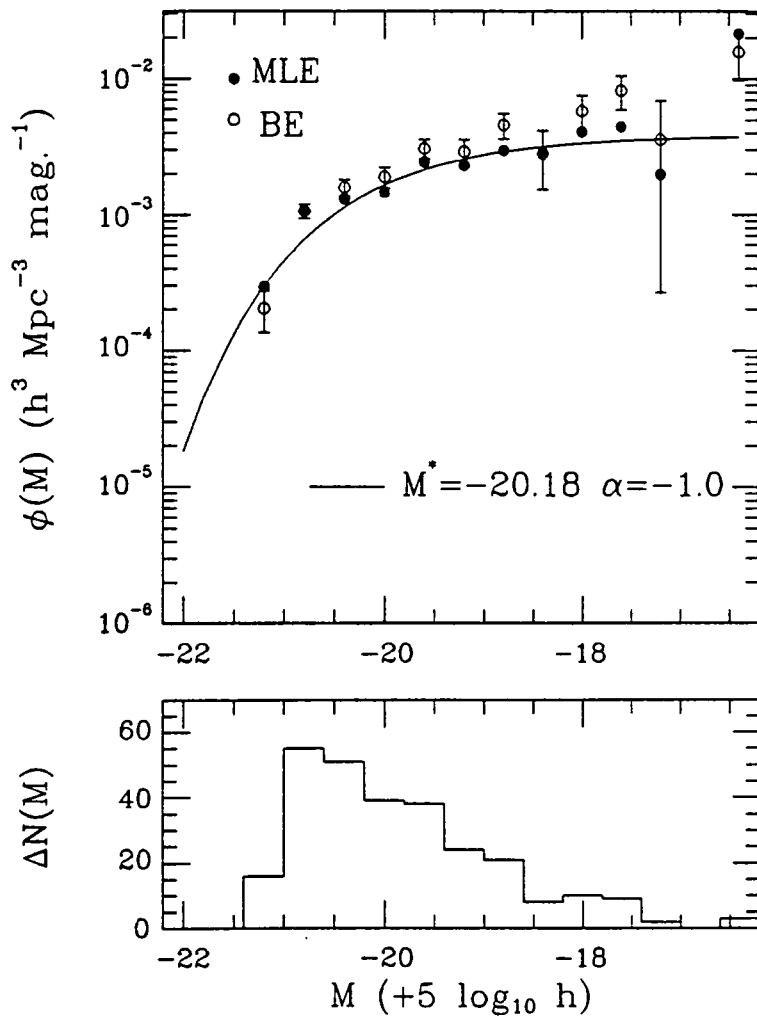
Figure 3.14. Intercomparisons between the estimates of the luminosity function $\phi(M)$ in the Durham/SAAO, Durham/AAT and Parker et al. surveys. In (a) the estimates are compared between the three samples for the BE method. Likewise in (b) the estimates are compared for the MLE method. The values shown here are the same as those in Figure 3.15 (a), (b) and (c). Errors are indicated for the Durham/SAAO Survey.

(a) BE

- Durham/SAAO
△ Parker et al.
□ Durham/AAT

$\phi(M)$ (h^3 Mpc^{-3} mag.$^{-1}$)

M ($+5$ $\log_{10}$ h)

(b) MLE

- Durham/SAAO
△ Parker et al.
□ Durham/AAT

$\phi(M)$ (h^3 Mpc^{-3} mag.$^{-1}$)

M ($+5$ $\log_{10}$ h)

representative of the overall luminosity distribution.

To obtain a parametric form for the shape of $\phi(M)$ in the Durham/SAAO and Parker et al. surveys the data in Figure 3.13 are fitted using a Schechter (1976) function (see equation 2-10). However, instead of using these estimates directly, a model for $\Delta N(M)$ was first obtained from $\phi(M)V_{max}(M)\Delta M$ with $\phi(M)\Delta M$ given by equation 2-10 and $V_{max}(M)$ calculated as in the BE method but, in the case of the MLE method, corrected for clustering using the MLE estimates for $\phi(M)$. This was then fitted to the observed $\Delta N(M)$ in the range $-22.2 \leq M(b_J) \leq -17.4$ using (Bean 1983) weighted least squares (with Poisson errors on $\Delta N(M)$) with α and M^* as free parameters (α was constrained to be -1.0 for the smaller Parker et al. sample). Figure 3.15 (a) shows the best fits and 1σ error contours for the measurements in the Durham/SAAO sample in the plane of these two parameters. Also shown in the same figure is the result of the measurements from the MLF estimator. To intercompare the results from this survey and from the Durham/AAT (Figure 3.15 (b)), Figures 3.16 (a) to (c) show the contours of the fits to $\phi(M)$ for the three methods individually.

From the 1σ contours in Figures 3-15 and 3-16, it is clear that all three estimators are reasonably consistent and, further, that both surveys agree reasonably well. The best estimates of M^* and α for each of the estimators and for each of the surveys (including the Parker et al. sample) are presented in Table 3.3. Since the contours in Figure 3.16 are highly correlated (Bean 1983) the final values for M^* to be used in the models of n(z) (equation 2-12) are taken to be the average of the clustering independent MLE and MLF methods with $\alpha=-1$. These are ($H_o=100 kms^{-1} Mpc^{-1}$)

$M^* = -19.90\pm0.15$ (Durham/SAAO)

$M^* = -20.00\pm0.24$ (Parker et al.)   (3-6)

$M^* = -20.18\pm0.20$ (Durham/AAT)

with the errors taken from the 1σ error contours (Table 3.3).

These best fit parameters for $\phi(M)$ in equation 3-6 are compared to the observations (using equation 2-10) of the MLE estimator in Figure 3-14 (a) to (c) (arbitrary normalisation) and it is seen that a good fit to the data is

Figure 3.15. Results of the fits to the observed luminosity functions in the Durham/SAAO and Durham/AAT surveys. In each figure are shown the best values (solid symbols) and 1σ error contours (lines) for the fits to the luminosity function in the plane of the Schechter (1976) parameters $M^*(b_J)$ and α using the BE, MLE and MLF methods.

(a) Durham/SAAO

BE
MLE
MLF

α

M^* (+5 $\log_{10}$ h)

(b) Durham/AAT

BE
MLE
MLF

α

M^* (+5 $\log_{10}$ h)
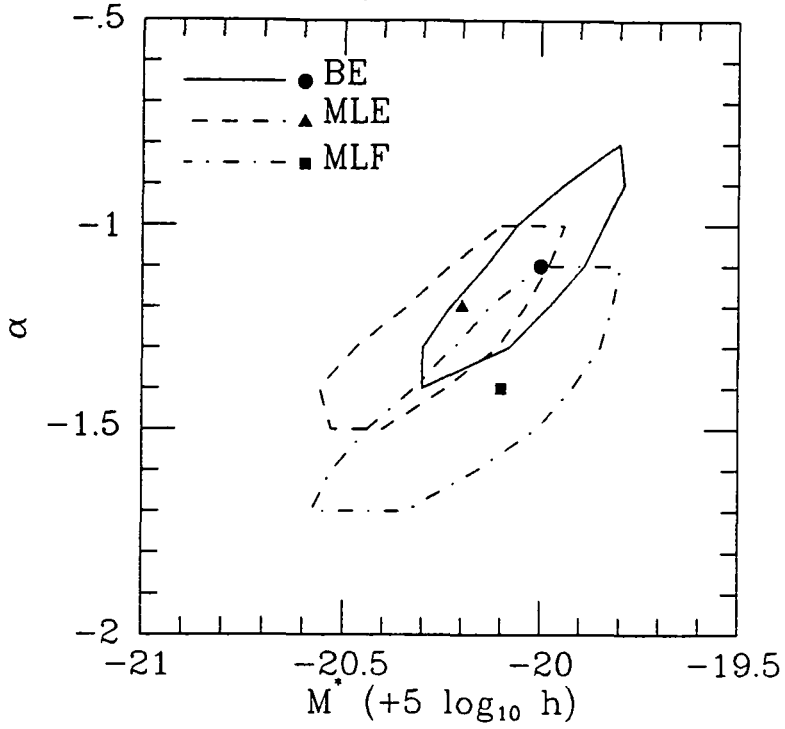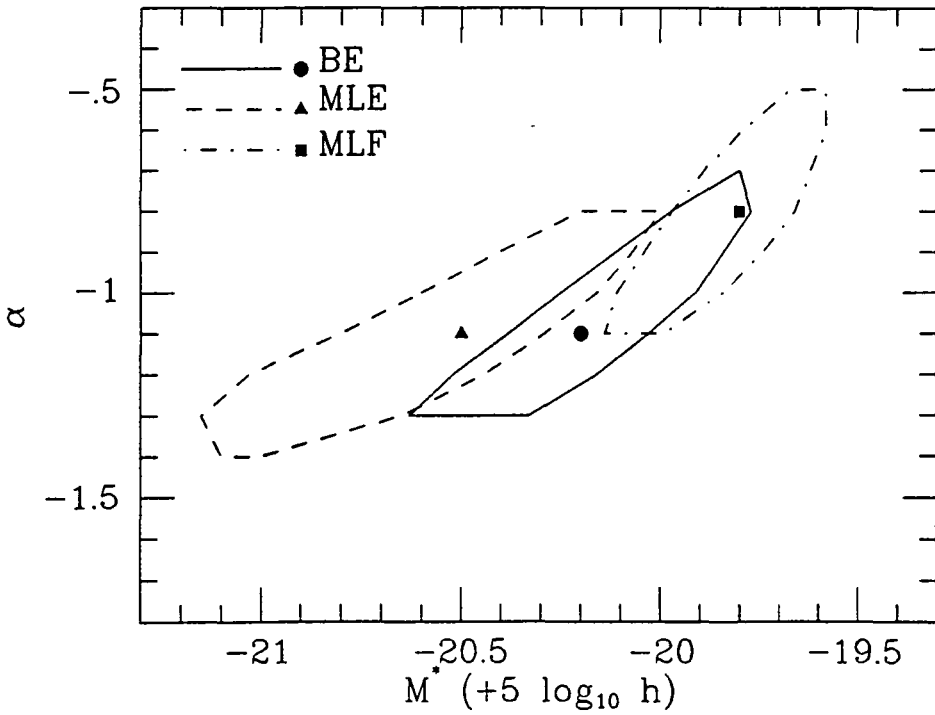
Figure 3.16. An intercomparison of the fits to the luminosity functions in the Durham/SAAO and Durham/AAT surveys. In (a), (b) and (c) the best fits (symbols) and 1σ error contours (lines) are compared between these two surveys in the plane of the parameters $M^*(b_J)$ and α for the BE, MLE and MLF methods, respectively. The best fits and error contours are the same as those in Figure 3-15.

(a) BE

Durham/SAAO
Durham/AAT

(b) MLE

Durham/SAAO
Durham/AAT
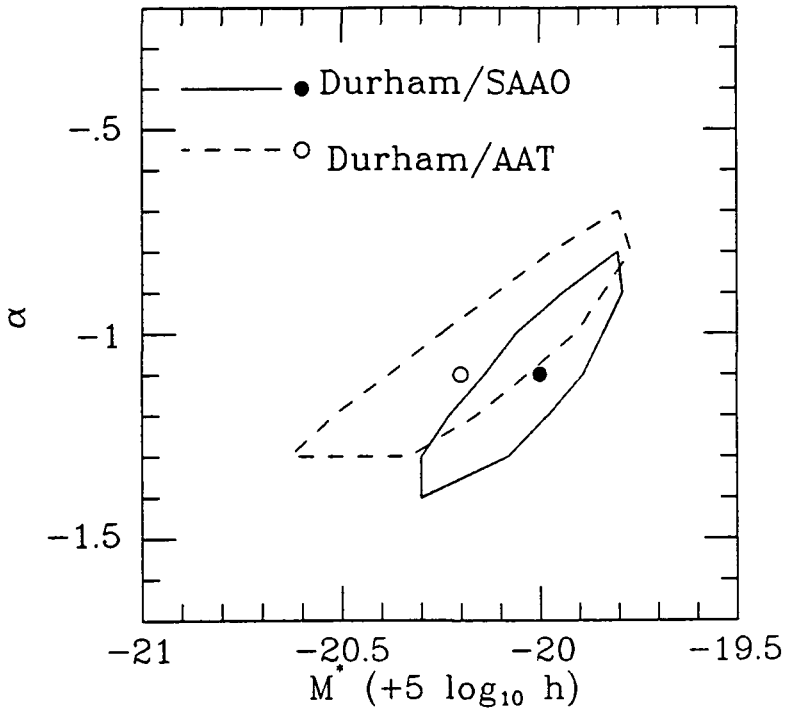
(c) MLF
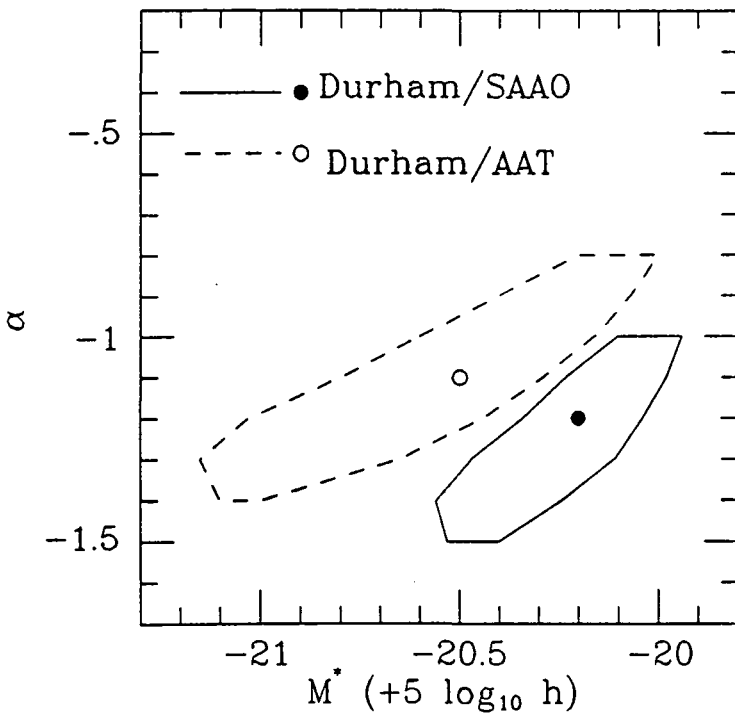
Durham/SAAO
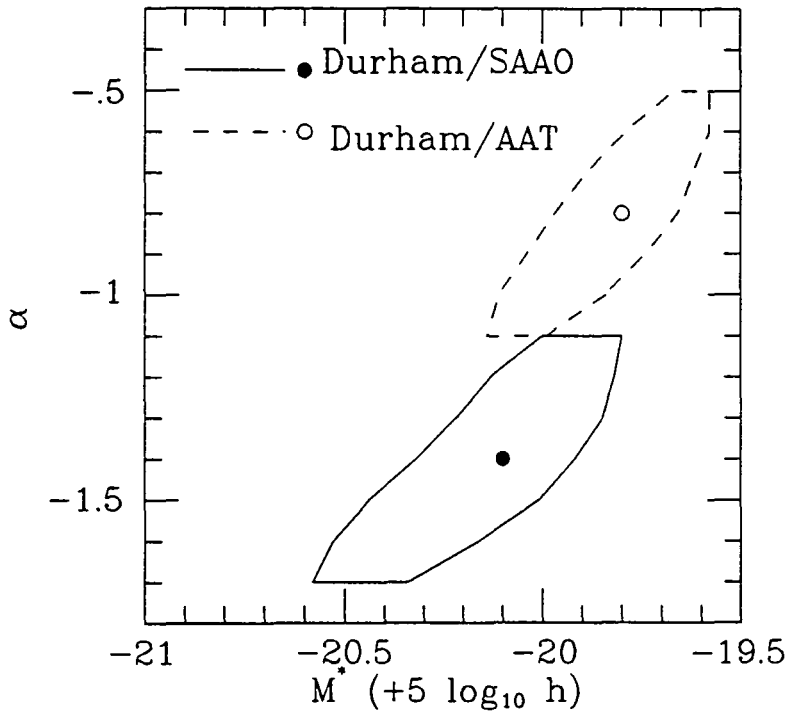
Durham/AAT

		Durham/SAAO	Parker et al.	Durham/AAT
BE	M*	-20.0±0.13		-20.2±0.18
	α	-1.1±0.14		-1.1±0.13
(α=-1)	M*	-19.9±0.12	-19.95±0.23	-20.1±0.17
MLE	M*	-20.2±0.15		-20.5±0.26
	α	-1.2±0.15		-1.1±0.14
(α=-1)	M*	-20.0±0.12	-19.9±0.20	-20.35±0.22
MLF	M*	-20.1±0.20		-19.8±0.16
	α	-1.4±0.21		-0.8±0.18
(α=-1)	M*	-19.8±0.18	-20.1±0.28	-20.0±0.18

Table 3.3. Estimates of the Schechter (1976) parameters M* and for α for the Durham/SAAO, Durham/AAT and Parker et al. surveys using the BE, MLE and MLF luminosity function estimators. For each estimator the first two rows represent the best fit M* and α for each sample whilst the third row is the best fit M* with the constraint that α=-1. All M* values are in the b_J magnitude system and are for $H_0=100 kms^{-1} Mpc^{-1}$.

obtained. As an overall estimate of the Schechter parameter M* it is found that, for the weighted average of the values in equation 3-6 (see the Appendix)

$$M^* = -20.00\pm0.11 \qquad \alpha = -1 \qquad\qquad (3\text{-}7)$$

and this is in reasonably good agreement with Shanks (1990) who finds that $M^*=-19.9$ ($\alpha=-1.2$) provides the best overall fit to the luminosity function in the samples he considers. The steeper faint end slope in this case arises because Shanks fits a wider range of absolute magnitudes than has been considered here; some hint of a steeper slope is indicated at $M>-17$ in Figure 3-14. As seen from Efstathiou et al. (1988, Table 8) the result in equation 3-7 may be somewhat on the bright end (by about 0.3^m) of the range of values for surveys discussed by those authors although part of this may arise from the uncertain transforms for the magnitudes systems.

3.2.3 The observed mean counts and tests for homogeneity

In the previous section clustering independent methods were used to measure the form of the luminosity function for the Durham/SAAO and Parker et al. surveys and there it was shown that the Schechter function provided a reasonable fit to these data over a wide range of absolute magnitudes. It follows, then, that the estimated values for the quantities M^* and α are appropriate descriptors for the observed shape of $\phi(M)$ and that these, and the Schechter function, can then be used to predict the form of the homogeneous density n(z) as a function of redshift (see Chapter 2, Section 2.1.1.1). In this section this model is compared with the observed data through the counts as a function of redshift ($\Delta N(z)$) and of apparent magnitude ($\Delta N(m)$) with the emphasis on testing the overall homogeneity of the Durham/SAAO and Parker et al. surveys. Comparisons with the Durham/AAT Survey will be made and this eventually leads to overall estimates of the counts from all three catalogues.

Before a model for n(z) is used, however, it needs to be normalised in some fashion. As discussed in Chapter 2 (Section 2.1.1.2) there are various ways to achieve this but the simplest approach is to normalise to the total number of galaxies with redshifts that are brighter than the magnitude limit. Since different selection procedures are used for the 17^m samples discussed

here, this normalisation is carried out in a self-consistent way to avoid introducing any non-clustering correlations of the type discussed in Chapter 2 (Section 2.1.1.1). However, as seen in Section 2.1.2.3 this does lead to a specific bias in the correlation function estimates (the integral constraint) but this can be approximately corrected for as specified in that earlier section.

The exact method for normalisation of the model for n(z) in the Durham/SAAO and Parker et al. surveys was as follows. Since α and M^* in equation 2-12 are determined from the luminosity function estimates for each survey (equation 3-6 with α constrained to have a value of -1.0), the only free parameter to determine is ϕ^*. Thus, from equations 2-7, 2-9, 2-12, 2-13 and 2-18 the expected number of galaxies contributing to a field k with magnitude limit m^k_{lim} and solid angle Ω_k can be modelled as

$$\Delta\langle N_k(\leq m^k_{lim})\rangle = \sum_i \frac{1}{3}\phi^*\Omega_k(c/H_0)^3\Gamma(0,10^{0.4(M^*-m^k_{lim}+DM(z_i))})[(z_i+\frac{\Delta z}{2})^3-(z_i-\frac{\Delta z}{2})^3]$$

$$= \phi^* \sum_i \chi_{ik} \qquad\qquad (3\text{-}8)$$

where it is assumed that Γ varies little over the bin Δz at redshift z_i. χ_{ik} is the selection function weighted volume of this bin in field k. The distance modulus $DM(z_i)$ is given by equation 2-6, in which, like the volume element, the q_0 term has been neglected and the K-correction is given a mean value of 3.0 (see Figure 2.1, Chapter 2). The sum extends over all redshifts with a well defined selection function and these, for Durham/SAAO and Parker et al. surveys, were chosen to be $1000\leq cz\leq30000$ kms^{-1} and $2000\leq cz\leq21000$ kms^{-1}, respectively. The velocity bin width was $c\Delta z=5$kms^{-1}. It follows, then, that from the total number of observed galaxies with redshifts, N_G, in the above ranges and brighter than the field magnitude limits,

$$\phi^* = N_G/(\sum_k \sum_i \chi_{ik}) \qquad\qquad (3\text{-}9)$$

Thus using the values of M^* estimated in equation 3-6 and the parameters concerning the fields in Table 3.2, the 232 galaxies in the Durham/SAAO Survey gave a ϕ^* of

$$\phi^* = (2.68\pm0.34)\times10^{-3} \, h^3 \, \text{Mpc}^{-3} \qquad\qquad (3\text{-}10)$$

where the error comes from variations in this quantity from field-to-field. Note that this value of ϕ^* is approximately a factor of 3 down on a complete redshift survey. For comparison, the 80 galaxies with redshifts brighter than $b_J=16^m.25$ in the Parker et al. Survey gave

$$\phi^* = 8.13\times10^{-3} \, h^3 \, \text{Mpc}^{-3} \qquad\qquad (3\text{-}11)$$

while in the Durham/AAT Survey

$$\phi^* = (5.41\pm0.59)\times10^{-3} \, h^3 \, \text{Mpc}^{-3} \qquad\qquad (3\text{-}12)$$

and allowing for the factor of 3 difference in the mean and error in the Durham/SAAO Survey these three values agree reasonably well. However, the numbers are not strictly comparable because the values of M^* in equation 3-6 differ slightly from survey-to-survey and also the redshift data have slightly varying levels of completeness.

Results for the counts of galaxies as a function of redshift velocity in the Durham/SAAO, Durham/AAT and Parker et al. Survey fields have already been presented in Section 3.2.1. There (Figure 3-10 (a) to (o)) the observed counts ΔN_{ik} were compared to the model $\Delta\langle N_{ik}\rangle=\phi^* \chi_{ik}$ (equation 3-8) by calculating the fluctuations $(\Delta N_{ik}-\Delta\langle N_{ik}\rangle)/\Delta\langle N_{ik}\rangle$ (with ϕ^* in this case normalised to the numbers seen in each field). As discussed in Chapter 2 (Section 2.1.1.2) a simple model for the variance in the count ΔN_{ik} (where the volume sampled in each redshift bin is much larger than the size of the typical clumps) is given approximately by $\varphi_{ik}m\Delta\langle N_{ik}\rangle$ (equation 2-22) where φ_{ik} is the selection function for field k at redshift z_i and m is the number of galaxies associated with each independent (but identical) clump.

In Figure 3.17 (a) and (b) the variance in the count ΔN_{ik} from field-to-field is plotted as a function of redshift velocity for the Durham/SAAO and Durham/AAT surveys, respectively, (the counts in each field were corrected to a uniform magnitude limit of $b_J=16^m.8$ and an area of 14.06 deg^2) and the scale is divided into intervals of 3000kms^{-1} to give sufficient counts in each bin. Comparing these variations with the appropriate model for $n(z)d\langle N(z)\rangle$ in Figure 2.2 of Chapter 2, it can be seen that there is a

Figure 3.17. The field-to-field variance in the count of galaxies as a function of redshift velocity in the Durham/SAAO and Durham/AAT surveys. The variance was calculated from the observed counts ΔN in each field in bins of 3000kms^{-1} (the counts being corrected to a uniform magnitude limit of b_J=16^m.8 and a field area of 14.06 deg^2).

(a) Durham/SAAO
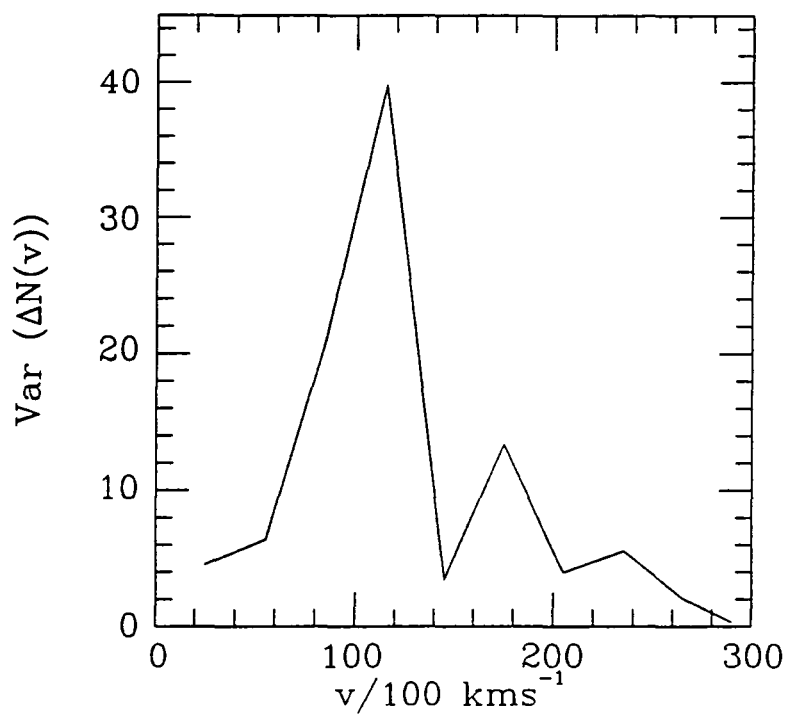
(b) Durham/AAT
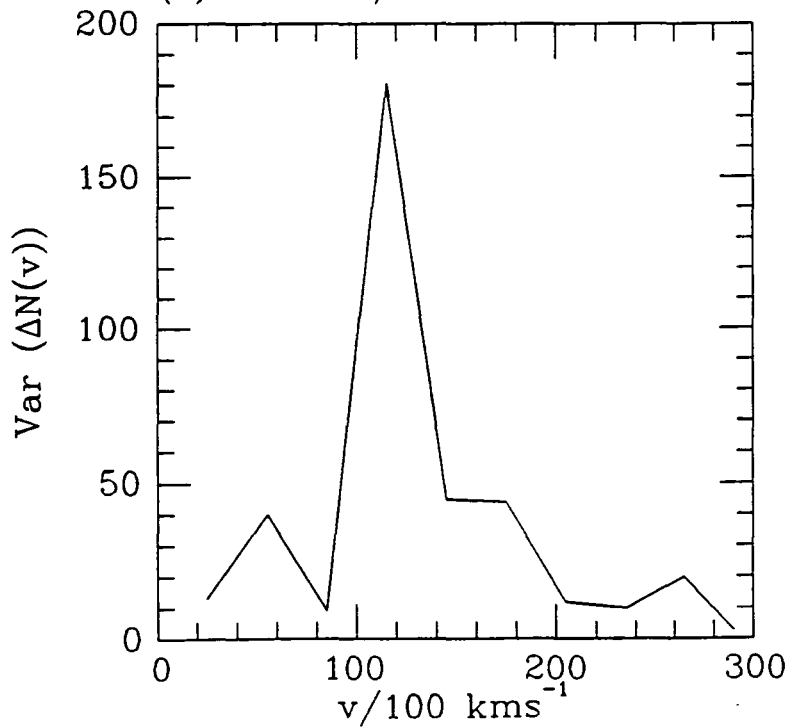
reasonable similarity between these two functions and this indicates that this model for the fluctuation in the count may be providing an appropriate description for the fluctuations observed here, and, further, some constant value of m may have been reached in the volumes sampled (at $v=25000$kms^{-1} this corresponds to $[20]^3 h^{-3}$ Mpc^3). As will be seen in Chapter 5 this seems to agree with the conclusions of the correlation analysis. However, it may be possible that the variations are suppressed by large-scale coherence between the fields, but given their wide angular spacing (Figure 3.8) this seems unlikely unless all the local volume ($z<0.1$) were correlated (see below).

In Figure 3-18 (a) (solid line) and (b) a test for the overall homogeneity of the Durham/SAAO and Parker et al. surveys is performed, by calculating the fluctuations $(\Delta N_i - \Delta \langle N_i \rangle)/\Delta \langle N_i \rangle$ for the summed counts, over the fields, of ΔN_{ik} in each catalogue (in bins of 3000kms^{-1}). Satisfactory agreement with the zero deviation line is seen over the entire range of velocities except for the first bin in the Durham/SAAO Survey (the errors in this sample come from a smooth fit to the field-to-field variance in Figure 3-17(a)). For comparison with the Durham/SAAO Survey, the results from the Durham/AAT Survey are plotted as a dashed line in Figure 3-18 (a). From this figure it appears that the slight trend of increasing overdensity in the Durham/AAT sample at $v>8000$kms^{-1} (Bean 1983) is reproduced in the Durham/SAAO catalogue. However, given the errors in these estimates this overdensity does not appear to be very significant. The large overdensity at $v<4000$kms^{-1} does seem to reproduce between the samples (the same effect can be seen for the individual fields in Figure 3.10) and this may be caused by the local supercluster (see also da Costa et al. 1988). In Figure 3-18 (c) the overall $\delta(\Delta N)/\Delta \langle N \rangle$ distribution for these two samples is shown (the estimate is obtained by averaging the solid and dashed lines in Figure 3-18(a) according to the relative errors; see the Appendix)

Whilst these observations seem to indicate that the Durham/SAAO, Durham/AAT and Parker et al. surveys may be approaching reasonably homogeneous and, thus, fair samples of the Universe, there is some indication that this may not be so if the surveys are divided into northern and southern Galactic hemisphere subsamples. The distributions of $\delta(\Delta N)/\Delta \langle N \rangle$ in the northern hemisphere fields in the Durham/SAAO and Durham/AAT surveys (solid and dashed lines, respectively) are compared to those in the

Figure 3.18. The relative fluctuations $\delta(\Delta N)/\Delta\langle N\rangle$ in the observed counts as a function of redshift velocity in the Durham/SAAO, Durham/AAT and Parker et al. surveys. In (a) the estimates are shown for the Durham/SAAO (solid line) and Durham/AAT (dashed line) samples with the Durham/SAAO errors obtained from a smooth fit to the field-to-field variance in Figure 3.17 (a). In (b) the results are presented for the Parker et al. Survey. Figure (c) shows the combined estimate from both samples in (a).

(a)

Durham/SAAO
Durham/AAT

$\delta(\Delta N)/\Delta \langle N \rangle$

v/100 kms^{-1}

(b)

Parker et al.

$\delta(\Delta N)/\Delta \langle N \rangle$

v/100 kms^{-1}

(c)
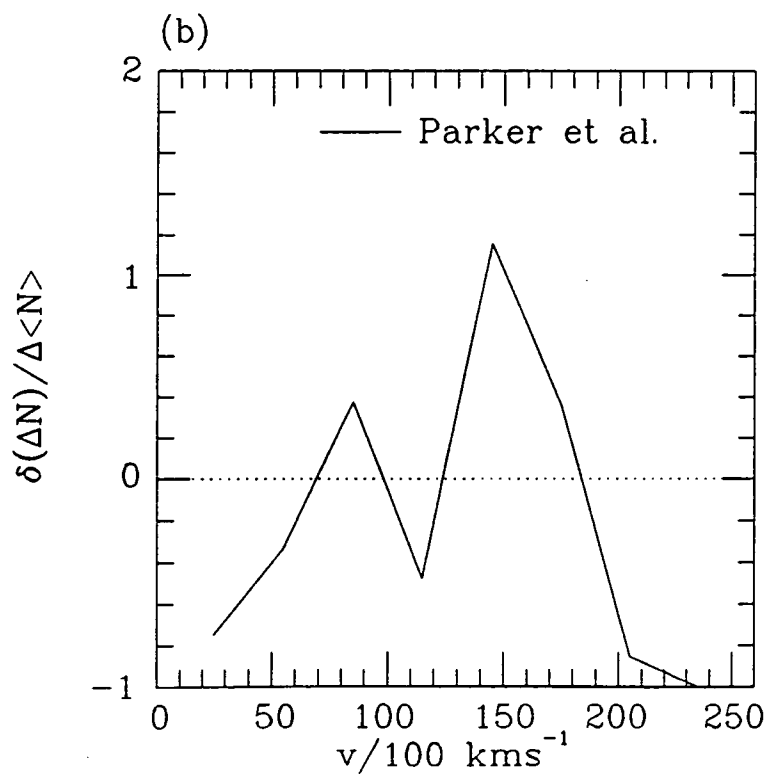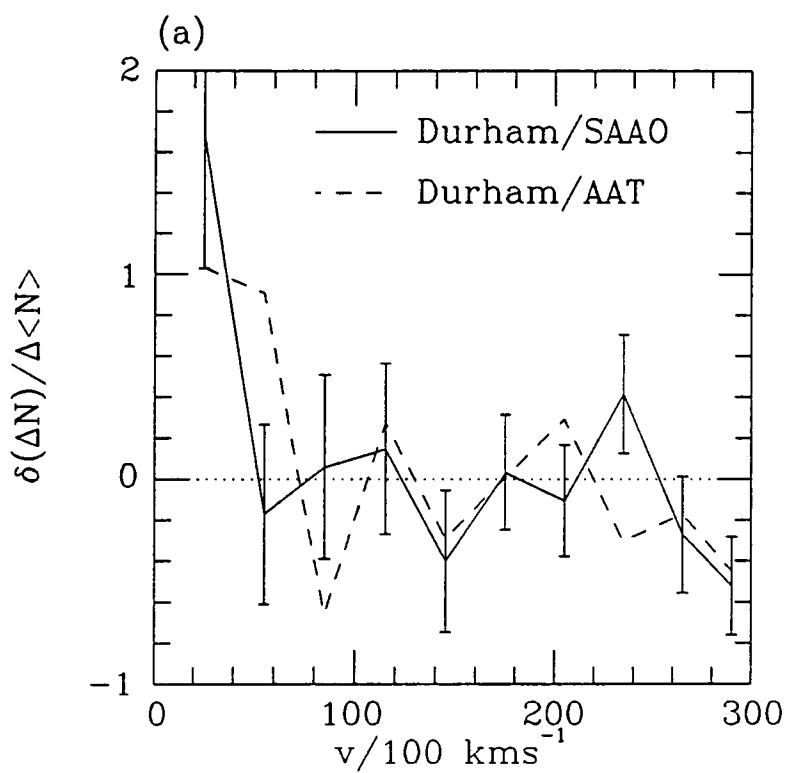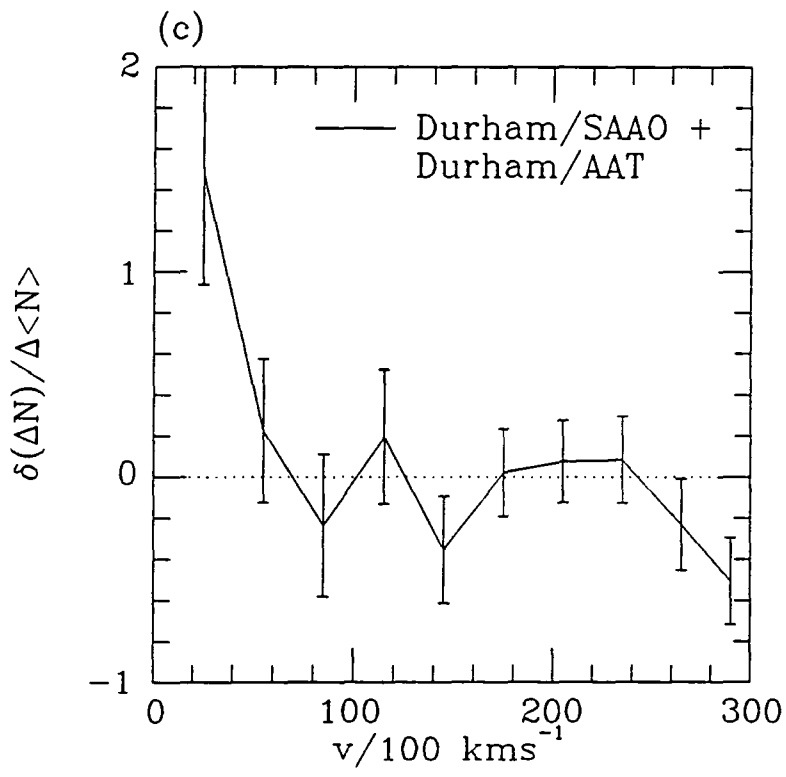
south (dotted and dot-dash lines, respectively) in Figure 3-19 (a). This figure suggests that there does appear to be some north/south anisotropy in the range $10000 \leq v \leq 23000 kms^{-1}$ with the northern fields being underdense with respect to the those in the south (see the overall north versus south distributions in Figure 3-19(b)) and this may be worth investigation in a larger survey. For comparison, however, these fluctuations do not appear as serious as those seen, for example, in the $\Delta N(z)$ distributions of the original CfA ($m_B < 14^m.5$) sample (see Figure 5 of Davis and Huchra 1982), or the CfA ($m_B < 15^m.5$) slices (see Figure 2 of de Lapparent et al 1986a). These surveys show considerable variation in the observed $\Delta N(z)$ from bin-to-bin and this makes a smooth fit to the counts very difficult to achieve. As will be seen in Chapter 5 this may lead to somewhat uncertain estimates of the correlation function in these shallower redshift surveys.

Finally, the differential number counts $\Delta N(m)$ as a function of apparent magnitude m are discussed in terms of the more global homogeneity of the Durham/SAAO and Parker et al. surveys. These counts (in numbers per square degree per 0.25 magnitude bins) are shown for these two samples in Figure 3.20 (a) and (b), respectively; in the case of the Durham/SAAO Survey the complete (i.e. non 1-in-3 sampled) numbers for each field are given together with their mean. The Parker et al. Survey counts show a marked decrease beyond $b_J \approx 16^m.25$ suggesting that the 20% incompleteness lies in the faintest magnitude interval (see Section 3.1.2 above).

For comparison with these figures the counts for the Durham/AAT Survey (corrected to the b_J system by equation 3-3) are shown in Figure 3.20 (c) and the mean counts (and representative field-to-field errors) from all three samples are presented in Figure 3.20 (d). These results show that the Durham/AAT Survey has a slightly lower overall count with respect to the other two surveys and a slightly lower dispersion in its values. The mean count from all three samples is shown in Figure 3.20 (e) with a Schechter model for $\Delta N(m)$ based on equation 2-18 (incorporating equations 2-12 and 2-13 with no q_0 terms) with the overall M^* from equation 3-7 ($\alpha = -1$). It can be seen that this model is somewhat shallower in slope than the observed data (it is arbitrarily normalised to m=15.25 where $\phi^* = 0.0069h^3$ Mpc^{-3}) with those counts giving quite accurately a -0.6 slope in log $\Delta N(m)$ versus m. According to the deeper Schmidt galaxy counts of Shanks (1990, see also Maddox et al. 1990d) the normalisation of a no-evolution model at $b_J \approx 19^m$ overestimates the

Figure 3.19. North and south subsample variations in the relative fluctuations $\delta(\Delta N)/\Delta\langle N\rangle$ in the counts as a function of redshift velocity. In (a) north and south subsample variations are compared between the Durham/SAAO and Durham/AAT surveys whilst in (b) the overall subsample variations are shown for both surveys combined together.

(a)

(b)
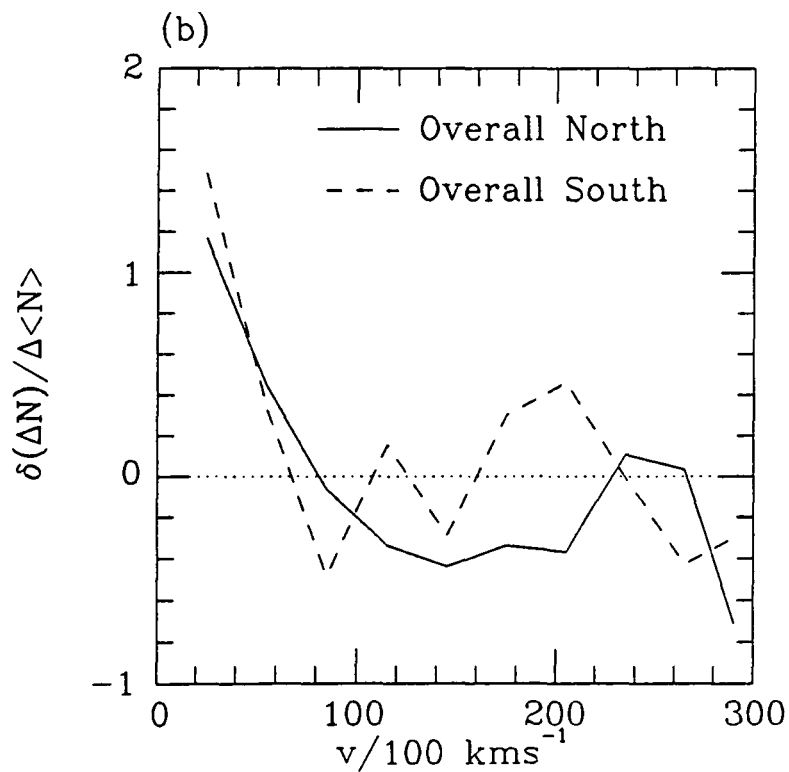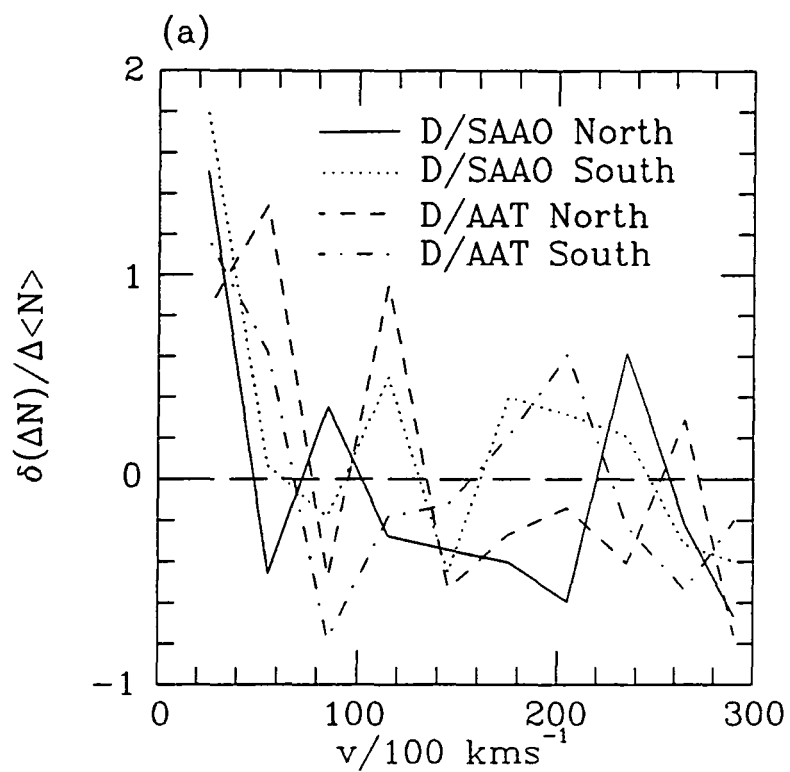
Figure 3.20. The differential number-apparent magnitude counts for the Durham/SAAO, Parker et al. and Durham/AAT surveys. In all the figures the counts per deg^2 $\Delta N(m)$ are for 0.25 bins in apparent magnitude $m(b_J)$ (the larger bins at the brighter magnitudes being corrected to this smaller bin size). In (a) the solid line and symbols are, respectively, the mean and individual field counts for the Durham/SAAO Survey. Figure (b) shows the counts in the Parker et al. sample and (c) the mean and individual counts for the Durham/AAT Survey. The mean counts from all three samples (with field-to-field errors on the Durham/SAAO estimates) are compared in (d) and in (e) the overall count from all three samples is compared to a no-evolution model for $\Delta N(m)$ based on equation 2-18.

(a) Durham/SAAO

□ GNX ⅄ GSM
△ GNY ○ GSI
■ GNH ● GSN
▲ GNZ + GSP
× GSG

—— Mean

$\Delta N(m)$ (deg^{-2})

m(b$_J$)

(b) Parker et al.

$\Delta N(m)$ (deg^{-2})

m(b$_J$)

(c) Durham/AAT

GSA
GSD
GSF
GNA
GNB

Mean

(d)

Durham/SAAO
Durham/AAT
Parker et al.

(e)
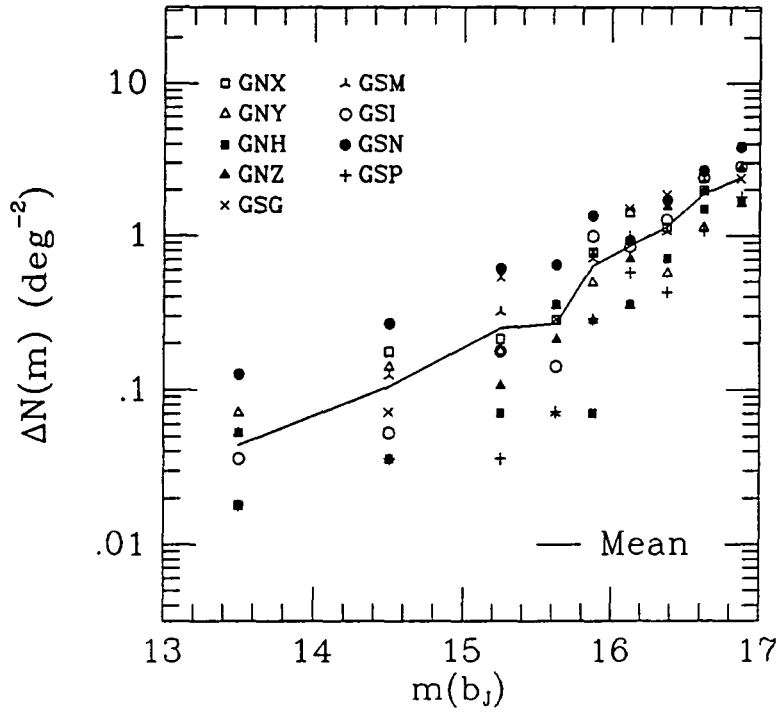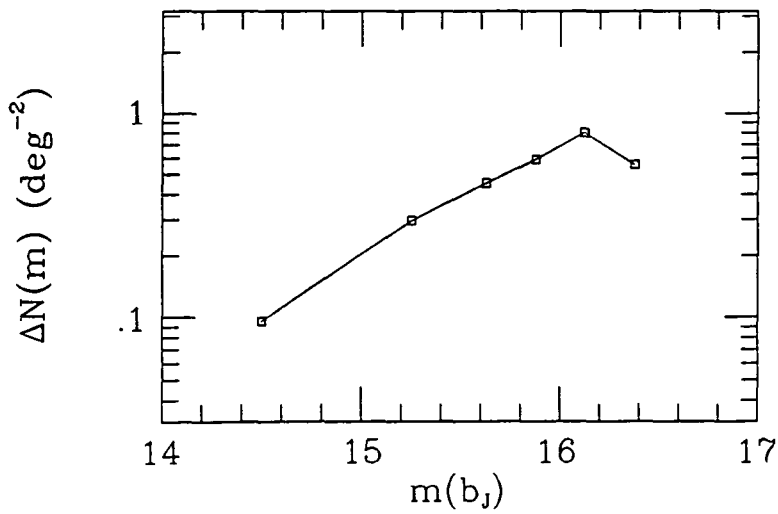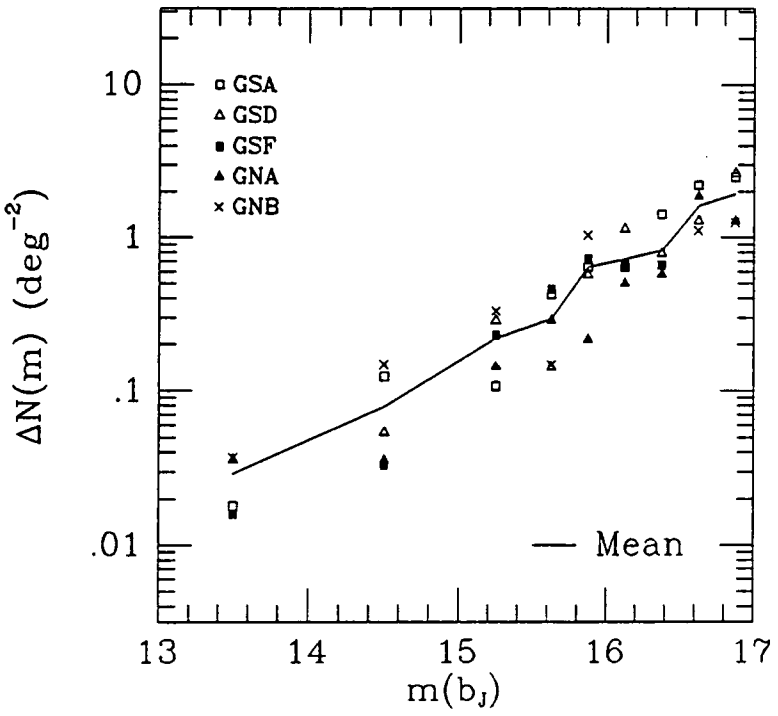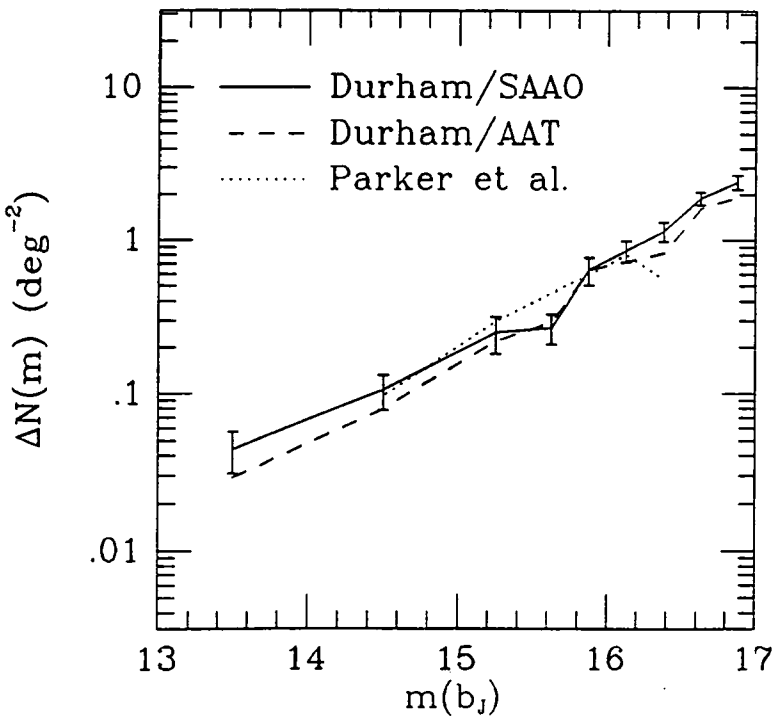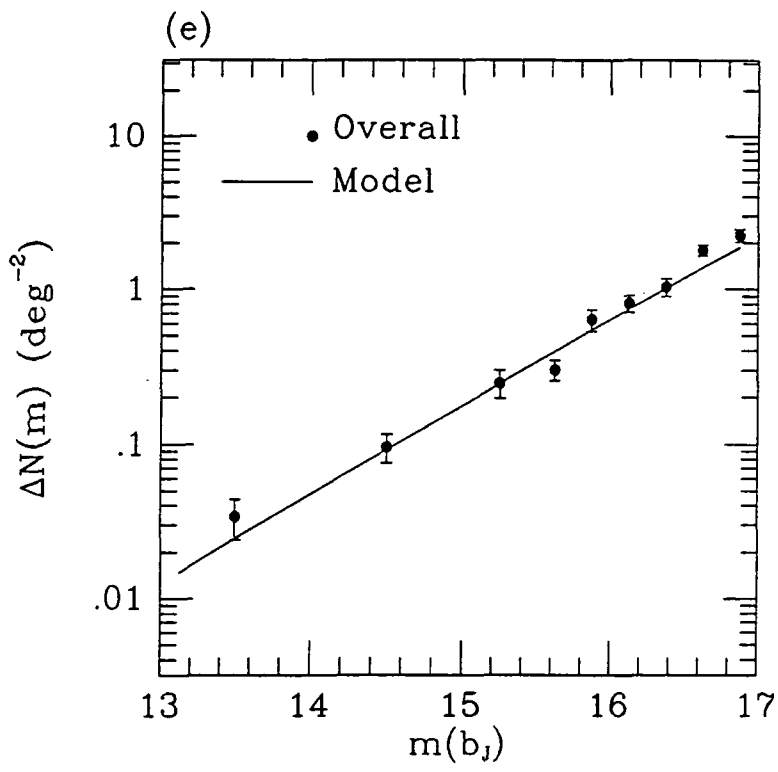
counts at $b_J \approx 16^m$ by about a factor of 2 and so this trend is continued into the deeper data.

The cause of this discrepancy could have far reaching consequences for cosmology if such a steep count is a real feature of the galaxy distribution (see Shanks 1990). Part of the discrepancy may arise from the fact that the measuring machine, COSMOS, has a tendency to underestimate magnitudes for bright ($\leq 17^m$) galaxies with high central surface intensities (Metcalfe et al. 1989, see also Section 3.1.1) but this is likely to occur only for elliptical and S0 type galaxies which represent ~30% of the count (Bean 1983). If the underdensity at bright magnitudes is real then there is the possibility that the steeper count is due to either evolution or inhomogeneity in the galaxy distribution. In the former case this would appear to disagree with the observations of Broadhurst et al. (1988) that the galaxy counts are non-evolving at a mean redshift of ~0.2 and in the latter case the underdensity would have to extend over a considerable volume (z<0.1). Some discussion of the latter suggestion is given in Chapter 5.

Finally, the mean and rms field-to-field variations in the total counts to $b_J \leq 16^m.8$ in the 14 Durham/SAAO and Durham/AAT fields is

$$N \ (\leq 16^m.8) = 5.8 \pm 2.1 \text{deg}^{-2} \tag{3-13}$$

and as discussed in Chapter 2 (Section 2.1.2.3) this can provide a useful alternative measure of the clustering in these surveys.

Chapter 4

The mean mass density of the Universe from observations of small-scale ($\leq 1h^{-1}$ Mpc) galaxy correlations and random peculiar motions.

This chapter is devoted to the study of the form of galaxy clustering and pair-wise random peculiar motions at small ($\leq 1h^{-1}$ Mpc) scales from what are believed to be approximately fair samples of the overall galaxy distribution. Using the information gathered about such systems, the dynamical theorems for their stability (see Chapter 2, Section 2.2.2.1) can be used to place constraints, not only on the magnitude of the underlying mass density, but also the form of its relationship to the observed galaxies. Both of these descriptions are highly relevant in the understanding of the formation of galaxies; the density parameter Ω_0 is critical, for example, in the rate of growth of large-scale structures (Peebles 1980) whereas the information on the relationship between the mass and galaxy distributions could specify any biassing mechanisms in their formation (Dekel and Rees 1987). As has been stressed earlier (Section 2.2, Chapter 2), the key point about this analysis is that mean properties of galaxies are being sought rather than making specific observations about certain aspects of the distribution (such as the velocity dispersions of structures in Abell galaxy clusters). This is clearly important if constraints are to be placed on the present form, and previous evolution, of the galaxy (or mass) distributions; analysis of specific structures may only lead to partial descriptions.

This chapter is divided into four sections. The first (Section 4.1) deals with the observed structure of the small-scale ($\leq 1h^{-1}$ Mpc) galaxy clustering deduced from the projected forms of the two- and three-point correlation functions in the Durham/SAAO and Parker et al. surveys. Following this, in Section 4.2, the rms peculiar velocities from the samples are obtained. The results from these two sections are then compared to observations from other surveys (in particular the Durham/AAT) in Section 4.3 and finally, in Section 4.4, the Cosmic Virial Theorem (see Section 2.2.2.1, Chapter 2) is used to estimate Ω_0.

4.1 The small-scale ($\leq 1h^{-1}$ Mpc) projected 2- and 3-point correlation functions

In this section the form of the clustering structure at small scales is deduced from the projected forms of the redshift two- and three-point correlation functions in the Durham/SAAO and Parker et al. surveys. As seen in Chapter 2 (Section 2.1.2.4 and Section 2.1.3) although this can lead to ambiguities in the interpretation of the spatial correlation functions, it does, nevertheless, allow for estimates which are reasonably independent of random peculiar motions (Figure 2.4). In Section 4.2.2 further estimates of $\xi(r)$ are obtained by directly fitting the redshift two-point function $\xi_v(\sigma,\pi)$ with an appropriate model and the results for the clustering are compared to those obtained here.

This section is divided into two parts; the first (Section 4.1.1) describes the observations of the projected redshift two-point function $\omega_v(\sigma)$ whilst the second (Section 4.1.2) that of the projected redshift three-point function $z_v(\sigma_1,\sigma_2,\sigma_3)$.

4.1.1 The projected two-point correlation function $\omega_v(\sigma)$.

In Figure 4.1 (a) and (b) estimates of the projected two-point correlation function $\omega_v(\sigma)$ are presented for the Durham/SAAO and Parker et al. surveys, respectively. The values have been calculated by summing estimates of $\xi_v(\sigma,\pi)$ in the π direction (see Section 4.2 below) in bins of $1h^{-1}$ Mpc up to a maximum of $\pi_{cut}=10h^{-1}$ Mpc and this choice of limit in π minimises the contribution of an uncertain ξ_v at larger scales (see Section 2.1.2.4, Chapter 2). The 1σ error bars in the figures are obtained from applying the same methods to the simulations and these are well backed up by the variations between the northern and southern hemisphere subsamples in Figure 4.1 (a).

Firstly, these results are compared to a simple model for $\omega_v(\sigma)$ (solid lines) in which $\xi(r)$ is a single power law, $\xi(r)=(r_0/r)^{1.8}$ (equation 2-90), integrated up to the maximum value of π, π_{cut} (equation 2-97, Section 2.1.2.4, Chapter 2). However, as seen from these models and as discussed in Chapter 2 (see also Bean 1983), a power-law correlation function in $\xi(r)$ does not project through to a power law in $\omega_v(\sigma)$ (or $\omega(\theta)$) when it is terminated at a finite cut-off in π (or r) (see Figure 2.4). For example, in Figure 4.1 (c) the

Figure 4.1. Estimates of the projected two-point correlation function $\omega_v(\sigma)$. In figures (a), (b) and (d) the $\pi_{cut}=10h^{-1}$ Mpc estimates of $\omega_v(\sigma)$ are shown for the Durham/SAAO, Parker et al. and Durham/AAT surveys, respectively. In (e) these estimates are shown together (with the errors on the Durham/AAT points) and in (f) they are combined to provide an overall estimate from these samples. In (a) are also shown the variations in $\omega_v(\sigma)$ from north and south subsamples of the Durham/SAAO Survey. In (a), (b), (d) and (f) the solid line is the model for $\omega_v(\sigma)$ in equation 2-97 (the power law in $\xi(r)$ integrated to π_{cut}) with $\gamma=1.8$ and $\pi_{cut}=10h^{-1}$ Mpc (the correlation lengths r_0 are as indicated in the figures). The mean estimates of $\omega_v(\sigma)$ from the simulations of the Durham/SAAO Survey are presented in figure (c); here the solid and dashed lines are the asymptotic ($\pi_{cut} \gg \sigma$) and non-asymptotic forms of equation 2-97, respectively (clustering lengths again as indicated).

(a) Durham/SAAO
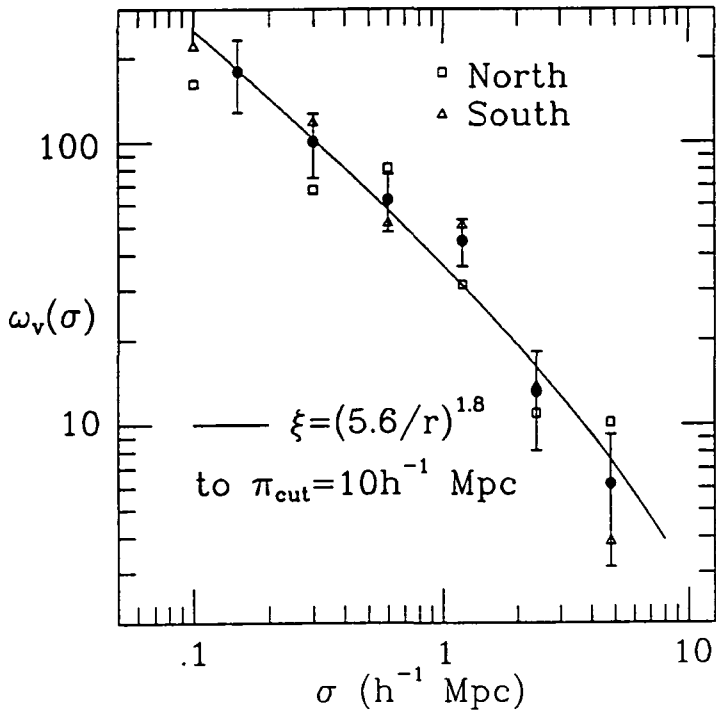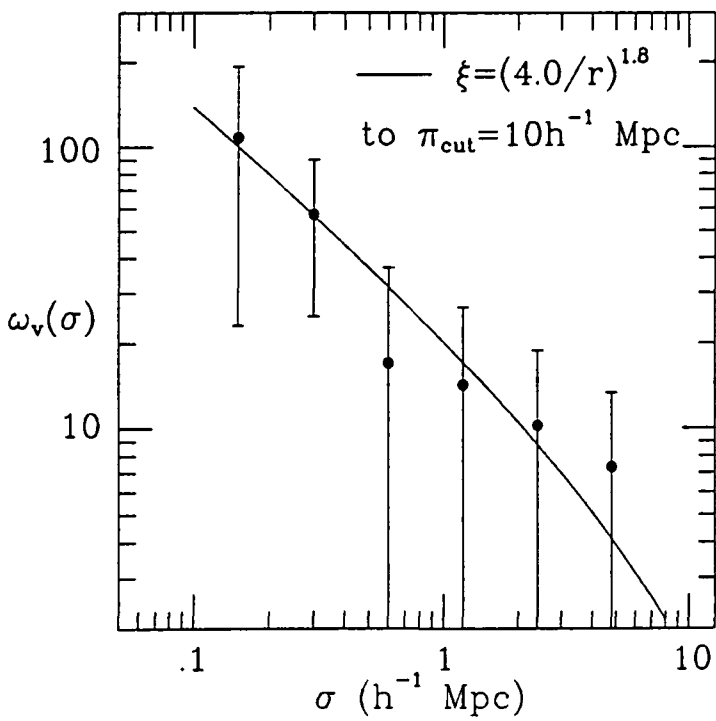
□ North
△ South

$\omega_v(\sigma)$

$\xi = (5.6/r)^{1.8}$

to $\pi_{cut} = 10h^{-1}$ Mpc

σ (h^{-1} Mpc)

(b) Parker et al.

$\xi = (4.0/r)^{1.8}$

to $\pi_{cut} = 10h^{-1}$ Mpc

$\omega_v(\sigma)$

σ (h^{-1} Mpc)

$\omega_v(\sigma)$

$\omega_v(\sigma)=1.84(4.9)^{1.8}\sigma^{-0.8}$

$\xi=(5.4/r)^{1.8}$

to $\pi_{cut}=10h^{-1}$ Mpc

σ (h^{-1} Mpc)

(d) Durham/AAT

$\omega_v(\sigma)$

$\xi=(5.0/r)^{1.8}$

to $\pi_{cut}=10h^{-1}$ Mpc

σ (h^{-1} Mpc)

(e)

$\omega_v(\sigma)$

• Durham/SAAO
□ Durham/AAT
△ Parker et al.

$\sigma \ (h^{-1} \ Mpc)$

(f) Overall

$\omega_v(\sigma)$

——— $\xi = (4.8/r)^{1.8}$

to $\pi_{cut} = 10h^{-1}$ Mpc
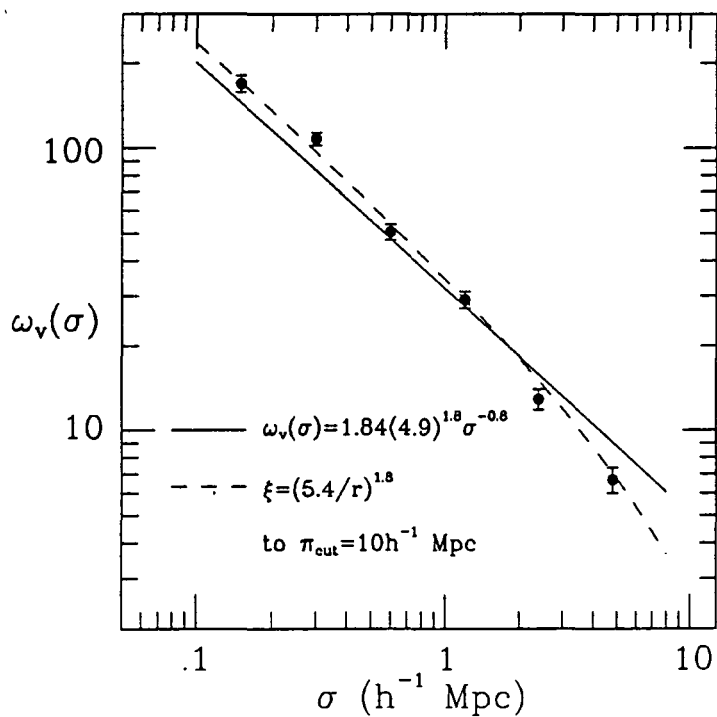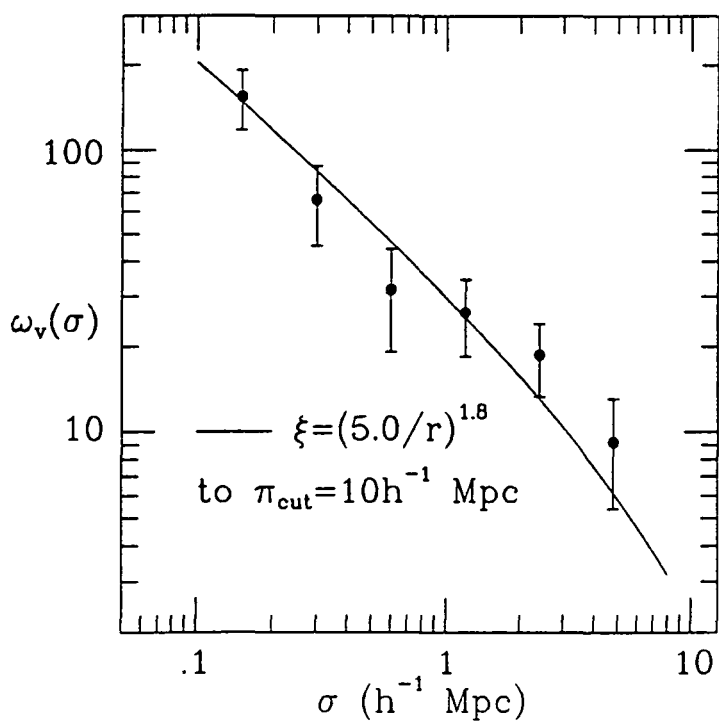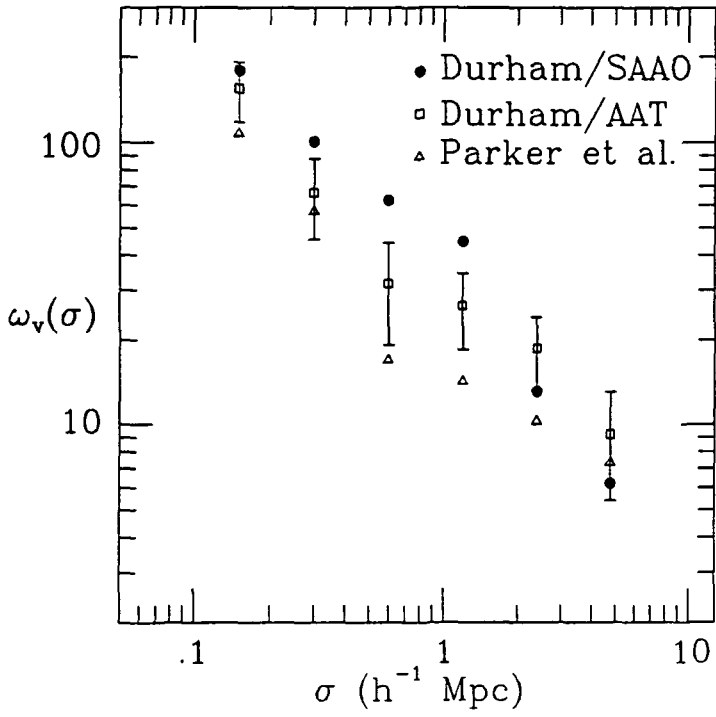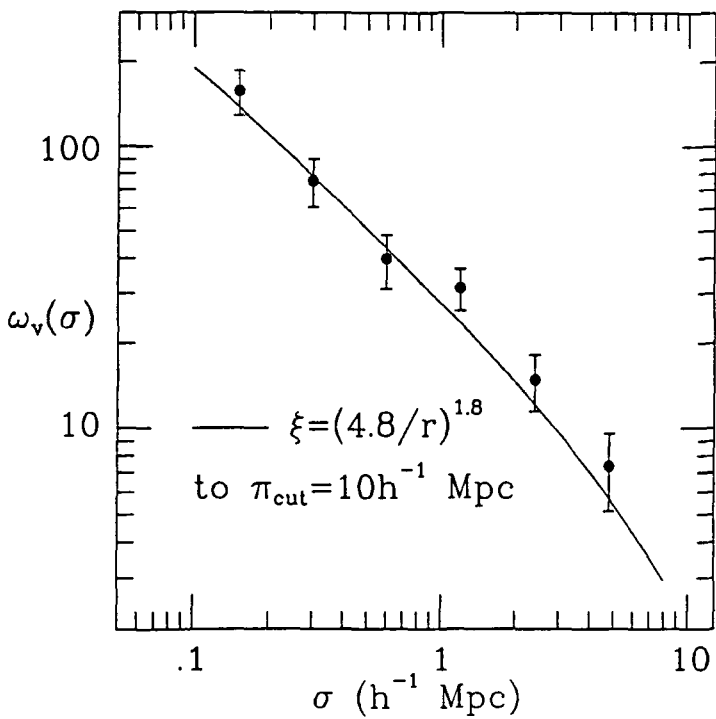
$\sigma \ (h^{-1} \ Mpc)$

mean estimates of $\omega_v(\sigma)$ from the simulations of the Durham/SAAO Survey with $\pi_{cut}=20h^{-1}$ Mpc are compared to the asymptotic form of equation 2-97 (with $\pi_{cut} \gg \sigma$) which has $\omega_v(\sigma)=1.84r_0^\gamma \sigma^{(1-\gamma)}$. The best least-squares fit of this model to this data gives $r_0=(4.9\pm0.1)h^{-1}$ Mpc with $\gamma=1.8$ and this is significantly lower that the value of $r_0=5.4h^{-1}$ Mpc displayed by the simulations at small ($\leq 3h^{-1}$ Mpc) spatial separations (see Figure 2.5). In Figure 4.1 (c) the best fit of this power-law $\omega_v(\sigma)$ is indicated as a solid line and this shows that the data is decreasing to smaller values faster than $\sigma^{-0.8}$. This observation can be understood since the simulated $\xi(r)$ is known to have a break at $r \approx 6h^{-1}$ Mpc. The dashed line in Figure 4.1 (c) is the non-asymptotic form of equation 2-97 with a π_{cut} of $10h^{-1}$ Mpc and the observed r_0 of $5.4h^{-1}$ Mpc for the simulations at small spatial scales. As can be seen this provides a much better description of the simulated data.

So following this method, the estimates of $\omega_v(\sigma)$ in Figure 4.1 (a) and (b) are first divided through by $H_\gamma(\pi_{cut}/\sigma)$ (equation 2-98) which allows the $\log_{10}(\omega_v(\sigma)/H_\gamma(\pi_{cut}/\sigma))$ versus $\log_{10}(\sigma)$ data to be fitted with a straight line using least squares. If γ is constrained to be 1.8 then it is found that $r_0=(5.6\pm0.5)h^{-1}$ Mpc for the Durham/SAAO Survey and $r_0=(4.0\pm1.0)h^{-1}$ Mpc for the Parker et al. sample.

These values of r_0 have been used in the solid model curves (equation 2-97) in Figure 4.1 (a) and (b) and it is seen that the fit to the points is quite reasonable over the entire range of σ. For comparison with these results, in Figure 4.1 (d) the $\pi_{cut}=10h^{-1}$ Mpc $\omega_v(\sigma)$ values for the Durham/AAT Survey are presented together with a best fit model of $r_0=(5.0\pm0.6)h^{-1}$ Mpc ($\gamma=1.8$). Given the errors on these estimates of r_0, the level of agreement between the correlation functions at $r \leq 10h^{-1}$ Mpc is very good and this is also shown in Figure 4.1 (e) where all three $\omega_v(\sigma)$ results are plotted together. Thus, to obtain an overall projected function, the values of $\omega_v(\sigma)$ from all three samples are combined by weighting the individual estimates at each separation according to the inverse square of their error (see the Appendix). This weighted average is shown in Figure 4.1 (f) together with the 1σ error bars obtained from the simulations assuming independence of the samples. The overall value of r_0, obtained in a similar fashion from the estimated values above, is $r_0=(5.2\pm0.4)h^{-1}$ Mpc.

As was discussed in Chapter 2 (Section 2.1.2.4), the uncertain form for

$\xi(r)$ at $r \geq 10h^{-1}$ Mpc can make the estimated $\omega_v(\sigma)$ difficult to interpret and the results sensitive to the choice of π_{cut}. A more stable estimate of the clustering in this case may come from $\sigma \leq 1h^{-1}$ Mpc; thus fitting the $\pi_{cut} = 10h^{-1}$ Mpc model for $\omega_v(\sigma)$ (equation 2-97) to the $\sigma \leq 1h^{-1}$ Mpc results in Figure 4.1 (f) a clustering length of $r_0 = 4.8h^{-1}$ Mpc was found and this is in reasonable agreement with the value above. This value of r_0 is used in the model curve shown in the figure. As will be seen in Chapter 5, and as noted by Bean (1983), there is some evidence that the observed correlation function rises above this simple model extended from small separations. This can be seen quite clearly in Figure 4.1 (e) for the Durham/AAT and Parker et al. surveys, and to some extent in the Durham/SAAO sample. However, because of the projection properties of $\omega_v(\sigma)$ a significant feature in $\xi(r)$ may appear to be quite small in this figure.

4.1.2 The projected three-point correlation function $z_v(\sigma_1, \sigma_2, \sigma_3)$.

The amplitude of the 3-point correlation function, Q, was estimated for the Durham/SAAO Survey using the method described in Chapter 2 (Section 2.1.3). The observed data-random pair and triplet counts DR, DRR and DDR were obtained from a catalogue of N_R random points homogeneously distributed in the field volumes like $d\langle N(z)\rangle$ (equation 2-14) using Monte Carlo techniques. The model for $d\langle N(z)\rangle$ in each field is as given in equation 3-8 above and the normalisation procedure was as is described in that section (Section 3.2.3, Chapter 3). To decrease the noise of the pair counts arising from fluctuations in the numbers of random points laid down, a total of $N_R = 160 N_G$ points were used where N_G (see equation 3-9) is the number of galaxies found in the volumes. The factor of N_R/N_G is then divided out once the pair counts have been obtained. To account for the smearing effect of random peculiar motions, pair and triplet counts were combined up to a maximum separation in π of $\pi_{cut} = 5h^{-1}$ Mpc.

As $z_v(\sigma_1, \sigma_2, \sigma_3)$ is assumed to be symmetric in its arguments, triplets of galaxies can be counted in order of their triangles' shape and size. Thus, with $\sigma_1 < \sigma_2 < \sigma_3$, the shape parameters $\sigma = \sigma_1$, $u = \sigma_2/\sigma_1$ and $v = (\sigma_3 - \sigma_2)/\sigma_1$ can be identified and the form of $z_v(\sigma, u, v)$ obtained for a range of bins in each parameter. The results for the measured parameter Q in the Durham/SAAO Survey are shown in Table 4.1. To make the significance of the data more

σ (h⁻¹ Mpc)	u			
	1-4			
0.25	1.11			0<v<0.5
	0.44			0.5<v<1.0
	1-2	2-3	3-4	
0.75	1.11	0.73	0.92	0<v<0.5
	1.14	0.47	0.08	0.5<v<1.0
1.50	0.09	-0.29	-0.07	0<v<0.5
	0.24	0.39	0.37	0.5<v<1.0

Table 4.1. The amplitude of the three-point correlation function Q as estimated from the Durham/SAAO Survey. The amplitude Q is shown at various values of the projected shape parameters σ, u, and v. Pairs and triplets of galaxies were counted up to a maximum separation of π_{cut}=5h⁻¹ Mpc.

uniform, the smaller sized triangles have been combined into a larger bin in the parameter u. The mean of the values in the table is

$$Q = 0.48\pm0.12 \qquad\qquad\qquad\qquad (4-1)$$

where the error is obtained from fluctuations in the various bins. Applying identical methods to the Durham/AAT Survey, Bean et al. (1983) found that Q=0.60±0.06 and this agrees very well with the above result. However, the Q for the largest σ value in Table 4.1 appears to be somewhat smaller than the other two; for $\sigma\leq1h^{-1}$ Mpc Q=0.75±0.14 whereas for $\sigma>1h^{-1}$ Mpc Q=0.12±0.11. Like the projected two-point function $\omega_v(\sigma)$, the form of $z_v(\sigma,u,v)$ may be sensitive to the large-scale form of $\zeta(r_1,r_2,r_3)$ (and in this model $\xi(r)$) and this may be the cause of the lower value of Q seen in the largest bin. The possibly larger value of Q for this sample will be borne in mind in the analyses below.

4.2 The small-scale ($\leq1h^{-1}$ Mpc) rms peculiar velocity $\langle\omega^2\rangle^{1/2}$

In this section the Durham/SAAO and Parker et al. surveys are used to measure the degree of pair-wise galaxy motions through the line-of-sight rms estimate $\langle\omega^2\rangle^{1/2}$ at small scales. In Section 4.2.1 the width of the distortion of $\xi(r)$ in redshift space is used to estimate this quantity and this method is reasonably independent of both amplitude fluctuations in $\xi(r)$ and variations in the form of the frequency distribution for ω. In the following section (Section 4.2.2) a specific model for the redshift correlation function $\xi_v(\sigma,\pi)$ is assumed and the data is fitted directly.

4.2.1 $\langle\omega^2\rangle^{1/2}$ from the width of $\xi_v(\sigma,\pi)$

This method for estimating the width of the pair-wise peculiar motion distribution was not favoured by Bean et al. (1983) but as shown in Chapter 2 (Section 2.2.1.1) it still provides a complementary approach to the direct fitting of $\xi_v(\sigma,\pi)$ described below. In Figure 4.2 (a) to (d), the estimated rms peculiar velocity $\langle\omega^2\rangle^{1/2}$ (solid line) and the width of $\xi_v(\sigma,\pi)$, $\langle\pi^2\rangle_{\xi_v}^{1/2}$ (dashed line) for the Durham/SAAO Survey are shown as a function of various separations σ and π_{cut} (see Section 2.2.1.1 for the method). Here $\langle\pi^2\rangle_{\xi_v}^{1/2}$ (see equation 2-127) has been calculated directly from the data; i.e. from $\pi^2\xi_v(\sigma,\pi)$ binned in

86

Figure 4.2. Estimates of $\langle\omega^2\rangle^{1/2}$ from the width of $\xi_v(\sigma,\pi)$ in the Durham/SAAO Survey. Estimates of $\langle\omega^2\rangle^{1/2}$ as a function of the limit in separation π, π_{cut}, are shown at various projected separations σ. The solid and dashed lines are the values which incorporate and neglect the Hubble expansion correction, $\langle\pi^2\rangle_\xi^{1/2}$, respectively. Open symbols indicate the variations between north and south subsamples.

(a) $\sigma=0.25$ h^{-1} Mpc

North
South

$\langle\omega^2\rangle^{1/2}$

$\langle\pi^2\rangle_{\xi_v}^{1/2}$

(b) $\sigma=0.75$ h^{-1} Mpc

North
South

$\langle\omega^2\rangle^{1/2}$

$\langle\pi^2\rangle_{\xi_v}^{1/2}$

(c) $\sigma=1.5$ h^{-1} Mpc

□ North
△ South

$\langle\omega^2\rangle^{1/2}$ ——

$\langle\pi^2\rangle^{1/2}_{\xi_v}$ - - -

(d) $\sigma=3.0$ h^{-1} Mpc

□ North
△ South

$\langle\omega^2\rangle^{1/2}$ ——

$\langle\pi^2\rangle^{1/2}_{\xi_v}$ - - -
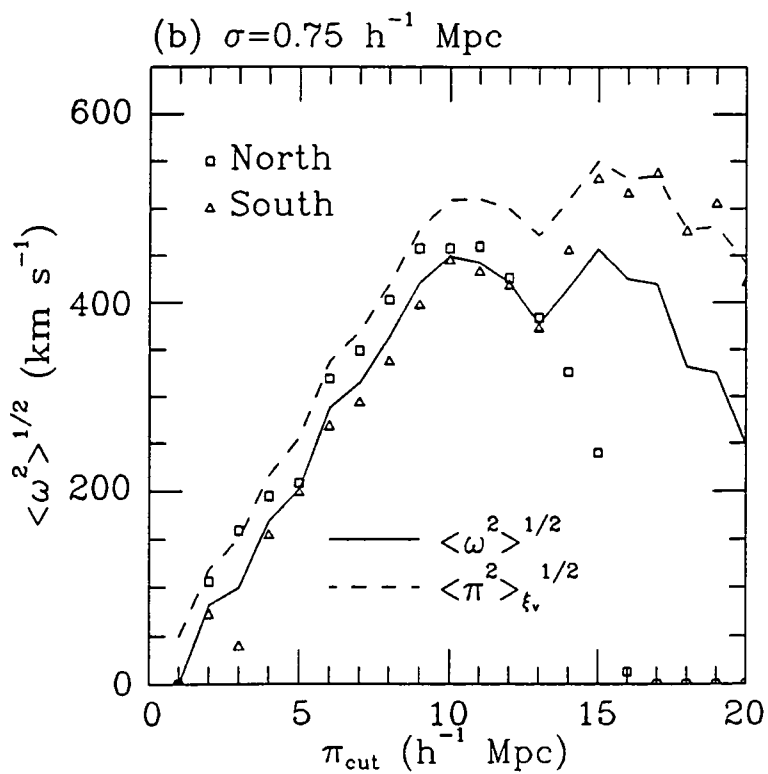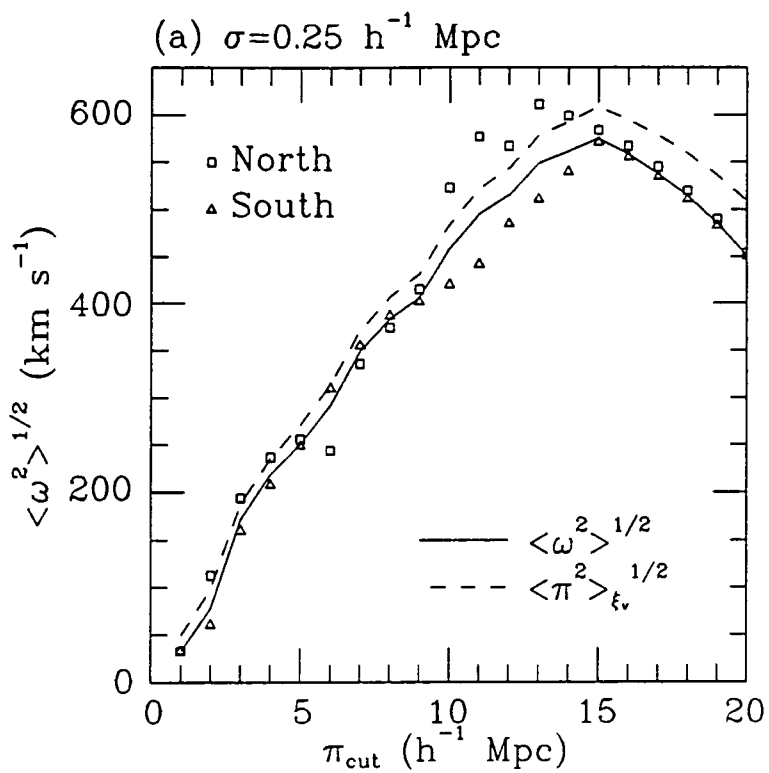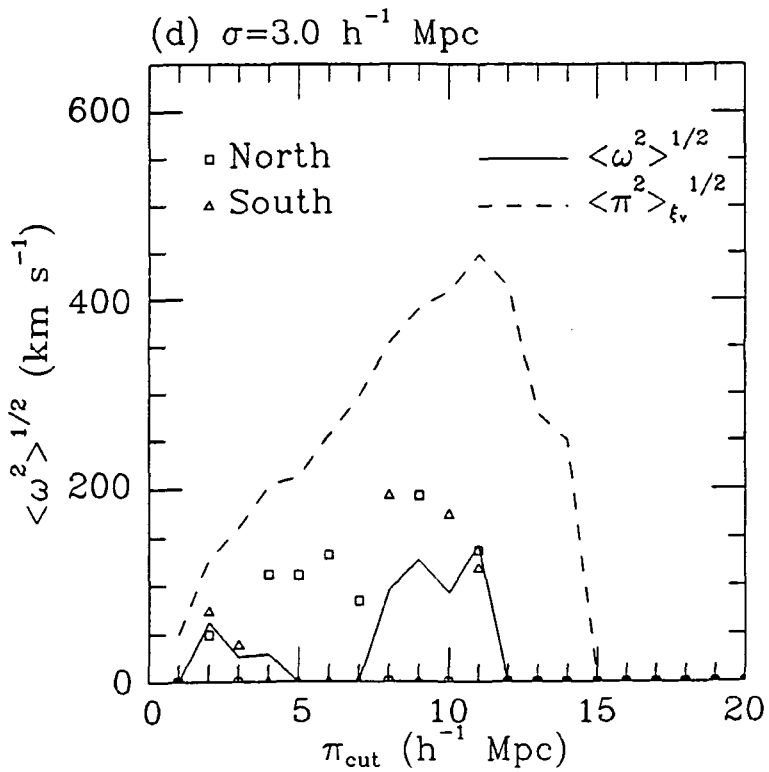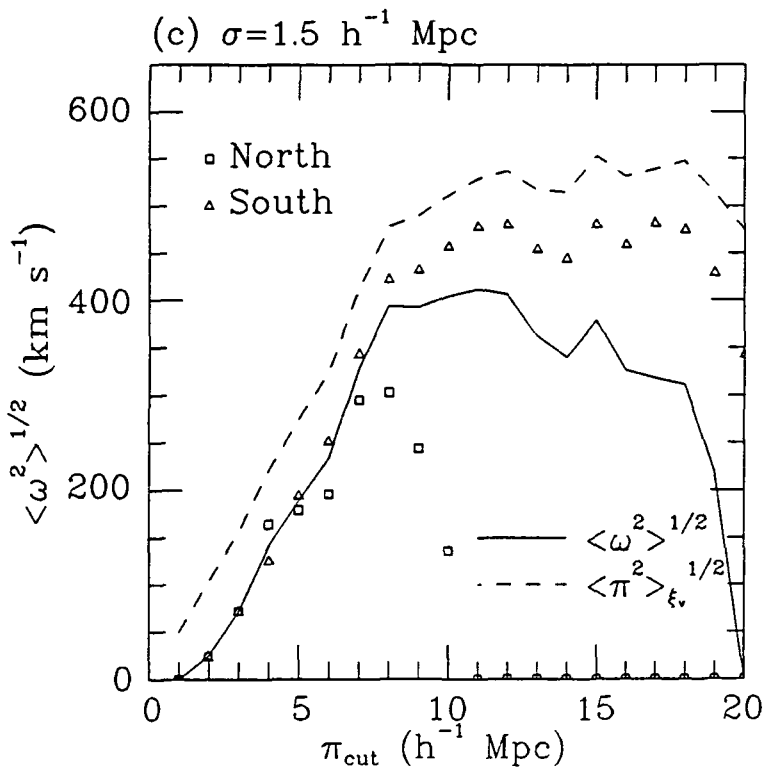
1h^{-1} Mpc intervals and summed over the bins to the appropriate π_{cut}. On the other hand the Hubble expansion correction to $\langle\pi^2\rangle_{\xi_V}^{1/2}$, $\langle\pi^2\rangle_{\xi}^{1/2}$, was obtained from the model in equation 2-128 with γ=1.8. The open symbols in the figures are used to represent the estimates from the north and south subsamples. The behaviour of these estimators, anticipated in Section 2.2.1.1 (Figure 2.6), is reproduced here; $\langle\omega^2\rangle^{1/2}$ rises steadily to a plateau as π_{cut} increases and then both $\langle\omega^2\rangle^{1/2}$ and $\langle\pi^2\rangle_{\xi_V}^{1/2}$ become unstable with $\langle\omega^2\rangle^{1/2}$ declining declining to small values (consistent with a break in $\xi(r)$).

As discussed in Section 2.2.1.1 the plateau in the form of $\langle\omega^2\rangle^{1/2}$ as a function of π_{cut} is taken to be a close estimator of the true random peculiar motions. In Table 4.2, the average values of $\langle\omega^2\rangle^{1/2}$ from the plateau region of the solid lines in Figure 4.2 (a) to (d) are shown together with the average π_{cut} at which these estimates were obtained. Also indicated are the average values of $\langle\pi^2\rangle_{\xi_V}^{1/2}$ over the same range. The better determined values of $\langle\omega^2\rangle^{1/2}$ of between 400 to 560kms^{-1} at $\sigma\le2$h^{-1} Mpc appear to be somewhat larger (although not significantly so) than the $\langle\omega^2\rangle^{1/2}$=200kms^{-1} measured by Bean (1983) for the Durham/AAT Survey. The uncertainties in $\langle\omega^2\rangle^{1/2}$, calculated from variations in $\langle\pi^2\rangle_{\xi_V}^{1/2}$ in the simulated catalogues of the sample, have been normalised up by a factor of 2 to take into account the larger variations in this quantity seen in the field-to-field errors (see Section 4.3.3 below); however, the variations between north and south subsamples (Figure 4.2) seem to indicate that the estimates here are more stable than this. Due to the possible systematic errors of this method, a full discussion of the Durham/SAAO Survey result is left until the direct fitting of $\xi_V(\sigma,\pi)$ has been employed.

In Section 2.2.1.1 it was seen that $\langle\pi^2\rangle_{\xi_V}^{1/2}$ is the upper limit to $\langle\omega^2\rangle^{1/2}$; in the situation in which galaxies have collapsed to virial equilibrium or are infalling this value is the more appropriate measure of peculiar motions. However, as can be seen from Figure 4.2 and Table 4.2, the effect is only apparent at the larger σ separations and even then not significantly so. This is further discussed in Section 4.2.2 below.

Finally, in Figure 4.3 and Table 4.3, the results of estimating $\langle\omega^2\rangle^{1/2}$ and $\langle\pi^2\rangle_{\xi_V}^{1/2}$ for the Parker et al. Survey are presented. These values indicate that $\langle\omega^2\rangle^{1/2}$ lies in the range of 230 to 520 kms^{-1} at $\sigma\le2$h^{-1} Mpc for this sample but again a discussion of this result will be left until Section 4.3.3 after the

(1) σ (h^{-1} Mpc)	(2) $\langle\omega^2\rangle^{1/2}$ (km s^{-1})	(3) $\langle\pi^2\rangle_{\xi_v}^{1/2}$ (km s^{-1})	(4) π_{cut} (h^{-1} Mpc)
0.25	560±210	590	15.0
0.75	430±400	510	13.0
1.50	400±450	510	10.0
3.00	110	400	9.5

Table 4.2. Estimates of the rms peculiar velocity $\langle\omega^2\rangle^{1/2}$ from the second moment of $\xi_v(\sigma,\pi)$ in the Durham/SAAO Survey. The values of $\langle\omega^2\rangle^{1/2}$ and the errors from the simulations (column (2)) are presented at various separations σ (column (1)). Column (3) lists the estimates of the peculiar velocity which omit the Hubble expansion correction to $\langle\omega^2\rangle^{1/2}$ and column (4) gives the average value of π_{cut} at which $\langle\omega^2\rangle^{1/2}$ and $\langle\pi^2\rangle_{\xi_v}^{1/2}$ were obtained.

Figure 4.3. Estimates of $\langle\omega^2\rangle^{1/2}$ from the width of $\xi_v(\sigma,\pi)$ in the Parker et al. Survey. Estimates of $\langle\omega^2\rangle^{1/2}$ as a function of the limit in separation π, π_{cut}, are shown at various projected separations σ. The solid and dashed lines are the values which incorporate and neglect the Hubble expansion correction, $\langle\pi^2\rangle_\xi^{1/2}$, respectively.

(a) $\sigma = 0.25 \ h^{-1} \ \text{Mpc}$

$\langle \omega^2 \rangle^{1/2}$

$\langle \pi^2 \rangle_{\xi_v}^{1/2}$

$\langle \omega^2 \rangle^{1/2} \ (\text{km s}^{-1})$

$\pi_{\text{cut}} \ (h^{-1} \ \text{Mpc})$

(b) $\sigma = 0.75 \ h^{-1} \ \text{Mpc}$

$\langle \omega^2 \rangle^{1/2}$

$\langle \pi^2 \rangle_{\xi_v}^{1/2}$

$\langle \omega^2 \rangle^{1/2} \ (\text{km s}^{-1})$

$\pi_{\text{cut}} \ (h^{-1} \ \text{Mpc})$

(c) $\sigma = 1.5 \ h^{-1}$ Mpc

$\langle \omega^2 \rangle^{1/2}$
$\langle \pi^2 \rangle^{1/2}_{\xi_v}$

$\langle \omega^2 \rangle^{1/2}$ (km s^{-1})

π_{cut} (h^{-1} Mpc)

(d) $\sigma = 3.0 \ h^{-1}$ Mpc

$\langle \omega^2 \rangle^{1/2}$ (km s^{-1})

$\langle \omega^2 \rangle^{1/2}$
$\langle \pi^2 \rangle^{1/2}_{\xi_v}$
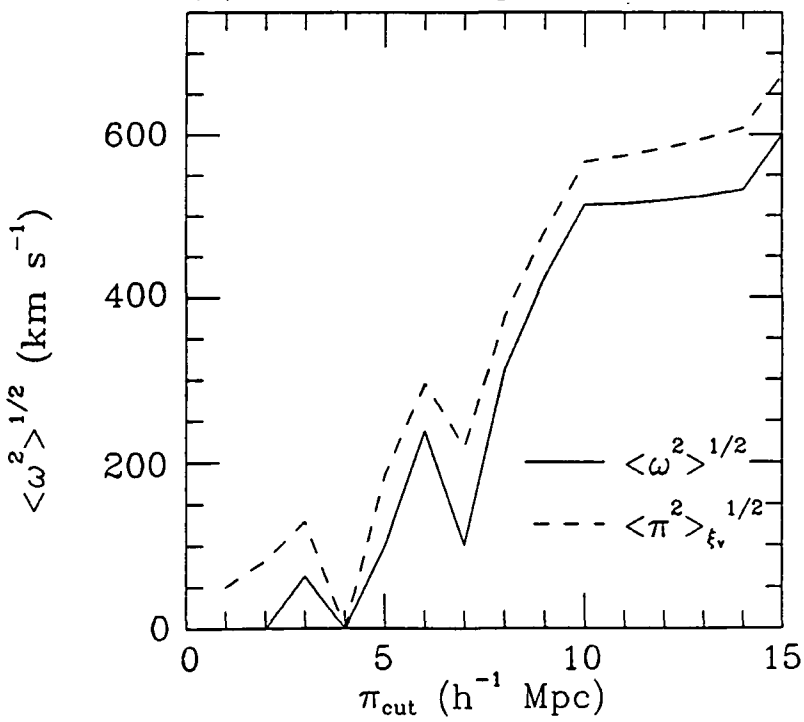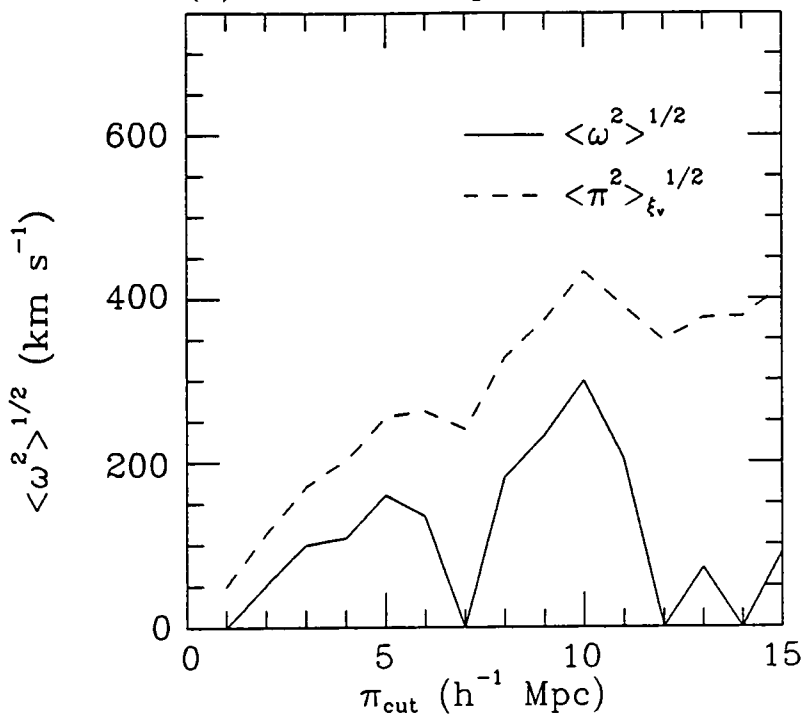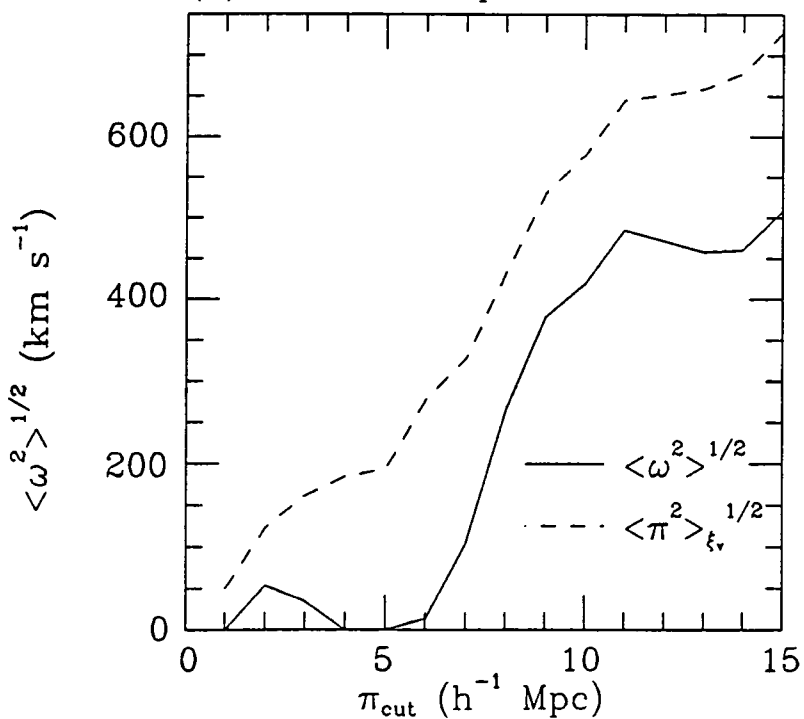
π_{cut} (h^{-1} Mpc)

(1) σ (h^{-1} Mpc)	(2) $\langle\omega^2\rangle^{1/2}$ (km s^{-1})	(3) $\langle\pi^2\rangle_{\xi_v}^{1/2}$ (km s^{-1})	(4) π_{cut} (h^{-1} Mpc)
0.25	300	330	8.5
0.75	520	590	12.0
1.50	230	380	9.5
3.00	460	640	12.0

Table 4.3. Estimates of the rms peculiar velocity $\langle\omega^2\rangle^{1/2}$ from the second moment of $\xi_v(\sigma,\pi)$ in the Parker et al. Survey. The values of $\langle\omega^2\rangle^{1/2}$ (column (2)) are presented at various separations σ (column (1)). Column (3) lists the estimates of the peculiar velocity which omit the Hubble expansion correction to $\langle\omega^2\rangle^{1/2}$ and column (4) gives the average value of π_{cut} at which $\langle\omega^2\rangle^{1/2}$ and $\langle\pi^2\rangle_{\xi_v}^{1/2}$ were obtained.

direct fits to $\xi_v(\sigma,\pi)$ have been performed.

4.2.2 $\langle\omega^2\rangle^{1/2}$ and r_o from direct models of $\xi_v(\sigma,\pi)$

The estimates of $\xi_v(\sigma,\pi)$ for the Durham/SAAO and Parker et al. surveys were obtained from the data-data and data-random pair counts $DD(\sigma,\pi)$ and $DR(\sigma,\pi)$, respectively, using the methods outlined in Chapter 2 (Section 2.1.2.2). In particular, the pair count $DR(\sigma,\pi)$ was estimated by summing contributions of $n(z)\Delta A_i(\sigma)\Delta\pi$ at (σ,π) and at $(\sigma,-\pi)$ from all galaxies i in the sample. As in Section 4.1.2 the mean homogeneous density $n(z)$ was normalised using the methods in Section 3.2.3 but unlike that earlier section of this Chapter $n(z)$ was calculated directly from the model. The area of the annuli $\Delta A_i(\sigma)$ were estimated by laying random points uniformly over the entire ring at (σ,π) (or $(\sigma,-\pi)$) and then counting the fraction of points that were contained by the field volume, as described by Peebles (1979).

In Figure 4.4 (a) to (d) are presented estimates of $\xi_v(\sigma,\pi)$ for the Durham/SAAO Survey as a function of both σ (dotted histogram) and π (solid histogram) in $1h^{-1}$ Mpc bins of either variable. In the absence of peculiar motions, $\xi_v(\sigma,\pi)$ in these figures would be symmetric in π and σ and so the significant difference between the solid and dashed histograms is evidence for strong anisotropy in this sample.

The method preferred by Bean et al. (1983) for estimating $\langle\omega^2\rangle^{1/2}$ from these figures is by fitting the model in equation 2-31 directly to the $\xi_v(\sigma,\pi)$ versus π data. Following their example, $\xi(r)$ is assumed to be a power law of the form $\xi(r)=(r_o/r)^\gamma$ (equation 2-90) with $\gamma=1.8$ and $f(\omega)$ is taken to be the distribution function of equation 2-122. In this procedure $\langle\omega^2\rangle^{1/2}$ and r_o are left as free parameters to be defined by the best fit to the data. In this case a simple least-squares method was applied to each figure in the range $0\leq\pi\leq16h^{-1}$ Mpc with equal weighting for each point. The best models using this procedure are shown as solid lines in Figure 4.4 and the best-fit parameters for $\langle\omega^2\rangle^{1/2}$ and r_o are given in Table 4.4 (columns (2) and (3), respectively).

Looking at the models applied to the observed data in Figure 4.4, it is seen that a good fit is obtained in each case, except, perhaps, for Figure 4.4

Figure 4.4. Estimates of the redshift two-point correlation function $\xi_v(\sigma,\pi)$ in the Durham/SAAO Survey. The solid and dotted histograms show the estimates as a function of the separations π and σ, respectively. The solid and dashed lines are the models of $\xi_v(\sigma,\pi)$ (which exclude and include infall, respectively) which best fit the $\xi_v(\sigma,\pi)$ versus π data (the best fit parameters are indicated in Table 4.4).

(a)

(b)

(c)

(d)

(1)	(2)	(3)	(4)	(5)	(6)	(7)
	$\pi_{cut}=16h^{-1}$ Mpc		$\pi_{cut}=10h^{-1}$ Mpc		Infall	
σ	$\langle\omega^2\rangle^{1/2}$	r_0	$\langle\omega^2\rangle^{1/2}$	r_0	$\langle\omega^2\rangle^{1/2}$	r_0
$(h^{-1}$ Mpc)	(km s^{-1})	$(h^{-1}$ Mpc)	(km s^{-1})	$(h^{-1}$ Mpc)	(km s^{-1})	$(h^{-1}$ Mpc)
0.25	680±150	5.8±0.7	720	6.0	710	5.8
0.75	560±220	5.7±0.8	830	6.5	650	5.7
1.50	620±450	7.3±0.7	940	8.4	700	7.1
3.00	70±560	4.5±1.0	90	4.5	320	3.4

(8)	(9)	(10)	(11)	(12)	(13)	(14)
	North		South		Simulations	
σ	$\langle\omega^2\rangle^{1/2}$	r_0	$\langle\omega^2\rangle^{1/2}$	r_0	$\langle\omega^2\rangle^{1/2}$	r_0
$(h^{-1}$ Mpc)	(km s^{-1})	$(h^{-1}$ Mpc)	(km s^{-1})	$(h^{-1}$ Mpc)	(km s^{-1})	$(h^{-1}$ Mpc)
0.25	800	5.7	650	6.0	368	5.4
0.75	600	5.7	550	5.7	375	5.4
1.50	350	6.0	750	8.1	310	5.2
3.00	200	6.0	0	3.4	320	5.1

Table 4.4. The line-of-sight rms peculiar velocity $\langle\omega^2\rangle^{1/2}$ and the correlation length r_0 as estimated from model fits to $\xi_v(\sigma,\pi)$ in the Durham/SAAO Survey. The values of $\langle\omega^2\rangle^{1/2}$ and r_0 that give the best fit of the model in equation 2-31 to the solid histograms in Figure 4.4 are presented at various separations σ (column (1)) in columns (2) and (3) ($\pi_{cut}=16h^{-1}$ Mpc) and in columns (4) and (5) ($\pi_{cut}=10h^{-1}$ Mpc). The values of these parameters that give the best fit of the infall model of equation 2-132 to the solid histograms are similarly given in columns (6) and (7). The variations between the north and south sub-samples are shown in columns (9) to (12) and the mean values of $\langle\omega^2\rangle^{1/2}$ and r_0 from the simulations are indicated in columns (13) and (14).

(c) where ξ_v appears to be somewhat flatter than the predicted model at $\pi < 8h^{-1}$ Mpc. The large range in π of the fits was so as to include the possibly correlated pairs of galaxies seen at separations $\pi > 10h^{-1}$ Mpc in the $\sigma \leq 1h^{-1}$ Mpc figures. Since this is larger than the $\pi_{cut} = 10h^{-1}$ Mpc used in the $\omega_v(\sigma)$ analysis of Section 4.1.1, Table 4.4 (columns (4) and (5)) lists the values of $\langle \omega^2 \rangle^{1/2}$ and r_0 when the fits are constrained to cover this smaller range in π. As can be seen, the measurements yield slightly larger estimates of $\langle \omega^2 \rangle^{1/2}$ and r_0, but not significantly so.

Table 4.4 (columns (2) and (4)) indicates that the better determined estimates of $\langle \omega^2 \rangle^{1/2}$ for the Durham/SAAO Survey at $\sigma \leq 2h^{-1}$ Mpc are in the range 560 to 680 kms^{-1} in good agreement with the previous result from the moments method (previous section) and this again appears to be larger than the $\langle \omega^2 \rangle^{1/2} = 200$ to 250 kms^{-1} estimated from the Durham/AAT sample by Bean (1983) and Bean et al. (1983). The errors in the table are again obtained from applying the same methods to the simulations of the Durham/SAAO catalogue and, as before, they are normalised up by a factor of 2 to take account of the larger variations seen in the field-to-field errors (see Chapter 3, Section 3.1.1 and Section 4.3.3 below). This level of uncertainty again appears somewhat larger than that shown by north and south subsample differences (columns (9) and (11), $\pi_{cut} = 16h^{-1}$ Mpc).

Also shown in Table 4.4 are the mean values of $\langle \omega^2 \rangle^{1/2}$ estimated from the simulations at the various σ bins (column (13)). As can be seen at $\sigma > 1h^{-1}$ Mpc the mean estimate falls below the expected value of ~ 350kms^{-1}, although the average value over all 4 bins of $\langle \omega^2 \rangle^{1/2} = (343 \pm 33)$kms^{-1} is close to the input value. This may indicate that the Bean et al. two-parameter fitting approach is reasonably unbiassed as predicted. The results from the Durham/SAAO Survey, and the magnitudes of the sample errors, are further discussed in the section below.

The values of the correlation length r_0 found here can be compared with the values obtained from $\omega_v(\sigma)$ in Section 4.1.1 above. In Table 4.4 (column (14)) are listed the mean values of r_0 from applying these methods to the simulations of the Durham/SAAO catalogue. The average value of r_0 over all four separations in this case is $r_0 = (5.3 \pm 0.2)h^{-1}$ Mpc which is in agreement with the known value of $r_0 = 5.4h^{-1}$ Mpc for the observed $\xi(r)$ below the simulated break scale at $r \approx 6h^{-1}$ Mpc (Figure 2.5). This shows that the method

is quite sensitive to the small-scale r_0 in spite of using a large π_{cut} of $13h^{-1}$ Mpc for the fits and this again indicates that the $\sigma \leq 4h^{-1}$ Mpc data can provide an accurate estimate of the small-scale correlation function. The mean value of r_0 in the Durham/SAAO Survey at this scale is $r_0 = 5.8h^{-1}$ Mpc and this agrees well with the $r_0 = (5.6 \pm 0.5)h^{-1}$ Mpc deduced previously for this sample from $\omega_v(\sigma)$. This again confirms the assertion of Bean et al. (1983) that these direct fitting methods give a reasonably unbiassed estimate of the small-scale r_0.

In Chapter 2 (Section 2.2.1.2) a simple linear infall model for $\xi_v(\sigma,\pi)$ was discussed (equation 2-130) and, similar to Bean et al. (1983) and Davis and Peebles (1983), this has been applied to the Durham/SAAO data to look for such effects. In this case, as with Bean et al., F and the bias parameter, b, in equation 2-132 have been set to unity corresponding to a high density Universe in which galaxies trace the mass. A pure power law for $\xi(r)$ was again assumed (equation 2-90) with $\gamma = 1.8$ and a two-parameter least-squares fit to the $\xi_v(\sigma,\pi)$ versus π data again performed with $\pi_{cut} = 16h^{-1}$ Mpc. However, in this case r_0 in the infalling velocity component (equation 2-130) was set to the value previously obtained without infall (Table 4.4, column (3)). The best fit models are shown as dashed lines in Figure 4.4 and the best fit values for r_0 and $\langle \omega^2 \rangle^{1/2}$ are indicated in Table 4.4 (columns (6) and (7), respectively).

As with the moments method of the previous section, the inclusion of infall makes little difference to either the values of $\langle \omega^2 \rangle^{1/2}$ or to the correlation length r_0, except, perhaps, at the largest σ separations but even then not significantly. The tendency, as with the moments estimates, is to slightly raise estimates of $\langle \omega^2 \rangle^{1/2}$ as expected; part of the Hubble motion included in the model in equation 2-31 is cancelled by the infall velocity in equation 2-130 (at large values of ξ it is completely cancelled). This is discussed further below.

Finally, in Figure 4.5 (a) to (d) are presented the $\xi_v(\sigma,\pi)$ results estimated from the Parker et al. Survey, and these are presented in a similar fashion to those for the Durham/SAAO Survey in Figure 4.4. The key feature to notice about these figures is that, unlike that latter survey, there is little or no anisotropy apparent in $\xi_v(\sigma,\pi)$ and this appears at odds with the results from the moments method in the previous section, where $\langle \omega^2 \rangle^{1/2}$ was measured to be ~230 to 520kms^{-1} at $\sigma \leq 2h^{-1}$ Mpc, although the errors on this

Figure 4.5. Estimates of the redshift two-point correlation function $\xi_v(\sigma,\pi)$ in the Parker et al. Survey. The solid and dotted histograms show the estimates as a function of the separations π and σ, respectively. The solid lines are the models of $\xi_v(\sigma,\pi)$ (equation 2-31) which best fit the $\xi_v(\sigma,\pi)$ versus π data (the best fit parameters are indicated in Table 4.5)

(a)

(b)

(c)

ξ_v

$\sigma = 1.5\ h^{-1}\ Mpc$

$\pi = 1.5\ h^{-1}\ Mpc$

$\pi/\sigma(h^{-1}\ Mpc)$

(d)

ξ_v

$\sigma = 3.0\ h^{-1}\ Mpc$

$\pi = 3.0\ h^{-1}\ Mpc$

$\pi/\sigma(h^{-1}\ Mpc)$
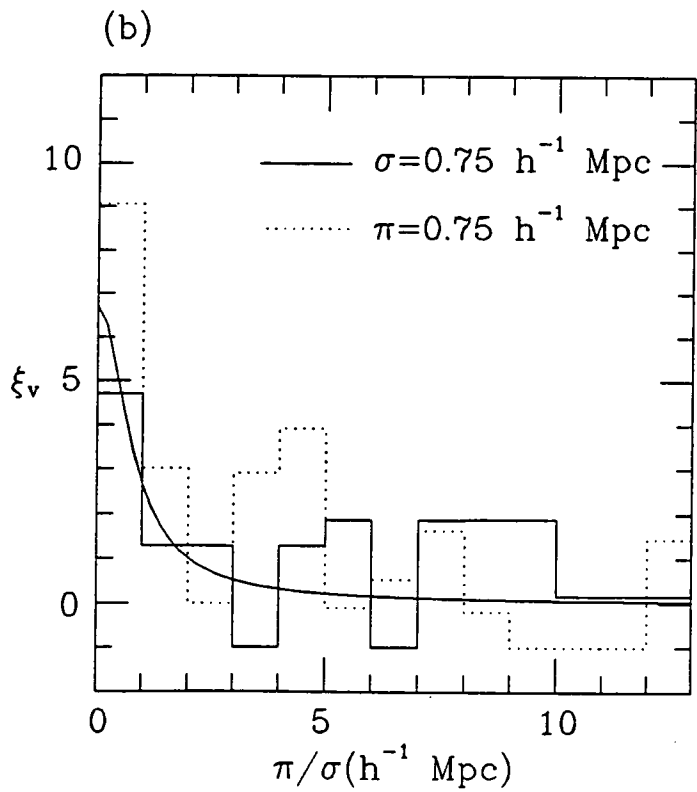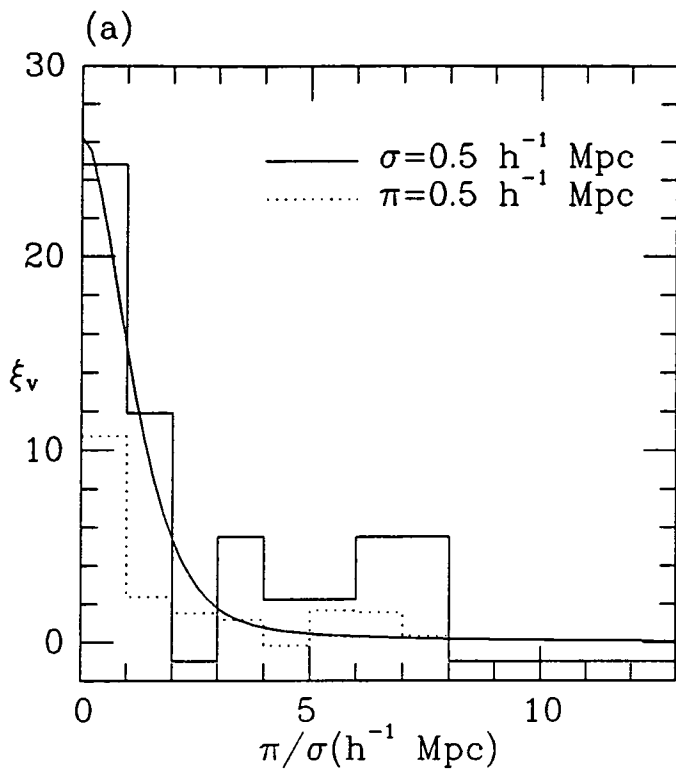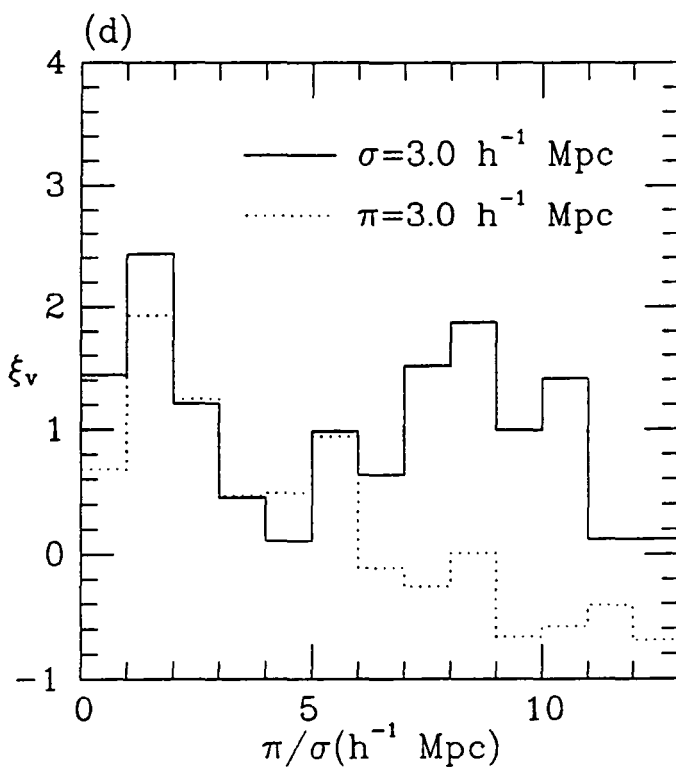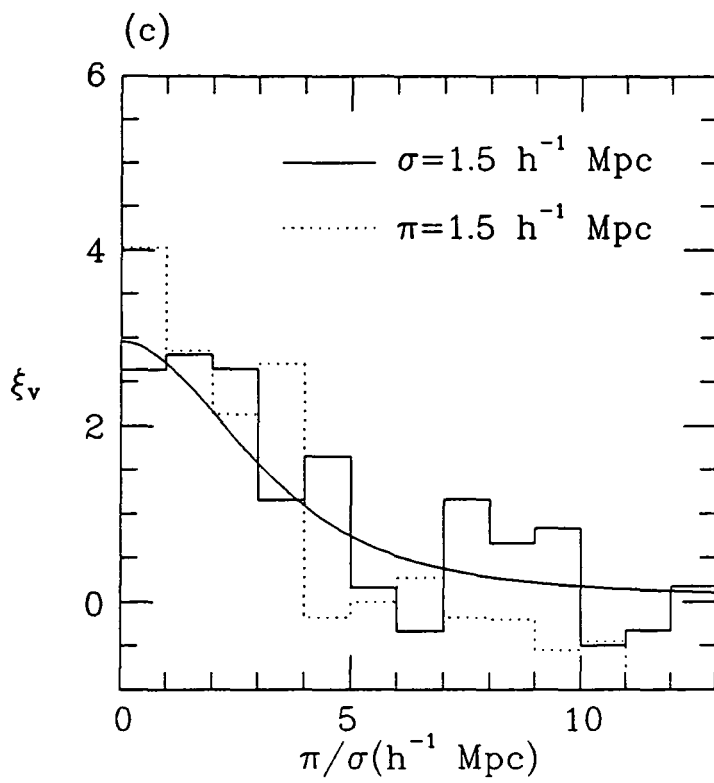
latter method (see Table 4.2) would suggest that $\langle \omega^2 \rangle^{1/2} \approx 0 \, kms^{-1}$ was, perhaps, a consistent result.

The solid lines in Figure 4.5 and the values of $\langle \omega^2 \rangle^{1/2}$ and r_0 in Table 4.5 are the non-streaming direct fits to the $\xi_v(\sigma,\pi)$ versus π data in the Parker et al. Survey ($\pi_{cut}=13h^{-1}$ Mpc). The largest bin in σ proved to be too unreliable for measurement of these parameters and so has been omitted. The peculiar motion results confirm the visual impression observed in the data; $\langle \omega^2 \rangle^{1/2}$ is measured to be in the range 0 to $200 kms^{-1}$ at $\sigma \leq 2h^{-1}$ Mpc. The difference between this and the results from the moments method can be seen to lie in the excess correlation or 'tail' in the ξ_v versus π data at $\pi \approx 7$ to $10h^{-1}$ Mpc in Figure 4.5. Since the errors in the moments method are larger than those in Table 4.5 (and the results consistent with $\langle \omega^2 \rangle^{1/2} \approx 100 kms^{-1}$) it is assumed that the values here are more reliable. The errors in the table are again from the simulations but increased by a factor of 2.

In terms of the correlation length r_0 the average value of $r_0 = 2.9h^{-1}$ Mpc over the three bins in Table 4.5 agrees well with the $r_0 = (4.0 \pm 1.0)h^{-1}$ Mpc from the $\omega_v(\sigma)$ analysis. Again, the similarity between these estimates suggest that the direct fitting method is reasonably unbiassed.

4.3 Comparison of the small-scale ($\leq 1h^{-1}$ Mpc) r_0, Q and $\langle \omega^2 \rangle^{1/2}$ results with other surveys

In this section the results obtained from the Durham/SAAO and Parker et al. surveys for the parameters r_0, Q and $\langle \omega^2 \rangle^{1/2}$ at small scales, are compared to the observations of these quantities from statistical studies of other complete redshift surveys (see Section 3.1 in Chapter 3 above). Particular attention is paid to comparisons with the Durham/AAT sample as this, very comparable survey, has been analysed using methods which are identical to those used in the previous sections. Using statistical weights derived in a consistent manner from the simulations of all three samples, overall values for these parameters are presented. This then prepares for the Virial analyses of the next section.

These overall values for the small-scale correlation functions and peculiar velocities are first compared to the results of other catalogues. In particular, comparisons are made with the detailed studies of Davis and

(1)	(2)	(3)
σ	$\langle\omega^2\rangle^{1/2}$	r_0
(h^{-1} Mpc)	(km s^{-1})	(h^{-1} Mpc)
0.25	100±250	2.9±0.8
0.75	0±320	2.2±0.9
1.50	200±510	3.6±1.3

Table 4.5. Estimates of $\langle\omega^2\rangle^{1/2}$ and r_0 from the model fits to $\xi_v(\sigma,\pi)$ in the Parker et al. Survey. The values of $\langle\omega^2\rangle^{1/2}$ and r_0 in columns (2) and (3) at various separations σ (column (1)) represent the parameters that give the best fit of the model in equation 2-31 to the solid histograms in Figure 4.5. The errors shown here are from applying similar methods to the simulations.

Peebles (1983) of the CfA (m_B<14^m.5) Survey (Huchra et al. 1983), Peebles (1979) for the Kirshner et al. survey (KOS, 1978) and Efstathiou and Jedrzejewski (1984) for the deeper Kirshner et al. Survey (1983). Further comparisons are also made for r_0 and Q with the results from the analysis of the Zwicky (Zwicky et al. 1961-1968) and Lick (Shane and Wirtanen 1967) magnitude galaxy catalogues by Groth and Peebles (1977).

4.3.1 The two-point correlation length r_0

Firstly, in Figure 4.6 the overall form of $\omega_v(\sigma)$ for the Durham/SAAO, Durham/AAT and Parker et al. surveys estimated in Section 4.1.1 (Figure 4.1 (f)) is compared to a similar analysis of $\omega_v(\sigma)$ in the CfA (m_B<14^m.5) Survey obtained from the $\xi_v(\sigma,\pi)$ diagrams of Davis and Peebles (1983, their Figure 5). In both estimates the summation in π is terminated at π_{cut}=10h^{-1} Mpc and the model for $\omega_v(\sigma)$ is as in Figure 4.1 (f) (a power law in $\xi(r)$ of the form $\xi(r)=(r_0/r)^{1.8}$ integrated to π_{cut}=10h^{-1} Mpc) which has an r_0 of 4.8h^{-1} Mpc. The level of agreement (<1σ deviations on all the points) between these two samples is remarkable given that they have been catalogued in quite different ways; the CfA survey is a relatively shallow (but large volume) sample and includes features of the nearby galaxy distribution (see Chapter 3, Section 3.2.3) whereas the combined survey is ~3 times deeper and has been obtained from many narrow shaped fields. Either this is a remarkable coincidence or it is indicating that the two-point galaxy correlation function estimated in this fashion (see Section 2.1.2.4 of Chapter 2) at separations ≤10h^{-1} Mpc is quite stable. This question of stability of these samples will be discussed more fully in Chapter 5 below.

The model $\omega_v(\sigma)$ that has been fitted to separations σ<1h^{-1} Mpc in the combined sample of the 17^m surveys appears not to match the data very well, at separations σ>1h^{-1} Mpc, in either this or the CfA sample. This rise above the model containing a simple power law for $\xi(r)$ has been noted earlier (Section 4.1.1) and by Bean (1983). In the absence of strong infall this may imply that the amplitude of $\xi(r)$ rises above its small-scale form at σ>1h^{-1} Mpc or that $\xi(r)$ has a larger index than -1.8. The significance of this deviation is further discussed in the following Chapter where the projection effects inherent in $\omega_v(\sigma)$ are not so prevalent.
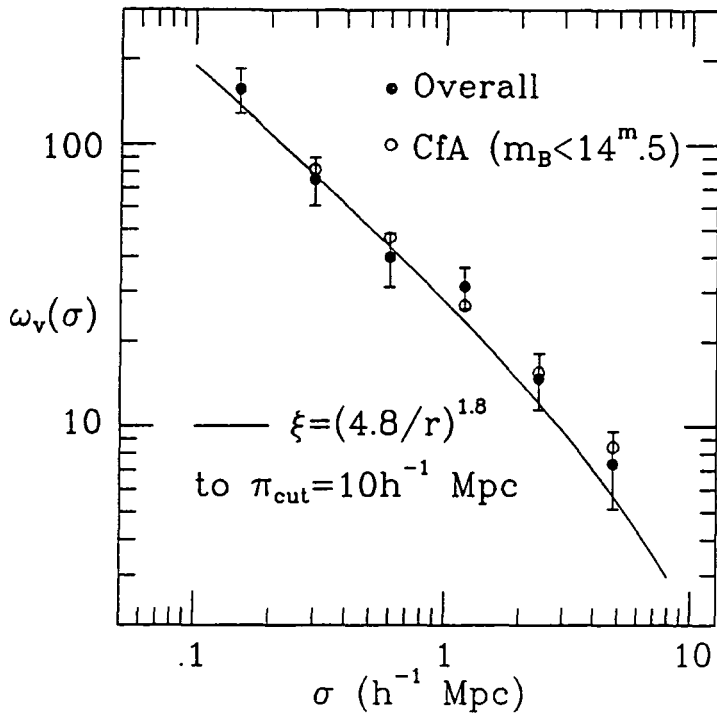
Figure 4.6. Estimates of the projected two-point correlation function $\omega_v(\sigma)$ from the combined sample of the 17^m surveys and from the CfA ($m_B < 14^m.5$) catalogue. The $\pi_{cut} = 10h^{-1}$ Mpc estimates shown here for the combined 17^m surveys are the same as in Figure 4.1 (f); those for the CfA sample were obtained by integrating the $\xi_v(\sigma,\pi)$ estimates of Davis and Peebles (1983, Figure 5) to the same π_{cut}. The solid line is the model for $\omega_v(\sigma)$ in equation 2-97 (the power law in $\xi(r)$ integrated to π_{cut}) with $\gamma = 1.8$ and $\pi_{cut} = 10h^{-1}$ Mpc (the correlation length r_0 are is as indicated)

For a further comparison of the estimates of the correlation length r_0, Table 4.6 lists the values obtained from the non-streaming and streaming (values in brackets) direct fits to $\xi_v(\sigma,\pi)$ in the Durham/SAAO, Durham/AAT and Parker et al. surveys (the estimates in Tables 4.4 and 4.5 being reproduced here for ease of study and in all cases apply to a power-law $\xi(r)$ with $\gamma=1.8$). The final column of Table 4.6 shows the combined values averaged together according to their error (obtained from the simulated catalogues) and the overall uncertainty again assumes independence of the samples (see the Appendix). The non-streaming values of r_0 are also reproduced in Figure 4.7, together with the estimates from the CfA ($m_B<14^m.5$) and KOS (1978) surveys (here r_0 was obtained directly from the estimates of $\xi_v(\sigma,\pi)$ in Davis and Peebles 1983 and Peebles 1979; at each point this $\xi_v(\sigma,\pi)$ was numerically integrated over π to $\pi_{cut}=10h^{-1}$ Mpc, as in $\omega_v(\sigma)$, and r_0 estimated using the model in equation 2-97 with $\gamma=1.8$). Note that the error bars in this figure apply to the overall estimates of r_0 in the 17^m surveys.

There appears, from this figure, to be some scatter in these small-scale values of r_0. Considering the range $\sigma<1h^{-1}$ Mpc, where the results are best defined and the scale is most appropriate for virial analyses, it is found that $r_0=(5.8\pm0.6)h^{-1}$ Mpc for the Durham/SAAO Survey, as compared to $r_0=(4.5\pm0.4)h^{-1}$ Mpc for the Durham/AAT and $r_0=(2.6\pm0.7)h^{-1}$ Mpc for the Parker et al. sample. Given the level of uncertainty in these estimates (and their errors) the scatter around the mean of $r_0=(4.5\pm0.3)h^{-1}$ Mpc seems reasonable. Note also that this estimate is in close agreement with the $r_0=4.8h^{-1}$ Mpc from the $\sigma<1h^{-1}$ Mpc fit to the overall $\omega_v(\sigma)$ in Figure 4.1 (f) (Section 4.1.1).

As with the projected function $\omega_v(\sigma)$ above, this overall value $r_0=(4.5\pm0.3)h^{-1}$ Mpc at this scale is in good agreement with the CfA value of $5.0h^{-1}$ Mpc from Figure 4.7, and the $r_0=(5.2\pm0.3)h^{-1}$ Mpc ($\sigma<2h^{-1}$ Mpc) or $r_0=(5.4\pm0.3)h^{-1}$ Mpc as estimated for this shallower sample by Davis and Peebles (1983) and Efstathiou and Jedrzejewski (1984), respectively. These latter authors also find $r_0=(5.2\pm0.3)h^{-1}$ Mpc from the survey of Kirshner et al. (1983). Thus it appears from these observations and those of Peebles (1979) for the KOS sample (Figure 4.7) that all the redshift survey results seem to be converging on a value of $r_0\approx4.7h^{-1}$ Mpc at $\sigma<1h^{-1}$ Mpc which is close to the mean estimate of Groth and Peebles for the Lick and Zwicky catalogues (this

		r_0 (h^{-1} Mpc)		
(1)	(2)	(3)	(4)	(5)
σ (h^{-1} Mpc)	D/SAAO	D/AAT	Parker	Overall
0.25	5.8±0.7 (5.8)	4.5±0.4 (4.3)	2.9±0.8	4.6±0.3 (4.8)
0.75	5.7±0.8 (5.7)	4.5±0.6 (4.3)	2.2±0.9	4.3±0.4 (4.8)
1.50	7.3±0.7 (7.1)	5.6±0.7 (5.3)	3.6±1.3	6.0±0.5 (6.1)
3.00	4.5±1.0 (3.4)	6.9±1.2 (1.2)		5.5±0.8 (4.6)

Table 4.6. Estimates of the correlation length r_0 from model fits to $\xi_v(\sigma,\pi)$ in the Durham/SAAO, Durham/AAT and Parker et al. surveys. The unbracketed values (together with the errors from the simulations) in columns (2), (3) and (4) are the parameters that give the best fit of the no infall model to the $\xi_v(\sigma,\pi)$ histograms in the Durham/SAAO, Durham/AAT and Parker et al. surveys, respectively. Likewise the bracketed values are the estimates for the model that does include infall. Column (5) shows the overall estimates from all three samples (the infall values in this case coming from the Durham surveys only).
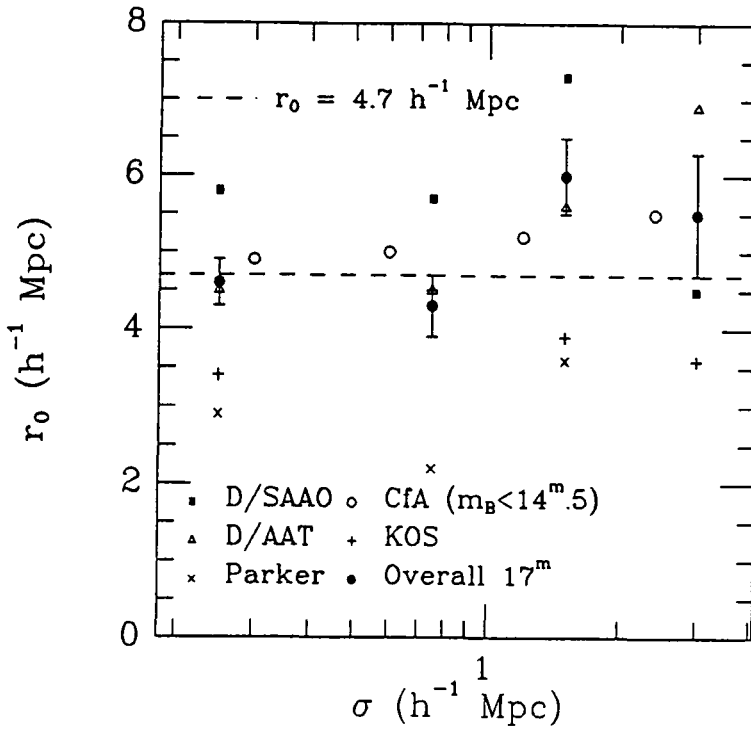
Figure 4.7. Small-scale estimates of the correlation length r_0 from direct model fits to $\xi_v(\sigma,\pi)$. The values for the Durham/SAAO, Durham/AAT and Parker et al. surveys were obtained from direct fits to $\xi_v(\sigma,\pi)$ without infall. The overall estimate (solid circles) from these samples (with error bars) was found by averaging these values (see Table 4.6). The estimates from the CfA and KOS surveys was found by integrating $\xi_v(\sigma,\pi)$ to $\pi_{cut}=10h^{-1}$ Mpc (see text). The dashed line, with $r_0=4.7h^{-1}$ Mpc, is the Groth and Peebles (1977) result for the clustering observed in the Lick and Zwicky 2-d catalogues.

value is shown as a dashed line in Figure 4.7).

At $\sigma > h^{-1}$ Mpc, there is again some evidence from Figure 4.7 for an increase in the value of the correlation scale-length, although the scatter is quite wide. Although the figures in brackets in Table 4.6 have been obtained using a high density Universe, infall model in the fits to $\xi_v(\sigma,\pi)$ there is still some weak evidence for a rise in r_o. However, a more detailed discussion of this behaviour of the data will be left until the estimator $\xi_s(s)$ has been presented in Chapter 5.

4.3.2 The three-point amplitude Q

In Section 4.1.2 above, this quantity estimated for the Durham/SAAO Survey gave $Q=0.48\pm0.12$ at $\sigma < 2h^{-1}$ Mpc although the more stable value of $Q=0.75\pm0.14$ at $\sigma < 1h^{-1}$ Mpc may be more appropriate. In either case, this agrees well with the $Q=0.60\pm0.06$ obtained from the Durham/AAT sample.

Similar estimates have also been observed in other samples; Efstathiou and Jedrzejewski find $Q=0.8\pm0.1$ for the CfA ($m_B < 14^m.5$) Survey and $Q=0.5\pm0.1$ for the sample of Kirshner et al. (1983). Peebles (1981a) also found $Q=0.68\pm0.05$ for the compilation of redshifts by Rood (1982). These and the 17^m samples seem to suggest that the overall value of Q is $Q\approx0.7$ and this is somewhat different from the $Q=1.3\pm0.2$ deduced from the Lick and Zwicky catalogues by Groth and Peebles (1977) and the $Q=1.3\pm0.3$ for the KOS Survey by Bean et al. (1983). However, in the case of the Zwicky Catalogue the result for Q is very sensitive to the inclusion (or removal) of 11 galaxies in the core of the the Coma cluster (the result being $Q=0.85$ when the 11 galaxies are omitted rather than $Q=1.4$) and so the former result from the magnitude catalogues should, perhaps, be viewed with caution. Similarly, most of the result in the KOS Survey comes from one rich field (NP4), the value of Q falling by a factor of 2 if this field is omitted (Bean 1983).

Previously, the low value, with respect to the Zwicky and Lick Catalogues, of $Q=0.6$ in the Durham/AAT Survey was taken, by Bean et al. (1983), to imply that this sample was lacking in rich areas of clustering. However, from the overall agreement of this value with that estimated from the Durham/SAAO and other samples, this conclusion seems no longer to be

justified. Certainly, this agrees with the observations in Chapter 3 (Section 3.2.2) that Abell type clusters have not been missed in the 17^m samples.

4.3.3 The pair-wise rms peculiar velocity $\langle \omega^2 \rangle^{1/2}$

In Table 4.7 the pair-wise rms peculiar velocity results from the non-streaming and streaming fits (in brackets) to $\xi_v(\sigma, \pi)$ in the Durham/SAAO and Parker et al. surveys are compared to the values estimated from the Durham/AAT Survey using identical methods. The Durham/SAAO and Parker et al. estimates, reproduced here for convenience, are the same as those in Tables 4.4 and 4.5 except that a correction has been made for the differences in redshift measuring error between the various surveys. This is

$$\langle \omega^2 \rangle^{1/2}_{corr} = (\langle \omega^2 \rangle_{obs} - 2\delta v_z^2)^{1/2} \qquad (4\text{-}2)$$

according to the assumption that the error in the redshift velocity measurement δv_z of a single galaxy (Table 4.8) adds in quadrature to to the true value of $\langle \omega^2 \rangle^{1/2}$.

At $\sigma < 1h^{-1}$ Mpc, where the estimates of the peculiar velocities in Table 4.7 appear to be well determined, there appears to be quite a wide spread in the observed values of $\langle \omega^2 \rangle^{1/2}$. In this scale range, $\langle \omega^2 \rangle^{1/2} = (600 \pm 140) kms^{-1}$ for the Durham/SAAO Survey, $\langle \omega^2 \rangle^{1/2} = (190 \pm 90) kms^{-1}$ for the Durham/AAT and $\langle \omega^2 \rangle^{1/2} = (0 \pm 240) kms^{-1}$ for the Parker et al. sample. Thus, according to these errors the Durham/SAAO Survey is 2.5σ and 2.2σ away from the Durham/AAT and Parker et al. values, respectively.

This seemingly quite large variation in the line-of-sight peculiar motions has been investigated fairly thoroughly. At first, the discrepancy, as measured directly by the error in the simulated catalogues, appeared even larger than this. In Chapter 3 (Section 3.1.1) the simulated and field-to-field errors on $\langle \omega^2 \rangle^{1/2}$ at $\sigma < 1h^{-1}$ Mpc were compared for both the Durham/SAAO and Durham/AAT samples (the 'field-to-field' errors for the Durham/SAAO Survey were obtained from dividing the sample in three groups of three fields to achieve enough signal). That table is reproduced in more detail in Table 4.9 below. It is apparent from this that the magnitude of the simulated errors is down on the field-to-field errors by a factor of ~2 and, on the assumption that

$$\langle \omega^2 \rangle^{1/2} \ (\text{km s}^{-1})$$

(1)	(2)	(3)	(4)	(5)
σ (h⁻¹ Mpc)	Durham/SAAO	Durham/AAT	Parker	Overall
0.25	660±150 (690)	220±120 (230)	0±250	300± 90 (400)
0.75	530±220 (630)	170±130 (220)	0±320	230±100 (230)
1.50	600±450 (680)	190±230 (280)	170±510	260±190 (360)
3.00	0±560 (270)	0±540 (190)		0±390 (390)

Table 4.7. Estimates of the rms peculiar velocity $\langle \omega^2 \rangle^{1/2}$ from model fits to $\xi_v(\sigma,\pi)$ in the Durham/SAAO, Durham/AAT and Parker et al. surveys. The unbracketed values (together with the errors from the simulations) in columns (2), (3) and (4) are the parameters that give the best fit of the no infall model to the $\xi_v(\sigma,\pi)$ histograms in the Durham/SAAO, Durham/AAT and Parker et al. surveys, respectively (these are similar to the values in Tables 4.4 and 4.5 except that a correction has been made for the redshift measuring error; see text). Likewise the bracketed values are the estimates for the model that does include infall. Column (5) shows the overall estimates from all three samples (the infall values in this case coming from the Durham surveys only)

| Survey	δv_z (kms^{-1})
Durham/SAAO	120
Durham/AAT	50
Parker et al.	75
CfA ($m_B < 14^m.5$)	50

Table 4.8. Redshift velocity measurement errors δv_z for four of the galaxy surveys discussed in the text.

	Durham/SAAO		Durham/AAT	
σ	(1)	(2)	(3)	(4)
(h^{-1} Mpc)	sim	f-to-f	sim	f-to-f
0.25	77	130	59	103
0.75	109	229	63	118

Table 4.9. Error estimates for the pair-wise rms peculiar velocity $\langle \omega^2 \rangle^{1/2}$ (in units of kms^{-1}) along the line-of-sight (see also Table 3.1 of Chapter 3, Section 3.1.1). Columns (1) and (2) are, respectively, the simulated and field-to-field errors for the Durham/SAAO Survey. Likewise, columns (3) and (4) are these quantities, respectively, for the Durham/AAT Survey.

the field-to-field errors are more likely to be representative of the true fluctuations in $\langle\omega^2\rangle^{1/2}$, this implies a deficiency in the model for the simulations.

An alternative explanation lies not in the simulated errors (although at odds with those from the field-to-field fluctuations) but in the estimate of the redshift velocity measurement δv_z for the Durham/SAAO sample. Figure 4.8 shows the distribution of Tonry and Davis (1979) r-factors for the absorption-line redshifts used in this sample (quality ratings 1 and 2; see Section 3.1.1 in Chapter 3) and these represent 79% of the total number of redshifts. According to Tonry and Davis this r-factor is related to the error δv_z by

$$\delta v_z = \frac{c}{1+r} \qquad\qquad (4\text{-}3)$$

Thus, using the mean calibration of $c=688\text{kms}^{-1}$ for these quality rating 1 and 2 objects from Metcalfe et al. (1989, this value accounts for the difference in c values between the observing runs) $\delta v_z = 112\text{kms}^{-1}$ for the mean r-factor of $r=5.17$ from Figure 4.8. The remaining redshifts (21% of the total) were from emission-line features which are known to give errors $\delta v_z \approx 100$ to150kms^{-1}.

Thus, the conservative estimate of $\delta v_z \approx 120\text{kms}^{-1}$ seems to rule out the suggestion that the 600kms^{-1} estimate for $\langle\omega^2\rangle^{1/2}$ was due to a large measurement error (δv_z needs to be $\sim 400\text{kms}^{-1}$ to reduce $\langle\omega^2\rangle^{1/2}{}_{obs} \approx 600\text{kms}^{-1}$ to $\langle\omega^2\rangle^{1/2}{}_{corr} \approx 200\text{kms}^{-1}$). Just to check this, the direct fits (no infall) to $\xi_v(\sigma,\pi)$ in the Durham/SAAO sample was repeated, but just on the galaxies with better determined absorption-line redshifts (r-factor ≥ 4.0 for the quality rating 1 and 2 galaxies in Metcalfe et al. 1989). At $\sigma < 1h^{-1}$ Mpc $\langle\omega^2\rangle^{1/2} = 630\text{kms}^{-1}$ (123 galaxies) in agreement with the value obtained previously (quality ratings 0,1,2 and 5).

Finally, it may be thought that the larger $\langle\omega^2\rangle^{1/2}$ value of 600kms^{-1} in the Durham/SAAO Survey was biassed by the clusters seen in fields GNX and GSG (see Chapter 3, Section 3.2.1), the line-of-sight dispersions of which were measured to be $\langle v^2\rangle^{1/2} \approx 409$ and 461kms^{-1}, respectively (this translates into pair-wise velocities of $\langle\omega^2\rangle^{1/2} \approx 578$ and 652kms^{-1}). Thus it could be conjectured that these clusters were responsible for raising the estimate of $\langle\omega^2\rangle^{1/2}$ for the whole sample. To test this, the direct fitting to $\xi_v(\sigma,\pi)$ was again
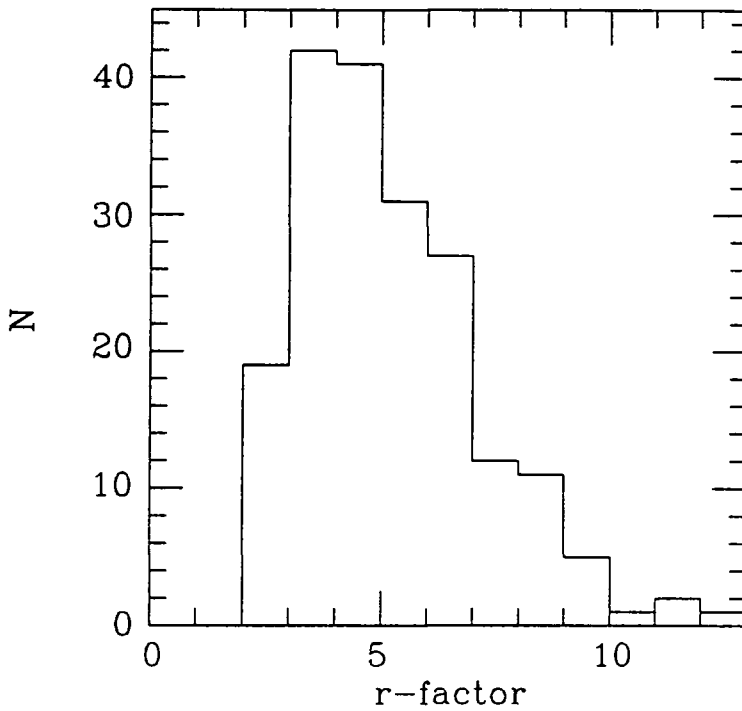
Figure 4.8. The distribution of Tonry and Davis (1979) r-factors for galaxies with absorption-line redshifts in the Durham/SAAO Survey (these galaxies have codes 1 and 2 in Metcalfe et al. 1989). The number of galaxies N with a given r-factor is plotted against r.

repeated on the Durham/SAAO sample with these two cluster fields excluded. The results at $\sigma < 1h^{-1}$ Mpc gave $\langle\omega^2\rangle^{1/2} = 700 kms^{-1}$ (172 galaxies) which again illustrates that this dispersion is a property of the whole sample. Such a conclusion appears also to be supported by the textural differences between the Durham/SAAO and Durham/AAT catalogues as discussed in Section 3.2.1 (Chapter 3).

Thus, in conclusion, it is believed that the range of rms peculiar motions observed in the Durham/SAAO, Durham/AAT and Parker et al. surveys is a result of real (i.e. statistical) fluctuations in these samples. The best estimate of the error on $\langle\omega^2\rangle^{1/2}$ comes from the field-to-field variations but as we have seen these may themselves not fully describe the observed fluctuations seen in the samples as a whole. In contrast to Bean et al. (1983), it is also believed that the static simulations do not provide large enough fluctuations in $\langle\omega^2\rangle^{1/2}$ (the errors in Table 4.7 have been increased by a factor of 2 to take account of this) and this may be improved by increasing the variety of clumps laid down in the simulated volumes, whilst, at the same time, maintaining the form of the two-point correlation function. Some of this could be achieved by increasing the amplitude of the three-point function (by introducing a varying number of levels to the simulated hierarchy; see Section 2.1.4, Chapter 2) from $Q \approx 0.5$ to $Q \approx 0.7$ or by increasing the higher order correlation functions. Certainly, the degree of textural variations between the Durham/AAT and Durham/SAAO surveys seen in Section 3.2.1, would allow for this.

As a final note to this, such variations in the rms peculiar velocities have already been anticipated, to some extent, by Davis and Peebles (1983). They point out that in the Soneira and Peebles (1978) clustering prescription rare rich clumps can make a large contribution to $\langle\omega^2\rangle^{1/2}$ and this may lead to appreciable sampling fluctuations. They conclude from this that for the CfA ($m_B < 14^m.5$) sample (see below) the true error may exceed their estimated internal errors.

Other authors have also found evidence for large sampling fluctuations in the estimates of peculiar motions. For example Peebles (1979) reported a value of $\langle\omega^2\rangle^{1/2} \approx 500 kms^{-1}$ (uncorrected) for the KOS (1978) Survey. Similarly, Efstathiou and Jedrzejewski (1984) find $\langle\omega^2\rangle^{1/2} \approx 540 kms^{-1}$ (uncorrected) for the extension to this work (Kirshner et al. 1983).

Thus, assuming that the variations seen in $\langle\omega^2\rangle^{1/2}$ above are due to sampling fluctuations, the results for the Durham/SAAO, Durham/AAT and Parker et al. surveys are combined according to their relative weight (see the Appendix) in the final column of Table 4.7. The overall errors again assume that the samples are independent. These results are compared to those from the CfA ($m_B<14^m.5$) Survey (Davis and Peebles 1983) in Figure 4.9; here the filled and open symbols are for the non-streaming and streaming estimates of $\langle\omega^2\rangle^{1/2}$. The CfA values were estimated in a similar way to the method described in Section 4.2.1 except that an exponential model (Peebles 1980, p290 equation 76.14) for the distribution of pair-wise peculiar velocities was used (for the estimates see F=0.1 and F=1 values in Table 3 of Davis and Peebles 1983). These results are in good agreement with the preliminary $\langle\omega^2\rangle^{1/2}$ estimates (Davis 1987) from the SSRS Survey of da Costa et al. (1988). At present no details of this work have been formally presented.

From Figure 4.9 it is seen that the overall estimates of $\langle\omega^2\rangle^{1/2}$ in the 17^m surveys agree very well with the CfA values, in spite of possible large sampling fluctuations. De Lapparent et al. (1988) also find a similar peculiar velocity of $\langle\omega^2\rangle^{1/2}=300\text{kms}^{-1}$ applies to their data in the CfA ($m_B<15^m.5$) slices (although they omit the Coma cluster). Unless this is just a coincidence, this would seem to suggest that these samples are tending to be large enough to incorporate the diversity of peculiar motions present in the Universe; i.e. that they are approaching fair samples. This is again encouraging, given the quite different methods of selection for these various catalogues and the local inhomogeneities present in the CfA and SSRS surveys (see Section 3.2.1, Chapter 3). This intimation of fairness will be borne in mind in the following chapter, when discussing estimates of large-scale structure.

As was discussed in Chapter 2 (Section 2.2.2.1) the form of the $\langle\omega^2\rangle^{1/2}$ versus σ relation can provide quite strong constraints on how the mass is distributed around galaxies. This is because galaxies act as test particles moving in the potential of their own (if the mass is held within galaxies) or the underlying (if the mass is a separate component) mass distributions. In Figure 4.9 the dashed line is the overall $\sigma<1h^{-1}$ Mpc estimate of $\langle\omega^2\rangle^{1/2}=(290\pm70)\text{kms}^{-1}$ from the Durham/SAAO, Durham/AAT and Parker et al. surveys. The solid and dotted lines are the predictions from the Cosmic Virial theorem (see Section 2.2.2.1); in the former case this is the model in
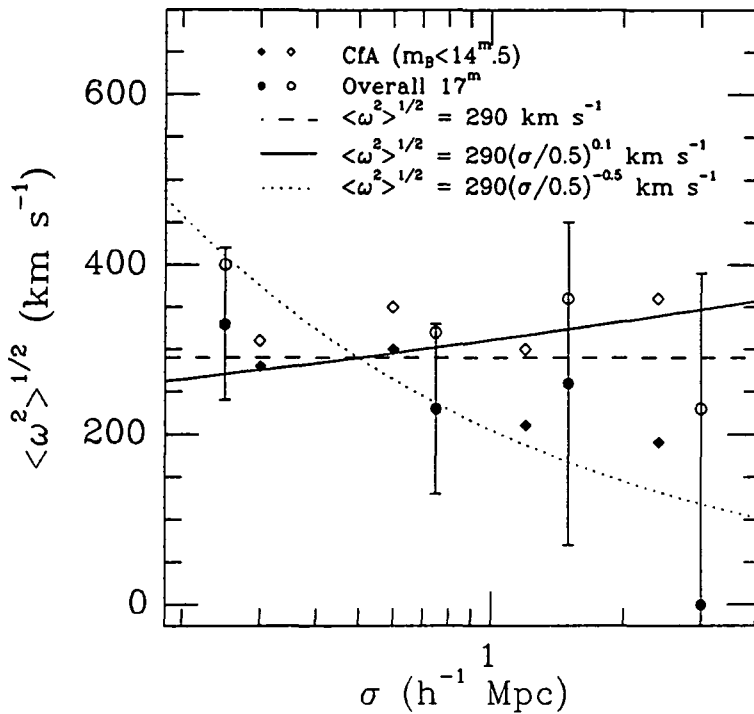
Figure 4.9. Small-scale estimates of the line-of-sight pair-wise peculiar velocity $\langle\omega^2\rangle^{1/2}$ from direct model fits to $\xi_v(\sigma,\pi)$. The open and filled symbols are the direct model fits to $\xi_v(\sigma,\pi)$ that include and exclude infall, respectively. The combined estimates for the Durham/SAAO, Durham/AAT and Parker et al. surveys are shown as circles (with errors on the points that exclude infall). The dashed line represents the overall value of $\langle\omega^2\rangle^{1/2}$ that applies to the 17^m surveys at $\sigma < 1h^{-1}$ Mpc. The solid and dotted lines are the predictions from the Cosmic Virial theorem of Peebes (1976); these are, respectively, the models in which either the collective or two-body interactions dominate the gravitational potential.

which the mass is distributed like the two- and three-point correlation functions (equations 2-90 and 2-105, respectively) and the collective term dominates in equation 2-137 ($\langle\omega^2\rangle^{1/2}\propto\sigma^{0.1}$, equation 2-138 with $\gamma=1.8$). In contrast, the latter is the model in which the two-body term predominates ($\langle\omega^2\rangle^{1/2}\propto\sigma^{-0.5}$ in equation 2-142) and in both cases the models have been normalised so as to give $\langle\omega^2\rangle^{1/2}=290\,kms^{-1}$ at $\sigma=0.5h^{-1}$ Mpc.

It can be see from Figure 4.9 that it is difficult to place constraints on the form of the $\langle\omega^2\rangle^{1/2}$ versus σ relation from the data in the combined 17^m samples. At best, it can be said that the observed $\langle\omega^2\rangle^{1/2}$ is consistent with being constant with separation, as was concluded by Bean et al. (1983) and Bean (1983). The lack of any tighter constraint on this observation is as a result of the larger estimates of error on the peculiar motions. Even with the CfA ($m_B<14^m.5$) data, the claimed rise with separation of $\langle\omega^2\rangle^{1/2}\propto\sigma^{0.13\pm0.04}$ is very sensitive to the inclusion or omission of an infall model to the fit to $\xi_v(\sigma,\pi)$ (see also Figure 6 of Davis and Peebles 1983). Certainly the estimates without infall seem to agree better with $\langle\omega^2\rangle^{1/2}\propto\sigma^{-0.5}$ but the strong up turn of such a model at very small scales may be rejected by the motions close binary pairs (e.g. Turner 1976)

4.4 The mean mass density parameter Ω_o

In the last section it was seen that the combined sample of the Durham/SAAO, Durham/AAT and Parker et al. surveys could not provide much new information on the form of the separation scaling of peculiar motions and, thus, direct tests of the Cosmic Virial Theorem (CVT) assumptions and theory (see Chapter 2, Section 2.2.2.1) could not be performed. This was seen to be a result of the larger peculiar motion variations detected in these surveys which had not previously been predicted by the static simulations of Bean et al. (1983). In what follows now, the normalisation of the CVT is the only parameter that is fixed by the new data and this gives an estimate of the mean mass density of the Universe, with the assumption that galaxies are accurate tracers of the mass distribution.

A brief discussion is now given of what values of the parameters, r_o, $\langle\omega^2\rangle^{1/2}$ and Q, should be adopted for use in the estimate of Ω_o from the various surveys described in this work. As has been seen in Chapter 2 (Section 2.2.2.1) the stability condition of the CVT requires that peculiar

motions have had sufficient time to bring the gravitating system to equilibrium, i.e. that $\langle \omega^2 \rangle^{1/2}/H_0 r \gg 1$. As $\langle \omega^2 \rangle^{1/2} \approx 300 kms^{-1}$ (see Section 4.3.3 above), this condition requires that $r \ll 3h^{-1}$ Mpc. Evidence that such stability occurs at these scales is seen in the dynamic simulations of Efstathiou and Eastwood (1981) and Davis et al. (1985). According to these latter authors, stability is reached at $r \lesssim 0.2h^{-1}$ Mpc (see their Figure 7) in both open ($\Omega_0 < 1$) and closed ($\Omega_0 = 1$) models of the Universe.

In this work, the small-scale ($\sigma < 1h^{-1}$ Mpc) results of Sections 4.1.2, 4.2.2 and 4.3 are considered to be applicable to this analysis. These estimates of r_0 and Q are well determined and avoid the effects of larger scale variations (such as a possible break in $\xi(r)$, see Section 2.1.2.4 of Chapter 2). The values of $\langle \omega^2 \rangle^{1/2}$ are also, of course, less affected by the influence of infall (see Sections 4.2.1 and 4.2.2).

Thus, in the absence of any further evidence which would select the exact form of the CVT to use, the methods of Bean et al. (1983) are followed. This, then, also allows a direct comparison of these results with those obtained previously. In particular, these authors find that for the collective effect CVT model with a finite cut-off in the gravitational potential of $\epsilon = 10h^{-1}$ kpc (see Chapter 2, Section 2.2.2.1)

$$\langle \omega^2 \rangle^{1/2} (\Omega_0 Q r_0^{1.8})^{-1/2} = 234 kms^{-1} \qquad (4\text{-}4)$$

at $\sigma = 0.5h^{-1}$ Mpc (see their Figure 7). Thus assuming that galaxies are accurate tracers of the mass distribution estimates of Ω_0 can be obtained from the measured values of r_0, Q and $\langle \omega^2 \rangle^{1/2}$.

In Section 4.3.1 it was found that at $\sigma < 1h^{-1}$ Mpc, the correlation length in the Durham/SAAO Survey was ($\gamma = 1.8$)

$$r_0 = (5.8 \pm 0.6)h^{-1} \text{ Mpc} \qquad (4\text{-}5)$$

and the corrected pair-wise rms peculiar dispersion was (Section 4.3.3)

$$\langle \omega^2 \rangle^{1/2} = (600 \pm 140) kms^{-1} \qquad (4\text{-}6)$$

along the line-of-sight. Hence, with $Q = 0.48 \pm 0.12$ for the three-point correlation function amplitude (equation 4-1) equations 4-4, 4-5 and 4-6 give

$$\Omega_o = 0.6 \pm 0.2 \qquad (4\text{-}7)$$

However, if the slightly larger value of $Q=0.75\pm0.14$ at $\sigma < 1h^{-1}$ Mpc is adopted

$$\Omega_o = 0.4 \qquad (4\text{-}8)$$

which is lower, but not significantly different from, the above value. Note that the error in equation 4-7 was obtained by assuming that the parameters r_o, Q and $\langle\omega^2\rangle^{1/2}$ are all independent from each other. For comparison, using the estimates of $r_o=(4.5\pm0.4)h^{-1}$ Mpc, $Q=0.60\pm0.06$ and $\langle\omega^2\rangle^{1/2}=(190\pm90)kms^{-1}$ quoted for the Durham/AAT Survey in the previous section at $\sigma < 1h^{-1}$ Mpc

$$\Omega_o = 0.1 \pm 0.1 \qquad (4\text{-}9)$$

which is in agreement with the Bean et al. (1983) value of $\Omega_o=0.14^{+0.28}_{-0.07}$. The Parker et al. Survey, on the other hand, measures $\Omega_o \approx 0$, since the corrected peculiar velocity for this sample is $\langle\omega^2\rangle^{1/2}\approx 0 kms^{-1}$ (Section 4.3.3).

As with estimates of the rms peculiar motions there appears to be quite a wide variation in the estimates of the density parameter. However, as discussed in the previous section, this variation in the peculiar motions is believed to be a sampling effect and this carries through to the estimates of Ω_o here. This is because $\Omega_o \propto (\langle\omega^2\rangle^{1/2})^2$ and this leads to a strong dependence of Ω_o on $\langle\omega^2\rangle^{1/2}$ both in magnitude and error. This is in contrast to Bean et al. (1983) who claimed that their strongest source of error in Ω_o was in their estimate of the amplitude Q which they believed to be uncertain by a factor of 2 (see above). However, as pointed out by Bean (1983), the internal (i.e. bin-to-bin) error in Q is a reasonable measure of the fluctuations in this parameter (as seen from the simulated catalogues) and this is supported by the apparently stable values of this quantity that are estimated from different redshift samples in this and other works (see Section 4.3.2 above).

Finally, for the Durham/SAAO, Durham/AAT and Parker et al. surveys together it was found that

$$r_o = (4.5 \pm 0.3)h^{-1} \text{ Mpc} \qquad (4\text{-}10)$$

and

$$\langle\omega^2\rangle^{1/2} = (290\pm70)\text{kms}^{-1} \qquad\qquad (4\text{-}11)$$

at $\sigma<1\text{h}^{-1}$ Mpc. With a mean value of $Q=0.58\pm0.05$ for the Durham surveys, this implies

$$\Omega_0 = 0.18\pm0.09 \qquad\qquad (4\text{-}12)$$

or if $Q=0.62\pm0.06$ (with $Q=0.75\pm0.14$ for the Durham/SAAO sample)

$$\Omega_0 = 0.17 \qquad\qquad (4\text{-}13)$$

Again the error in equation 4-12 was obtained by assuming independence of the various parameters.

For comparison with these overall values, using the $\sigma<1\text{h}^{-1}$ Mpc estimates of $r_0=5.0\text{h}^{-1}$ Mpc, $\langle\omega^2\rangle^{1/2}=290\text{kms}^{-1}$ and $Q=0.8$ quoted for the CfA $(m_B<14^m.5)$ Survey in the previous section, the density parameter is found to be $\Omega_0=0.11$ in good agreement with the overall values deduced above. This also concurs with the Davis and Peebles (1983) estimate of $\Omega_0=0.14^{+0.3}_{-0.1}$ using similar methods.

Hence, unless the agreement between these various observations is just a coincidence, it seems to suggest that, overall, the combined sample in this work and the CfA Survey may be approaching reasonably representative volumes, in spite of the larger variations in the peculiar motions observed from sample-to-sample. However, the constraint on Ω_0 (assuming that galaxies are tracers of the mass distribution) is similar to that obtained previously by Bean et al. and Davis and Peebles because of the larger sampling errors found.

4.5 Discussion

The above estimate of $\Omega_o \approx 0.18 \pm 0.09$ for the combined sample used in this work seems to suggest that favoured models of the Universe with $\Omega_o = 1$ are ruled out by about 9 s.d. It may be thought that this situation could be alleviated somewhat by the inclusion of an infall model in the analysis as this will tend to raise the estimates of $\langle \omega^2 \rangle^{1/2}$ and lower those of r_o, thus increasing the estimated Ω_o (see equation 4-4). However, as seen in Sections 4.3.2 and 4.3.3, incorporating such a high density streaming motion model into the fits to $\xi_v(\sigma,\pi)$ does little to change these parameters at this separation. Alternatively, it may be thought that this particular form of the CVT model is not applicable, but again, according to Bean et al. (1983), there is only ~40% variations in Ω_o using quite different assumptions (see, again, their Figure 7).

As has been suggested in the introduction to Section 2.2, the approach to reconciliation of equation 4-12 with $\Omega_o=1$ models is to assume that galaxies are biassed tracers of the mass distribution. However, this bias must not contradict the observation that the $\langle \omega^2 \rangle^{1/2}$ versus σ scaling relation is consistent with being constant or slowly rising, and so the approach (e.g. Davis et al. 1985) has been to assume that the matter and galaxy correlations differ by some simple normalisation factor (see equations 2-131 and 2-141). However, it is not clear that the same biassing mechanism will apply at all scales since, for example, there is no a priori reason why biassing in the linear ($\delta\rho/\rho_b < 1$) and non-linear ($\delta\rho/\rho_b > 1$) regimes should operate in the same way. From the analysis above, if all the bias was in the two-point function and, as in equations 2-131 and 2-141, $\xi^g = b^2 \xi^m$ then equation 4-4 implies that $b = (\Omega_o/\Omega_o^{eff})^{1/2}$. Here, Ω_o^{eff} is again the Ω_o estimated by assuming galaxies trace the mass (c.f. equations 2-118 and 2-136), whereas Ω_o is the true density parameter. In this case equation 4-12 would imply for $\Omega_o=1$ that $b \approx 2.4$.

This value of the bias is similar to that used to obtain 'realistic' models of the galaxy distribution from Cold Dark Matter particles with $\Omega_o=1$ (Davis et al. 1985, White et al. 1987 and Lilje and Efstathiou 1989). The latter authors find that in the linear regime the bias factor is $b=2.05 \pm 0.05$ similar to the above value. However, the value of Ω_o^{eff} obtained above is measured at $\xi^g \approx 15$ ($r \approx 1h^{-1}$ Mpc, $r_o \approx 4.5h^{-1}$ Mpc) which implies, with $b \approx 2.4$ that $\xi^m \approx 3$. Clearly, this is approaching the non-linear regime where the thresholding that

gives $\xi^g = b^2 \xi^m$ in the CDM simulations is going to start to break down. In any case Ω_0 in equation 4-4 depends not only on r_0, but also on the three-point amplitude Q. In the simulations of Davis et al. (1985) Q appears to be biassed to slightly **lower** values (Q decreases by about 20%) and this **increases b** to around b≈2.7 at this scale.

Clearly, an important consideration for future observations of galaxy peculiar motions is the measurement of the bias (i.e. Ω_0^{eff}) relative to the mass as a function of scale as this will help to constrain models of galaxy clustering in which such mechanisms operate. As will be seen in the next chapter biassing may be an important factor in our understanding of large-scale structure and the formation of galaxies.

Chapter 5

Galaxy correlation analysis at scales $\geq 1 h^{-1}$ Mpc

Galaxies are the most numerous and most identifiable tracers of large-scale structures in the Universe and, as such, observations of their spatial distribution may provide significant insight into the processes of the formation and evolution of large-scale mass fluctuations. Observations of the second moment of this distribution have already motivated much study of the physical processes involved in the evolution of large-scale structure. Since estimates of $\xi(r)$ at separations $r \leq 10 h^{-1}$ Mpc indicate density contrasts to be greater than or of the order of unity, this would seem to imply that, at these scales, the second moment is directly measuring the formation properties of galaxies themselves (as galaxies have, of course, $\delta\rho/\rho_b \gg 1$). For example, early observation of $\xi(r)$ suggested that there were no preferred cluster sizes in the galaxy distribution at these separations and this has led to a series of studies of evolutionary models which mimic this observation (Peebles 1974, Efstathiou and Eastwood 1981, Davis et al. 1985)

At larger scales, where the density contrasts are small ($\delta\rho/\rho_b \ll 1$), galaxies may trace, and accurately constrain, the largest scale inhomogeneities in the mass density of the Universe. Since, under the influence of gravity, low density contrast fluctuations grow in a linear way (see Chapter 2, Section 2.2) these large-scale inhomogeneities may contain the initial imprint of fluctuations from a very early epoch in the history of the Universe. Thus, such observations will provide vital information concerning the progenitors of the large-scale structures we see today.

It is again emphasised that, in this work, mean properties of the galaxy distribution are being sought, and it is hoped that the samples from which such observations are made, are reasonably representative of the Universe as a whole. In this chapter the visual impressions of large-scale structure discussed in Chapter 3 are investigated more thoroughly, using, primarily, the redshift correlation function $\xi_s(s)$, (Sections 5.1 and 5.2). An important part of this study is to use the peculiar motion observations of Chapter 4 to better constrain the spatial correlation function $\xi(r)$. The results obtained from the

surveys described in this work are then compared to similar analyses of other redshift samples and to other measures of large-scale structure.

Finally, in Section 5.3 the observations of large-scale structure made in this chapter are then discussed with relevance to evolutionary models of the mass distribution. A key issue in this is whether spatial galaxy correlation function $\xi(r)$ has been correctly extracted from estimates of the redshift function $\xi_s(s)$ and what relation $\xi(r)$ has to that of the mass. Some discussion of future methods for dealing with these uncertainties are given.

5.1 Galaxy clustering at scales $\leq 10\ h^{-1}$ Mpc

In the previous chapter it was seen how peculiar motions distort estimates of galaxy clustering in redshift space making the two-point correlation estimator ξ_v a function of two variables, σ and π; the separations perpendicular and parallel to the line-of-sight, respectively. In this section, and the next, the direction-averaged correlation estimator, $\xi_s(s)$, is considered and, since it is a function of one variable, it has the advantage over $\xi_v(\sigma,\pi)$ of better signal-to-noise. Further, since the redshift separation s will approach the true spatial separation r, in the limit that $r \gg |v_p|/H_o$, where $|v_p|$ is a measure of the inherent peculiar velocities, then $\xi_s(s)$ will in the same limit approach the spatial function $\xi(s)$, i.e. $\xi(r)$ (see Chapter 2, Section 2.1.2.2).

In these two sections the approach to studying $\xi(r)$ is to model estimates of redshift function $\xi_s(s)$ (see Chapter 2, Section 2.1.2.2) using the parameters for peculiar motion obtained from the estimates of $\xi_v(\sigma,\pi)$ in the previous chapter. As will be seen this iterative procedure is very profitable as it leads to a better determination and understanding of the distortions in $\xi_s(s)$ and hence better estimates of the true spatial clustering.

5.1.1 Observations of $\xi_s(s)$ at $s \le 10h^{-1}$ Mpc

Prior to presenting details of the observed redshift correlation functions in the Durham/SAAO and Parker et al. surveys, the model for $\xi_s(s)$ described in Chapter 2 (equation 2-34) is discussed in more detail. Firstly, in Figure 5.1, the solid line is the numerically integrated form for $\xi_s(s)$ from equation 2-34 with the random peculiar motion model for $\xi_v(\sigma,\pi)$, as in equation 2-31. The distribution function for these pair-wise motions is again the $\exp(-C|\omega|^{3/2})$ form of equation 2-122 with $\langle\omega^2\rangle^{1/2}$ set to the observed mean value of ~300kms^{-1} at $\sigma < 1h^{-1}$ Mpc taken from the previous chapter (equation 4-11). The spatial correlation function $\xi(r)$ is, again, a single power law of the form $\xi(r)=(r_o/r)^\gamma$ with $\gamma=1.8$ (dotted line, assuming s=r) and r_o is set to the mean value of 4.5 h^{-1} Mpc also obtained in Chapter 4 (equation 4-10).

As can be seen from this figure, random peculiar motions tilt the power law to lower values of $\xi_s(s)$ at separations $s \le 3$ h^{-1} Mpc making the slope in the log $\xi_s(s)$ versus log s plane shallower than -1.8 at these separations (Bean 1983). At larger scales $\xi_s(s)$ is very close to the true spatial power law; the slight rise above the dotted line in the figure at between 3 and 10 h^{-1} Mpc is consistent with equation 2-31 (and, thus, 2-34) being a convolution (i.e. pairs of galaxies are conserved). Also shown in this figure are similar models to the solid line but with $\langle\omega^2\rangle^{1/2}$=200kms^{-1} (dashed line) and $\langle\omega^2\rangle^{1/2}$=600kms^{-1} (dot-dash line). From these different dispersions it is seen that the tilt in the power-law below 3h^{-1} Mpc increases as $\langle\omega^2\rangle^{1/2}$ increases but the correlation function $\xi_s(s)$ at larger scales remains virtually the same as the spatial power-law $\xi(r)$.

These results would seem to suggest that, although there is observed to be quite a wide variation in the estimates of $\langle\omega^2\rangle^{1/2}$ from sample-to-sample (see Chapter 4, Section 4.3.3), the redshift correlation function $\xi_s(s)$ will be quite stable at separations $s \ge 3h^{-1}$ Mpc, at least when the spatial correlation function is a single power law. This seems quite encouraging for the determination of $\xi(r)$ from $\xi_s(s)$ but it does not, however, take into account the narrow shape of the fields in the surveys discussed here. As shown in Chapter 2 (Section 2.1.2.2) not all the pairs in the spherical shell at separation s are available for the average indicated in equation 2-34. In this case $\xi_s(s)$ is preferentially weighted to the π rather than the σ direction and this may make the distortion for this function more like that observed in $\xi_v(\sigma,\pi)$ at small σ
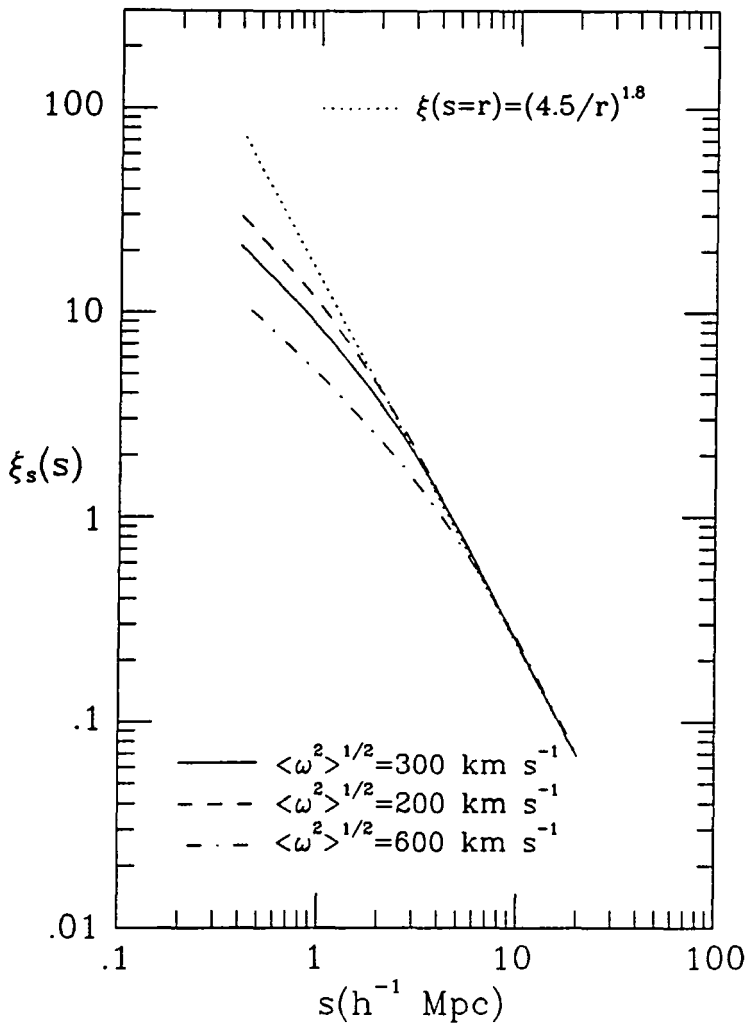
Figure 5.1. Models for the redshift correlation function $\xi_s(s)$. Each model is based on equation 2-34 and convolves the power-law correlation function $\xi(r)$ of clustering length $r_0=4.5h^{-1}$ Mpc (dotted line) with line-of-sight rms peculiar velocity dispersions of $\langle \omega^2 \rangle^{1/2}=200 \text{kms}^{-1}$ (dashed line), 300kms^{-1} (solid line) and 600kms^{-1} (dot-dash line).

(Peebles 1989).

As discussed in Chapter 2 (Section 2.1.2.2) a suitable approach to the modelling of $\xi_s(s)$ is through the static hierarchical simulations. The advantage here is that complicated numerical integrals involving field shape and selection function can be handled indirectly and so this avoids the necessity of making simplifying assumptions in the model. In Figure 5.2 the $\xi_s(s)$ estimated from the simulations with $\langle\omega^2\rangle^{1/2}=350\mathrm{kms}^{-1}$ (filled circles) is compared to the spatial form of $\xi(r)$ (open circles) shown in Figure 2.5. As with the approximate models for $\xi_s(s)$ discussed above, this figure again shows that $\xi_s(s)$ is fairly stable between $2\leq s\leq 6\mathrm{h}^{-1}$ Mpc although at larger separations there does appear to be some increase in $\xi_s(s)$ beyond the scale at which $\xi(r)$ exhibits a break in its power law. The apparent amplification in $\xi_s(s)$ between $2\leq s\leq 6\mathrm{h}^{-1}$ Mpc is <20% and this is much smaller than the 50% claimed by Peebles (1989). To compare with these simulations, the solid line in this figure is the model for $\xi_s(s)$ from equation 2-34 with $\langle\omega^2\rangle^{1/2}=350\mathrm{kms}^{-1}$ and $\xi(r)$ based on a three power law approximation (dashed line) to the spatial form of $\xi(r)$ in the simulations (open circles). This model again seems to slightly underestimate the observed $\xi_s(s)$ beyond the break scale but is a reasonable approximation otherwise.

Turning now to the observations of $\xi_s(s)$, in Figures 5.3 and 5.4 (solid circles) are the within-field estimates of this function from the Durham/SAAO and Parker et al. surveys, respectively. These values of $\xi_s(s)$ have been obtained from the straight pair counts DD(s) and DR(s) in bins of 0.1 in $\log_{10} s$ using the methods outlined in Chapter 2 (Section 2.1.2.1, see equation 2-27), and the results in these figures beyond $\sim 10\mathrm{h}^{-1}$ Mpc are not shown. To generate catalogues of random positions for the pair count DR(s), the method described in Section 4.1.2. was used. Again, the homogeneous number density n(z) was normalised to the numbers in each survey (Chapter 3, Section 3.2.3) using the appropriate Schechter parameters (equation 3-6). Here, $N_R/N_G=300$ for the Durham/SAAO Survey and 450 for the Parker et al. sample. The errors in these figures are from the catalogues of simulations and these are well backed up, in the Durham/SAAO sample, by field-to-field fluctuations (see Chapter 3, Section 3.1.1) and variations from north and south subsamples (shown as open symbols in Figure 5.3). For a direct inter-comparison of these results and that obtained previously from Shanks et al. (1983, see Figure 5.5), Figure 5.6 shows the Durham/SAAO, Parker et al.
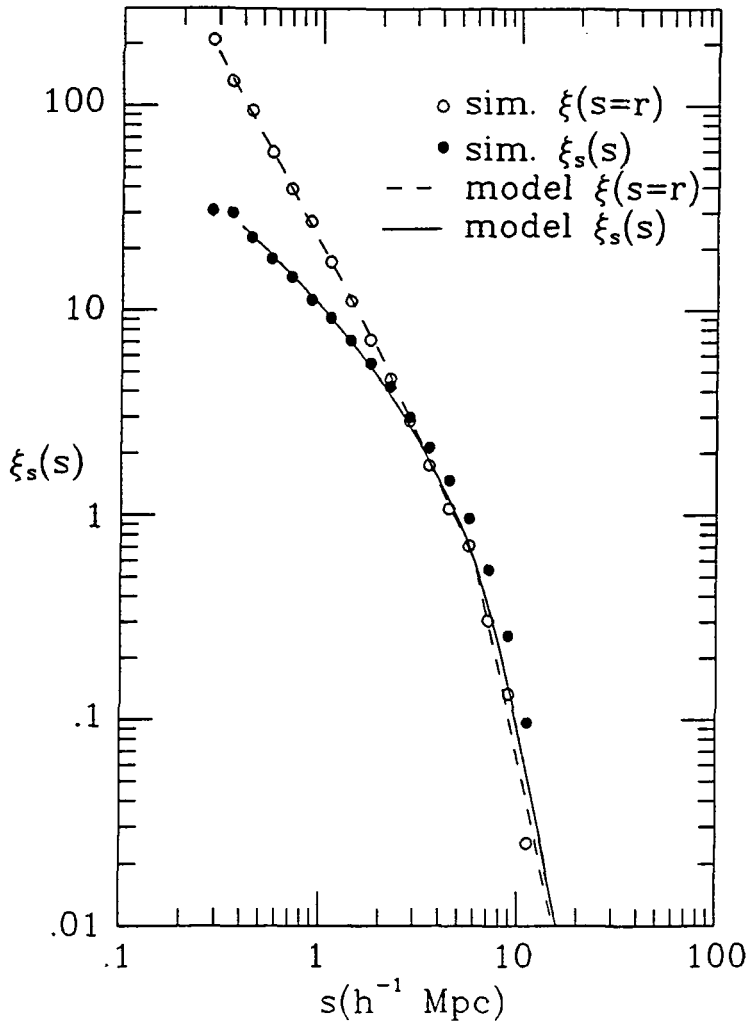
Figure 5.2. The spatial and redshift correlation functions for the simulations of the Durham/SAAO and Durham/AAT surveys. The solid and open circles are the mean estimates of $\xi_s(s)$ and $\xi(r)$, respectively, from the 20 catalogues of simulations of the Durham/SAAO and Durham/AAT surveys. The solid line convolves the dashed line (a three power-law fit to the observed form of $\xi(r)$) with an rms peculiar velocity dispersion of 350kms^{-1} using the model for $\xi_s(s)$ in equations 2-34 and 2-31.
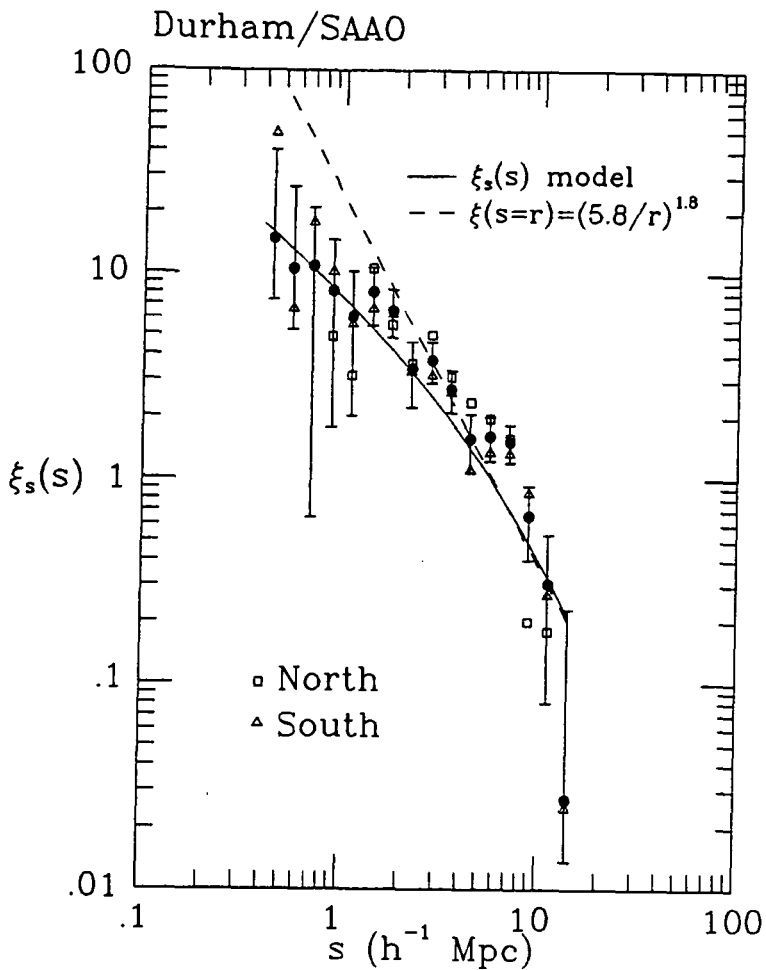
Figure 5.3. The small-scale redshift two-point correlation function $\xi_s(s)$ estimated from the Durham/SAAO Survey. The estimates from this sample (with errors) are indicated as solid symbols. Variations between the north and south subsamples are shown as open symbols. The solid line convolves the dashed power-law $\xi(r)$ with an rms peculiar velocity dispersion of 620kms[-1].

Parker et al.

$\xi(s=r)=(2.6/s)^{1.8}$

$\xi_s(s)$

s $(h^{-1}$ Mpc$)$
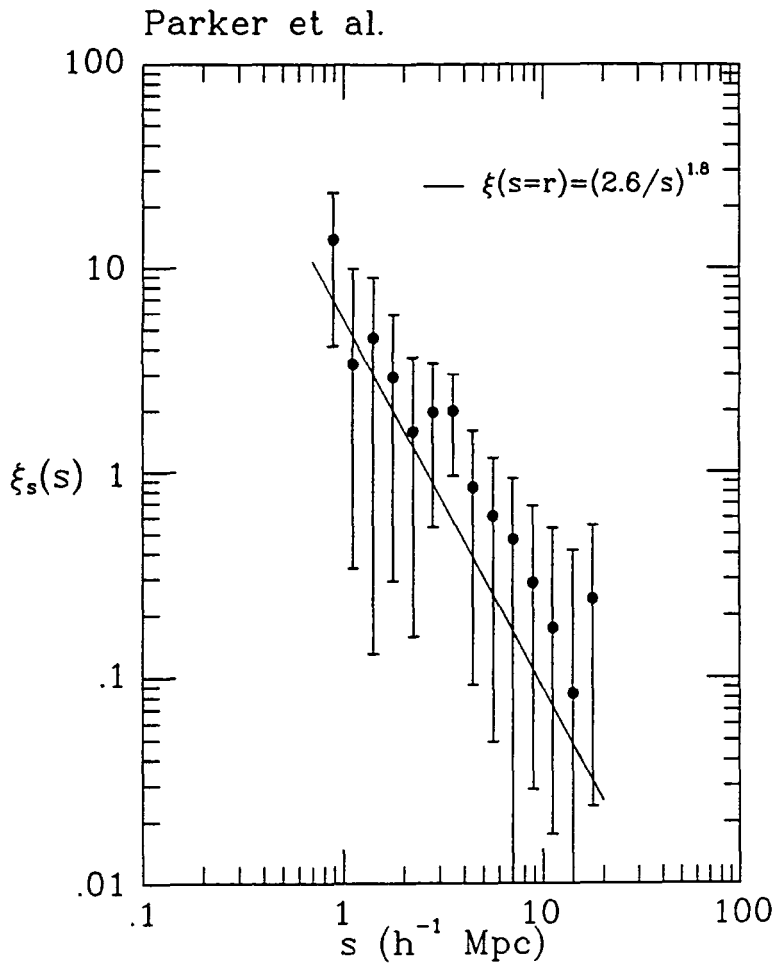
Figure 5.4. The small-scale redshift two-point correlation function $\xi_s(s)$ estimated from the Parker et al. Survey. The solid line is the power-law $\xi(r)$ indicated.
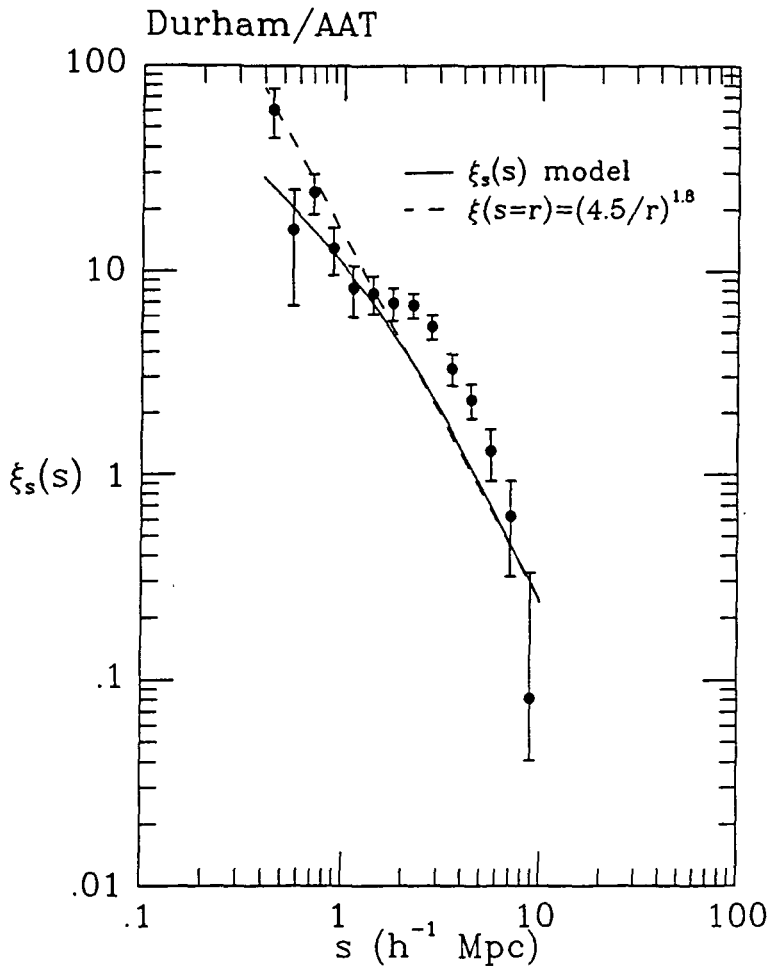
Figure 5.5. The small-scale redshift two-point correlation function $\xi_s(s)$ estimated from the Durham/AAT Survey (see Shanks et al. 1983). The solid line convolves the dashed power-law $\xi(r)$ with an rms peculiar velocity dispersion of 210kms^{-1}.
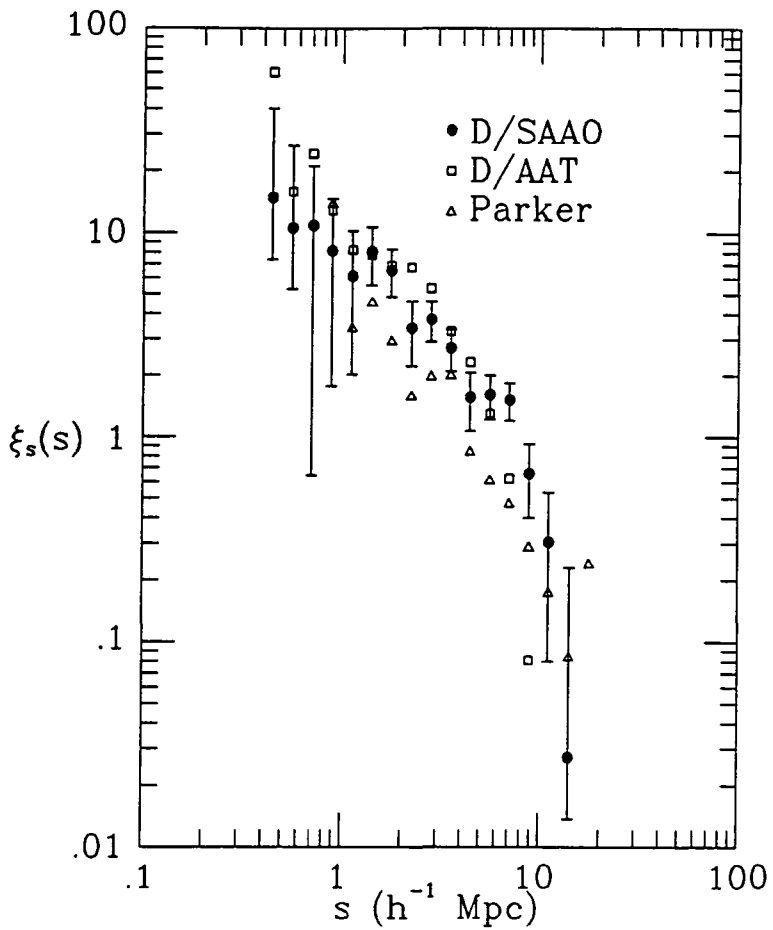
Figure 5.6. The small-scale redshift two-point correlation function $\xi_s(s)$ estimated from the Durham/SAAO, Parker et al. and Durham/AAT surveys. The points shown here are the same as in Figures 5.3, 5.4 and 5.5 above (the errors are for the Durham/SAAO estimates).

and Durham/AAT surveys together. As can be seen the level of agreement between these samples is excellent; the result between $1 \leq s \leq 7h^{-1}$ Mpc appears to be very stable, as was anticipated above.

To study these observations in more detail, in Figure 5.3 the estimates of $\xi_s(s)$ from the Durham/SAAO Survey are compared to the $\xi_s(s)$ model of equation 2-34. As above, this model (solid line) convolves a power law of the form $\xi(r)=(r_0/r)^{1.8}$ (dashed line, assuming s=r) with the random peculiar velocity distribution of equation 2-122. Here the parameters of $r_0=5.8h^{-1}$ Mpc and $\langle\omega^2\rangle^{1/2}=620kms^{-1}$ are taken from the $\sigma<1h^{-1}$ Mpc direct fits to $\xi_v(\sigma,\pi)$ in Chapter 4 (Section 4.2.2, Table 4.4). As is seen, the model accurately predicts the form of $\xi_s(s)$ below $s \leq 1h^{-1}$ Mpc and this shows good self-consistency of the models and methods. However, at larger scales the observed $\xi_s(s)$ appears to rise above this model, with the data consistently giving a larger value for r_0 in the range $1 \leq s \leq 10$ h^{-1} Mpc. From the observed $\xi_s(s)$ in the range $2 \leq s \leq 7h^{-1}$ Mpc it is found that $r_0=(7.1\pm0.8)h^{-1}$ Mpc where the estimate and error (from the simulations) comes from a large bin over this range.

In Figures 5.4 and 5.5 similar models for $\xi_s(s)$ are compared to the observations in the Parker et al. and Durham/AAT surveys, with the parameters r_0 and $\langle\omega^2\rangle^{1/2}$ also taken from the $\xi_v(\sigma,\pi)$ analysis of Chapter 4, Section 4.2.2 (here $r_0=2.6h^{-1}$ Mpc and $\langle\omega^2\rangle^{1/2}=50kms^{-1}$ for the former and $r_0=4.5h^{-1}$ Mpc and $\langle\omega^2\rangle^{1/2}=210kms^{-1}$ for the latter). These data again show good self-consistency between the predictions and observations at $s \leq 1-2h^{-1}$ Mpc, as expected. The somewhat wider variation in the estimates of $\xi_s(s)$ at these scales for the 3 surveys (see Figure 5.6) is due primarily to the variations observed in $\langle\omega^2\rangle^{1/2}$. However, as discussed in the previous chapter (Section 4.3.3) such variations are believed to be consistent with sampling fluctuations.

As with the Durham/SAAO sample, these data are again showing clear evidence for an enhanced amplitude in $\xi_s(s)$ between $2 \leq s \leq 7h^{-1}$ Mpc. As above, by estimating $\xi_s(s)$ for a large bin in s ($2 \leq s \leq 7h^{-1}$ Mpc), it is found that $r_0=(4.4\pm1.1)h^{-1}$ Mpc and $r_0=(7.1\pm0.8)h^{-1}$ Mpc for the Parker et al. and Durham/AAT surveys, respectively, and these values are in good agreement with the $r_0=(7.1\pm0.8)h^{-1}$ Mpc for the Durham/SAAO sample above for the same range in s. The errors are again from the simulations. This non-unique

power law behaviour, referred to as a shoulder in $\xi_s(s)$, has been previously noted by Bean (1983) and Shanks et al. (1983). From the discussion above, and in contrast to the claim by Peebles (1989), this feature is not believed to be caused by the combined effect of random peculiar motions and narrow field shape, since the spatial and redshift correlation functions differ little in this region of separation (see Figure 5.2). However, it remains a possibility that the enhanced amplitude is caused by infall (see Section 5.1.3 below).

Assuming that the Durham/SAAO, Durham/AAT and Parker et al. samples are independent and that the variations seen in Figure 5.6 are statistical, Figure 5.7 shows the average estimate of $\xi_s(s)$ for these surveys obtained by weighting the individual sample values according to their error at each point (see the Appendix). The overall errors are the combined estimates of the simulated errors for each survey assuming statistical independence. The solid model line in this case is the convolution of the distribution of peculiar velocities with $\langle\omega^2\rangle^{1/2}=310$ kms^{-1} with a power-law $\xi(r)$ with $r_0=4.5h^{-1}$ Mpc (dashed line). Again these parameter values are the combined estimates from the $\sigma<1h^{-1}$ Mpc $\xi_v(\sigma,\pi)$ analysis of the previous chapter (see Tables 4.6 and 4.7). In spite of obtaining an excellent match to the estimates of $\xi_s(s)$ at $s\lesssim 1h^{-1}Mpc$ for the respective samples (Figures 5.3, 5.4 and 5.5) this model is a poorer fit to this data at these separations, and this may be caused by better determined results for the correlation function in the Durham/AAT Survey at the smallest separations.

The overall estimate of $\xi_s(s)$ in Figure 5.7 indicates that the correlation function is, now, very well determined as was implied by the high level of agreement between the various surveys in Figure 5.6 and the division into north and south galactic hemispherical parts (Figure 5.3, see also Figure 6.3 of Bean 1983). As with the individual correlation function observations, the solid model line underestimates the data at all points between $2\lesssim s\lesssim 7h^{-1}$ Mpc. Thus, taking the values of r_0 estimated for this range of s above it is found that, overall, $r_0=(6.6\pm0.5)h^{-1}$ Mpc and this clustering length is indicated in the dotted line in Figure 5.7. As can be seen from this figure, this model is a good match to the observations where the enhanced amplitude is seen.

This shoulder feature observed in $\xi_s(s)$ seems to exclude the possibility that $\xi(r)$ is a continuous power law, on the assumption that peculiar motions do not distort $\xi_s(s)$ from $\xi(r)$ at s $\geq 3h^{-1}$ Mpc. If the small-scale (s $\leq h^{-1}$ Mpc)
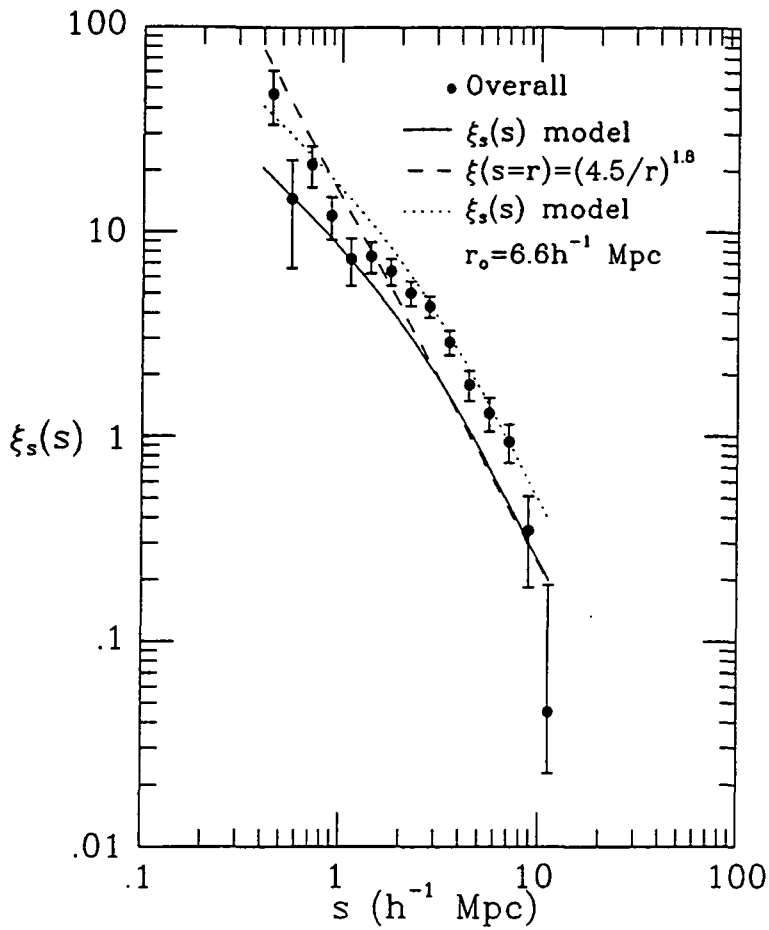
Figure 5.7. The overall small-scale redshift two-point correlation function $\xi_s(s)$ estimated from the combined 17m surveys. The solid line convolves the dashed power-law $\xi(r)$ with an rms peculiar velocity dispersion of 310kms[-1]. The dotted model is the same model but with $r_0 = 6.6h^{-1}$ Mpc.

correlation function has a clustering length of $r_0=4.5h^{-1}$ Mpc, as suggested by the data in this work, then the continuation of this power law to separations $2 \leq s \leq 7h^{-1}$ Mpc is rejected at the 4.2 sigma level, according to the above estimate of $r_0=(6.6\pm0.5)h^{-1}$ Mpc of the shoulder from the combined sample in this work. If r_0 at $s \leq 1h^{-1}$ Mpc is as high as $5h^{-1}$ Mpc, as perhaps allowed by sampling fluctuations, then the rejection is at the 3.2 sigma level. However, as mentioned above, it remains a possibility that the enhanced amplitude is caused by infall, and this is discussed below (Section 5.1.3).

At separations larger than $\sim 7h^{-1}$ Mpc, $\xi_s(s)$ in Figure 5.7 appears to show a further deviation from its behaviour in the region $2 \leq s \leq 7h^{-1}$ Mpc with the data decreasing more rapidly than a continuation of the -1.8 power law with $r_0 \approx 6.6h^{-1}$ Mpc. This 'break' in $\xi_s(s)$, although positionally uncertain, appears to occur in both the Durham samples (Figure 5.6) and is similar to the break expected from observation of $\omega(\theta)$ (see Chapter 2, Section 2.1.2.4). However, this larger-scale form of $\xi_s(s)$ will be discussed in more detail in the following section and there direct comparisons will be made with the observations of $\omega(\theta)$.

Finally, some observations of the dependence of galaxy clustering on luminosity are presented here as this is very relevant to possible mechanisms of biassing in the formation of galaxies. In Figure 5.8 are the estimates of $\xi_s(s)$ for the combined sample of the Durham/SAAO and Durham/AAT surveys divided into two regimes of absolute luminosity; galaxies with absolute magnitudes M brighter than the Schechter parameter M^* are shown as filled circles, those fainter than M^* as open circles. These estimates were obtained in a similar way to that above except for the limits placed on M calculated from equation 2-6 (q_0 term omitted). This requires an alteration to the background density model n(z) (equation 2-11) as follows;

Durham/SAAO and Durham/AAT
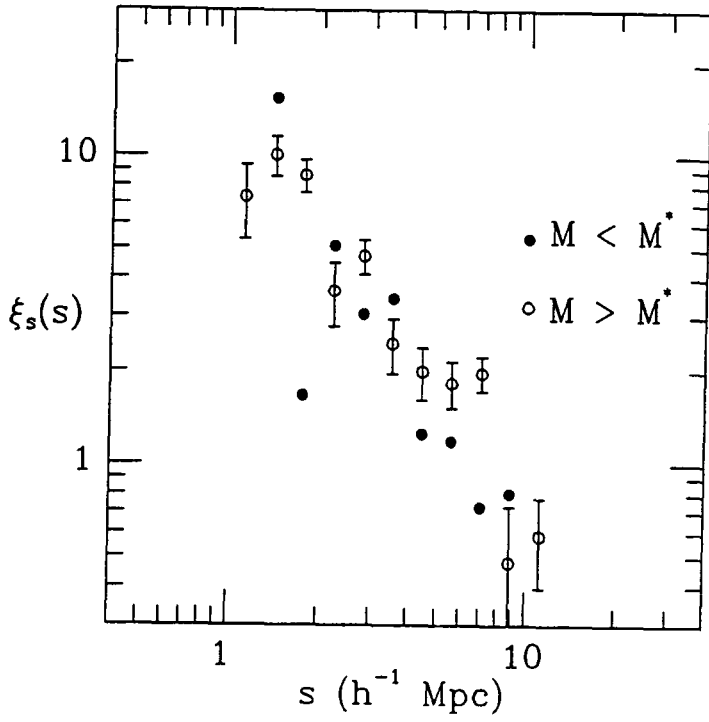
Figure 5.8. The small-scale redshift two-point correlation function $\xi_s(s)$ for the intrinsically bright (M<M*) and faint (M>M*) galaxies in the combined sample of the Durham/SAAO and Durham/AAT samples. Here M* refers to the Schechter parameter estimated for the individual surveys (equation 3-6, Section 3.2.2, Chapter 3). The error estimates are shown for the faint galaxy correlation function.

$$n(z) = \int_{-\infty}^{M_{max}(z)} \phi(M)dM \quad M_{max}(z) \leq M*$$

M≤M*

$$n(z) = \int_{-\infty}^{M*} \phi(M)dM \quad M_{max}(z) > M*$$

$$(5\text{-}1)$$

$$n(z) = 0 \quad M_{max}(z) \leq M*$$

M>M*

$$n(z) = \int_{M*}^{M_{max}(z)} \phi(M)dM \quad M_{max}(z) > M*$$

where $M_{max}(z)$ is the limit on the observable absolute magnitude at redshift z (equation 2-7). Separate catalogues of random points were then generated in the way described above for the Durham/SAAO Survey in Chapter 3, Section 3.2.3, both for the two surveys and for the two regimes (i.e. 4 in all). The parameter M* was again the value appropriate to each survey with α=-1 (equation 3-6) and the model for n(z) was normalised to the numbers observed in each of the 4 sub-samples. To combine the data from the two surveys a simple approach of co-adding the DD(s) and DR(s) pairs from each of the surveys was adopted with each galaxy in the Durham/AAT Survey given a weight of 1/3 (i.e. 1/9 for a pair; this is a similar approach to third sampling the Durham/AAT Survey, see Section 5.2.1 below).

To check equations 5-1 above, Figure 5.9 (a) to (d) shows the observed $\Delta N(z)$ data and fits using the truncated forms of n(z) in both the Durham/SAAO and Durham/AAT surveys. These figures show that there are no serious discrepancies between the observed and predicted $\Delta N(z)$ distributions and so the estimates of $\xi_s(s)$ will be reasonably representative.

Thus, turning to the observations in Figure 5.8, it is clear that, in this combined sample of 247 bright and 259 faint galaxies, $\xi_s(s)$ is not a strong function of absolute magnitude although there is some hint that the brighter sample estimates have a steeper power law. The representative errors on the faint galaxy estimates (based on the ratio of pair counts observed here in each bin to those obtained in the entire, bright and faint, samples) indicate that an increase, for example, in the amplitude (r_0^{γ}) of the correlation function of about a factor of 2 or more would probably be detected in this data. Hamilton (1988) finds some evidence in the CfA ($m_B < 14^m.5$) Survey for an increase of this order but the statistical significance again seems low (see his

Figure 5.9. The observed $\Delta N(v)$ distributions for the intrinsically bright (M<M*) and faint (M>M*) galaxies in the Durham/SAAO and Durham/AAT surveys. The histograms and dashed lines are, respectively, the observed and model counts as a function of redshift velocity v.

(a) Durham/SAAO M>M*
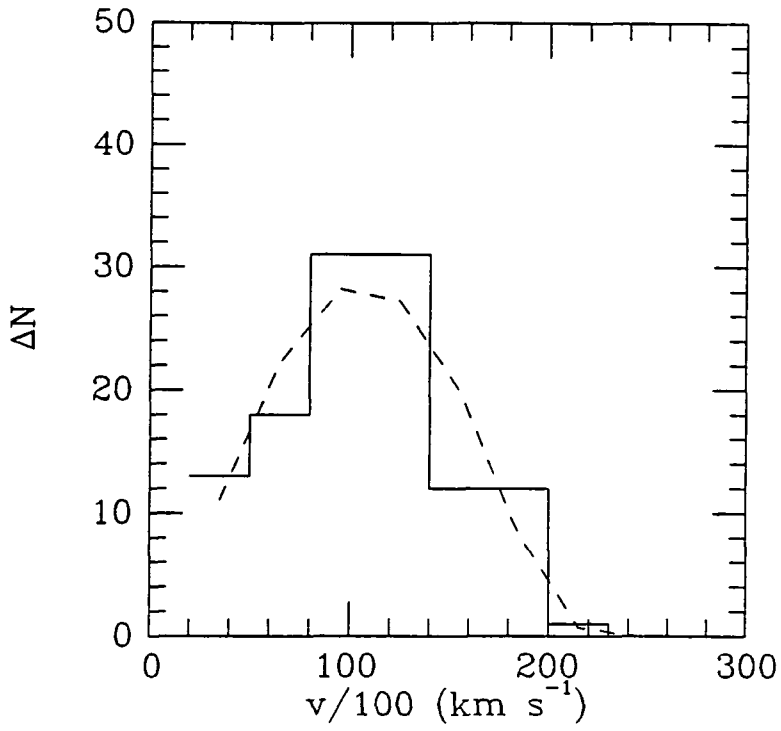
(b) Durham/SAAO M<M*
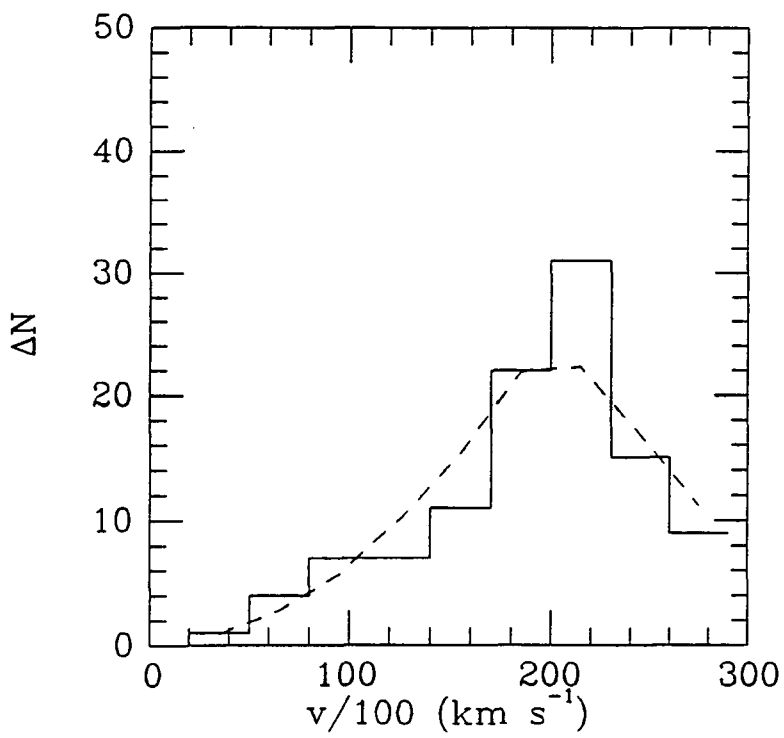
(c) Durham/AAT M>M*
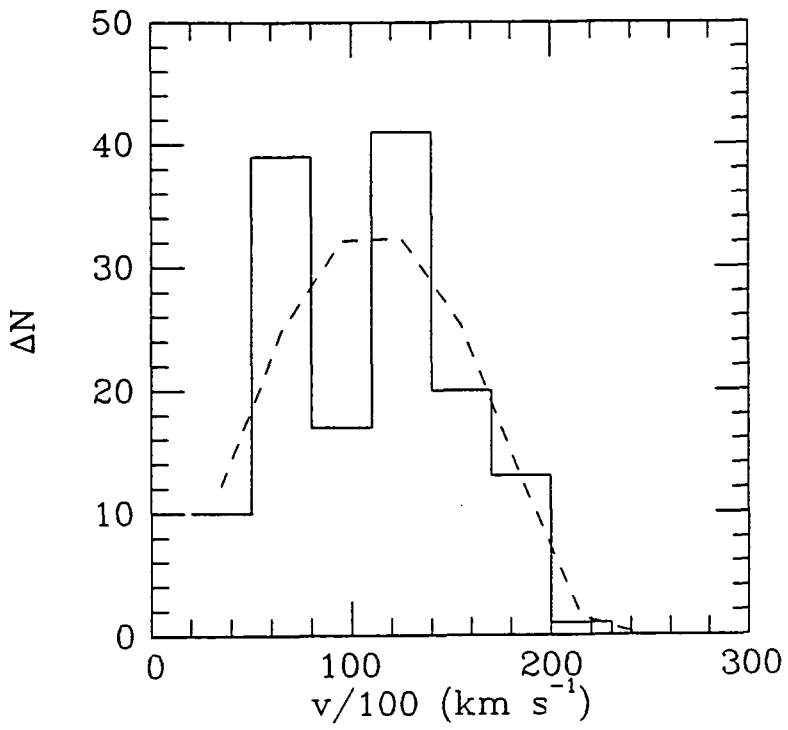
(d) Durham/AAT M<M*
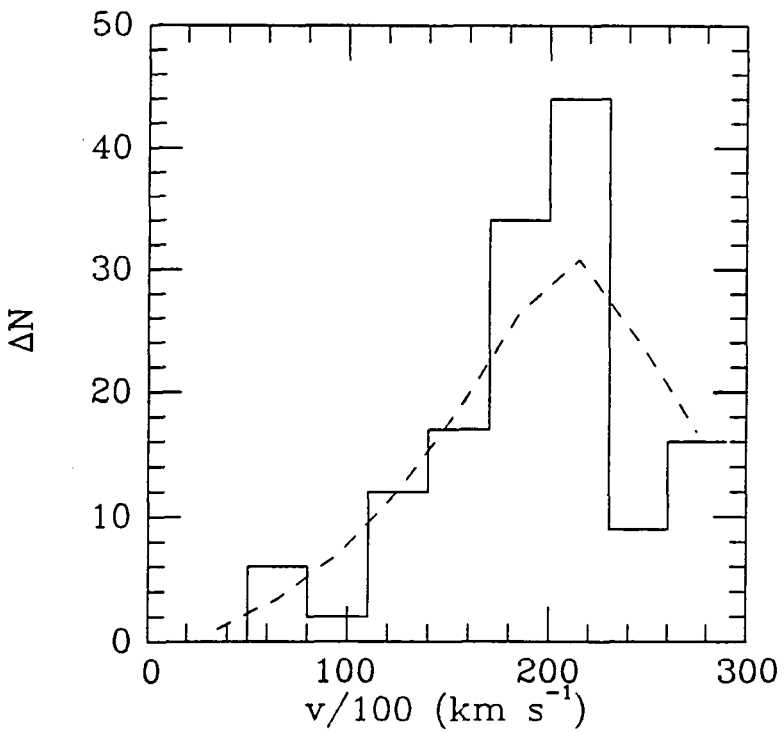
Figure 1). Davis et al. (1988) find a similar result from this sample and from the SSRS Survey but the conclusions are based only on about 2% and 8% of the data, respectively, which can only be regarded as highly uncertain. Other authors (Phillips and Shanks 1987) have, similar to the analysis in this work, found a null result for this observation.

Clearly, such observations are important if an understanding is to be reached about the relationship between the clustering of galaxies and the clustering of mass in the Universe. As was discussed in Chapter 2 (Section 2.2) and at the end of Chapter 4 (Section 4.5), if there is considerably more 'invisible' matter in the Universe than the virial estimates of Ω_0 seem to suggest (Chapter 4, Section 4.4), then this matter must be clustered less strongly than galaxies to avoid giving rise to larger peculiar motions than observed. Since, in general, the galaxy correlations measured are dominated by galaxies with $M \approx M^*$ this might imply that objects with $M \ll M^*$ will be correlated less strongly. However, such observations are only starting to be made and it is not clear from the present evidence as to what the situation is in reality.

5.1.2 Comparison with other results

In Figure 5.10 the combined within-field $\xi_s(s)$ result for the Durham/SAAO, Durham/AAT and Parker et al. surveys (Figure 5.7) is compared to observations of the same quantity from the CfA ($m_B < 14^m.5$) northern redshift survey (filled triangles, Davis and Peebles 1983), the diameter limited Southern Sky Redshift Survey (open triangles, Davis 1987) and the CfA ($m_B < 15^m.5$) $6°$ slice through the NGP (open squares, de Lapparent et al. 1987). The points in this graph beyond $20h^{-1}$ Mpc are not shown. At first sight, this figure would seem to suggest that, whereas the estimates of $\xi_s(s)$ at small ($s \le 1-2h^{-1}$ Mpc) and large ($s \ge 10h^{-1}$ Mpc) scales are somewhat variable, the results from the different surveys in the intermediate range ($2 \le s \le 10h^{-1}$ Mpc) are exhibiting remarkable stability. The agreement between the different samples is well within the error bars of the combined Durham/SAAO, Durham/AAT and Parker et al. result and this again seems to confirm the suggestion that $\xi_s(s)$ shows an enhanced amplitude over a simple power law with $r_0 = 4.5h^{-1}$ Mpc (dashed line) in this region. The close similarity between the correlation function for the overall sample presented here and
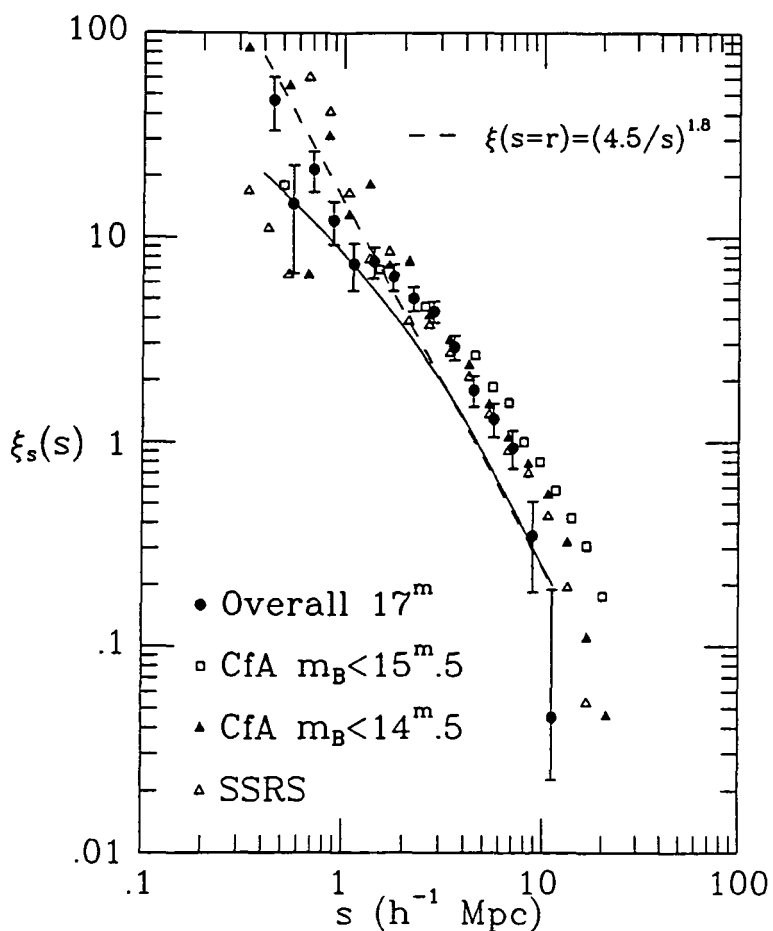
Figure 5.10. A comparison of the overall small-scale $\xi_s(s)$ from the combined 17^m sample with estimates from other redshift surveys. The overall 17^m estimates (solid circles with errors) and models (solid and dashed lines) are the same as those in Figure 5.7. The other redshift surveys (open symbols) are as described in the text.

the original ($m_B < 14^m.5$) CfA Survey has already been anticipated, to some extent, in the projected correlation function $\omega_v(\sigma)$ (see Section 4.3.1, Figure 4.6); there the results also seemed to indicate that the CfA Survey could be within the sampling fluctuations of the total sample discussed in this work (as was also observed with the peculiar motions, see Section 4.3.3).

In spite of these observations, it still remains a possibility that the agreement between these samples in Figure 5.10 between $2 \leq s \leq 10 h^{-1}$ Mpc is just a coincidence. For example, none of the authors for the comparison samples chosen above have indicated the level of uncertainty in their estimates and given the previous discussion in Chapter 3 (Section 3.1) about the relatively shallow depth of these surveys, the error on these estimates could be larger than that implied from the observed sample-to-sample variation in Figure 5.10. Indeed, Shanks et al. (1983) have pointed out that, according to the analysis of Davis and Peebles (1983), the CfA ($m_B < 14^m.5$) correlation function results have a strong estimator dependence at small scales ($s \leq 2 h^{-1}$ Mpc) and suffer from sampling fluctuations at large scales ($s \geq 10 h^{-1}$ Mpc). The possible uncertainty in the estimates from the shallow depth surveys has been further taken up by de Lapparent et al. (1988) and by Davis et al. (1988); the first set of authors consider estimator dependencies in a new 12° strip of sky (consisting of the above mentioned 6° strip plus an adjacent 6° strip, see Chapter 3, Section 3.1) and the original CfA ($m_B < 14^m.5$) survey, whereas the second consider variations in the estimates of $\xi_s(s)$ from different volume limited samples in the CfA ($m_B < 14^m.5$), SSRS and IRAS (Strauss and Davis 1988) catalogues.

Discussing the former work first, de Lapparent et al. (1988) have used three different forms for the estimator of $\xi_s(s)$; the simple pair weighted estimator (equation 2-27) and the two similar estimators formed by giving each pair either $1/\varphi(z_1)$ or $1/\varphi(z_1)\varphi(z_2)$ weighting (where $\varphi(z)$ is the selection function of equation 2-19; see also Chapter 2, Section 2.1.2.3). These estimators are denoted by these authors as ξ_{11}, $\xi_{1\varphi}$ and $\xi_{\varphi\varphi}$, respectively. Thus, de Lapparent et al. find that the correlation length s_0 (based on fitting a power law of the form $\xi_s(s)=(s_0/s)^\gamma$ to $\xi_s(s)$) is 5.1, 8.5 and 8.2h^{-1} Mpc for $\xi_{11}, \xi_{1\varphi}$ and $\xi_{\varphi\varphi}$, respectively, for the CfA ($m_B < 15^m.5$) slice and 8.8, 5.8 and 5.9h^{-1} Mpc in the original CfA ($m_B < 14^m.5$) northern survey. These values have been corrected to $\gamma=1.8$ and are appropriate to the range $3.5 \leq s \leq 13.7 h^{-1}$ Mpc in the $m_B < 15^m.5$ sample and $3.5 \leq s \leq 9.5 h^{-1}$ Mpc in the $m_B < 14^m.5$ sample,

and this makes the estimates directly comparable to the overall estimate of the correlation length from the samples discussed in this work.

The values of s_0 from these surveys would seem to indicate that these samples are quite unstable to the application of different estimators; the fluctuations in the correlation length from estimator-to-estimator implies that the rms scatter $\sim\pm1.8$ (the mean and standard deviations are $s_0=(7.3\pm1.9)h^{-1}$ Mpc and $s_0=(6.8\pm1.7)h^{-1}$ Mpc for the $m_B<15^m.5$ and $m_B<14^m.5$ samples, respectively) and this is about a factor of 3.5 times larger than the uncertainty of ±0.5 obtained for the combined sample of the Durham/SAAO, Durham/AAT and Parker et al. surveys. Thus, if this larger error estimate were more representative of the true fluctuations in $\xi_s(s)$ at this scale then it would make the shoulder feature much more likely to have arisen by chance, although it should be noted that the mean of $s_0=7.1h^{-1}$ Mpc agrees with the overall estimate of $s_0=6.6h^{-1}$ Mpc obtained previously.

De Lapparent et al. have suggested that the fluctuations in $\xi_s(s)$ observed with these different estimators is as a result of (at $\geq10h^{-1}$ Mpc) **large-scale clustering** in the CfA samples. They point out that the largest clustered structures that they see in these surveys are comparable in extent to the depth of these volumes and, on the basis that such structures are a common feature of the galaxy distribution, they arrive at the conclusion that large density fluctuations are to be expected from sample-to-sample (see equations 2-71 and 2-85). As evidence for this they show that the s_0 fluctuation in the $m_B<15^m.5$ and $m_B<14^m.5$ samples is as a result of large structures seen in these volumes. The $1/\varphi$ weighting of the galaxies gives more weight to volumes at larger distances, and so in the $m_B<15^m.5$ sample the over-density at $\sim10,000$ kms^{-1} leads to an enhanced correlation function for the $\xi_{1\varphi}$ and $\xi_{\varphi\varphi}$ estimators (see Chapter 3, Section 3.2.1, Figure 3.4) whereas in the $m_B<14^m.5$ sample the opposite effect occurs; here Virgo at ~1000kms^{-1} leads to an enhanced correlation for ξ_{11} (see Figure 5 of Davis and Huchra 1982). As further evidence for inhomogeneity, they quote a 25% difference in their measured values for the density ϕ^* between the faint and bright samples, where the Schechter parameter ϕ^* has been normalised to the numbers in each sample (see Chapter 3, Section 3.2.3).

There are various points that can be made about the interpretation of these data. Firstly, it should be emphasised that apparently large structures

seen in redshift survey plots do not necessarily imply average large-scale correlations of the same order of size; it is easy for the eye to pick out connected structures which may in reality be the overlap of several randomly placed smaller units (see, for example, the simulated slices in Figure 3.4, Section 3.2.1). Thus, one should be careful about making conclusions about the fairness of samples on the basis of visual inspections of the data. However, the $\Delta N(z)$ distributions for the $m_B < 15^m.5$ and $m_B < 14^m.5$ samples (see Section 3.2.3 of Chapter 3) do appear to be quite noisy as compared to the quite smooth distributions of the Durham/SAAO and Durham/AAT samples (see Figure 3-18 of the same section), and a smooth model fit to the mean density in these brighter samples may lead to noisy estimates of $\xi_s(s)$.

It should also be noted that the weighting of pairs by $1/\varphi(z_1)$ or $1/\varphi(z_1)\varphi(z_2)$ will lead to estimates of $\xi_s(s)$, at $s \leq 10h^{-1}$ Mpc, which are more uncertain than the simple pair-weighted estimate ξ_{11} (Davis and Peebles 1983) since a reliance is being made on fewer pairs of galaxies (see Chapter 2, Section 2.1.2.3). If, coupled with this, the mean density model is, in some sense, a 'poor fit' to the data, then again quite large variations in $\xi_s(s)$ may occur. De Lapparent et al. do see this in the CfA data; using a V/V_{max} estimator for the luminosity function rather than the inhomogeneity independent technique (Lynden-Bell 1971, Turner 1979) they obtain a better fit to the $\Delta N(z)$ distributions in the two samples and, accordingly, a reduction in the spread of the estimators $\xi_{11}, \xi_{1\varphi}$ and $\xi_{\varphi\varphi}$ by a factor of about 2. This would seem to indicate that poor modelling of the mean density, rather than large-scale density fluctuations, could be leading to the observed fluctuations in the correlation estimators. For example, a source of uncertainty may arise from the inconsistent use of the $1/\varphi$ weighting; de Lapparent et al. adopt $1/\varphi$ weighting in the pair counts for $\xi_s(s)$, but fail to use it in the normalisation of $n(z)$ (see Chapter 2, Section 2.1.1.2).

Finally, the 25% difference in the density ϕ^* between the $m_B < 14^m.5$ and $m_B < 15^m.5$ samples could be explained by effects other than those of clustering induced large-scale density fluctuations. Using the observed projected two-point correlation function $\omega(\theta)$ for the whole Zwicky (Zwicky et al. 1961-1968) catalogue at $m_B < 15^m.0$, it is possible to predict what density fluctuations might be present in the $m_B < 15^m.5$ slice. Thus, scaling the $m_B < 15^m.0$ Groth and Peebles (1977) result for $\omega(\theta)$ (Chapter 2, Section 2.1.2.4, equation 2-89) to $m_B < 15^m.5$ via equation 2-92, and integrating the

power law to a maximum of θ_{cut} (in degrees), equation 2-71 (Section 2.1.2.3) can be used to predict the expected fluctuations in the number of galaxies in the $m_B<15^m.5$ slice. The result (see also Section 5.2.2, equations 5-4 and 5-5) gives rms fluctuations of $\delta N/N \approx 0.042\theta_{cut}^{0.6}$ and so $\theta_{cut} \approx 20°$ is required to obtain fluctuations ~25%. Since the observed $\omega(\theta)$ at $m_B<15^m.0$ is observed to break at ~6° (~4.8° to $15^m.5$) this would seem to suggest that 25% fluctuations (or 100% fluctuations in the case of the $14^m.5$ sample) may be on the large side.

Some evidence for this comes from the knowledge that Zwicky magnitudes in the range $15^m.0<m_B<15^m.5$ may be systematically in error (e.g. Felten 1985), in the sense that Zwicky included many more galaxies in the catalogue which were fainter than $m_B=15^m.5$ and this was as a result of not being able to successfully judge galaxy magnitudes fainter than $m_B=15^m.0$. Figure 5.11 shows Zwicky magnitudes for a set of galaxies for which there are photographic (b_J) magnitudes calibrated via CCD sequences (Shanks priv. comm.), and this indicates that Zwicky magnitudes fainter than 15^m .0 are poorly defined. Thus, it can be questioned as to what extent the 25% variation between the $m_B<14^m.5$ and $m_B<15^m.5$ samples is due to this sort of effect.

Davis et al. (1988) have also examined the correlation estimates $\xi_s(s)$ in the northern CfA ($m_B<14^m.5$), SSRS and IRAS (Strauss and Davis 1988) catalogues in more detail. By volume limiting each of these surveys in three samples of D_{max}=20, 40, and $80h^{-1}$ Mpc they find that, with a simple pair-weighted estimator (equation 2-27) for $\xi_s(s)$, s_0 (as determined from where $\xi_s(s)=1$) is 2.8, 6.0 and $8.0h^{-1}$ Mpc respectively in the CfA ($m_B<14^m.5$) sample, 3.4, 5.6 and $8.5h^{-1}$ Mpc in the SSRS Survey, and a more or less constant 4.4, 4.2 and $5.0h^{-1}$ Mpc in the IRAS catalogue. The mean and rms error for these samples are, respectively, $s_0=(5.6\pm2.6)h^{-1}$ Mpc, $s_0=(5.8\pm2.6)h^{-1}$ Mpc and $s_0=(4.5\pm0.4)h^{-1}$ Mpc. This would again seem to suggest that the optically selected bright samples may be exhibiting larger fluctuations in $\xi_s(s)$ than the estimate of $r_0=(6.6\pm0.5)h^{-1}$ Mpc from the combined Durham/SAAO, Durham/AAT and Parker et al. surveys. However, Davis et al. claim that the $D_{max}=20h^{-1}$ Mpc sample estimates may be low because they are dominated by the rich clustering of Virgo in the north, and the Fornax-Eridanus clusters in the south and that the $D_{max}=80h^{-1}$ Mpc sample values are high because these galaxies have a larger luminosity
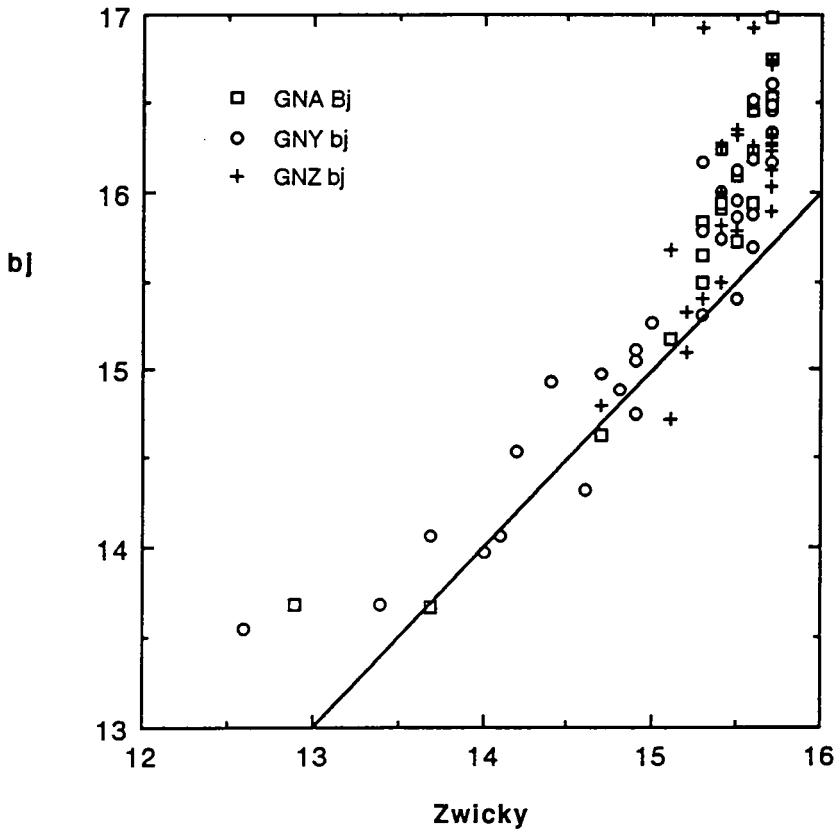
Figure 5.11. A comparison between Zwicky (1961-1968) and bɪ magnitudes (Shanks priv. comm.)

and thus exhibit richer clustering (see the previous section). The IRAS Survey, on the other hand, is remarkably stable and it seems to indicate a certain insensitivity to strong clustering which may result from these galaxies being of mainly late-type. In clusters and in the field there is evidence that these objects avoid richer areas of clustering (Dressler 1980, Davis and Geller 1976).

Thus, in conclusion, the observation of the bright optically selected galaxy samples may indicate larger fluctuations in the estimate of $\xi_s(s)$ than the agreement between the various surveys in Figure 5.10 would seem to suggest. If rms density fluctuations due to clustering are responsible for the error in $\xi_s(s)$ then equations 2-71, 2-89 and 2-92 suggest that, in the $m_B < 15^m$ .5 CfA Survey, for example, rms clustering length variations of

$$\frac{\delta r_o}{r_o} \approx \frac{1}{\gamma} \frac{\delta \xi}{\xi} \approx 0.023 \theta_{cut}^{0.6} \tag{5-2}$$

might be expected for $\xi \approx 1$. Thus with $\theta_{cut} \approx 6°$, $\delta r_o/r_o \approx 7\%$ which is close to what is observed for the total Durham/SAAO, Durham/AAT and Parker et al. surveys. To obtain 25% fluctuations in r_o then, $\theta_{cut} \approx 53°$ and this would certainly require the presence of large-scale structure, a matter which is currently a subject of strong debate (see following sections). However, in spite of these remarks the agreement between the surveys in Figure 5.10 remains an inspiring result.

5.1.3 Discussion

In the previous Section 5.1.1, it was seen that, on the observation that random peculiar motions are negligible at $s \approx 5h^{-1}$ Mpc, the correlation estimator $\xi_s(s)$ in the combined sample of the Durham/SAAO, Durham/AAT and Parker et al. samples showed evidence for a correlation of length $r_o \approx (6.6 \pm 0.5)h^{-1}$ Mpc in the range $2 \leq s \leq 7h^{-1}$ Mpc, and this is significantly larger than the $r_o \approx 5h^{-1}$ Mpc that is often used to compare with models of the large-scale distribution of matter (Peebles 1981c, White et al. 1983, Davis et al. 1985). In the previous section (Section 5.1.2) these results were compared to similar observations from other, larger solid angle, but shallower, redshift surveys and, although these other results appear to be less stable, there seemed to be some agreement that the 'shoulder' was a real feature of $\xi_s(s)$.

Here, possible uncertainties in the interpretation of the shoulder in terms of a real spatial feature are discussed and, given that these uncertainties are small, the spatial form for $\xi(r)$ and the spatial integrals $J_2(r)$ and $J_3(r)$, are predicted.

As was seen in the previous Section 5.1.2, clustering induced large-scale density fluctuations may lead to significant errors in $\xi_s(s)$ through modelling of the mean background density $n(z)$ (see Chapter 2, Section 2.1.2.3, equation 2-70), and it remains a possibility that these uncertainties will affect the conclusions concerning the significance of the shoulder in $\xi_s(s)$ observed in the combined sample of the Durham/SAAO, Durham/AAT and Parker et al. surveys. In Chapter 3 (Section 3.2.3) it was seen that the observed $\Delta N(z)$ distributions for the two larger Durham/SAAO and Durham/AAT samples were in good agreement and, using the inhomogeneity independent results for the luminosity functions (Section 3.2.2), satisfactory model fits to the $\Delta N(z)$ distributions in these samples were obtained. This seems to suggest that the fluctuation in density from sample-to-sample is small and that $\xi_s(s)$ should be reasonably stable. The only suggestion of larger fluctuations in $\Delta N(z)$ comes from differences in this count between the north and south subsamples, but even here, this does not seem to affect the conclusion of $\xi_s(s)$ at small scales (see Figure 5.3 and Bean 1983, Figure 6.3).

Similar evidence is also available from the field-to-field variations in the observed counts brighter than $m(b_J) < 16^m.8$ (see Chapter 3, Section 3.2.3). The rms fluctuation about the mean count of 5.8 deg^{-2} was ± 2.1 deg^{-2} from field-to-field (equation 3-13). Thus, from the discussion in Chapter 2 (equations 2-68 and 2-69) it might be expected that, at small scales, $\delta\xi/\xi \approx (2.1/\sqrt{14})/5.8 \approx 10\%$ for the overall sample and hence $\delta r_0/r_0 \approx 5\%$ (equation 5-2) which is close to the error quoted on r_0. However, it still remains a possibility that there is more large-scale structure in the Universe than has been detected in this data or has been included in the simulations. In the first instance correlations between the fields would tend to make the rms variation in the counts smaller and thus possibly reduce the expected error on r_0. For example, it is still a matter of debate as to whether the number-magnitude counts at $b_J < 17^m$ are low with respect to those at deeper magnitudes (see Chapter 3, Section 3.2.3), implying, in the absence of evolution, a large under-density in our ($z < 0.1$) neighbourhood or whether this is due to some

other effect (such as evolution).

If more large-scale (≥ 10 h^{-1} Mpc) structure was introduced into the simulations this would naturally make the rms fluctuations in $\xi_s(s)$ from simulation-to-simulation larger since the number of independent points in each is reduced (Chapter 2, Section 2.1.2.3, equation 2-51). However, from Figure 3.8 (Chapter 3, Section 3.2.1) it can be seen that the redshift fields are quite well separated on the sky, and unless the correlations extend over quite large scales then the error on $\xi_s(s)$ depends just on the integral of $\xi(r)$ over the volume of the bin (see equations 2-4, 2-43 and 2-51 of Chapter 2), and this makes the contribution from larger scale correlations ($\geq 10 h^{-1}$ Mpc) less important.

This uncertainty in $\xi_s(s)$ from fluctuations in the density should, perhaps, be added in quadrature to the simulated rms error on r_0 anyway since the density for each simulated catalogue was taken to be a fixed value (rather than drawn from a distribution; see Chapter 2, Section 2.1.4). **However**, as was discussed in Chapter 2 (Section 2.1.2.3) the estimator $\xi_e=(DD/DR)-1$ (equation 2-53), normalised to the numbers in a sample, is expected to be **less sensitive** to density fluctuations than global density estimates since DD and DR are of $\sim n_e{}^2$ where n_e is the estimated density (Davis and Peebles 1983). For example, some evidence for this can be observed in the 20 simulations of the coherent sample of 14 Durham/SAAO and Durham/AAT fields (see Chapter 2, Section 2.1.4). Taking the 5 Durham/AAT fields from each simulation it is found that the total count in this sample varies by 29 galaxies rms about a mean of 398 (this latter value being close to the expected value of 406). Thus, estimating the correlation function in each simulation by both a local and global density the observed variance for a small bin at $s\approx4.5h^{-1}$ Mpc is larger by about 20% in the latter estimator, whereas the mean values of $\xi_s(s)$ at this scale are negligibly different. Using equations 2-68 and 2-69 (Section 2.1.2.3) the predicted difference in variance between the two estimators (for $\xi_s(4.5)=1.3$) should be ~0.03 and since the variance with the local estimator is ~0.14 this increase is well matched to the observed value. Thus in conclusion, from the evidence of the surveys discussed in this work, it is believed that the shoulder **is a significant** feature in $\xi_s(s)$ and that this should warrant a more careful appraisal of its physical significance.

120

One such physical consideration that has not been accounted for so far in the interpretation of $\xi_s(s)$ is the effect of coherent infall. Thus, although random peculiar motions have been shown to have a small effect on the direction-averaged redshift correlation function at separations $s \geq 3h^{-1}$ Mpc, this may not be true with peculiar motions due to infall since these are prevalent where $\xi_m < 1$ (Kaiser 1987). For example in Figure 5.12 the solid model line is the pair-wise infall model of equation 2-132 (Section 2.2.1.2, Chapter 2) integrated via equation 2-34 (Section 2.1.2.2) with $\xi(r)$ a pure power-law ($\xi(r) = (4.5/r)^{1.8}$) and $F = b = 1$ (equation 2-132; this corresponds to the Bean et al. 1983 model where galaxies trace the mass). As in previous models the width of the random peculiar velocity distribution (equation 2-122 and 2-123, Section 2.2.1.1) is set to $\langle \omega^2 \rangle^{1/2} = 300 \text{kms}^{-1}$ which is close to the observed value in Chapter 4 (equation 4-11, Section 4.4) for the combined sample discussed in this work. The dashed and dotted lines are, respectively, comparison models with no infall but random motions ($F = 0$), and no infall and no random motions ($F = 0 = \langle \omega^2 \rangle^{1/2}$, $\xi_s(s) = \xi(s) = \xi(r)$).

The solid model line in Figure 5.12 clearly shows that infall can lead to a significant amplification of the spatial correlation function $\xi(r)$ observed in redshift space on the assumption that galaxies trace the mass distribution. The constant difference at $s \geq 2h^{-1}$ Mpc between this model and the dashed line (no infall) in log space implies an amplification factor of ~ 1.4, and this may be compared with the prediction of Kaiser (1987), based on an analytic integration of equation 2-132 with $\xi \ll 1$. Since $F = 1$ and $b = 1$ this implies the mean mass density in this model is $\Omega_o = 0.43$ ($= 0.6^{5/3}$, equation 2-130) and, thus, according to equation 2-135 $\xi_s(s) = 1.4\xi(s)$ in agreement with the direct numerical integration. On the assumption that the shoulder observed in $\xi_s(s)$ is due to infall, this amplification falls significantly below the observed rise of a factor ~ 2.0 in the combined sample of the Durham/SAAO, Durham/AAT and Parker et al. surveys. However, on the assumption that galaxies trace the mass, Kaiser's models predict that with $\Omega_o = 1.2$ (equation 2-134) or $\Omega_o = 1.9$ (equation 2-135, the Bean model) such an amplification factor can be achieved. These analytic results of Kaiser (1987) for the amplification of $\xi(r)$ in redshift space have been confirmed using N-body simulations of Cold Dark Matter (White et al. 1987) by Lilje and Efstathiou (1989). Thus it seems likely that using observations of $\xi_s(s)$ it is possible to directly constrain Ω_o provided some knowledge of the spatial form $\xi(r)$ is known.
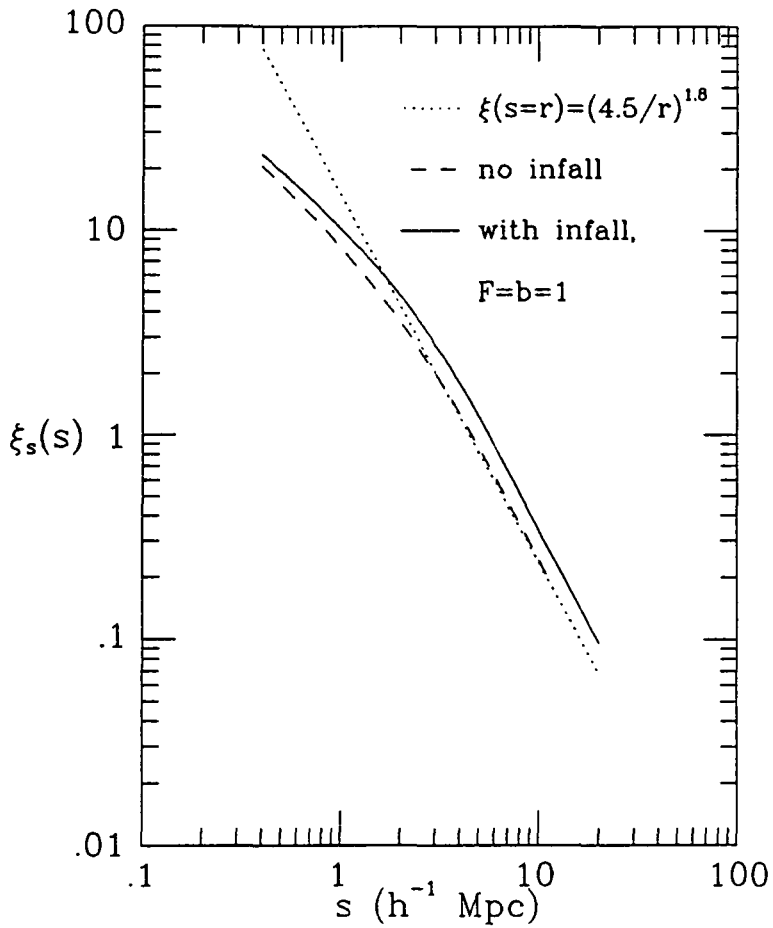
Figure 5.12. The effect of coherent infall on the redshift two-point correlation function $\xi_s(s)$ at small scales. The solid line convolves the spatial power-law $\xi(r)$ with an rms peculiar velocity dispersion of 300kms^{-1} using the model for $\xi_s(s)$ in equations 2-34 and 2-31. The solid line is a similar model but incorporates the Bean et al. model for infall (equation 2-132 with F=b=1).

The suggestion ~~that the shoulder~~ observed in $\xi_s(s)$ can be explained by infall with $\Omega_o \approx 1$ is in direct contradiction to the virial estimate of Ω_o of ~0.2±0.1 measured from the combined surveys presented in this work (see Chapter 4, Section 4.4, equation 4-12). In the discussion at the end of Chapter 4 (Section 4.5) it was argued that models of the Universe with $\Omega_o=1$ could be reconciled with the observed virial estimates of Ω_o if galaxies were biassed tracers of the mass distribution. There it was shown that if $\xi_g \approx b^2 \xi_m$ as in equation 2-131, a biassing factor of $b \approx \sqrt{5}$ is required if all the bias is in the two-point function. Thus if this biassing applies to scales larger than where the virial estimate was obtained, and galaxies infall with the same velocity as the mass, then the effective mass density parameter Ω_o^{eff} is (equation 2-136) ~$5^{-5/3}=0.068$ in the BBGKY model at $\xi^m \ll 1$ and $\Omega_o^{eff}=(\sqrt{5})^{-5/3}=0.26$ in the Kaiser description. This immediately implies that the amplification of $\xi_s(s)$ for the galaxies is down to a factor of 1.1 in the former model (equation 2-135) and 1.4 in the latter (equation 2-134), and again this is significantly below the amplification of ~2 that is observed.

The decrease in the amplification of $\xi_s(s)$ is understandable because of the lower infalling velocity of the galaxies induced by smaller density contrasts in the mass. If the biassing between the non-linear and linear regimes is not constant so that, for example, $b=1$ where $\xi_m \ll 1$ then infall with $\Omega_o \approx 1$ could explain the shoulder in $\xi_s(s)$ for the galaxies. However, this situation would then be somewhat contrived since $\xi(r)$ for the galaxies would have a pure power law form whereas $\xi^m(r)$ for the mass would have a shoulder beginning at where $\xi^m \approx 1$. All these arguments would seem to suggest that the shoulder observed in the galaxy correlation function $\xi_s(s)$ is a real spatial feature in $\xi(r)$ and it is, at this point, now worth considering a computational form for $\xi(r)$ which will represent the observed data.

In Figure 5.13, the approach used is to assume, as did Bean (1983), that $\xi(r)$ takes the form of 3 power laws. Thus, the shoulder in $\xi(r)$ is represented as a sharp (discontinuous) rise in $\xi(r)$ from a power law of the form $\xi(r)= (4.5/r)^{1.8}$ at $r \leq 1.6 h^{-1}$ Mpc to the higher amplitude (by a factor of ~2) function $\xi(r)=(6.6/r)^{1.8}$ at larger separations. The break observed in $\xi(r)$ is then included as a rapid decline in $\xi(r)$ of the form $\xi(r)=(6.9/r)^{7.5}$ at separations $r>7h^{-1}$ Mpc. To compare this with the observed form of $\xi_s(s)$ this numerical model for $\xi(r)$ was convolved with a peculiar velocity distribution (equations 2-122 and 2-123, Section 2.2.1.1, Chapter 2) with an rms width of
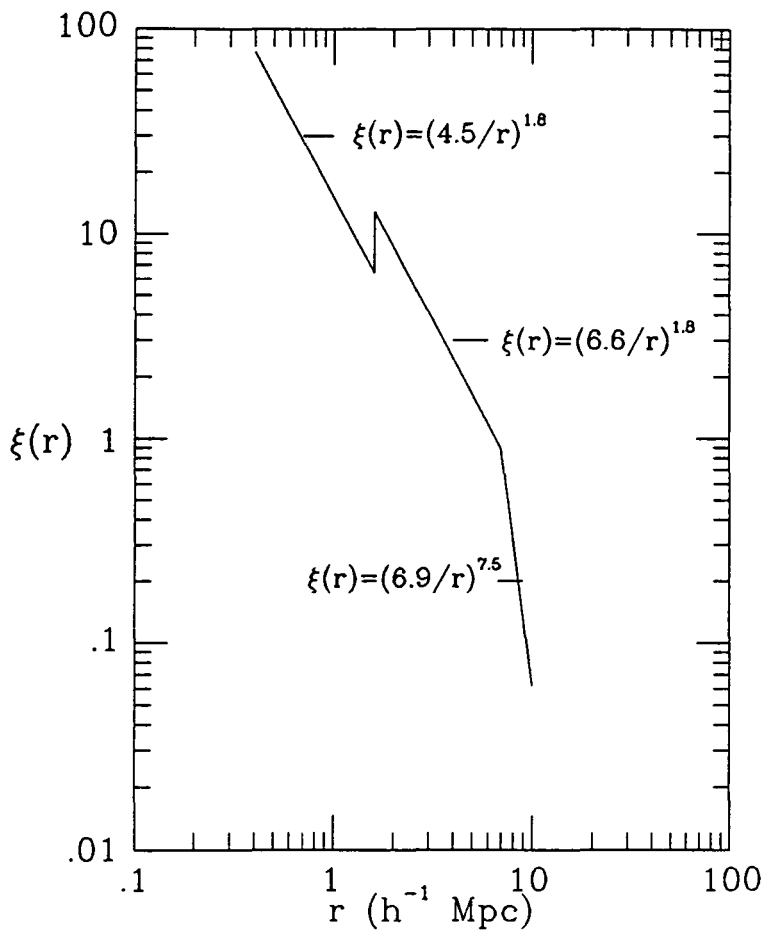
Figure 5.13. A simple model for the small-scale spatial correlation function $\xi(r)$ in the combined sample of the 17m surveys. The spatial function $\xi(r)$ is based on the three power laws shown with transitions between the forms occuring at r=1.6 and 7.0h^{-1} Mpc.

310kms^{-1} and the form for $\xi_s(s)$ computed via equations 2-31 and 2-34 (Section 2.1.2.2). In Figure 5.14 this convolved model (solid line) is compared to the combined $\xi_s(s)$ result for the Durham/SAAO, Durham/AAT and Parker et al. surveys from Figure 5.7. The close agreement between the data and model suggests that the 3 power law approach is a useful representation. Note how the sharp discontinuous rise in $\xi(r)$ at the shoulder is smoothed out by the peculiar motions.

The proposed functional form for $\xi(r)$ in Figure 5.13 can now be used directly to predict values for the integrals over $\xi(r)$, $J_2(r)$ and $J_3(r)$ (equations 2-151 and 2-46, respectively), that are often used to normalise models for the evolution of the galaxy distribution. In Table 5.1, columns (2) and (4), the results of the integrations are shown as a function of separation r out to a maximum of 20h^{-1} Mpc and in columns (3) and (5) these values can be compared to the model in which $\xi(r)$ is the often assumed power law of the form $\xi(r) = (5/r)^{1.8}$. It can be seen that the shoulder in $\xi(r)$ does lead to a larger normalisation for J_2 and J_3 in the important region where r$\approx$r$_0$ and this should, perhaps, be taken account of in evolutionary models of the galaxy distribution. At separations r$\geq$10h^{-1} Mpc J_2 and J_3 in columns (2) and (4) approach asymptotic values as the correlation function rapidly tends to zero whereas, in contrast, the single power-law model continues to increase. This is because these integrals are very sensitive to the large-scale ($\geq$10h^{-1} Mpc) form of $\xi(r)$ and in the case of a pure power law with γ=1.8 J_2 and J_3 would diverge as r$\rightarrow\infty$.

As will be seen in the following section this sensitivity is an important consideration for estimates of large-scale structure; power in $\xi(r)$ of only a few percent at separations »10h^{-1} Mpc can lead to large values of J_2 and J_3 as ξ is being weighted by r and r^2 respectively (equations 2-151 and 2-46). This in turn leads to large rms fluctuations in the observed counts (equations 2-71 and 2-85) and large streaming velocities (equation 2-150), if galaxies trace the mass. This is important to bear in mind when either proposing that there is truly large-scale power in $\xi(r)$ or when concluding there is large-scale structure from visual impressions of maps of the galaxy distribution.
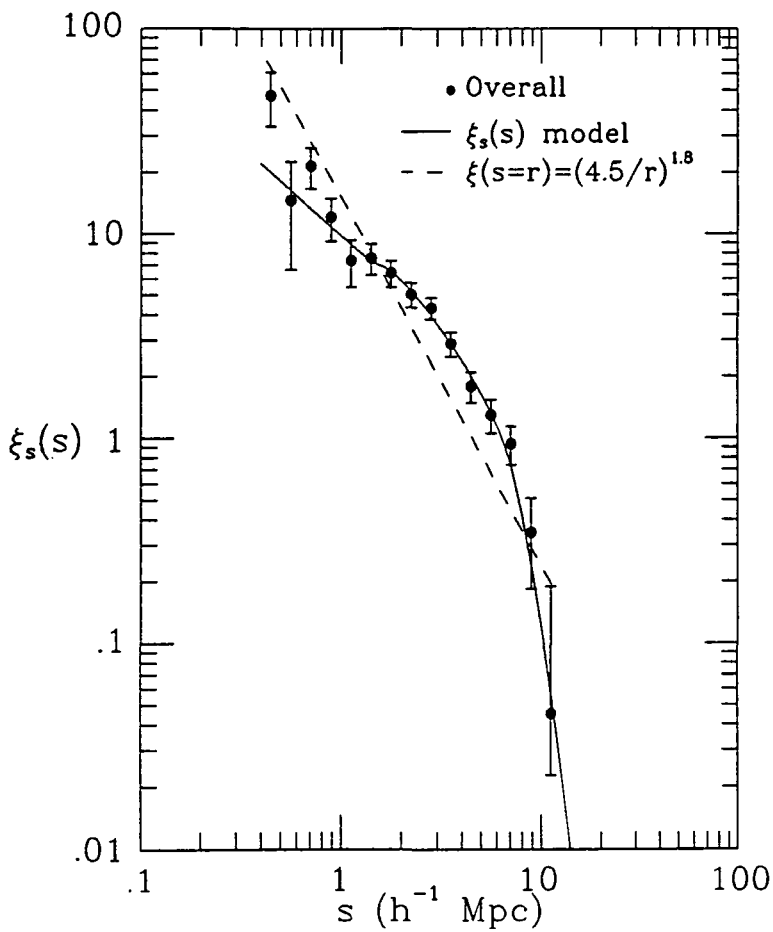
Figure 5.14. A comparison between the redshift correlation function form of the three power law model for $\xi(r)$ and the overall small-scale $\xi_s(s)$ estimated from the combined 17m sample. The solid line convolves the form for $\xi(r)$ shown in Figure 5.13 with an rms peculiar velocity dispersion of 310kms⁻¹. The dashed line is the power-law $\xi(r)$ indicated.

(1) r (h^{-1} Mpc)	(2) J_2 (h^{-2} Mpc^2)	(3) J_2 ($r_0=5$) (h^{-2} Mpc^2)	(4) J_3 (h^{-3} Mpc^3)	(5) J_3 ($r_0=5$) (h^{-3} Mpc^3)
1.0	74.9	90.6	12.5	15.1
2.0	89.8	104.1	35.4	34.7
4.0	115.5	119.5	109.9	79.7
6.0	132.2	129.6	192.5	129.6
8.0	143.1	137.3	267.2	183.1
10.0	145.8	143.6	291.1	239.3
12.0	146.5	148.9	298.9	297.8
15.0	146.8	155.7	302.7	389.3
20.0	146.9	164.9	304.3	549.8

Table 5.1. Models for the integrals $J_2(r)$ and $J_3(r)$. Columns (2) to (4) tabulate the values of the integrals $J_2(r)$ and $J_3(r)$. The correlation function $\xi(r)$ integrated in columns (2) and (4) is the three power law model (see Figure 5.13) that is a good approximation to the correlation function observed in the combined Durham/SAAO, Durham/AAT and Parker et al. surveys. In columns (3) and (5) $\xi(r)=(5/r)^{1.8}$.

5.2 Galaxy clustering at scales $\geq 10h^{-1}$ Mpc

This section deals with the attempts to constrain the homogeneity of the galaxy distribution on scales much larger than the observed clustering length of galaxies. Observations in Section 5.1.1 of the galaxy-galaxy correlation function in the combined Durham/SAAO, Durham/AAT and Parker et al. surveys seemed to indicate that the distribution was rapidly approaching rms fluctuations in the number density of $\langle (\delta n/n)^2 \rangle^{1/2} \approx 30\%$ (see Figure 5.7) at separation scales $\sim 10h^{-1}$ Mpc. However, as was seen at the end of the last section even as small a contribution as this to the correlations of galaxies on larger scales may lead to apparent superclusters of galaxies (with many members per supercluster, see equation 2-45, Section 2.1.2.3, Chapter 2) and large density fluctuations within the survey volumes (equation 2-43). This apparent insensitivity of the estimator to large structures in the Universe (resulting from its direction averaged nature) is further compounded by the poor signal-to-noise of its estimates and this makes measuring large-scale structure from $\xi(r)$ a statistically hard process. However, it should be emphasised that, as mass correlations at this scale are also expected to be small, then such perturbations will have grown in a linear fashion under the influence of gravity (see Section 2.2, equation 2-112). If these primordial fluctuations are Gaussian in origin (with random phase between the Fourier components) as is expected from inflationary models of the Universe (see for example Guth 1984) then the two-point function $\xi(r)$ is the **only** statistic that provides information about large-scale ($\geq 10h^{-1}$ Mpc) structure (Maddox et al. 1990a) and this makes it clear that such observations are highly relevant.

In this section observations of the redshift galaxy correlation function $\xi_s(s)$ are continued to separation $\geq 10h^{-1}$ Mpc in the Durham/SAAO and Parker et al. surveys and, by combining these results with those of Bean (1983) and Shanks et al. (1983) for the Durham/AAT Survey, the aim is to accurately constrain correlations of optically selected galaxies on scales of up to $\sim 100h^{-1}$ Mpc for, perhaps, the first time. In the previous section it has been suggested that random and coherent motions may not be important in these surveys in determining the form of $\xi_s(s)$ at $2 \leq s \leq 10h^{-1}$ Mpc and at larger scales it may be expected that $\xi_s(s) \rightarrow \xi(s) \rightarrow \xi(r)$ (for $r \approx s$). Thus these observations, with some knowledge of the relationship between galaxy and mass clustering, will provide strong constraints on the homogeneity of the Universe at large scales.

5.2.1. Observations of $\xi_s(s)$ at $s \geq 10h^{-1}$ Mpc.

The results so far for the redshift correlation function $\xi_s(s)$ have been obtained from the within-field estimator (see Section 5.1.1), but now, at larger scales, it is also possible to obtain estimates from between the 15 similar fields in the combined sample of the Durham/SAAO, Durham/AAT and Parker et al. surveys (see Section 2.1.2.1 of Chapter 2). In Chapter 3, Figure 3.8 shows the distribution of angles between the fields in these surveys and this can be used to illustrate the sampling properties of the interfield correlation function estimate. Thus as the maximum depth sampled by $\xi_s(s)$ in this case is $\sim s/2\sin(\theta/2)$ (where θ is the angle subtended by s) then, at $s=10h^{-1}$ Mpc, only the first 2 pairs of fields below $\sim 12.5°$ separation are sampled to $\sim(1/3)D_{peak} \approx 46h^{-1}$ Mpc and this small volume makes the interfield estimate very uncertain at this scale. However by $s \approx 40h^{-1}$ Mpc the 37 pairs of fields below 52° are sampled by $\xi_s(s)$ to this depth and this leads to an increasingly better estimate of $\xi_s(s)$.

This dependence of the interfield correlation function estimator on scale may, in the presence of magnitude errors (see Chapter 2, Section 2.1.2.3), lead to spurious bin-to-bin variations in $\xi_s(s)$ which will tend to be absent in the within-field estimate. This arises because, as seen above, different fields can contribute to different separations in s in the former estimate, leading to fluctuations of the type indicated in equation 2-61, whereas in the latter all the fields contribute to each scale equally (save for the variations in the observed magnitude limits) and so the magnitude error tends to average out in the mean of the data-random pair count, DR, over the fields. However, the small rms scatter of $\sim\pm0.1^m$ on the photometric calibration for the fields in these three surveys (see Chapter 3, Sections 3.1.1 and 3.1.2) will only lead to, at most, $\delta\xi \approx 0.1$ (see equations 2-61 and 2-64) and, even then, the effect will tend to be seen more in the smaller ($s \leq 40h^{-1}$ Mpc) rather than larger bins. As will be seen below (Figure 5.17) this error of $\delta\xi \approx 0.1$ is comparable to or smaller than the observed rms fluctuation in the interfield $\xi_s(s)$ below this scale, and this means that reasonable confidence can be placed in this estimate.

The within-field and interfield estimates for $\xi_s(s)$ in the Durham/SAAO,

Durham/AAT and Parker et al. surveys have been obtained from the straight pair counts DD(s) and DR(s) using the methods outlined in Chapter 2 (Section 2.1.2.1). To generate catalogues of random points for the pair count DR(s) in the within-field estimator the methods of Section 5.1.1 were followed except that here the ratio of random to observed galaxies N_R/N_G was reduced to 100 in the Durham/SAAO and Parker et al. samples. This reduction in the ratio saved on computational time without significantly increasing the noise in the data-random pair count.

For the interfield correlation function similar methods were used (here N_R/N_G=40) but random catalogues were again generated self-consistently for each survey using the appropriate models and normalisation for n(z) (Section 3.2.3, Chapter 3). Since the pair counts DD(s) and DR(s) are being combined directly in the interfield estimator some choice had to be made for the weighting of galaxies in the Durham/SAAO survey relative to the Durham/AAT and Parker et al. samples. Given the discussion in Chapter 2 (Section 2.1.2.3) and in the previous section, the rms error in ξ at these larger scales is $\delta\xi\approx$ $m/\sqrt{N_p}$ for a bin in separation that is much larger than the typical size of largest clustering scale length. Since, in the case where the average number per cluster $m\gg 1$ (equation 2-45), $m\propto n$, the main density, and N_p, the number of independent pairs contributing to the bin, is proportional to n^2, it follows that the error $\delta\xi$ will be approximately independent of the density. This would seem to indicate that as much weight should be given to the Durham/SAAO sample at this scale as would be given to a fully sampled survey of the same dimensions (provided that m was still >1 in the third sampled case) and so to **prevent** pair counts DD(s) and DR(s) in the Durham/AAT and Parker et al. surveys from swamping the Durham/SAAO counts, each galaxy in the former surveys was given 1/3 weight. However, as before, when it comes to combining the within-field estimates of $\xi_s(s)$ from the different surveys (and the overall within-field results with the interfield estimate) the usual method of point-by-point weighting each $\xi_s(s)$ estimate according to its simulated error is used (see the Appendix).

In Figure 5.15 (a) and (b) are presented the within-field $\xi_s(s)$ results for the Durham/SAAO and Parker et al. surveys respectively, again in 0.1 bins in log s as for the small-scale results (Section 5.1.1). The errors have again been determined from the catalogues of simulations and, as before, these are well backed up by the field-to-field variations in the observed $\xi_s(s)$ (see

Figure 5.15. The large-scale within-field correlation function $\xi_s(s)$ estimated from the Durham/SAAO, Parker et al. and Durham/AAT surveys. The individual estimates of the within-field $\xi_s(s)$ from the Durham/SAAO, Parker et al. and Durham/AAT surveys are shown in (a) (solid circles), (b) and (c). Figure (d) shows the Durham/SAAO and Durham/AAT survey estimates together (with errors indicated on the former). Variations in $\xi_s(s)$ between north and south subsamples of the Durham/SAAO Survey are presented in (a) (open symbols). In (a), (b) and (c) the solid lines are the extrapolated behaviour of $\xi_s(s)$ observed in each sample between $2 \leq s \leq 7h^{-1}$ Mpc.

(a) Durham/SAAO within-field

$\xi(s=r)=(7.1/r)^{1.8}$
□ North
▲ South

$\xi_s(s)$

$s\ (h^{-1}\ \mathrm{Mpc})$

(b) Parker et al. within-field

$\xi(s=r)=(4.4/r)^{1.8}$

$\xi_s(s)$

$s\ (h^{-1}\ \mathrm{Mpc})$

(c) Durham/AAT within-field

$\xi(s=r)=(7.1/r)^{1.8}$

$\xi_s(s)$

$s\ (h^{-1}\ Mpc)$

(d)

• Durham/SAAO
○ Durham/AAT
(within-field)

$\xi_s(s)$

$s\ (h^{-1}\ Mpc)$
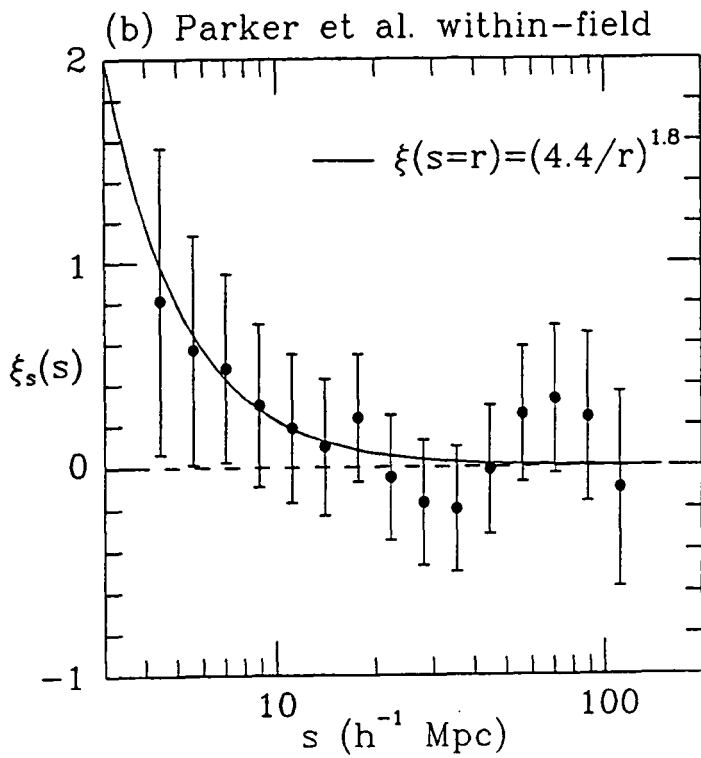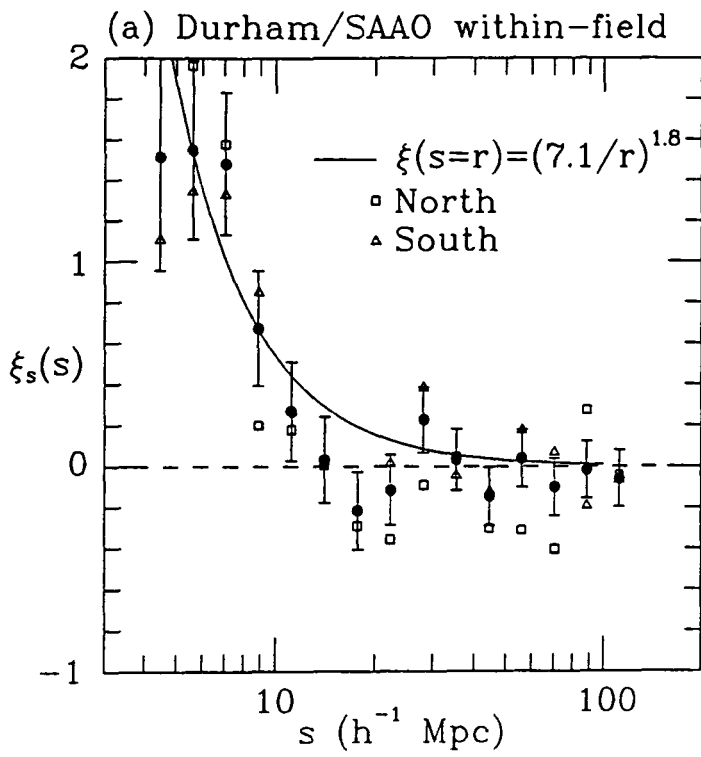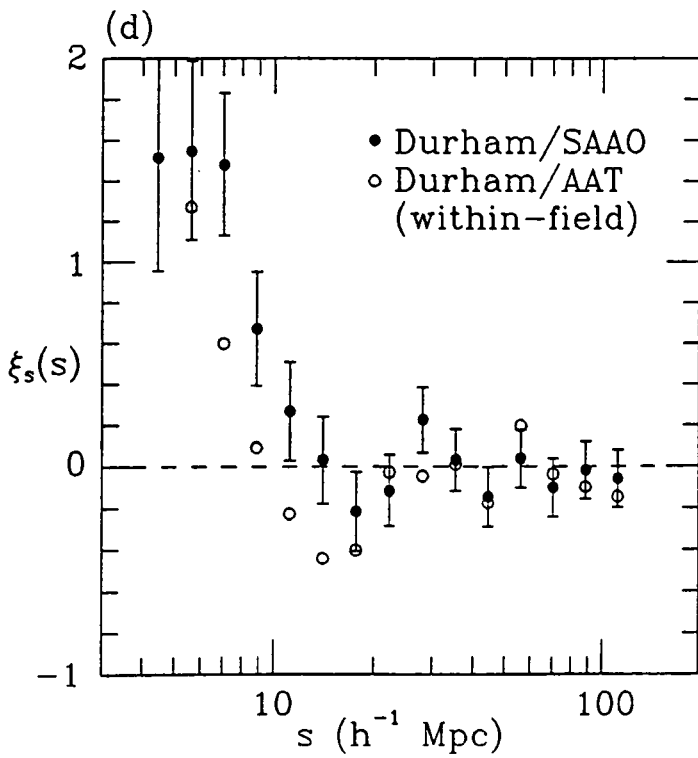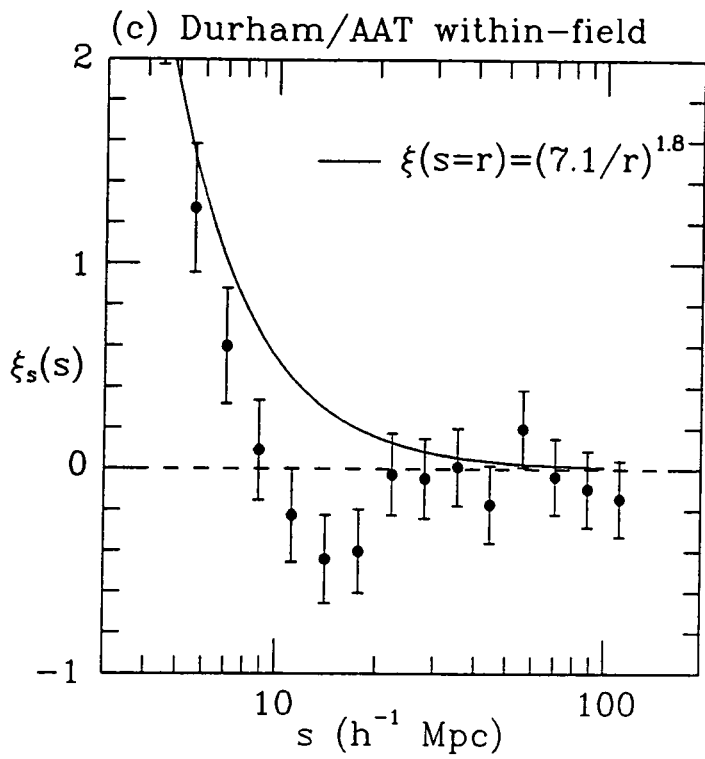
Figures 3.2 and 3.3, Section 3.1.1, Chapter 3) and by variations between north and south subsamples (shown as open symbols in Figure 5.15 (a)). The solid model line in each of these figures is the continuation of the power-law correlation function observed previously in the range $2 \leq s \leq 7h^{-1}$ Mpc. In Figures 5.3 and 5.4 random peculiar motions have a relatively small effect on $\xi_s(s)$ at this separation and so $\xi_s(s)$ is represented by $\xi(s=r)=(7.1/r)^{1.8}$ in Figure 5.15 (a) for the Durham/SAAO Survey and $\xi(s=r)=(4.4/r)^{1.8}$ for the Parker Survey. For the better determined Durham/SAAO estimates, $\xi_s(s)$ is observed to decrease more rapidly than this model to ~ -0.2 in ξ by $\sim 15h^{-1}$ Mpc and the modulus of the point-to-point fluctuation about zero is always ≤ 0.2 thereafter. According to the errors these estimates of $\xi_s(s)$ are consistent with the hypothesis that $\xi(r)=0$ at separations $r \geq 10h^{-1}$ Mpc. This also seems to apply to the Parker et al. Survey results in Figure 5.15 (b).

For comparison with the observations of Bean (1983) and Shanks et al. (1983) for the Durham/AAT Survey, in Figure 5.15 (d) the Durham/SAAO within-field estimates of $\xi_s(s)$ of Figure 5.15 (a) are compared to their within-field estimates of $\xi_s(s)$ in Figure 5.15 (c). As with the estimates of $\xi_s(s)$ at smaller scales, these results are showing excellent agreement, to within the errors (shown representatively on the Durham/SAAO points), over the entire range of s up to $\sim 100h^{-1}$ Mpc. However, there is some evidence for a slightly more rapid decline observed in the Durham/AAT sample $\xi_s(s)$ below $s \approx 10h^{-1}$ Mpc (with some evidence that ξ is anti-correlated at $s \approx 15h^{-1}$ Mpc).

At separations $s \geq 20h^{-1}$ Mpc Figure 5.15 (d) indicates that in both surveys the modulus of the point-to-point fluctuation in $\xi(r)$ about zero is again ≤ 0.2. However, as pointed out by Shanks (1985) the degree of correlation between these estimates is remarkable, with the peaks and troughs tending to oscillate in a very similar fashion. Hence, unless this is just a coincidence, this would seem to suggest that very stable estimates of $\xi_s(s)$ have been obtained from these two samples and this perhaps warrants further investigation as was suggested by Shanks (1985). However, as seen before in just the Durham/SAAO estimate, errors on these observations do not rule out that $\xi(r)=0$ on scales $\geq 20h^{-1}$ Mpc. Thus, to obtain an overall estimate of $\xi_s(s)$ Figure 5.16 shows the combined results from all 3 surveys with the solid model $\xi(s=r)=(6.6/r)^{1.8}$ showing the continuation of the behaviour in the region $2 \leq s \leq 7h^{-1}$ Mpc. As before the overall estimate is obtained by weighting point-by-point each sample according to the inverse of its squared error and
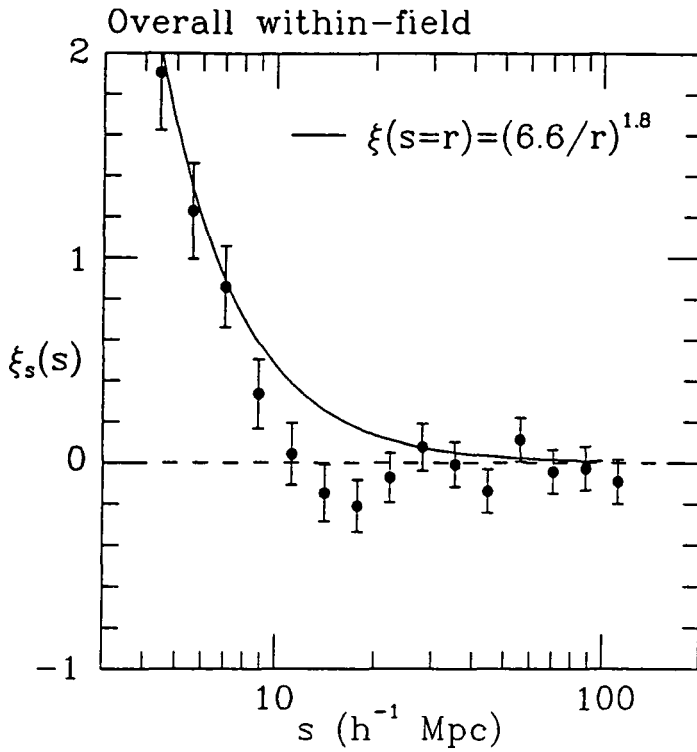
Figure 5.16. The overall within-field correlation function $\xi_s(s)$ estimated from the combined sample of the 17^m surveys. The mean estimates of the within-field $\xi_s(s)$ from the Durham/SAAO, Durham/AAT and Parker et al. surveys are indicated. The solid line is the extrapolated behaviour of these estimates from between $2 \le s \le 7 h^{-1}$ Mpc.

the combined error assumes independence of the samples (see the Appendix).

To compare with this within-field estimate of $\xi_s(s)$, in Figure 5.17 is presented the interfield correlation function result for the 15 fields in the Durham/SAAO, Durham/AAT and Parker et al. samples. The errors here are based on the 14 field simulations (Chapter 2, Section 2.1.4) but these are not expected to be much different from those estimated from 15 fields. As discussed above the results below $\sim 20h^{-1}$ Mpc are very uncertain but there is some indication that $\xi_s(s)$ for this total estimate is positive at $s \approx 15h^{-1}$ Mpc which is in contrast to the negative values of the within-field $\xi_s(s)$ of this scale. Some evidence for this correlation between fields is seen in the comparison in Chapter 3, Section 3.2.1, of the $\Delta N(z)$ plots for fields lying close together on the sky (Figure 3.11) and it is tempting to speculate on the origin of the slight differences between the within and interfield results. As discussed previously, infall would tend to flatten $\xi(r)$ along the line-of-sight making the interfield correlation function (which in this case is more dominated by pairs perpendicular to the line-of-sight) larger than the within-field function (which is more dominated by pairs along the line-of-sight). However, again the results are not showing any really significant differences. At larger separations, where the interfield estimates become increasingly more well determined, there is good statistical agreement between the within and interfield observations, but the detailed shape of $\xi_s(s)$ as in the within-field estimates (Figure 5.16) is not repeated, except, perhaps for the peak at $s \approx 28h^{-1}$ Mpc.

On the assumption that the interfield correlation function is not too strongly subject to magnitude errors, as discussed above, Figure 5.18 shows the combined results from the within and inter-field correlation estimates. As previously, it is assumed that the observations from these two methods are independent and so the averaging methods in the Appendix are employed. The correlation function is increasingly dominated by the interfield result at $s \gtrsim 40h^{-1}$ Mpc but below this scale is fairly similar to the within-field $\xi_s(s)$ in Figure 5.16. The solid line in Figure 5.18 is again, $\xi(s=r)=(6.6/r)^{1.8}$ as extrapolated from $\xi_s(s)$ between $2 \lesssim s \lesssim 7h^{-1}$ Mpc and, given the errors on these estimates, the observed break away from a continuation of the smaller scale power law appears to be fairly significant. The data points in the range $7 \lesssim s \lesssim 30h^{-1}$ Mpc lie consistently below the solid model line, with the points at $s=14$ and $18h^{-1}$ Mpc representing 2.8 and 2.5 standard deviations. However,
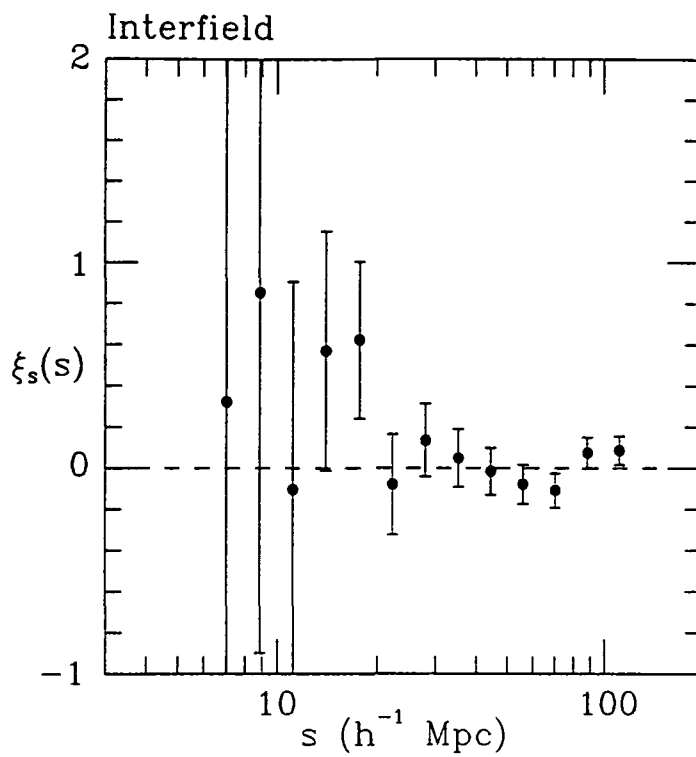
Figure 5.17. The large-scale interfield correlation function $\xi_s(s)$ estimated from the Durham/SAAO, Durham/AAT and Parker et al. surveys.
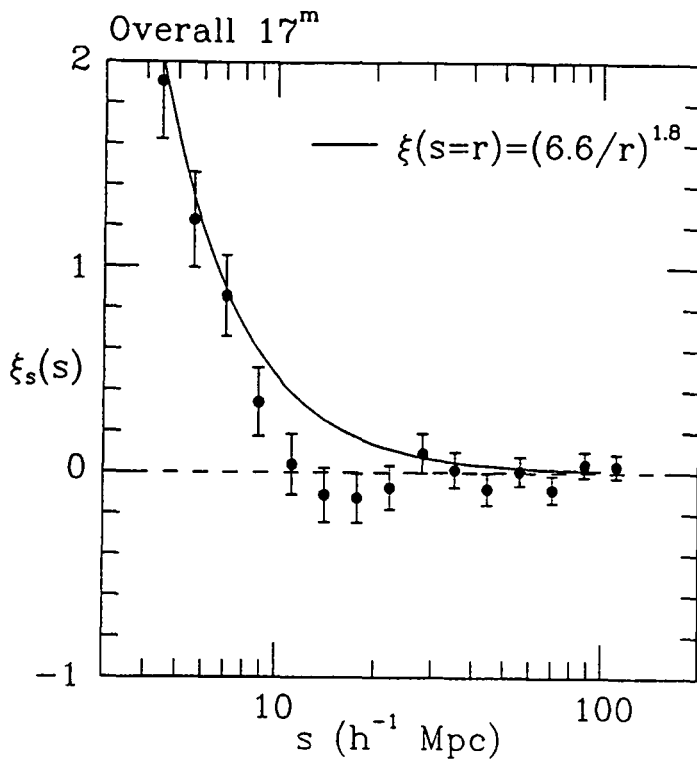
Figure 5.18. The overall estimate of the large-scale redshift correlation function $\xi_s(s)$ from the combined sample of the Durham/SAAO, Durham/AAT and Parker et al. surveys. The points shown here are the mean estimates from the within and interfield correlation functions of Figures 5.16 and 5.17, respectively. The solid line is again the extrapolated form of $\xi_s(s)$ from between 2 and $7h^{-1}$ Mpc.

before firm conclusions can be made about the significance of the break, a careful appraisal needs to be made of the errors determined here and this will be left until the discussion in Section 5.2.3.

Finally, at scales larger than $\sim 10h^{-1}$ Mpc, the overall conclusion is that, for this sample of 15 fields in Figure 5.18, $\xi_s(s)$ is consistent with $\xi(r)=0$ at all separations between $10 \lesssim s \leq 100h^{-1}$ Mpc at the $\sim 1\sigma$ (0.1 at $s=10h^{-1}$ Mpc to 0.05 at $s=100h^{-1}$ Mpc) confidence level. Indeed, with the mean of the estimates lying close to $\xi_s=0$ these results seem to **reject** large-scale clustering of the form $|\xi(r)| \geq 0.2$ to between ≥ 2 (at $s=10h^{-1}$ Mpc) and ≥ 4 (at $s=100h^{-1}$ Mpc) standard deviations. However, this observation, and the degree to which a continued power-law in $\xi(r)$ is rejected, again depends on the appropriateness of the uncertainties calculated, the methods of estimation of $\xi_s(s)$ and the fairness of the observed samples. A full discussion of this is left until comparisons with other observations of large-scale structure have been made.

5.2.2 Comparison with other results

In the previous section quite stringent constraints were placed on the large-scale ($10 \leq s \leq 100h^{-1}$ Mpc) inhomogeneity of the galaxy distribution from observations of galaxy correlations in the total sample of 15 fields in the Durham/SAAO, Durham/AAT and Parker et al. surveys. In this section other measures of large-scale ($\geq 10h^{-1}$ Mpc) structure are described so as to provide a comparison for these data; in the first instance this will come from direct measurements of galaxy correlations in similar 'complete' redshift surveys but, after this, other, perhaps more indirect, constraints on large-scale structure will be obtained from other sources. In the following section (Section 5.2.3) this information is used to attempt to conclude upon the likely upper limit of galaxy fluctuations at large scales, and, with an assumption of how galaxies trace the mass, the implications for the inhomogeneity of the overall mass distribution will be considered. This then paves the way for the brief discussion in Section 5.3 of models of the evolution of the mass distribution which can mimic the current observations.

Firstly, from Figure 5.10 of Section 5.1.2, it can be seen that the estimate of the break away from a power-law of the form $\xi(s=r)=(6.6/r)^{1.8}$ in

the combined Durham/SAAO, Durham/AAT and Parker et al. sample seems to occur at a smaller separation ($\sim$7h^{-1} Mpc) than in the shallower, but larger solid angle, redshift surveys. In the CfA ($m_B<14^m.5$) and SSRS samples this break-scale appears to occur at $\sim$10h^{-1} Mpc but in the CfA ($m_B<15^m.5$) slice the power-law continues to at least $\sim$20h^{-1} Mpc. The statistical stability of these other, brighter catalogues has already been discussed in detail in Section 5.1.2 and, although the variations in the observed $\xi_s(s)$ for these samples appears to be quite large, there does seem to be some evidence that the break-scale might have been underestimated in the combined 15 field sample. Some larger correlations in the latter surveys are seen in the interfield estimate (Figure 5.17) but these are not significantly different from those obtained from within fields in Figure 5.16. As will be seen in Section 5.2.3. part of this discrepancy in the break-scale could arise from the integral constraint (see Chapter 2, Section 2.1.2.3).

Given the level of uncertainty obtained for the estimates of $\xi_s(s)$ at separations $\leq$10h^{-1} Mpc in the shallower surveys (see Section 5.1.2) it is difficult to judge the accuracy of any results deduced from these samples at larger scales. Turning now to the observations of $\xi_s(s)$ from deeper flux limited redshift surveys Kirschner, Oemler and Schechter (1979) found some evidence for unity correlations in their complete sample of eight $\sim$4°x4°, $m_J<15^m.0$ fields (Kirschner, Oemler and Schechter, KOS 1978) to separations $\sim$30h^{-1} Mpc but the result could not be reproduced by Shanks et al. (1983) using the same data set; in contrast these latter authors found that $\xi_s(s)$ from this sample was in good agreement with $\xi_s(s)$ from the Durham/AAT Survey (Figure 5.15 (c)). More recently Rowan-Robinson et al. (1990) have completed a one-in-six redshift survey of galaxies in the 0.6<s<2Jy flux range of the all sky IRAS Point Source Catalogue (Chester et al. 1987). Although this sample, known as the QDOT Survey, has a $\Delta N(z)$ redshift distribution which is skew to low redshifts ($D_{peak}\approx$50h^{-1} Mpc) this data does sample some of the deeper redshift volumes ($d\langle N(z)\rangle/d\langle N(z_{peak})\rangle\approx$0.15 at $cz\approx$20000kms^{-1}).

In Figure 5.19, the preliminary large-scale redshift correlation function $\xi_s(s)$ obtained from the northern ($b^{II}\geq$40°) part of this survey (Efstathiou 1988), is compared to the results from the total sample of the Durham/SAAO, Durham/AAT and Parker et al. surveys (Figure 5.18). In this analysis Efstathiou gave each IRAS galaxy a weight of $1/(1+4\pi n(z)J_3)$ as discussed in Chapter 2 (Section 2.1.2.3, equation 2-52) and this allows a better sampling
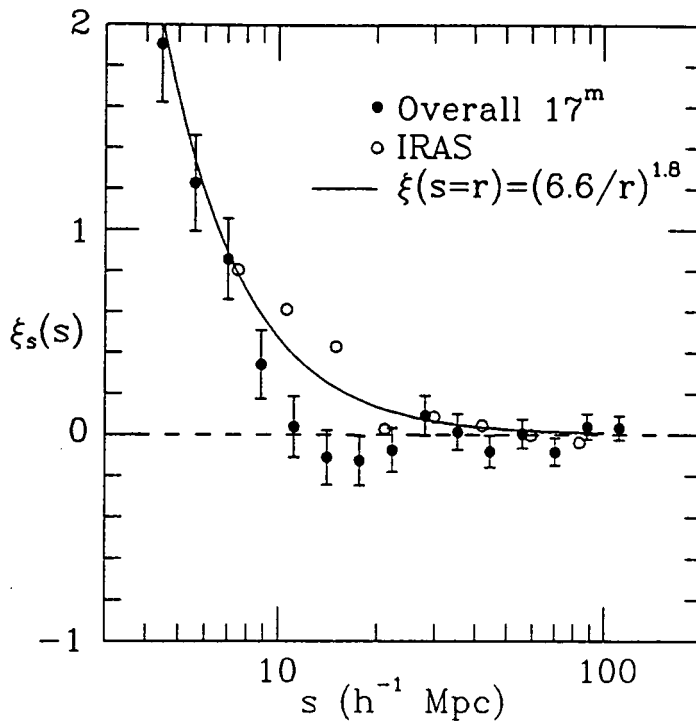
Figure 5.19. A comparison between the overall large-scale form of $\xi_s(s)$ observed in the combined 17^m sample and that found by Efstathiou (1988) for a northern subsample of the QDOT IRAS Survey. The 17^m estimates (solid circles) and model (solid line) are from Figure 5.18.

of the deeper redshift volumes. The exact value of $4\pi J_3$ used was quite a large 13000h^{-3} Mpc^3 which corresponds to $\xi(r)=(5.4/r)^{1.8}$ integrated to 30h^{-1} Mpc (equation 2-46). As can be seen from Figure 5.19 there is very good agreement between these two observations at separations $\geq$20h^{-1} Mpc, with the IRAS sample giving similar estimates for ξ at these scales, but below this separation the larger solid angle survey is again suggesting that the small-scale power law of $\xi(s=r)=(6.6/r)^{1.8}$ (solid line) continues to larger separations as in the CfA and SSRS surveys.

More recently, Efstathiou et al. (1990) have obtained estimates of the volume integral of $\xi_s(s)$ from the entire 1-in-6 QDOT Survey using a new estimator based on the variance in the count of galaxies (see equation 2-43) in spherical shells centred on the observer. This again seems to confirm that a large-scale power law of clustering length r_0=6.6h^{-1} Mpc to 20h^{-1} Mpc is consistent with the observations, in agreement with the preliminary work. The larger value of the clustering length needed at these scales seems at odds with the value of s_0=(4.5$\pm$0.4)h^{-1} Mpc obtained by Davis et al. (1988) for the IRAS galaxies (Strauss and Davis 1988) at smaller (4-5h^{-1} Mpc) separations, and this may be a source for concern. Previously it was noted that the low value of $\xi_s(s)$ at ~5h^{-1} Mpc may be a result of these objects avoiding rich areas of clustering; however, the rise in amplitude as a function of scale may be indicating that the IRAS galaxies have a more complicated clustering distribution than initially thought and at present this is not fully understood.

The discussion so far has concentrated mainly on the distribution of galaxies in complete redshift surveys within the local (z<0.1) volume of space; however, there has been some attempt to study the galaxy distribution at deeper redshifts in smaller areas of the sky, primarily, in order to place constraints on galaxy evolution. Provided these surveys are drawn from complete samples of galaxies in specified areas, then the clustering distributions can be probed for structures on much larger scales than the z<0.1 samples. For example, Broadhurst et al. (1990) have lately claimed that they see, in two, nearly oppositely aligned fields near the SGP-NGP axis, strong periodic peaks in the $\Delta N(z)$ distributions, with inter-peak separations of ~128h^{-1} Mpc in co-moving co-ordinates (q_0=0.5). However, in spite of this quite remarkable result, such structure does not appear to show up as strongly in other fields to a similar redshift of z$\approx$0.5 and an analysis of the two-point correlation function in the 5, 20^m.0<b_J<21^m.5 SGP fields of

Broadhurst et al. (1988) shows that $\xi_s(s)$ is, again, not inconsistent with $\xi(r)=0$ to ~1σ (~0.2) in the range $10<r_{co-moving} \leq 600h^{-1}$ Mpc (Broadhurst 1988).

The situation at nearer distances (z<0.1) is also not clear since the best fit peak positions (x[>0 for NGP]=90+128n, where n=0,±1,±2,... and x is the distance along the SGP-NGP axis) do not seem to coincide with any particularly remarkable structures in these volumes. For example, GSA, GSN and the Parker et al. fields all lie within ~13° of the SGP-NGP axis and the $\Delta N(z)$ distributions for these fields in Figure 3.10 do not show particularly significant peaks at the positions stated. Further, the axis ($\alpha_{NGP} \approx 12.8$hrs, $\delta_{NGP} \approx 27°.4$, and $\alpha_{SGP} \approx 0.8$hrs, $\delta_{SGP} \approx -27°.4$) also passes through the lower declination CfA $m_B<15^m.5$ slice in the north (Figure 3.4, Section 3.2.1, Chapter 3) and the $-30° \leq \delta \leq -17°.5$ part of the SSRS Survey in the south (Figure 3.12). Again, although there is structure around the positions of the peaks suggested by Broadhurst et al. (1990) (the n=0 and n=-1 peaks lie close to the 'walls' described in Section 3.2.1) there is also significant clustering elsewhere and this appears to confuse the simple picture. Indeed it is not clear why, for example, the large known over-density near $z \approx 0$ comprising of the clusters of Virgo, Fornax and Eridanus are not included in the study of Broadhurst et al. (1990).

Other evidence for large-scale structure from deeper redshift volumes may come from the steep slope of the log $\Delta N(m)$ versus m differential number count relation in the Durham/SAAO and Durham/AAT surveys at bright ($b_J \leq 18^m$) magnitudes (see Chapter 3, Section 3.2.3). Previously, it was seen that a no evolution model of the differential $\Delta N(m)$ counts (Shanks 1990) fitted to the deeper data in the range $18^m \leq b_J \leq 20^m.5$ over estimated the counts at bright magnitudes ($14^m \leq b_J \leq 17^m$) by about a factor ~2 and various reasons for this discrepancy were discussed in that section. However, for the purposes of the discussion here it can be considered as to whether this under-density in the redshift survey fields could be caused by large-scale structure or whether it is, perhaps, a likely random fluctuation in the numbers observed.

In Chapter 3, Section 3.2.3 it was shown that the rms field-to-field variation in the count of galaxies in the 14 Durham/SAAO and Durham/AAT survey fields at $b_J \leq 16^m.8$ was ± 2.1deg^{-2} about a mean 5.8deg^{-2} and thus with the assumption that these fields are independently sampling the galaxy distribution, this implies that the total count for 14 fields is underdense with

respect to model count by ~5.8/(2.1/$\sqrt{14}$)≈10 standard deviations. However, it can alternatively be asked, what would the rms fluctuation be on the total count for 14 fields if a model for the count and its variation is assumed.

This question can be answered using the relation in equation 2-71 (Chapter 2, Section 2.1.2.3) between the variance in the counts, the expected mean count and the angular correlation function $\omega(\theta)$. For a power-law spatial correlation function of the form $\xi(r)=(r_0/r)^\gamma$ (equation 2-90) the angular function is given by $\omega(\theta)=A\theta^{1-\gamma}$ (equation 2-91) where

$$A\approx93(r_0/D*)^{1.8} \qquad (5\text{-}3)$$

(θ in degrees) for a Schechter parameter of $\alpha=-1$ and $\gamma=1.8$ (equation 2-92). Equation 2-71 then says that the percentage rms fluctuation in the count N for a single field is

$$\frac{\delta N}{\langle N \rangle} = \frac{\langle (N-\langle N \rangle)^2 \rangle^{1/2}}{\langle N \rangle} = \frac{(1+2\pi N \int_0^{\theta_{eff}} \omega(\theta)\theta d\theta)^{1/2}}{\langle N \rangle^{1/2}} \qquad (5\text{-}4)$$

where the double integral of $\omega(\theta)$ over the small solid angle of the field, $\Delta\Omega$, has been replaced by a single integration of up to an effective separation θ_{eff}, i.e.

$$\int_0^{\theta_{eff}} 2\pi\omega(\theta)\theta d\theta \equiv \frac{1}{\Delta\Omega} \int \int_{\Delta\Omega} \omega(\theta_{12})d\Omega_1 d\Omega_2 \qquad (5\text{-}5)$$

Hence, using equations 2-91, 5-3 and 5-4 with $\Delta\Omega\approx(3°.75)^2$, $\theta_{eff}\approx(3°.75/2)$ and $D*\approx208h^{-1}$ Mpc (obtained for $b_J\leq16^m.8$, $M*\approx-20+5\log_{10}h$ and K=3.0, equation 2-6, Section 2.1.1.1, Chapter 2) as for the Durham/SAAO and Durham/AAT fields

$$\frac{\delta N}{\langle N \rangle} \approx (\frac{1}{\langle N \rangle} + 0.0049\ r_0^{1.8})^{1/2} \qquad (5\text{-}6)$$

Thus, assuming independence of the survey fields equation 5-6 predicts that, with r_0 as large as $6.6h^{-1}$ Mpc, the field-to-field rms fluctuation on the observed counts at $b_J\leq16^m.8$ should be $\pm2.3\deg^{-2}$ about a mean of $5.8\deg^{-2}$, and this is close to what is observed. On the other hand if the mean count is

11.6deg^{-2} the predicted rms fluctuation is ±4.6deg^{-2} and so the 14 fields are then underdense by only ~5.8/(4.6/$\sqrt{14}$)≈4.7 standard deviations.

The decrease by about a factor of 2 in the significance level arises here simply from the fact that δN is scaled up by a factor of 2 to account for the increase in density. However, the underdensity in the 14 fields still appears to be unlikely even in this model. Introducing correlations between the fields might be thought to alleviate the problem since rms fluctuations on the total count for 14 fields will increase through the integral of $\omega(\theta)$ between fields. If, for example, $\omega(\theta)$≈constant, C, at large angular scales then the contribution to the rms fluctuation on the total 14 field count from between fields is δN≈11.6(CN$_F$(N$_F$-1)/N$_F^2$)$^{1/2}$ deg^{-2} (N$_F$=14). Adding this in quadrature to the fluctuation of ±4.6/$\sqrt{14}$=±1.2deg^{-2} implies that to obtain the observed 14 field count as a 2.5σ deviation the constant C has to be ~0.03 and thus if $\xi(r)$ was similarly a constant at large scales equation 2-85 (Chapter 2, Section 2.1.2.4) predicts that $\xi(r)$ is similarly ~0.03 in the range 10<r<100h^{-1} Mpc.

Whilst the observations of $\xi_s(s)$ in the combined sample of the Durham/SAAO, Durham/AAT and Parker et al. surveys may not be able to exclude such a low level of clustering over such a scale, this may not be so if the clustering is more concentrated into a smaller separation. For example, if this structure at large scales was contained in a single peak in $\xi(r)$ between separations of 50 and 60h^{-1} Mpc, and ξ was zero elsewhere, then to obtain the same effective J$_3$ as having a constant ξ of order 0.03 between 10 and 100h^{-1} Mpc, the peak would have to be ξ≈11 at this scale, and this is clearly excluded by the data. Similar constraints on the large-scale correlation function may now also be obtained from the observed estimates of $\omega(\theta)$ (see below).

At present , the evidence for underdensity in the local (z<0.1) galaxy distribution from other bright magnitude (14^m≤b$_J$≤17^m) galaxy counts is not very conclusive mainly because of the difficulty in transforming magnitude systems. Metcalfe et al. (1990b) find, for example, that there is some suggestion that the galaxy counts in the Zwicky (Zwicky et al. 1961-1968) and Kirshner et al. (1978) catalogues lie closer to the extrapolation of the no-evolution model from faint magnitudes. On the other hand the IRAS 60μm source counts at s>1 Jy (Hacking et al. 1987) are again steeper than a no evolution model (D$_{peak}$≈80h^{-1} Mpc for s>1 Jy) but this has been attributed to

evolution. A better understanding of the exact form for these bright galaxy numbers will come from the large area APM (Maddox et al. 1990b,c) and COSMOS (Collins et al. 1988b) galaxy catalogues currently being constructed (see Maddox et al. 1990d). In the mean time it appears that either the low counts in the Durham/SAAO and Durham/AAT surveys have occurred by chance (which seems unlikely unless there is a very significant amount of large-scale structure) or some of the other effects mentioned in Chapter 3 (Section 3.2.3) have caused the apparent underdensity (or it could be a combination of both).

As was discussed in Chapter 2 (Section 2.1.2.4) other constraints on the large-scale galaxy distribution can be obtained from the angular two-point correlation function $\omega(\theta)$ and with the advent of automated plate scanning machines, such as COSMOS (MacGillivray and Stobie 1984) and APM (Kibblewhite et al. 1984), uniform large area catalogues of galaxies can be created which probe deeper depths than current redshift surveys. Thus the aim here is to create statistically large and fair samples of the galaxy distribution which can be used to compare with the data from redshift samples. However, the price paid here lies in the loss of signal-to-noise of the observed correlations, and the difficulty in interpretation (i.e. inversion) of the projected correlation function. For example, the loss in signal-to-noise of the observations means that at large angular scales, where $\omega(\theta)$ is small, the results are more subject to systematic measuring errors than equivalent redshift catalogues and this remains a difficult obstacle to overcome.

In Chapter 2, Section 2.1.2.4 it was shown how at small angles Limber's formula (Limber 1953, Peebles 1980) could be used to predict the form of $\omega(\theta)$ for any spatial function $\xi(r)$. In Figure 5.20, the solid model line is the projection, via equation 2-88, of the three power-law model for $\xi(r)$ (Figure 5.13, Section 5.1.3) which is a convenient simplistic representation of the observed correlation function in the combined Durham/SAAO, Durham/AAT and Parker et al. surveys. Here the projection is carried out at the $m_B < 15^m.0$ depth of the Zwicky Catalogue ($D^* = 76h^{-1}$ Mpc, $\alpha = -1$) where the Euclidean version of Limber's equation is applicable. Also shown is a similar model (dashed line) in which $\xi(r) = (4.5/r)^{1.8}$ to the break-scale at $7h^{-1}$ Mpc followed by a rapid decline of $\xi(r) = (6.3/r)^{7.5}$; i.e. a model which does not contain a shoulder feature in $\xi(r)$.
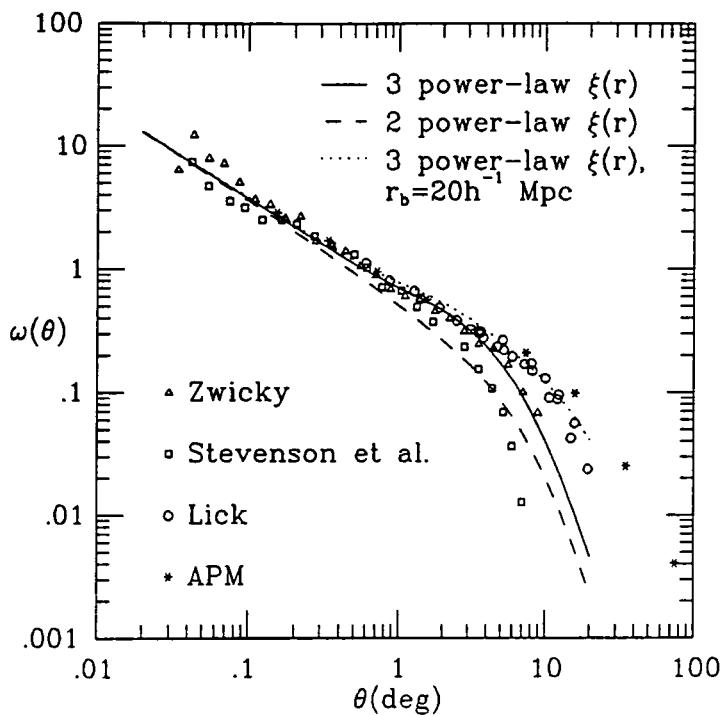
Figure 5.20. A comparison between the observations of $\omega(\theta)$ at the Zwicky depth and models based on Limber's formula. The observations of $\omega(\theta)$ are as discussed in the text. The solid line is a projection, via equation 2-88 (Section 2.1.2.4, Chapter 2), of the three power law $\xi(r)$ in Figure 5.13. The dashed line is a similar model that omits the shoulder in $\xi(r)$. The dotted line is the three power law model but with a break at 20 rather than $7h^{-1}$ Mpc.

For comparison with these models are shown observations of $\omega(\theta)$ as in Figure 2.3 of Chapter 2, together with the more recent estimates of this function from the APM (Maddox et al. 1990a) southern galaxy catalogue. In the case of the deeper galaxy catalogues the results have been scaled to the Zwicky depth using curvature dependent equivalents of the scaling relation in equation 2-88.

Firstly, both the solid and dashed model lines agree quite well at angular separations of up to 1° and this is consistent with the fact that the spatial correlation functions are equal at around this equivalent spatial scale ($\sim 1h^{-1}$ Mpc). At larger angular separations, however, the models are somewhat different with the dashed model line again showing the behaviour seen in Figure 2.3 of Chapter 2, in that the break in $\omega(\theta)$ appears to occur at a smaller angular separation than might be expected on the basis of the peak in the $d\langle N(z)\rangle$ distribution (the predicted angular break-scale is $\theta_{break} \approx (7/50)(180/\pi) \approx 8°$ whereas the observed $\theta_{break} \approx 3°$) and this is a result of the smoothing of the power-law $\xi(r)$ below $r=7h^{-1}$ Mpc with the break in projection. A similar situation also seems to occur with the three power-law function and here the quite pronounced spatial feature is quite effectively washed out in $\omega(\theta)$ (Bean 1983), so that, with the added observational error, it might not be easy to distinguish this model from one with a single power-law $\xi(r)$ to a larger spatial break-scale.

Thus the extra power in the spatial correlation function coming from the shoulder feature in $\xi(r)$ between 2 and 7 h^{-1} Mpc may show up in the angular function as an increased break-scale in $\omega(\theta)$, and hence the more rapid decline of the dashed model in Figure 5.20 may be boosted up by the extra feature in $\xi(r)$. This has already been noted by Soneira and Peebles (1978) in their static simulations of the Lick Catalogue where they included a shoulder in $\xi(r)$ at $\sim 10h^{-1}$ Mpc to obtain a better fit to the roll-off in $\omega(\theta)$ at the break-scale and a better visual map of the Lick data. Similarly Fall and Tremaine (1977) concluded that it was quite easy to hide quite significant features in $\xi(r)$ below ~ 10 h^{-1} Mpc in the presence of a break at larger separations.

Turning now to the observations of $\omega(\theta)$ in Figure 5.20, it can be seen that there is reasonably good consistency between the estimates of $\omega(\theta)$ and the predictions of the models at angular separations below $\theta \approx 1°$. At angular

scales larger than ~1° the estimates of $\omega(\theta)$ are quite diverse and the break-scale ranges from ~3° in the catalogue of Stevenson et al. (1985) to ~20° in the APM Survey (corresponding to roughly 3 and 17h^{-1} Mpc respectively with r=θD$_{peak}$). The predicted form of $\omega(\theta)$ from the redshift surveys seems to lie somewhere in between these results and does not appear to be excluded by the observations.

The current debate concerning $\omega(\theta)$ centres around its observed form at large angular scales. Since $\omega(\theta)$ is small (~0.1 at $\theta\approx 10°$) at these separations it is possible that the variations in the observed positions of the break arise through systematic errors in the construction of the galaxy catalogues. Since all the catalogues discussed have been prepared from many inter-meshed photographic plates there is always the possibility that differences in counting efficiency from plate-to-plate (arising from variations in photographic sensitivity, observing conditions, etc.) may permeate the catalogue as large-scale gradients in the mean density (Groth and Peebles 1977). As seen in Chapter 2, Section 2.1.2.3 such gradients can lead to errors of the form equivalent to equation 2-56 and thus where $\omega(\theta)$ is small at large angular scales such variations may lead to the uncertain break-scale in the observed data.

For example, as the Lick Catalogue was generated by different observers counting galaxies from uncalibrated plates it has been criticised extensively as a data base for statistical studies of the galaxy distribution (Geller et al. 1984, de Lapparent et al.1986b). However, Maddox et al. (1990a) claim that the difference between the break scale in this and the APM Catalogue is a result of Groth and Peebles (1977,1986a,b) over filtering the Lick Catalogue to remove large-scale gradients in the data and, thus, Maddox et al. believe that such large-scale gradients in the APM Catalogue are real gradients in the galaxy distribution. Recent estimates of $\omega(\theta)$ from the Durham/ROE Southern Galaxy Catalogue appear to confirm this larger break scale although earlier estimates (Collins et al. 1988a) gave better agreement with that from the Zwicky catalogue.

The implied break-scale ~20h^{-1} Mpc in the APM data would be in better agreement with the similar break-scale observed in $\xi(r)$ in the IRAS (Efstathiou 1988, Efstathiou et al. 1990) and CfA (m$_B$<15^m.5) samples. For example, the dotted model line in Figure 5.20 is the same model as in Figure

5.13 of Section 5.1.3 except that the break has been moved to 20 h^{-1} Mpc. This shows that even this model (which has a large break and a shoulder feature in $\xi(r)$) still underestimates the degree of large-scale structure seen in the APM Catalogue. However it remains to be seen if this extra large-scale power is really present in the data.

Turning now to other measures of large-scale structure, the galaxy-galaxy two-point correlation estimates from the combined sample of the Durham/SAAO, Durham/AAT and Parker et al. surveys is very much lower than the rich (richness class ≥ 1) Abell cluster-cluster correlation function determined using similar techniques to the galaxy correlation function (Bahcall and Soneira 1983, Klypin and Kopylov 1983). In Figure 5.21 the galaxy correlation estimates of Figure 5.18 are compared to a power law of the form $\xi_{cc} \approx (25/r)^{1.8}$ that is observed to match the cluster-cluster estimates out to ~50 to 100 h^{-1} Mpc and the amplitude of ξ_{cc} can be seen to be a factor of ~11 times larger than the galaxy result. Thus, if rich Abell clusters are accurate tracers of the mass distribution then this result would seem to indicate that the Universe is considerably more inhomogeneous than the observations of the galaxy distribution would suggest. However, rich Abell clusters contribute only a small fraction to the total number of observed galaxies (only 2-5% of galaxies lie within an Abell radius of a cluster centre; Bahcall and Soneira 1983) and in some sense they must represent extreme aspects of the distribution of galaxies. Recently it has been shown that (Kaiser 1984) if Abell clusters form at the peaks of a Gaussian density field then the cluster correlation function can be biassed high with respect to the galaxy correlation function by a simple amplitude factor which is comparable to the observed ratio of $((r_0)_{cc}/(r_0)_{gg})^{1.8}$. This mechanism is similar to that used to obtain realistic models of the galaxy distribution in Cold Dark Matter (Davis et al. 1985)

On the basis that this biassing model was correct this would still seem to suggest that $\xi_{gg}(r)$ continues as a power law out to separations of ~50h^{-1} Mpc (where $\xi_{cc}(r)$ lies above the noise, Kaiser 1986a) and this again implies more large-scale structure than is observed in the galaxy correlation function (see Figure 5.20). Nevertheless there is some evidence that the cluster-cluster function may not be as high as expected due to possible biasses in the selection of the clusters in 2-dimensions (Sutherland 1988). 2-d selection tends to pick out over-densities that lie close together on the sky
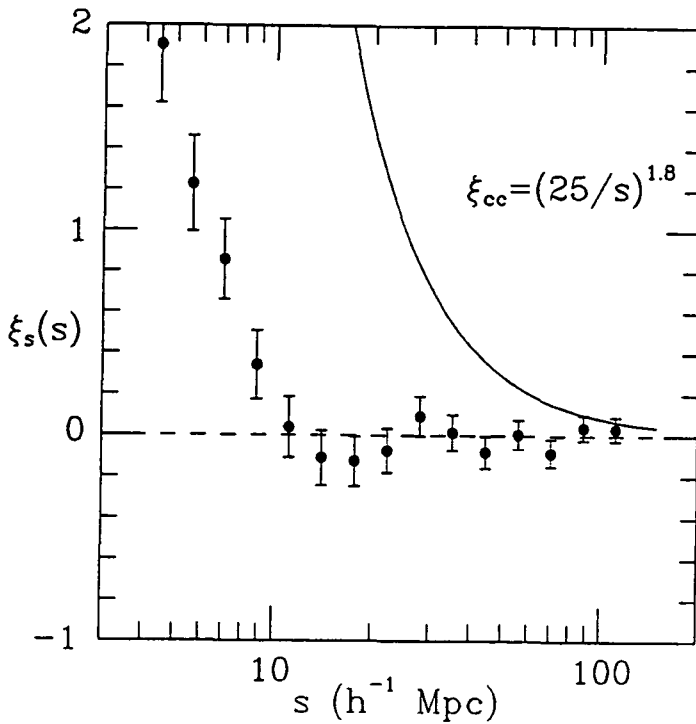
Figure 5.21. The form of the rich Abell cluster correlation function compared to the overall large-scale galaxy correlation function $\xi_s(s)$ estimated from the combined sample of the 17m surveys. The galaxy correlation estimates are as in Figure 5.18. The solid line is a power law with a clustering length of 25h⁻¹ Mpc.

(e.g. Lucey 1983) and this may artificially raise the correlation of clusters at large-scales. Thus, until more objective catalogues of clusters become available, and a better understanding of how the cluster distribution is related to that of the galaxies, it may be wise to view the cluster result with some caution.

The lack of evidence for large-scale structure at the ~2σ ($\xi \approx 0.1$ to 0.2) confidence level in the galaxy correlation function (Figure 5.18) is in better agreement with that of the QSO's (Shanks et al. 1987, Shanks and Hale-Sutton 1988). In the range $10 < r < 100h^{-1}$ Mpc the QSO correlation function of Shanks and Hale-Sutton (1988) is again consistent with $\xi(r)=0$ to the 1σ ($\xi \approx 0.4$ at $10h^{-1}$ Mpc to ≈ 0.05 at 100 h^{-1} Mpc) confidence level and similarly at larger scales to ~$1000h^{-1}$ Mpc. Although QSO's are believed to exist in regions of clustering somewhere intermediate between Abell clusters and galaxies (Yee and Green 1984) these objects do not show a tail of correlations to large scales as seen in the rich Abell clusters.

Other more indirect constraints on large-scale structure come from the isotropy measurements of the cosmic X-ray and microwave background radiations (Rees 1980). The cosmic X-ray background is believed to be generated by sources within the redshift range $1 \leq z \leq 10$ and as such its isotropy may help to constrain large-scale structure on scales of a ~100 to ~1000 h^{-1} Mpc. Measurements of the X-ray background by the HEAO-I satellite suggested that the energy spectrum in the 3-50 keV range could be adequately fitted by thermal bremsstralung from a diffuse plasma at a temperature of 45keV (Marshall et al. 1980) but observations from the lower energy (0.5-3 keV) but higher spatial resolution Einstein Observatory (HEAO-II) has provided evidence that point sources such as active galactic nuclei (quasars, seyfert galaxies, etc.) may contribute significantly to the X-ray background.

Thus, to use the observed isotropy upper limits on the X-ray background to constrain large-scale (≥ 10 h^{-1} Mpc) structure (for example, HEAO-I measured rms fluctuations in the observed intensity of $\Delta I/I < 2$-3% on scales of 5°; Schafer and Fabian 1983) it is essential to know how much different sources contribute to the total intensity observed (i.e. their luminosity function), how those sources evolve in luminosity and number density, and what contribution (if any) small-scale clustering (and its evolution) contributes

to the fluctuations. A further complication is, that, like the variance in the counts of galaxies (equation 2-43, Chapter 2, Section 2.1.2.3), in a large volume the isotropy can measure anti-clustering as well as clustering and so it is possible to obtain quite small limits on the isotropy and yet significant fluctuations in $|\xi|$. Attempts to constrain large-scale clustering models (e.g. Mészáros and Mészáros 1988) with models containing voids ~30h^{-1} Mpc (de Lapparent et al. 1986a) conclude that such models approach or just exceed the upper limits on the isotropy.

The degree of isotropy of the Cosmic Microwave Background has long been recognised as placing quite stringent constraints on the homogeneity of the mass distribution at large-scales (see e.g. Kaiser and Silk 1986 for a review). In the general interpretation, fluctuations in the black-body microwave temperature T observed at the current time are an 'imprint' of the fluctuations in the coupled matter-energy density at the time just prior to, and during the epoch (at a redshift $z_d \approx 1000$) where free electrons 're-'combine with baryonic matter. After this epoch the small scattering cross-section of the newly formed neutral particles meant that photons could arrive virtually unimpeded to the current day observer.

Thus, if the rms fluctuations in the temperature, $\Delta T/T$, are observed over an angular scale θ on the sky, then this angle is approximately related to a proper scale length d at a redshift z ($z \gg 1/\Omega_o$) by

$$\theta \approx \frac{H_o d}{c} \frac{\Omega_o z}{2}$$

(5-7)

where Ω_o and H_o are the current values of the density parameter and Hubble's constant, respectively, and c is the velocity of light. This model is roughly applicable up to redshifts z_{eq} where matter and radiation contributed equally to the energy density

$$1+z_{eq} = 4.2 \times 10^4 (T/2.7)^4 (\Omega_o h^2)$$

(5-8)

(T is in Kelvin and H_o=100h kms^{-1} Mpc^{-1}) and so $z_d < z_{eq}$ for $(T/2.7)^4(\Omega_o h^2) > 0.024$. Hence, equation 5-7 can be used to predict the current day co-moving scale to which the measurement angle θ corresponds. Since the equivalent co-moving scale at the current epoch is

$$d_0 = (1+z)d \tag{5-9}$$

this implies that for θ in arc minutes

$$d_0 \approx 1.8\theta(\Omega_0 h)^{-1} \text{ Mpc} \qquad (z \gg 1/\Omega_0) \tag{5-10}$$

Since galaxies are strongly correlated on scales of up to $d_0 \approx 10h^{-1}$ Mpc, the above relation (equation 5-10) seems to indicate that clues to the origin and formation of galaxies can be seen in temperature fluctuations on scales of up to 5-6 arc minutes. However, the evolution of the matter distribution at this scale is expected to be strongly non-linear and so it is not trivial to relate the clustering observations of galaxies today to the earlier density fluctuations. At larger ($\geq 10h^{-1}$ Mpc) spatial scales the evolution of the mass is expected to be linear and so it is possible, for example, to take the upper limit on the clustering measured from the combined sample of the Durham/SAAO, Durham/AAT and Parker et al. surveys and compare it to the upper limits on the fluctuations in the microwave background at the equivalent angular scale.

In Section 5.2.1 it was seen that the measured 2σ (~95% confidence) upper limit on the present day clustering was $\xi_0 < 0.2$ at ~$10h^{-1}$ Mpc ($\theta \approx 5.7\Omega_0$ arc minutes) and $\xi_0 < 0.1$ at ~$100h^{-1}$ Mpc ($\theta \approx 56\Omega_0$ arc minutes). If galaxies are accurate tracers of the mass distribution and $\delta\rho/\rho_b$ evolves in a linear fashion then

$$(\delta\rho/\rho_b)_{z_d} \approx (\xi_0)^{1/2} (1+z_d)^{-1} \tag{5-11}$$

for an $\Omega_0 = 1$ Universe since $\xi \approx (\delta\rho/\rho_b)^2$ and $\delta\rho/\rho_b$ grows like $t^{2/3} \propto (1+z)^{-1}$ (Chapter 2, Section 2.2). If it is assumed that, just prior to recombination, fluctuations in the density were adiabatic then

$$(\Delta T/T)_{z_d} \approx \frac{1}{3} (\delta\rho/\rho_b)_{z_d} \tag{5-12}$$

and so using equations 5-11 and 5-12 an upper limit of $\xi_0 < x$ now implies that at $z = z_d$ an upper limit in $\Delta T/T$ of

$$(\Delta T/T)_{z_d} < \frac{1}{3} x^{1/2} (1+z_d)^{-1} \tag{5-13}$$

Thus the equivalent upper limits on $\Delta T/T$ at $z \approx z_d \approx 1000$ from

observations of galaxy clustering at the current epoch are 1.5×10^{-4} at $\theta \approx 6$ arc minutes to 1.1×10^{-4} at $\theta \approx 1°$ and this is close to but a little above what the upper limits are observed to be (see, for example, Wilkinson 1988). If galaxies are biassed tracers of the mass distribution (as is required, for example, if the virial estimate of $\Omega_0 \approx 0.2$ is to be reconciled with $\Omega_0 = 1$, see Chapter 4, Section 4.5) then the upper limit on $\delta\rho/\rho_b$, and hence $\Delta T/T$, needs to be reduced by a factor of $\sim\sqrt{5}$.

Whereas such simple numerical calculations can be used to predict the order of size of the fluctuations in the microwave background, exact calculations require a knowledge of the spectrum of density irregularities, the processes that couple matter and radiation, the dominant mass particles (whether these be baryons, neutrinos and so on), etc. (more will be said about this in Section 5.3). However, at spatial scales larger than the horizon at decoupling the fluctuations in $\Delta T/T$ have a relatively simple form since processes like scattering become causally unimportant. As shown first by Sachs and Wolfe (1967) fluctuations in $\Delta T/T$ arise from Doppler frequency changes in photons emerging from within the gravitational potentials of density irregularities at the surface of last scattering. Since the horizon at decoupling has a proper size

$$d_H \approx c t_d \tag{5-14}$$

and the epoch, t_d, of decoupling is given by

$$t_d = \frac{2}{3}(1+z_d)^{-3/2}(\Omega_0 H_0^2)^{-1/2} \tag{5-15}$$

for $|1-1/\Omega_0| < z_d < z_{eq}$, then this implies that at decoupling the Sachs-Wolfe effect is important on angular scales of

$$\theta > \theta_H \approx \frac{1}{3}(\Omega_0/z_d)^{1/2} \text{ radians} \tag{5-16}$$

which corresponds to $\sim 36(\Omega_0)^{1/2}$ arc minutes at $z_d \approx 1000$.

Peebles (1981b) has used the Sachs-Wolfe effect to predict the amplitude of temperature variations arising from uncorrelated clumps of galaxies at large scales assuming galaxies trace the mass distribution.

Expanding the temperature distribution on the sky in terms of spherical harmonics he finds that for $\Omega_o \approx 1$, the amplitude of the quadrupole ($\theta = 90°$) moment has the form

$$a_2 = 2.10 \times 10^{-6} \, \Omega_o^{-0.2} \, \sqrt{J_3} \qquad (5\text{-}17)$$

where the integral over the galaxy correlation function, J_3 (in units of h^{-3} Mpc^3), is given by equation 2-46 (Chapter 2, Section 2.1.2.3) since $\xi(r)$ is assumed to be zero for separations $r > r_{max}$. Current constraints on the observed amplitude of the quadrupole moment suggest that

$$a_2 < y \times 10^{-5} \qquad (5\text{-}18)$$

where y ranges from ~1 to 10 and so with equation 5-17 this implies

$$J_3 < 22.7 \, y^2 \, \Omega_o^{0.4} \, h^{-3} \, Mpc^3 \qquad (5\text{-}19)$$

For example, Fixsen et al. (1983) have measured $y \approx 8.8$ at the 90% confidence level from balloon borne measurements of the quadrupole anisotropy and more recently Strukov et al. (1988) obtained a similar result of $y \approx 3$ from the Relikt experiment aboard the Prognoz-9 satellite (Wilkinson 1988). From equation 5.21 these results suggest that the upper limit on J_3 lies in the range 204 to 1758h^{-3} Mpc^3 with $\Omega_o = 1$ and extrapolating to smaller Ω_o, the limit could be as small as the range 107 to 923 h^{-3} Mpc^3 with $\Omega_o \approx 0.2$. Thus, comparing these upper limits on J_3 with the asymptotic value of ~304h^{-3} Mpc^3 ($r_{max} \approx 20h^{-1}$ Mpc) from the J_3 values in Table 5.1 (Section 5.1.3; these values apply to the combined sample of the Durham/SAAO, Durham/AAT and Parker et al. surveys) it can be seen that these upper limits on the quadrupole moment are becoming very close to what would be predicted from current measurements of galaxy clustering on the assumption that galaxies trace the mass. The Relikt experiment, for instance, seems to be placing quite a severe constraint on J_3 and would seem to exclude a continuation of the power law $\xi(r) = (6.6/r)^{1.8}$ to 20h^{-1} Mpc ($J_3 = 1130h^{-3}$ Mpc^3) as suggested by the CfA ($m_B < 15^m.5$, de Lapparent et al. 1987), IRAS (Efstathiou 1988, Efstathiou et al. 1990) and APM (Maddox et al. 1990a) galaxy surveys, and a continuation to 50h^{-1} Mpc ($J_3 = 3438$ h^{-3} Mpc^3) as suggested by the Abell cluster correlation function. Also, both experiments would seem to rule out $\xi \approx 0.03$ ($J_3 \approx 10233h^{-3}$ Mpc^3) needed to explain the under-density in the bright ($z \lesssim 0.1$) galaxy counts (Chapter 3 Section 3.2.3).

These constraints on $\xi(r)$ from galaxy clustering studies could be alleviated somewhat if, for instance, galaxies were found not to trace the mass distribution or if there was anticlustering at some scale. In the first instance, if galaxies were biassed with respect to the mass so that $\xi^g(r)=b^2\xi^m(r)$ (equation 2-131, see also Section 4.5, Chapter 4) then the quadrupole amplitude predicted from the galaxies would decrease by a factor of ~b (b>1, equations 2-46 and 5-17), and the upper limit on J_3 would increase by a factor of ~b^2. In the second instance anticlustering would lead to negative contributions to J_3 which would tend to cancel the positive J_3 from clustering on smaller scales. In either case such conclusions have an important bearing upon clustering formation and evolution and any further reduction on the upper limits of the quadrupole moment will yield even better limits on the large-scale form of $\xi(r)$. It should be noted, in any case, that, generally, other effects will contribute to the observed quadrupole moment and this tends to make the observed upper limit on a_2 even stronger than quoted here.

Finally, constraints on large-scale ($\geq 1h^{-1}$ Mpc) structure may also come from measurements of large-scale streaming velocities as discussed in Section 2.2.2.2 (Chapter 2). In Chapter 4 the Cosmic Virial Theorem (Peebles 1976a) was used to relate the gravitational potential energy of the galaxy clustering to random peculiar motions at small scales where the galaxy distribution is expected to be in virial equilibrium. The Cosmic Energy Equation (equation 2-145, Fall 1979), on the other hand, can be used to relate all particle peculiar motions to the gravitational potential associated with the clustering of the mass distribution. For example, the observed motion of the Local Group with respect to the Microwave Background of ~600kms^{-1} towards $l^{II}=269°$, $b^{II}=28°$ (see, for example, Lynden-Bell 1987) may constrain the amount of large-scale structure in the local neighbourhood (Davis 1986). Thus, if the one-dimensional frequency distribution for peculiar motions on large scales is given by a Gaussian with an rms width of σ kms^{-1} (see Chapter 2, Section 2.2.1.1) and zero mean, then the probability of observing a galaxy with a three-dimensional velocity $v_p=|\underline{v}_p|$kms^{-1} in the range v_p to v_p+dv_p is given by a Maxwellian distribution;

$$P(v_p)dv_p = \frac{2}{(2\pi)^{1/2}} v_p^2 \exp[-\frac{1}{2}(v_p/\sigma)^2]dv_p \qquad (5-20)$$

Hence, by having an estimate of σ, the probability, say, of obtaining a velocity v_p as small as $600\mathrm{kms}^{-1}$ can be measured.

The expected three-dimensional mean square peculiar velocity, $\langle v_p^2 \rangle$, is related, in this instance, to the one-dimensional width, σ, by

$$\langle v_p^2 \rangle = 3\sigma^2 \qquad\qquad (5\text{-}21)$$

and the Cosmic Energy Equation (equation 2-150) predicts that

$$\langle v_p^2 \rangle^{1/2} \approx 61.2\ \Omega_o^{1/2} J_2(\infty)^{1/2}\ \mathrm{kms}^{-1} \qquad\qquad (5\text{-}22)$$

for $J_2(\infty)$ in h^{-2} Mpc and $K=7/12$ which is intermediate of the range indicated in equation 2-149. If galaxies trace the mass and $\xi(r) \approx 0$ beyond $20h^{-1}$ Mpc, then Table 5.1 (Section 5.1.3) predicts that $J_2 \approx 147h^{-2}$ Mpc for the combined sample of the Durham/SAAO, Durham/AAT and Parker et al. surveys. Thus, using the integral of equation 5-20, equations 5-21 and 5-22 predict that

$$P(v_p < 600\mathrm{kms}^{-1}) = 0.76 \qquad\qquad (5\text{-}23)$$

for $\Omega_o = 0.2$ (equation 4-12, Section 4.4, Chapter 4). In other words, this probability indicates that the observed galaxy clustering at separations $\leq 20h^{-1}$ Mpc and the virial estimate of Ω_o is sufficient to explain the motion implied by the dipole in the microwave background, on the assumption that galaxies trace the mass. A similar result is obtained if galaxies are biassed tracers of the mass distribution and $\Omega_o = 1$ since if $\sqrt{J_2^g} = b\sqrt{J_2^m}$ (equations 2-131 and 2-151), the increase in $\langle v_p^2 \rangle^{1/2}$ due to the larger Ω_o is just balanced by the decrease by a factor of $1/b = (\Omega_o^{eff}/\Omega_o)^{1/2}$ in J_2.

If there is more large-scale structure in the galaxy distribution than is measured in the combined sample then the associated increase in $\langle v_p^2 \rangle^{1/2}$ will make the observed velocity of $\sim 600\mathrm{kms}^{-1}$ a less likely occurrence. With $\Omega_o = 0.2$ and a break in $\xi(r)$ at $20h^{-1}$ Mpc ($J_2 \approx 200h^{-1}$ Mpc)

$$P(v_p < 600\mathrm{kms}^{-1}) = 0.62 \qquad\qquad (5\text{-}24)$$

whereas with a break at $50h^{-1}$ Mpc ($J_2 \approx 257h^{-2}$ Mpc)

$$P(v_p < 600 kms^{-1}) = 0.51 \qquad\qquad (5\text{-}25)$$

The constraint on large-scale structure here is not as strong as the quadrupole constraint from the microwave background mainly because of the weaker dependence of J_2 on r. Thus, for $\xi(r)=(r_0 /r)^\gamma$ for $r \leq r_{max}$ and $\xi(r)=0$ at larger separations $\langle v_p^2 \rangle^{1/2} \propto \sqrt{J_2} \approx r_0^{\gamma/2} r_{max}^{(2-\gamma)/2} \approx r_0 r_{max}^{0.1}$ for $\gamma \approx 1.8$. Further, as with the quadrupole moment, if there is anti-clustering at some scale in the galaxy distribution this will again tend to counteract the positive clustering at smaller scales making it possible to have quite significant structure in $\xi(r)$ but only small resulting peculiar motions.

5.2.3 Discussion

In the previous section it was seen that various other measures of large-scale ($\geq 10h^{-1}$ Mpc) structure seemed to indicate that, perhaps, there were more large-scale correlations in the two-point galaxy correlation function than has been measured in the combined sample of the Durham/SAAO, Durham/AAT and Parker et al. surveys. Whereas the overall $\xi_s(s)$ for this sample (Figure 5.18, Section 5.2.1) exhibits a break in the power law of the form $\xi(s=r)=(6.6/r)^{1.8}$ at $\sim 7h^{-1}$ Mpc, and is consistent with $\xi(r)=0$ at separations larger than $\sim 10h^{-1}$ Mpc, studies of other galaxy samples suggest that this break-scale may continue to 20, 50 or even $100h^{-1}$ Mpc. Although the evidence for structure in $\xi(r)$ to 50 or $100h^{-1}$ Mpc is tenuous, the continued power law to $20h^{-1}$ Mpc seen in the CfA ($m_B < 15^m.5$) slice (de Lapparent et al. 1987), the IRAS Survey (Efstathiou 1988, Efstathiou et al. 1990) and the APM Galaxy Catalogue (Maddox et al. 1990a) needs to be taken seriously and so, in this section, the significance of the break in the combined 17^m surveys is re-evaluated in the light of these observations.

In Figure 5.18 (Section 5.2.1) the observed break from a power law of the form $\xi(s=r)=(6.6/r)^{1.8}$ appeared to be significant at the 2.8 and 2.5 sigma level at $s \approx 14$ and $s \approx 18h^{-1}$ Mpc, respectively, in the overall estimate of $\xi_s(s)$. However, the rms errors indicated in this figure are obtained from simulated catalogues in which the spatial correlation function exhibits a break at $\sim 6h^{-1}$ Mpc and exactly zero correlations on scales larger than $28h^{-1}$ Mpc (see Figure 2.5, Section 2.1.4, Chapter 2). If the break-scale in the simulated galaxy distribution was increased to $\sim 20h^{-1}$ Mpc then this would, via equation 2-51 (see Section 2.1.2.3, Chapter 2), increase the rms error on $\xi_s(s)$ since

the larger average number of galaxies per cluster m (equation 2-45) would necessarily decrease the number of independent clusters in the simulated volumes (for the same mean density n). According to equation 2-45 and 2-46, extending the power law to $20h^{-1}$ Mpc would imply that m would increase by a factor of $\sim(20/6)^{1.2}\approx4$ (provided m»1) and taking equation 2-51 to hold exactly $\delta\xi$ would increase by this factor, given the same number of independent pairs N_p. This would then, of course, make the $\xi_s(s)$ observations consistent with a continued power-law $\xi(r)$ to $20h^{-1}$ Mpc (the significance would be reduced to $\sim(2.8/4)\sigma$ at $s=14h^{-1}$ Mpc) and the constraints on large-scale structure would be less strong.

However, this simplistic model for the rms error on $\xi(r)$ may need to be modified significantly to take account of the shape and selection function properties of the fields belonging to these surveys and so the prediction of a factor of ~4 increase in $\delta\xi$ may not be appropriate. For example, as stated previously in Section 5.1.3, the fields in these surveys are quite well separated on the sky (Figure 3.8, Section 3.2.1, Chapter 3) and so increasing the break-scale to $20h^{-1}$ Mpc will not make the field volumes much less independent ($20h^{-1}$ Mpc corresponds to $\theta\approx8°$ at $D_{peak}\approx137h^{-1}$ Mpc). Thus, the full spherical integral J_3 in equation 2-45 for m should be modified at some scale to a more linear integral (see equation 2-43) to incorporate the narrow shape of the survey fields (and also the bin size) and this smaller value for J_3 will not increase $\delta\xi$ as much as factor of 4 (see Chapter 2, Section 2.1.2.3). As discussed before, the size of the errors shown in Figure 5.18 are in agreement with the field-to-field fluctuations in $\xi_s(s)$ for these surveys (Figures 3.2 and 3.3, Section 3.1.1, Chapter 3) but, again, if considerably more large-scale structure ($\sim50-100h^{-1}$ Mpc) has been missed in these catalogues through the lack of having a fair sample then these errors may be underestimating the true sample variations.

The significance of the break away from a large-scale ($\geq10h^{-1}$ Mpc) power law in $\xi(r)$ and the constraint on large-scale structure is also subject to further uncertainties associated with the estimation of the mean background density of galaxies (Chapter 2, Section 2.1.2.3). The case of clustering induced fluctuations in the background density has already been discussed in Section 5.1.3 while considering the significance of the observed shoulder feature in $\xi_s(s)$. There it was seen that the observed field-to-field variations in the counts at $m(b_J)\leq16^m.8$ in the 14 Durham/SAAO and Durham/AAT fields

was $\pm2.1\text{deg}^{-2}$ about a mean of 5.8deg^{-2} implying, via equation 2-68, an rms error of $\delta\xi\approx(2.1/\sqrt{14})/5.8\approx0.1$ for the within-field $\xi_s(s)$ at large scales. Although this error is comparable to the rms error on the overall $\xi_s(s)$ at $s=14$ to $18h^{-1}$ Mpc (Figure 5.18) and should be added in quadrature to that result (see Section 5.1.3), it is expected that the estimator in equation 2-53 is likely to be less sensitive than this to such clustering dependent fluctuations. With a larger break-scale in $\xi(r)$ of $\sim20h^{-1}$ Mpc it might be expected that the field-to-field variations in the counts would again be increased making this type of error more significant. However, as discussed above the fields are probably independent and narrow enough that the larger break-scale will not lead to much larger variations in the observed counts.

Finally, the overall $\xi_s(s)$ in Figure 5.18 is also subject to a further uncertainty due to the integral constraint which arises from the use of the observed number of galaxies in a survey to normalise the mean background density $n(z)$. In the heuristic model for this effect (Section 2.1.2.3), it is expected that the mean value of the correlation function $\xi_s(s)$ estimated over many equivalent surveys will be biassed low at large scales (where $\xi(r)\approx0$) by a constant $I_c\approx-m/\langle N\rangle$ where $\langle N\rangle$ is the expected number of galaxies in a volume V and m is, as usual, the mean number of galaxies per cluster. As discussed in Chapter 2, Section 2.1.2.3, the difficulty in applying this model to the magnitude limited redshift surveys described here again lies in the dependence of I_c on the field shape and selection function properties of the fields. Using the exact integral constraint appropriate to a magnitude limited redshift survey (equation 2-75) an alternative estimate for I_c was derived which relates I_c to the expected variance in the counts within the survey volume (equation 2-80)

$$I_c \approx -(\delta N/\langle N\rangle)^2 \qquad\qquad (5\text{-}26)$$

where $\langle N\rangle$ is now the expected count within the magnitude limited sample.

The estimates of the within-field correlation function were obtained by normalising $n(z)$ to the numbers of galaxies within each sample and since these estimates for the Durham/SAAO and Durham/AAT surveys dominate the overall $\xi_s(s)$ in Figure 5.18 at $s=14$ and $18h^{-1}$ Mpc equally, it is appropriate to calculate an average value for the integral constraint from these two samples. As discussed above increasing the break-scale to $20h^{-1}$

Mpc will not make the fields in these surveys much less independent and so it is possible to use the model for $\delta N/\langle N \rangle$ discussed in the previous section (equation 5-6) to calculate I_c for fields at this depth. Thus, as the percentage variance $(\delta N/\langle N \rangle)^2$ for N_F fields is $1/N_F$ times the percentage variance for a single field it follows that

$$I_c \approx - \frac{1}{\langle N \rangle} - \frac{0.0049(r_0)^{1.8}}{N_F} \tag{5-27}$$

for the model discussed in Section 5.2.2 (equation 5-6). This is a fairly good approximation since the fields in the two surveys are, on average, the same size and depth. Hence with a model in which $\xi(r) = (6.6/r)^{1.8}$ to a break-scale of $20h^{-1}$ Mpc, equation 5-27 predicts $I_c \approx -0.021$ ($\langle N \rangle = 232$) and $I_c \approx -0.033$ ($\langle N \rangle = 280$) for the Durham/SAAO and Durham/AAT surveys, respectively. On repeated measurements of $\xi_s(s)$ using similar surveys to the Durham/SAAO and Durham/AAT samples a constant of ~0.027 would have to be added to the estimates at large scales to prevent a bias in the data. Adding a constant of this size to the overall estimate of $\xi_s(s)$ in Figure 5.18 only reduces the significance of the break to ~2.6 s.d. at $s = 14h^{-1}$ Mpc and so the continued power law to $20h^{-1}$ Mpc is still rejected on this basis.

It is interesting to point out that there may be other biasses introduced into the data which may counteract the effect of the integral constraint. For example, as discussed in Chapter 2 (Section 2.1.2.3), magnitude errors can cause a positive bias in $\xi_s(s)$ at large scales of the order $(0.6\ln10\langle\Delta m^2\rangle^{1/2})^2$ (equations 2-64 and 2-67) and so an rms magnitude error of the order 0.1 from field-to-field implies a positive bias ~0.02 which is of the same order as the integral constraint above.

Thus, in conclusion, although some other samples of galaxies may indicate that correlations of galaxies extend to ~$20h^{-1}$ Mpc there is still tentative evidence from the 17^m galaxy surveys that $\xi_s(s)$ breaks at a smaller separation of ~$7h^{-1}$ Mpc. From the discussion above it would seem that the errors on the overall $\xi_s(s)$ in Figure 5.18 will still be roughly appropriate even in the presence of a larger break in $\xi(r)$ and so the conclusions in Section

5.2.1 on the constraint on large-scale structure still apply. With the assumption that peculiar motions have little effect on $\xi_s(s)$ at scales greater than a few h^{-1} Mpc this implies $\xi_s(s) \approx \xi(r)$ and together with some knowledge of how galaxies trace the mass, constraints on the large-scale mass distribution can be discussed. This is the subject of the following, and final, section.

5.3 Constraints on evolutionary models of the mass distribution

The aim of this section is to briefly review the current models for the formation of galaxies and to compare the predictions of these models with the observations of galaxy peculiar motions and clustering made in this and the last Chapter. This review is not intended to be comprehensive and for ease of discussion will generally follow the historical development of the subject. The main objective will be to draw attention to the general predictions of each model in terms of the properties measured in the preceding chapters.

In Chapter 2 (Section 2.2) it was implied that most of the large-scale structures that are seen today (ranging from galaxies, groups, clusters and up to superclusters of galaxies) have developed under the influence of gravity from small perturbations in the mass (or energy) density. Whilst the degree of isotropy of the Cosmic Microwave Background (see Section 5.2.2) certainly places quite stringent constraints on the form of perturbation at early epochs in the life of the Universe (the upper limits of $\Delta T/T \leq 10^{-4}$ to 10^{-5} suggest that the upper limits on the density fluctuation are similarly small at a redshift ~ 1000; see equation 5-12), gravitational growth of mass perturbations is not necessarily the most important mechanism for the formation of large-scale structure, although this tends to be the main mechanism considered.

For example, Ostriker and Cowie (1981) have proposed that the formation of galaxies could be quite simply seeded by the interaction of the protogalactic medium with shock waves emitted from explosive events such as the demise of massive stars or the birth of young galaxies or quasars. In their models an energy output of $\sim 10^{54}$ J may produce a shell of galaxies $\sim 10E_{54}^{0.2} h^{-1}$ Mpc in diameter whereas a larger energy output of 10^{58} J (such as may be produced by super-conducting 'cosmic strings', if they exist; Ostriker et al. 1986) may be sufficient to produce large ($\sim 30 h^{-1}$ Mpc) voids

such as those currently seen in the CfA ($m_B < 15^m.5$) slices and the Southern Sky Redshift Survey (see Chapter 3, Section 3.2.1). Further, it is envisaged that the interstitial overlaps of these shells may produce filaments (for 2 shells) or even rich clusters (for 3 shells Ostriker 1988).

At this point it is worthwhile to consider what effects such common large-scale features would have upon the appearance of the auto-correlation function for galaxies. For example, consider the highly symmetric model in which galaxies are found on 'infinite' thin parallel sheets each of width Δx and separated by constant distance L ($\Delta x \ll L$). By symmetry it is easy to show that if galaxies are placed at random within the sheets with average density n, then the mean overall density is just $n\Delta x/L$. The auto-correlation function estimated on the basis of equation 2-27 (Chapter 2, Section 2.1.2.1) is quite simple to evaluate since choosing a random galaxy necessarily places the centre of the pair count on a sheet and by symmetry the pair distribution around that centre looks much the same wherever that centre is, provided $r \gg \Delta x$ or $r \ll \Delta x$. Thus at $r \ll \Delta x$, $DD \approx 4\pi r^2 n\Delta r$ and $DR \approx 4\pi r^2 (\Delta x/L)n\Delta r$ and so $\xi(r)$ becomes

$$\xi(r) \approx \frac{L}{\Delta x} - 1 \qquad r \ll \Delta x \qquad (5\text{-}28)$$

whereas for $r \gg \Delta x$ but $r < L$, $DD \approx 2\pi r n\Delta x \Delta r$ and $DR \approx 4\pi r^2 n(\Delta x/L)\Delta r$ and so

$$\xi(r) \approx \frac{L}{2r} - 1 \qquad \Delta x \ll r < L \qquad (5\text{-}29)$$

This model therefore has the property that $\xi(r)$ approximates a power law of index -1 in the range $\Delta x \ll r \ll L/2$ which then steepens rapidly to become anticorrelated in the range $(L/2) < r \leq L$ with the minimum of the anti-correlation ~ -0.5 at $r \approx L - \Delta x/2$. Peaks in the correlation function occur at regular intervals of $r = nL$ (n=1,2,...) but with decreasing amplitude as n becomes larger due to averaging over an increasing number of sheets. The height of the first peak can be estimated from the area of the pair-count shell that intersects sheets on either side of the pair-count centre. From the geometry, the pair count could be as large as $DD \approx 6\pi L n\Delta x \Delta r$ and so $\xi \approx 0.5$ at $r \approx L$. Thus, this model seems to reproduce some of the features observed in the galaxy correlation function of the 17^m redshift surveys.

For example, in Figure 5.22 the within-field correlation function estimates $\xi_s(s)$ for the combined Durham/SAAO, Durham/AAT and Parker et al. surveys (Figures 5.7 and 5.16) is compared to the model with a sheet separation of L=28h^{-1} Mpc and thickness Δx=3h^{-1} Mpc (solid line) similar to the suggestions made by de Lapparent et al. 1988 in their void analysis of the CfA m$_B$<15^m.5 NGP slices (see Chapter 3, Section 3.2.1). It is quite remarkable how using this model with its single parameter L (as long as Δx«L) can reproduce both the slope and amplitude of $\xi(r)$ at small ($\leq$10h^{-1} Mpc; see (a)) scales and the positions of the tentatively observed anti-correlation and peak at larger scales (see (b)). However, it appears that the amplitude of these larger scale features is much stronger in the model and if such structures were present in the data they would probably have been detected at this signal-to-noise.

Thus, this simple picture illustrates that quite significant amounts of large-scale structure in $\xi(r)$ can be generated using geometrical models of this type and it would be worthwhile to constrain more sophisticated models of such bubble or frothy-like distributions by analysing $\xi(r)$ and comparing it with the observed $\xi_s(s)$ data (see Pierre et al. 1988 and Bahcall et al. 1990). However, it should be recalled that dynamic and static simulations of clustering with no ($\geq$10h^{-1} Mpc) large-scale structure can produce quite acceptable replicas of the observed galaxy distribution (see Figure 3.4, Section 3.2.1,Chapter 3).

The explosion scenarios of Ostriker and Cowie (1981) may, in any case, be excluded on the basis of observations of the Microwave Background. In the first instance large voids ~30h^{-1} Mpc may generate fluctuations in $\Delta T/T$ which are above the current upper limits at small scales (Vishniac and Ostriker 1986, see also Section 5.2.2). In the second instance, the large amount of energy input into the proto-galactic medium may lead to spectral distortions of the background (Ostriker and Thompson 1987) which are in excess of what has recently been observed by the Infrared satellite COBE. Thus, although these particular models of large-scale structure may be excluded on the basis of these observations it should be remembered that hydrodynamic processes play an important rôle in galaxy formation since most of the objects that are 'seen' today have been formed by such mechanisms. In the discussion below it will be seen, however, that such processes are all too often neglected in the non-linear regime as a result of

Figure 5.22. The parallel plane model discussed in the text as compared to the overall within-field correlation function estimated from the combined sample of the Durham/SAAO, Durham/AAT and Parker et al. surveys. This solid model line approximately describes the correlation function of thin parallel sheets that are large in extent.

(a) Small scales

- Overall 17^m
— Plane model

$\xi_s(s)$

s (h^{-1} Mpc)

(b) Large scales

— Plane model
- 17^m within-field

$\xi_s(s)$

s (h^{-1} Mpc)
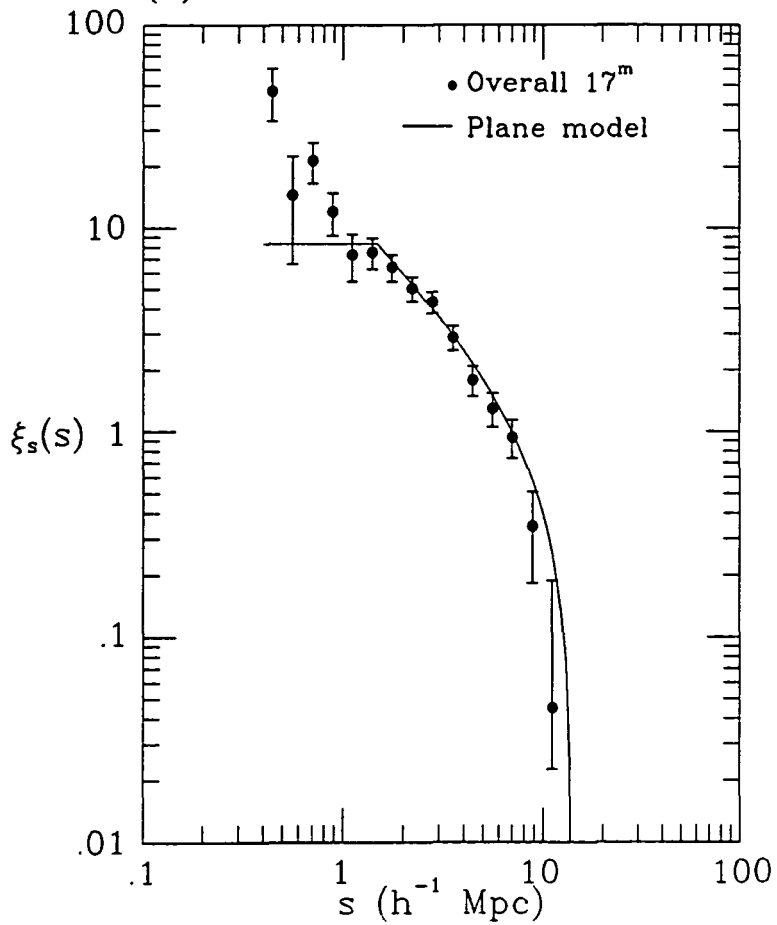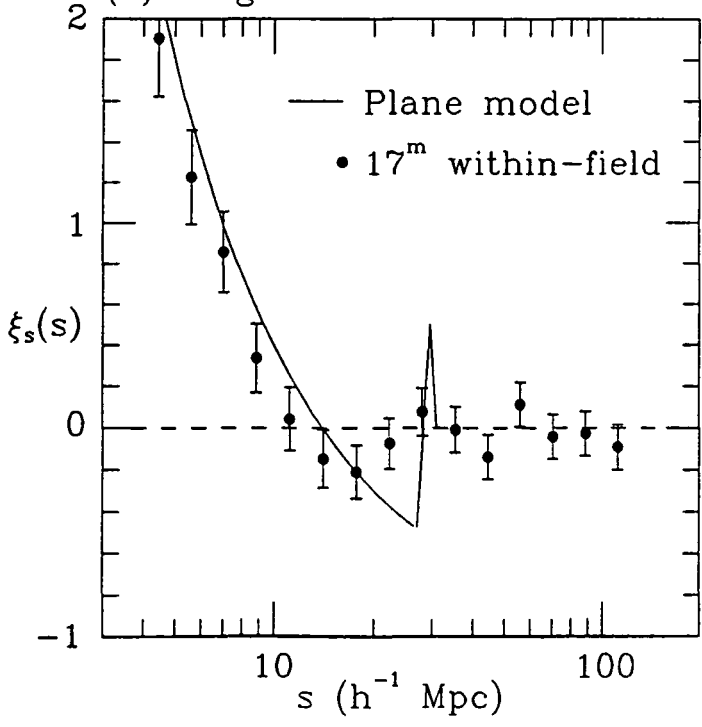
the complexity of calculation.

On the assumption that large-scale structure has evolved by gravitational growth of small ($\delta\rho/\rho_b \ll 1$) mass or energy perturbations the evolution can be followed in a reasonably straight forward manner, up to the point where $\delta\rho/\rho_b \approx 1$, since the equations of motion can be dealt with in linear theory (see also Chapter 2, Section 2.2). Generally, the evolution of $\delta\rho(\underline{x},t)/\rho_b$ at a certain position $\underline{x}$ and at cosmic time t is monitored in Fourier space

$$\delta_{\underline{k}}(t) = f\, (\delta\rho(\underline{x},t)/\rho_b) \qquad (5\text{-}30)$$

where f represents the spatial Fourier transform. Thus, if $\delta\rho(\underline{x},t)/\rho_b$ is a plane wave with wavelength λ, this corresponds to a single frequency $k=2\pi/\lambda$ in Fourier space. The two-point correlation function of the matter perturbations at time t is just

$$\xi^m(r,t) = f^{-1}(\langle|\delta_{\underline{k}}(t)|^2\rangle) \qquad (5\text{-}31)$$

where $\langle|\delta_{\underline{k}}(t)|^2\rangle$ is referred to as the power spectrum of density perturbations.

It is generally assumed that in the absence of any process that picks out a particular spatial scale the initial power spectrum is taken to be a power law of the form

$$\langle|\delta_{\underline{k}}(t)|^2\rangle = Ak^n \qquad -3 < n < 4 \qquad (5\text{-}32)$$

where A is an undetermined amplitude. This specifies the initial two-point function $\xi^m(r)$ but not its amplitude. The initial conditions for the higher order moments of the galaxy distribution (see Chapter 2, Section 2.1.1) are generally set to zero by assuming random phases between the Fourier components $\delta_{\underline{k}}(t)$. This makes the frequency distribution of mass within a random volume V Gaussian with a width set by equations 5-31 and 5-32. The favoured index n for the power spectrum in equation 5-32 is n=1 which is referred to as the Harrison-Zel'dovich spectrum (Harrison 1970, Zel'dovich 1972). This power law has the property that, whilst all the other permitted spectra cause a divergence in the space-time geometry at either large or small wavelengths, this spectrum diverges logarithmically at both limits.

This constant curvature spectrum seems to come quite naturally out of Grand Unified Theories of matter which predict an inflationary phase (e.g. Guth 1984) of the Universe at epoch $t \approx 10^{-35}$s. The spectrum is then a result of quantum noise generated in at very early times in the life of the Universe. Inflationary phases of the Universe also allow a way out of (see, for example, Guth 1986) the so called 'flatness' problem (why the microwave background appears to be so isotropic when initially the different parts of the Universe which generated it were not causally connected) and the 'fine tuning' of Ω_0 (if Ω_0 is close to unity at the present epoch it will be infinitely close to unity at very early times). Thus $n=1$ is the only spectrum with some physical justification.

Thus with the initial set of conditions and the linearised equations of motion for the density perturbation (which incorporate all the relevant physical processes, such as the coupling between matter and radiation, damping, etc.) it is possible to follow the evolution of the perturbation up to the time when $\delta\rho/\rho_b$ becomes ~1. In this regime the resulting power spectrum at some late time t can be written as

$$\langle|\delta_{\underline{k}}(t)|^2\rangle = T_{\underline{k}}\,\langle|\delta_{\underline{k}}(t)|^2\rangle \qquad (5\text{-}33)$$

where $T_{\underline{k}}$ is the transfer function. Of particular interest is the evolution up to the epoch of decoupling of matter and radiation since at later times dissipation processes are negligible and so $\delta_{\underline{k}}(t)$ evolves like

$$\delta_{\underline{k}}(t) = \frac{A(t)}{A(t_d)}\,\delta_{\underline{k}}(t_d) \qquad (5\text{-}34)$$

(see equation 2-112, Chapter 2, Section 2.2). Thus the imprint of the fluctuations at $t \approx t_{dec}$ may be visible in the linear regime part of $\xi^m(r)$ observed today.

Initial attempts to model the formation of galaxies centred on baryonic matter as the main component for the mass density with either adiabatic or isothermal perturbations prior to decoupling. Adiabatic perturbations are fluctuations in the mass and photon distributions which conserve the number of photons per mass particle, whereas isothermal perturbations just involve fluctuations in the mass density. The isothermal model became very popular in the early 1970's as a result of the apparent scale-free nature of the angular

two- and three-point correlation functions being observed from galaxy catalogues at that time (see Section 2.1.2.4, Chapter 2 and Section 5.2.2), and from the low rms variations predicted in the temperature fluctuations in the microwave background at scales of arc minutes. In this model fluctuations in the mass density at scales below the horizon are prevented from growing by the viscosity between the photons and electrons. Thus, after decoupling at $z_d \approx 1000$ the spectrum of irregularities in equation 5-32 is preserved and the first objects that could collapse under gravity and overcome their internal gas pressure have a mass greater than

$$M_J \approx 5 \times 10^5 \Omega_o^{-1/2} \, h^{-1} \, M_{sun} \qquad\qquad (5\text{-}35)$$

where M_J is the Jean's mass of the matter density just after the time of decoupling. It was therefore invisaged (see Peebles 1980 Section 26) that the first objects to form had masses $\sim 10^5 \, M_{sun}$ and that these clustered together hierarchically thus generating apparently scale-free (or uniform power law) correlation functions.

In this hierarchical model (Davis et al. 1977) the index of the two-point correlation function power law (equation 2-90) generated from a power spectrum of the type in equation 5-32, is, in the non-linear regime,

$$\gamma = \frac{9+3n}{5+n} \qquad \Omega \approx 1 \qquad\qquad (5\text{-}36)$$

and so with an observed slope of $\gamma \approx 1.8$, the implied spectral index is $n \approx 0$, which corresponds to Poisson noise initial conditions.

As has been seen in Section 5.1.3, the observed spatial galaxy correlation function seems to indicate that there is in fact a strong feature in $\xi(r)$ at $\sim 2h^{-1}$ Mpc which was previously hidden in the observations of $\omega(\theta)$ as a result of projection effects. In spite of the fact that this single observation weakens the arguments for a hierarchical model (favouring instead models in which there is a proto-cluster scale length), such mechanisms still play an important rôle in many of the currently favoured models for galaxy formation (see below). The isothermal model became unfavourable in the early 1980's when it was realised that, at early epochs, isothermal perturbations could not survive the period when the baryonic matter was in equilibrium with the photons (Weinberg 1979). However, Peebles (1987) has recently revised this

model by assuming that the fluctuations are isocurvature, i.e. that fluctuations in the matter and radiation are such that the local curvature of space is constant. Although this loses the simplicity of the original hierarchy there is a suggestion that this formation picture could lead to a feature in $\xi(r)$ at $\sim 5h^{-1}$ Mpc.

In contrast to the isothermal model, baryonic adiabatic perturbations give rise to several scale lengths in the matter distribution after decoupling of matter and radiation (Peebles 1981c). The afore mentioned Jean's scale λ_J divides those perturbations which undergo uninterrupted growth up to the time of decoupling $(\lambda > \lambda_J)$ from those perturbations which oscillate like acoustic waves $(\lambda < \lambda_J)$. The present size of the Jean's scale just prior to decoupling is (Peebles 1980)

$$\lambda_J \approx 50 \ (\Omega_o h^2)^{-1} \ \text{Mpc} \tag{5-37}$$

and this feature in the power spectrum $\langle |\delta_{\underline{k}}(t_d)|^2 \rangle$ will lead to structure of about this scale in the currently observed correlation function. At smaller scales the acoustic behaviour of the perturbations will be damped by photons streaming out of the density enhancements (Silk 1967) and so modes with wavelengths smaller than

$$\lambda_s \approx \frac{2}{0.036 + \Omega_o h^2} \ \text{Mpc} \tag{5-38}$$

just prior to decoupling are severly damped. Thus, the cut off in the power spectrum at $k > 2\pi/\lambda_s$ similarly introduces a feature in $\xi^m(r)$ at about the scale of λ_s. The acoustic oscillation of perturbations with wavelengths $\lambda_s < \lambda < \lambda_J$ may also lead to a further, single peak in $\xi^m(r)$ at

$$r \approx 2w \approx 68(\Omega_o h^2)^{-1/2} \ \text{Mpc} \quad (n=4) \tag{5-39}$$

since the power spectrum $\langle |\delta_{\underline{k}}|^2 \rangle$ has a sinusoidal form

$$\langle |\delta_{\underline{k}}|^2 \rangle \propto \cos^2(wk) \tag{5-40}$$

in this range at decoupling.

As pointed out by Shanks (1985) the baryon dominated adiabatic model looks to be quite a promising way of providing quite a wide range of structures in the two-point correlation function. If $\Omega_o h^2$ is of order unity and h lies in the currently acceptable range of 0.5<h<1 then according to equation 5-38 the Silk scale is quite close to the position of the shoulder observed in $\xi_s(s)$ assuming galaxies trace the mass (see Section 5.1.3). Further, these values of $\Omega_o h^2$ and h will also put the features predicted at larger scales into the range where similar tentative peaks and troughs have been observed in the range $10 \lesssim s \leq 100h^{-1}$ Mpc (see Section 5.2.1). However, in spite of these attractive possibilities for $\xi(r)$ this model has been taken to be excluded by the constraints placed on it due to the upper limits on the fluctuations in the microwave background at a few arc minutes (Uson and Wilkinson 1984) and by nucleosynthesis in the Big Bang. To match the abundance of light elements this latter constraint requires (see, for example, Olive et al. 1981)

$$\Omega_o^{baryon} h^2 < 0.05 \qquad\qquad (5\text{-}41)$$

and so with the currently favoured value of $\Omega_o=1$ (see Section 4.5, Chapter 4 for a discussion) for the mean mass density parameter (as required if the Universe passes through an inflationary epoch) h is outside the currently accepted values (h<0.22).

However, the baryon adiabatic scenario may yet be retrieved as a suitable model for the formation of galaxies as it is one of the simplest ways of generating large-scale structure. As Shanks (1985) notes if H_o is as low as 25 kms^{-1} Mpc^{-1} then the above nucleosynthesis constraint can still be met with $\Omega^{baryon}=1$. However, the n=1 power spectrum that is also predicted by inflation has to be dropped in favour of the minimal n=4 spectrum (Peebles 1981c) to avoid the Jean's scale (equation 5-37) from collapsing at the same time as the Silk scale (equation 5-38) thus leading to a too large a coherence length for galaxies and a too large a fluctuation in the microwave background.

Thus with the advent of Grand Unified Theories of matter which allow inflationary phases in the Universe more emphasis was placed on models of galaxy formation with $\Omega_o=1$ and initial power spectra with n=1. These theories also allow the existence of a plethora of exotic weakly interacting particles which could provide the missing mass required to make up $\Omega_o=0.05\text{-}0.2$ (equations 5-41 and 4-12) to $\Omega_o=1$ and which would also be, conveniently,

undetectable. Whilst this conveniently surmounts the problems of causality in the early Universe and the fine tuning of Ω_o, it leaves yet another coincidence in the form of the close similarity between $\Omega_o{}^{baryon}$ and $\Omega_o{}^{exotic}$ (Shanks 1988). Such models do have the additional attractive features, however, of inducing small fluctuations in the microwave background (since the main component of the mass distribution decouples from the radiation at an earlier epoch where the fluctuations in the density are smaller) and being fairly straight forward to calculate numerically (via simulation) even in regions of the fluctuation where $\delta\rho/\rho_b \gg 1$ (since the equations of motion are dissipationless).

Initially, much attention was focussed on neutrinos as the likely candidate for the dark matter especially since a mass of ~30eV was reported by Lyubimov et al. (1980) and Reines et al. (1980). This so called 'hot' dark matter has a characteristic scale in the power spectrum after decoupling which arises from neutrinos having undergone relativistic free-streaming out of density enhancements (Landau damping) smaller than the horizon size at that epoch. This characteristic proto-pancake scale at the current epoch is (White et al. 1983)

$$\lambda_v = 41 m_{30}{}^{-1}\theta^{-1} = 13(\Omega_o h^2)^{-1}\theta^2 \text{ Mpc} \qquad (5\text{-}42)$$

where m_{30} is the mass of the neutrino in units of 30eV and θ is the microwave background temperature in units of 2.7K.

Although this model produces a correlation function that approximates a power law (the simulations, in fact, seem to show possible features in $\xi(r)$) this model has grown out of favour because for Universes with $n=1$ and $\Omega_o=1$ the formation of galaxies occurs at a too recent an epoch ($z_f \approx 1\text{-}2$ for $h=0.5$ to 1) with the normalisation that $r_o \approx 5h^{-1}$ Mpc for galaxies now. With $\Omega_o h^2$ smaller than this λ_v becomes even larger (equation 5-42) and this makes the clustering length for galaxies considerably larger than $5h^{-1}$ Mpc. Perhaps with new measures of the neutrino mass and larger values of r_o some aspects of this model may be retrieved.

Finally, the currently most popular model for large-scale structure and the one that has received considerable attention has been models for the dominant mass contribution being composed of 'Cold Dark Matter' (CDM, Davis et al. 1985, White et al. 1987). These particles are named as such

since being massive (except the axion which is formed in a low excitation state), their velocities at early times are non-relativistic. The only modification to a Cold Dark Matter spectrum as it evolves is the so called Mézáros effect (Mézáros 1974) which causes a gradual bend in a power law spectrum from n to n-4 at scales below the horizon. This arises because in the radiation dominated era fluctuations within the horizon are 'frozen', since the rate of expansion exceeds that at which matter can collapse. Although with an n=1 spectrum mass fluctuations at scales below the horizon at the time of decoupling behave like $\delta M/M \propto k^{3+n-4} \approx k^0$ (and so are Poisson as in the original isothermal model), the non-linear part of the correlation function does not evolve in a self-similar way as expected for a hierarchy. Indeed $\xi(r)$ below the scale at which $\xi^m(r) \approx 1$ proceeds at a faster rate than at scales where $\xi^m(r) < 1$ (Figure 5 of Davis et al. 1985) and so there has to be a fortuitous time to obtain a single power law. This may be regarded as more hopeful for observations where there are features in $\xi(r)$ (such as a shoulder); however the $\Omega_o=1$ models give too large peculiar motions without introducing biassing of the form indicated in equation 2-117 (see Chapter 2, Section 2.2). Even then the form of the peculiar motions appears to decrease with separation, where there is some evidence in the data that it increases (see Chapter 4, Section 4.3.3).

Currently, however, this model gives the best fit to the observation in Section 5.2.1 that $\xi_s(s)$ is consistent statistically with $\xi(r)=0$ on large scales. As discussed before in Chapter 3 (Section 3.2.1) it is remarkable how such dynamical simulations can reproduce features in the observed 3-d galaxy distribution (such as voids, filaments, etc.) without any large scale power in the two-point (or higher order) correlation functions. Thus, it can be seen that as yet there is no single model for the evolution of large-scale structures in the Universe which can reproduce all the necessary observed features.

Chapter 6

Forward Look

In the preceding chapters it has been seen how the statistically complete Durham/SAAO, Durham/AAT and Parker et al. redshift surveys have been used to provide significant information on the dynamical and clustering properties of galaxies and how these observations may constrain the formation and evolution of large-scale structures in the matter distribution. However, in spite of the success of these samples as statistical probes of large-scale structure it is clear that these surveys have lost some of the essential 3-d information about the galaxy distribution through the selection of small angle fields from random areas of the sky. In any future development which significantly advances our understanding of this subject it is important that such potential drawbacks in the physical choice of a redshift survey should not be over looked whilst at the same time still sampling sufficiently many of the representative large-scale structures that are likely to occur.

As seen earlier (see, for example, Chapter 5, Section 5.2.2), the UK Schmidt telescope (UKST) together with automated photometer machines such as COSMOS (MacGillivray and Stobie 1984) and APM (Kibblewhite et al. 1984) can already provide homogeneous and well-calibrated maps of the galaxy and other source distributions to $b_J \approx 21^m$. In this chapter, some recent advances are described which utilize the large ($\sim 6° \times 6°$) focal area of the 1.2m UKST to obtain spectroscopic information for galaxies to $b_J \approx 17^m$ (redshifts $z < 0.1$) using the multi-object spectroscopic fibre system FLAIR. With some initial results from a new 9 field redshift survey using FLAIR the potential of this instrument for mapping a large contiguous area in 3-d to $b_J \approx 17^m$ in the southern galactic cap is discussed.

Thus Section 6.1 briefly describes the UKST-FLAIR instrumentation and current set-up. In Section 6.2 the details of the preparation and observation of the new nine field survey are given and in Section 6.3 the techniques for measuring the redshifts of the galaxies are described. In Section 6.4 some initial tests of the system from observations of a single Durham/AAT survey field are presented together with some preliminary

results from the nine-field survey. In Section 6.5 are discussed some future developments to the instrumentation and some aspects of the proposed Durham/ROE galaxy redshift survey.

6.1 Instrumentation

Following the successful application of multi-object fibre-optic spectroscopic systems to 4m class diameter optical telescopes such as the Anglo-Australian Telescope (Gray 1983) it was soon realised that developing such a system for the UKST offered a unique opportunity for the spectroscopic observation of certain classes of object through the large area coverage (~6°.4x6°.4) of that telescope (Dawe and Watson 1984). For example, if each equivalently bright object within the telescope imaging area Ω has a fibre to carry its light to a spectrograph, then the number of such objects, N_{obs}, that can be observed per unit time is

$$N_{obs} \simeq N\Omega d^2 \qquad\qquad\qquad (6\text{-}1)$$

where N is the surface density of the objects on the sky and d is the diameter of the telescope. The factor of d^2 accounts for the fact that larger diameter telescopes take a shorter time to reach the same signal-to-noise ratio in the observed spectrum. Thus comparing the Schmidt with the 40 arcmin diameter FOCAP system on the AAT (Gray 1983), it is seen that the rate of collection of objects of the same brightness and surface density on the sky is ~$(6.4/0.35)^2(1.2/4.0)^2 \approx 31$ times faster on the Schmidt assuming all other aspects of the instrumentation (such as light transmission efficiencies etc.) are the same. Thus, with 100n fibres available for the gathering of light from objects, the UKST attains this advantage when $N \approx 2.4n$ per square degree.

As suggested above, galaxy redshift surveys are potentially a very appropriate project for fibre spectroscopy on the UKST. In the Durham/SAAO Survey, sufficient signal-to-noise in the spectra of 17^m galaxies at a resolution of ~120kms^{-1} rms could be achieved in less than 60 minutes on a 1.9m telescope (Metcalfe et al. 1989). Thus with the same set-up on a 1.2m Schmidt, the same signal-to-noise could be reached in <2.5hrs, which is not unreasonable. In fact the simple optical set-up for the Schmidt (see below) means that the efficiency of the system can be much better than this (by

about 50%) which offsets the effect of the smaller aperture of the Schmidt. As seen in Chapter 3 (Section 3.2.3, equation 3-13) the mean number of galaxies expected on the sky at b_J=16^m.8 is N =5.8 deg^{-2} and so ~240 fibres would be required on average to observe every galaxy within the Schmidt imaging area. However, the experience with the Durham/SAAO Survey has shown that sufficient visual and statistical mapping of the galaxy distribution can be achieved at a somewhat lower sampling rate and so ~80 fibres (one-in-three) may be a practicable target.

The spectrographic system at the UKST thus consists of three parts (Watson 1986, 1988); a fibre-optic coupler (FLAIR; a Fibre-Linked-Array-Image-Reformator), to transport the collected light from the focus of the UKST to an optical bench on the dome floor, a simple spectrograph consisting of a collimator (one Pentax lens to image the ends of the fibres and another to image the spectra onto the detector) and a blazed reflection grating, and, thirdly, a sensitive linear detector in the form of a liquid nitrogen cooled CCD mounted in a dewar (Oates 1990) and driven by a PDP11 computer. The light from the target objects is collected from the poorly accessible curved focus of the Schmidt by mounting the fibres on a plate copy of the appropriate field to be observed. Thus by aligning the telescope to that field (using 5 fibres situated on bright fiducial stars) light can be collected from the targets by centring the fibres on the equivalent target images on the copy plate.

Initially, the fibres were bonded using a non-permanent UV curing cement on the rear (i.e. non-emulsion) side of a thin positive plate copy whilst the plate was supported in its curved shape by a specially constructed perforated (honeycomb) mandrel to be held in the plate-holder. Although this perforation gave the fibres access to the plate, up to 40 % of the area of the plate remained obstructed. Following the successful commissioning of Auto-fib (Parry and Gray 1986) at the AAT, this obstruction was eliminated by cementing 90° prisms to the front surface (i.e. emulsion side) of the negative copy plate which reflected the incoming light into the attached fibre. This allows almost complete access to all the targets for observation; the only limitation being that two objects closer than 2mm (2.2 arcmins at the 67.1 arcsecs mm^{-1} plate scale of the Schmidt) cannot be observed simultaneously.

The first fibre-coupler to be constructed consisted of 39 40μm diameter

(2.7 arcsec) fibres which covered only a small fraction of the area of a typical galaxy on the plate (the apparent diameter being ~52(x/y) arcsecs where x is the diameter of the object in units of 25kpc and y is its distance in units of 100Mpc) and which had poor transmission properties at wavelengths $\lambda<5500$Å. At the same time as the modifications to the coupler were made at the focal surface, 35 larger diameter (100μm=7 arcsec) fibres were employed which had a much better efficiency in the blue part of the spectral region (85% in 10m of fibre at $\lambda=4200$Å). The number of fibres that can currently be employed in the coupler is limited by the unvignetted size of the imaging area at the input side of the collimator. The new modifications to FLAIR became known as PANACHE (PANoramic Area Coverage with High Efficiency; Watson 1988).

The spectrograph can currently be used with a variety of dispersion gratings with various blaze wavelengths, but its properties in the blue are fairly limited because of the poor transmission and rapid defocussing with wavelength of the Pentax lenses at $\lambda<5000$Å (see below). However, the placement of the spectrograph on a vibrationally-isolated optical bench and the use of a CCD detector makes it possible to attain very stable wavelength calibration of the spectra.

Initially only red sensitive GEC CCD's were available as the detector but with the advances in coating technology a more blue responsive GEC CCD was obtained by coating it with a blue sensitive dye at ESO (Cullum et al. 1985, Deiries 1986). This dye results in an enhanced quantum efficiency at 4000Å of approximately 15%. This current CCD images an area of 400x578 pixels (1 pixel has a size of 44μmx44μm) and when optimally cooled to ~150K induces a read-out noise ~4-5ADU per pixel with a gain of 2e⁻/ADU. Thus, assuming that the electron count in a pixel is Poissonian the observed spectrum becomes read-out noise limited at fluxes of 32 to 50 ADU per pixel. Since this noise source can become important at these low light levels (i.e. for faint galaxies or for the blue, $\lambda<4500$Å regions of the spectrum - see Section 6.2 below) and since the imaged 100μm fibre covers ~6 CCD pixels, on-chip binning was implemented on the CCD so that pixel counts could be co-added prior to reading out the chip.

The general performance of the CCD is very good with only low levels (a few ADU) of 'dark current' being recorded over exposures of ~3000s and

negligible charge smearing seen on the high count pixels. There is only one significant defect in the imaging area, that is an LED in one pixel; however some non-permanent LED effects have been seen. Background radiation or 'cosmic ray' events were initially a serious problem but this has been rectified somewhat by replacing the dewar window with a fused-silica glass. Events are now seen at ~2 per minute over the CCD imaging area.

These improvements described above, primarily in the blue (λ<5000Å) spectral range, meant that it was now possible to attempt spectroscopy in the range λ=4000-5000Å where it is expected that redshifted absorption features, such as the strong Ca II K and H (λ3934Å and λ3969Å) lines, are likely to be seen, whereas prior to these improvements galaxy spectroscopy was limited to λ>5500Å where there are relatively few of such features to be found. In the following section the set-up for the nine field Schmidt survey, which attempted to use this new information, is described in more detail.

6.2 Observations

The main aim of this work was to assess the performance of FLAIR in the field of galaxy spectroscopy and, in particular, to evaluate its potential in the construction of systematic redshift surveys. Once this assessment was complete, it was envisaged that a new redshift sample of galaxies could be formed which would enhance and supplement the information gathered from the previously observed Durham surveys. Whilst this evaluation is now complete and all the spectroscopic (and some of the photometric) data on the new nine field survey has been obtained, there currently remains much work to be completed on this catalogue. In this section the methods of assessment of the FLAIR/UKST instrument are discussed together with a description of the choice for the final observing set-up. Following this a brief description of the construction of the 9 field survey is given and the current status of the spectroscopic and photometric observations are presented. In Section 6.3 a detailed account of the methods for obtaining the redshifts from FLAIR is discussed and in Section 6.4 the results from the spectroscopic tests and some preliminary results from the nine field survey are presented.

Clearly two important factors in the potential use of the UKST/FLAIR instrument in the construction of a systematic redshift survey are, firstly, to

what accuracy can the redshift velocities be measured with the system and, secondly, to what limiting magnitude can a complete sample of galaxies be measured with this accuracy. As discussed in the previous section a magnitude limit of $b_J \approx 16^m.8$ might be achievable with this system, and so as a direct test of the UKST/FLAIR instrument it was decided to re-observe a redshift field which already possessed complete and accurate redshift information to this limit.

The Durham/AAT redshift field GNA at ~13h40+00 (UKST SERC field 864) satisfied these requirements (the rms error on these velocities is ~50kms^{-1}; see Peterson et al. 1986 and Chapter 3, Section 3.1.2) and was observable during the first commissioning observing run in May 1988. According to the lists of Peterson et al. there are 57 galaxies to this limit (with magnitude relation of equation 3-3) and so sampling their list, in magnitude order at a rate of 1-in-2, gave 28 suitable objects for observation. It was decided that of the remaining 7 fibres available, 6 would be devoted to monitoring blank regions of the sky (this, in future runs, became standard) and one would be placed on a bright 'template' galaxy (see below) with a known (non-Durham/AAT) and accurate catalogue redshift velocity. Thus, by re-observing these 28 objects sampled uniformly in apparent magnitude it was possible to test for the internal and external accuracy of the measured FLAIR velocities and the completeness to $b_J \approx 16^m.8$.

The following methods that were used in the observation of field 864 became a standard for the observations of the 9 field survey.The main aim of these spectral measurements was take advantage of the improved blue sensitivity shortwards of $\lambda 5000\text{Å}$ as discussed above. Since the large diameter 100μm fibres tended to dominate the spectral resolution (the FWHM of the arc lines remains approximately a fixed 6 pixels on the CCD at both reciprocal dispersions of 190 and 98Å/mm) a choice had to be made between wavelength coverage and spectral resolution. The final choice of the 1200V grating (with a blaze wavelength at $\lambda 4620\text{Å}$) and a grating angle of ~175°, gave a wavelength coverage, on average, of 3940-5160Å (Ca II H and K occur at ~$\lambda 4123\text{Å}$ at a mean redshift of $z \approx 0.043$) at a resolution of 11Å FWHM (at $\lambda > 4500\text{Å}$) although worse in the blue (see Section 6.3 below). In the Durham/SAAO Survey Metcalfe et al. (1989) achieved a velocity accuracy of ~120kms^{-1} rms on average from a spectroscopic resolution of ~7Å FWHM, and so working at the same signal-to-noise the velocity accuracy for this

FLAIR set-up was predicted to be in the range 150 to 200kms^{-1} rms.

With this optical configuration the CCD was set-up to co-add 3 pixels perpendicular to and 2 pixels parallel to the dispersion direction giving an average dispersion of ~4.2Å per (binned) pixels and a resolution of ~2.6 FWHM (binned) pixels. The CCD images thus had on average 2 (binned) pixels per spectrum across the dispersion direction with an inter-fibre spacing of 1 (binned) pixel. Since this set-up was used throughout the pixel sizes mentioned below will refer to those as appearing on the CCD image after read-out.

Since the combination of the CCD and fixed platform for the spectrograph makes the system a very stable one for wavelength calibration, it was only necessary to take arc spectra at the beginning and end of each observing session. For this purpose Mercury-Cadmium and Helium arc lamps were used, but the former was preferred in the data reduction since high signal-to-noise spectra could be obtained in short (20s) exposures with virtually no cosmic ray contamination.

As fibre transmission varies because of prism tilt and inherent fibre differences high signal-to-noise flat-field frames were taken of the twilight sky, so that this vignetting could be accounted for in the data reduction. On one occasion dome flat-fields were also successfully used for this purpose. CCD bias and dark frames were taken throughout the observing session to monitor the performance of the CCD.

To calibrate the redshift velocity scale and to provide template spectra for the purposes of cross-correlation (see Section 6.3 below), at least one bright ($m_B \approx 11/12^m$) galaxy with an accurate (catalogued) velocity was sought on each field so as to provide a suitably high signal-to-noise spectrum. With the addition of 2 stellar spectra (one of which was a solar spectrum) and several other suitable templates found in the lists of target galaxies after observation, 19 templates were available for cross-correlation purposes (see Table 6.3 of Section 6.4 below).

Thus out of the 35 fibres available 28 were used on average to observe the spectra of target galaxies. A rough estimate of the signal-to-noise of the resulting spectra could be judged from initial estimates of the flux from

galaxies and from the sky. Thus as 2 pixels from each fibre are co-added from the CCD image to give one pixel in the final spectrum, the signal-to-noise per pixel is (see the previous section)

$$S/N = \frac{F_{source}}{[(F_{source}+F_{sky})/g+2\sigma_R^2]^{1/2}} \qquad (6\text{-}2)$$

where g is the gain in e⁻/ADU and σ_R and F (in the final spectrum) are the read-out noise and flux per pixel in ADU ($\sigma_R \approx 4\text{-}5$ ADU). Thus as fluxes of $F_{source} \approx 200$ ADU and $F_{sky} \approx 150$ ADU are obtained from a limiting magnitude ($b_J \approx 16^m.8$) galaxy in an exposure of 3000s at $\lambda=5000\text{Å}$ this implies the final spectrum has a signal-to-noise ~13 at this wavelength. At 4100Å the read-out noise becomes more important with $F_{source} \approx 25$ ADU and $F_{sky} \approx 35$ ADU in 3000s and so the signal-to-noise ~3. However, to detect Ca II H and K, for example, a signal-to-noise ~5 or 6 is required and this can be achieved in a minimum of 3 to 4 such 3000s exposures (2.5 to 3.3 hrs).

The methods of construction of the 9-field Schmidt survey follows very closely those of Peterson et al. (1986) and Metcalfe et al. (1989) (see also Chapter 3, Sections 3.1.1 and 3.1.2) and so only a brief description of these methods are given here. The basic photometric and source material for the new survey comes from COSMOS scans of UKST photographic J plates in nine UKST-SERC fields at high ($|b^{JI}| \geq 40°$) galactic latitudes. High quality copies of SERC Atlas plates were used for the scans and COSMOS was set to threshold map the intensity distribution at a faint isophote of ~8% of the sky background intensity (~$24^m.74$ arcsec⁻² at $m_{sky}=22^m$ arcsec⁻²) which makes the calibrated galaxy magnitudes approximately total (see Section 3.1.1). However, unlike the Durham/SAAO and Durham/AAT surveys the area scanned for these nine-fields covered ~5°.35x5°.35, and this makes these fields approximately twice the area of the fields in the earlier surveys.

The main aim of this survey was to attempt to continue obtaining galaxy redshifts down to a competitively deep limit of $b_J \approx 16^m.8$ (z<0.1) as in previous Durham surveys. However, as discussed in the introduction to this chapter, a stronger bias towards a more visually acceptable 3-d map of the galaxy distribution was felt to be needed (c.f. the slice maps of De Lapparent et al. 1986a and Da Costa et al. 1988 as in Figures 3.4 and 3.5 of Chapter 3, Section 3.2.1) and so the approach to the choice of fields was to aim for more contiguous areas. Figure 6.1 shows the position and area of the 9 Schmidt

fields with respect to the earlier Durham/SAAO and Durham/AAT survey fields on a plot of right-ascension and declination (see also Figure 3.6). Subject to the availability of UKST Atlas plate material it was decided that the RA strip along zero degrees declination from ~10.5hrs to 15.5hrs afforded a useful place for the FLAIR work since there were already 4 previous survey areas in this RA range. This also had the potential advantage that overlaps between the COSMOS measured areas could be used to provide a uniform photometric calibration. Figure 6.1 shows that some continuity was achieved at ~12.5hrs to 14hrs ($0°$ dec.) and at 21.5hrs (-25° to -35° dec.).

At $b_J \approx 16^m.8$ it is expected that ~166 galaxies will be available for observation in each Schmidt field and thus a sampling rate of 1-in-6 allows on average 28 of the 35 100μm fibres to be used for observation (leaving 6 fibres for offset sky and 1 for a template object; see above). In practice galaxies were sampled at a rate of 1-in-6 from complete lists of galaxies in order of apparent magnitude until ~28 of the fibres were filled with a target object. This constant surface density of observed objects will necessarily mean that the magnitude limit ot the fields will vary from field-to-field.

Thus it is expected that the final catalogue will have redshifts for up to ~250 galaxies covering a volume which is about equal to (if not a bit larger than) the original Durham surveys. Thus the large-scale ($\geq 10h^{-1}$ Mpc) statistical power of $\xi_s(s)$ of this sample will be similar to that observed in Figure 5.18 of Chapter 5 (Section 5.2.1), whereas at smaller scales the velocity resolution of ~150-200kms^{-1} rms will allow some further description of the small-scale $\xi_s(s)$ and the peculiar motions of galaxies.

The methods for preparing the complete magnitude limited and calibrated samples of galaxies have been described quite thoroughly elsewhere (for example, Shanks et al. 1984) and so only a brief description is given here. Initial star-galaxy separation of the COSMOS detected images to $b_J \approx 20^m$ was carried out using the image parameters of logarithmic isophotal area and apparent magnitude. Prior to this, nine areas of the plate were examined for variations of the stellar locus from area to area in the plane of these two parameters. Due to the limited dynamic range of COSMOS, stellar (but generally not galaxy) images sometimes had a tendency to saturate in magnitude causing an apparent variation (with local sky intensity) of the stellar locus across the plate (Heydon-Dumbleton et al. 1989). In this case no

Figure 6.1. A cartesian map of the Equatorial coordinates R.A. and Dec. (1950.0) showing the positions of the fields in the new Schmidt survey (solid symbols of approximately proportionate area). The other fields are from the Durham/SAAO, Durham/AAT and Parker et al. surveys. The dashed lines are the Galactic coordinates $b^{II}=\pm20°$. The R.A. coordinate is in hours the Dec. coordinate in degrees.
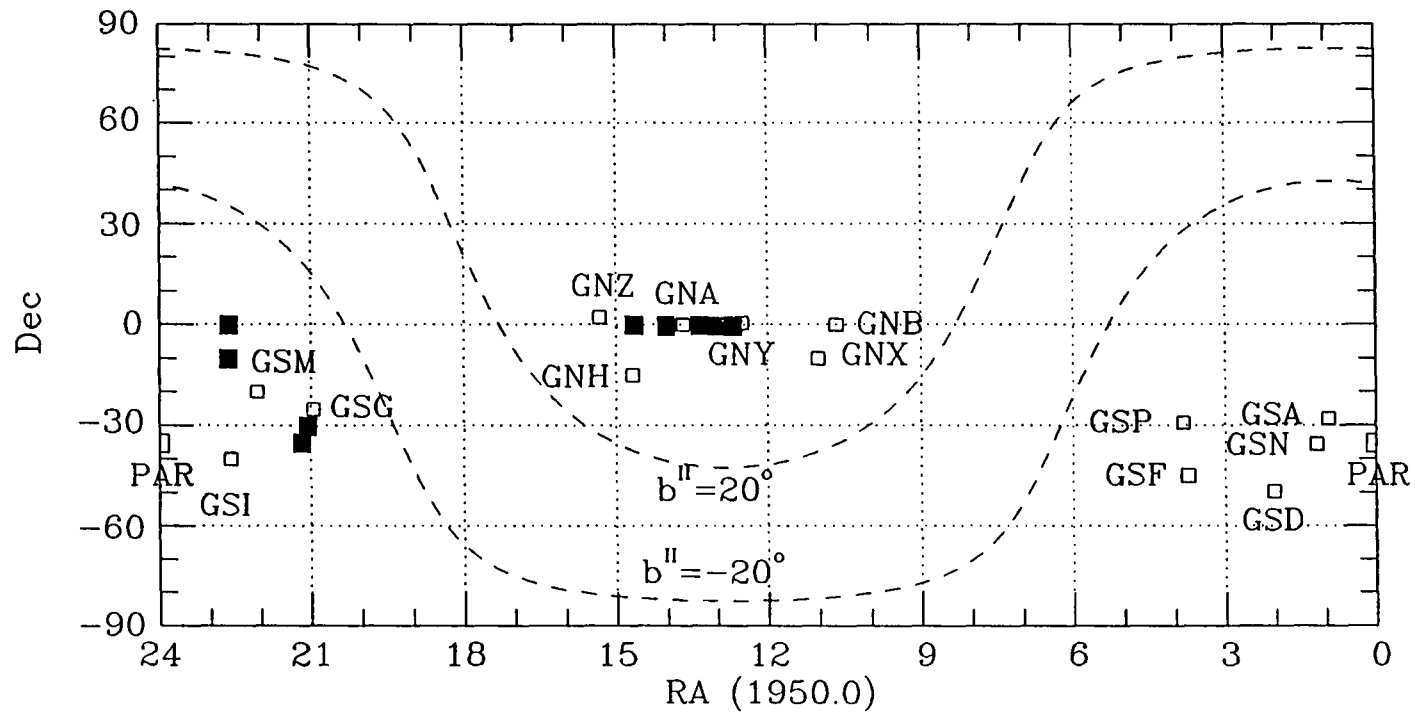
machine based star-galaxy separation could be relied upon at any magnitude to give an accurate sample of galaxies and so generally, in this case, the entire plate was separated by eye to ~17^m. Where such variations in the stellar magnitudes were not seen, the star-galaxy separation could be used to classify galaxy images at magnitudes fainter than ~16^m and in the final lists, all objects brighter than this limit and all classified galaxies fainter than this limit (to ~17^m) were checked visually.

Rough photometric calibration of the COSMOS magnitudes for the Schmidt fields was achieved by matching the observed number-apparent magnitude counts at $b_J \approx 18^m$ to 19^m to calibrated counts at the SGP (Shanks et al. 1984). Other preliminary photometric calibration has been provided from CCD B and V observations of galaxies on the INT 2.5m and SAAO 1.0m telescopes (Metcalfe priv. comm.). In Table 6.1 are listed the relevant details associated with the physical characteristics, sample lists and photometric calibrations of the 9-fields.

The spectroscopic observations for this Schmidt survey were carried out over 5 runs at the UKST from May 1988 to February 1989. Table 6.2 lists the observations carried out on each field (including the 864 field). In two instances (SERC fields 464 and 891) some attempt was made to complement the blue observations with other exposures in the red ($\lambda \approx 5780$-6980Å) as this will, hopefully, enable a better detection of later-type galaxies with, for example, Hα (λ=6563Å) or N II (λ=6584Å) in emission. Some degree of success in this mode of observation has already been reported by Parker and Watson (1990).

6.3 Reduction techniques

The following techniques used for reducing the spectroscopic observations from the 864 'test' field (Peterson et al. 1986) also apply, in general, to the 9 field Schmidt survey. As the methods of reduction are similar to those of Metcalfe et al. (1989) only a brief overview is given here. Figure 6.2 shows a raw, 3000s exposure, data frame of the 28 galaxies chosen from the 864 field. Fibres marked with an S are sky fibres while that marked by a T is a template galaxy (NGC5329, see Table 6.3 below); the remainder are target galaxies. It can clearly be seen that prominent absorption features such as Ca II H and K

(1)	(2)	(3)	(4)	(5)	(6)	(7)	(8)
SERC	R.A.	Dec.	m_{sky}	source	m_{lim}	N_{obs}	N_{lim}
	h m	° ´	bJ		bJ		
862	13 00.4	-00 23	21.90	CCD	16.81	26	151
865	14 00.4	-00 22	22.10	N(m)	16.79	27	157
867	14 38.7	-00 08	21.62	CCD	16.69	28	163
464	21 03.6	-30 07	22.00	N(m)	17.01	27	157
402	21 10.2	-35 08	22.02	N(m)	16.90	27	169
891	22 38.5	-00 09	21.88	CCD	16.74	28	163
747	22 38.5	-10 09	21.72	N(m)	16.68	27	163
861	12 40.5	-00 22	22.03	O/L	16.76	27	158
863	13 20.3	-00 21	22.08	O/L	16.76	27	159

Table 6.1. Details of the fields in the Schmidt survey. The R.A. and Dec. (1950) of the fields (SERC Nos. in column (1)) are given in columns (2) and (3). The sky brightness of the photographic plate is given in column (4) (in units of mag $arcsec^{-2}$) together with its calibration source (N(m) refers to a number count, O/L is from an overlap; in 861 and 863 this was with 862). The numbers of galaxies observed to the magnitude limit (column (6)) is given in column (7). Column (8) gives the numbers of galaxies catalogued to the same limit.

| (1) | (2) | (3) | (4) | (5) |
| | | No. of Frames | | |
Field	Date	Blue	Red	Comments
864	10/11.5.88	5		Moon affecting 1
862	12/13.5.88	6		
865	19/20.5.88	4		Cloud affecting 4
	20/21.5.88	1		Cloud affecting 1
	21/22.5.88	6		
867	08/09.6.88	5		
464	10/11.7.88		3	
	11/12.7.88	8		
402	13/14.7.88	8		Cloud affecting 4
891	12/13.9.88		2	Cloud affecting 2
	13/14.9.88	7		λ-scale affected on 2
747	16/17.9.88	4		Cloud affecting 1
861	05/06.2.89	3		
863	08/09.2.89	4		

Table 6.2. Spectroscopic observations carried out for the 9 field Schmidt survey. Columns (1) and (2) list the UKST/SERC fields and their date of observation, respectively. The number of CCD frames taken with the blue and red blazed gratings is indicated in columns (3) and (4) (the blue exposures were all of 3000s duration; those taken in the red were either 1800s, in the case of 464, or 3000s in the case of 891). Column (5) provides some comments on the quality of the frames (in the case of the blue observations for field 891 the spectrograph box was disturbed towards the end of the night).

Figure 6.2. A CCD image of galaxy spectra in the 13h40+00 field. This is a single raw exposure of 3000s (with the CCD binning in 3x2 mode) and shows 35 spectra (vertically spaced) with increasing wavelength running from left to right. The numbers on the overlay refer to the galaxy identification in column (1) of Table 6.4 whereas spectra marked with an S are of the sky background. The single spectrum marked with a T is the template galaxy (NGC5329, see Table 6.3). Several strong absorption and emission features seen in the spectra are marked. Approximately 100 cosmic ray events are recorded on this frame and these appear as white, sharply defined, spots (about 4 pixels in area) in this presentation.
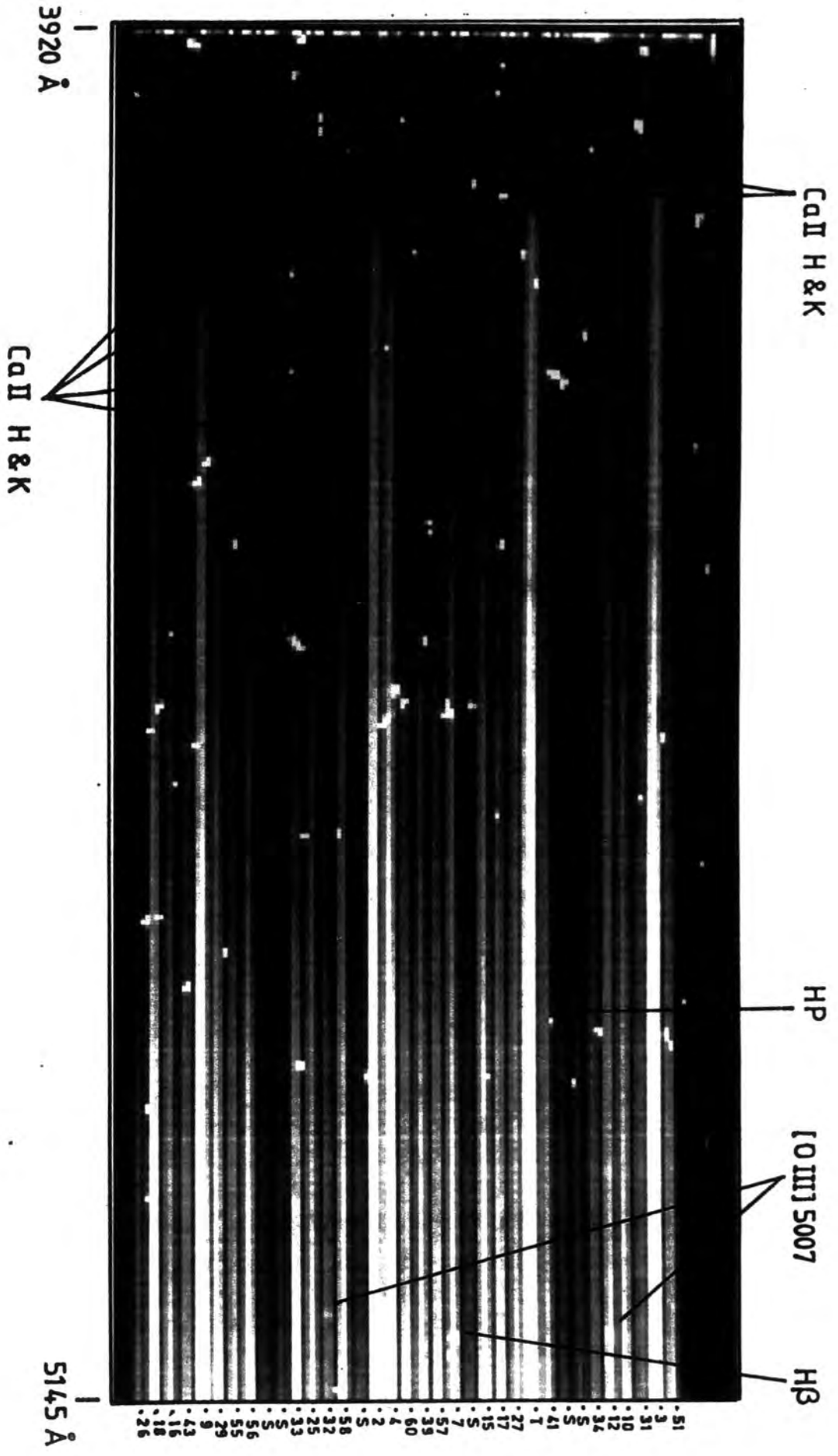
are visible in the spectra (galaxy Nos. 9 and 56 at the blue end) as well as strong emission lines (galaxy Nos. 12 and 32 at the red end). The blue end of the spectra show evidence for the defocussing as discussed above (Section 6.1) and arc spectra confirm that the resolution decreases from ~11Å FWHM in the range λ=4500-5000Å to ~21Å at λ=4000Å. This frame also shows a large number (~100) of cosmic ray events which have to be removed in the data reduction procedure.

The reduction of the data was carried out using a variety of STARLINK and local software on various VAX machines at Durham. Firstly, the arc frames taken at the beginning and end of the night were inspected for any noticeable shift in the position of the arc lines over the course of the observations. Such shifts were rarely seen. With the data frames, parameters such as read-out noise, scattered light, sky and source levels were monitored and frames that were of too low signal-to-noise were removed from the reduction. The arc and data frames were then debiassed by subtracting a mean background count from 'unexposed' areas on the CCD away from the fibres. In general, as the dispersion of the fibres lay parallel to the columns of the CCD, arc and galaxy spectra were extracted by co-adding the two highest count columns of each fibre. In cases where the dispersion direction did not fall parallel to the CCD columns, the dispersion had to be followed on the twilight sky frames using routines available in FIGARO (FINDSP) and then 2 pixels width of spectra extracted (using POLEXT).

The next step in the reduction was to remove the cosmic ray events in the extracted data frames by individually median filtering each spectrum over generally more than three renormalised 3000s exposures. Figure 6.3 shows the application of this median filtering to the 4 debiassed (but not extracted) exposures in the 864 field. As can be seen this process removes the vast majority of the original events.

The extracted and co-added (over several exposures) arc frames were then used to calibrate the wavelength scale in each fibre using FIGARO routines (ARC, IARC). Figure 6.4 shows an example of the Mercury-Cadmium arc spectrum and, although there are only 5 arc lines, this is sufficient to fit the pixel number/wavelength relationship given the low level of non-linearity in the wavelength scale. Using a second order polynomial for the fit, rms dispersions of typically 0.3Å for the arc line positions were obtained. The individual

Figure 6.3. A median filtered image of galaxy spectra in the 13h40+00 field. This frame is median filtered over 4x3000s exposures and is presented in an identical fashion to that in Figure 6.2. Note that all the cosmic ray events, save 4, are removed (the white spot marked HP on the overlay is a hot pixel)
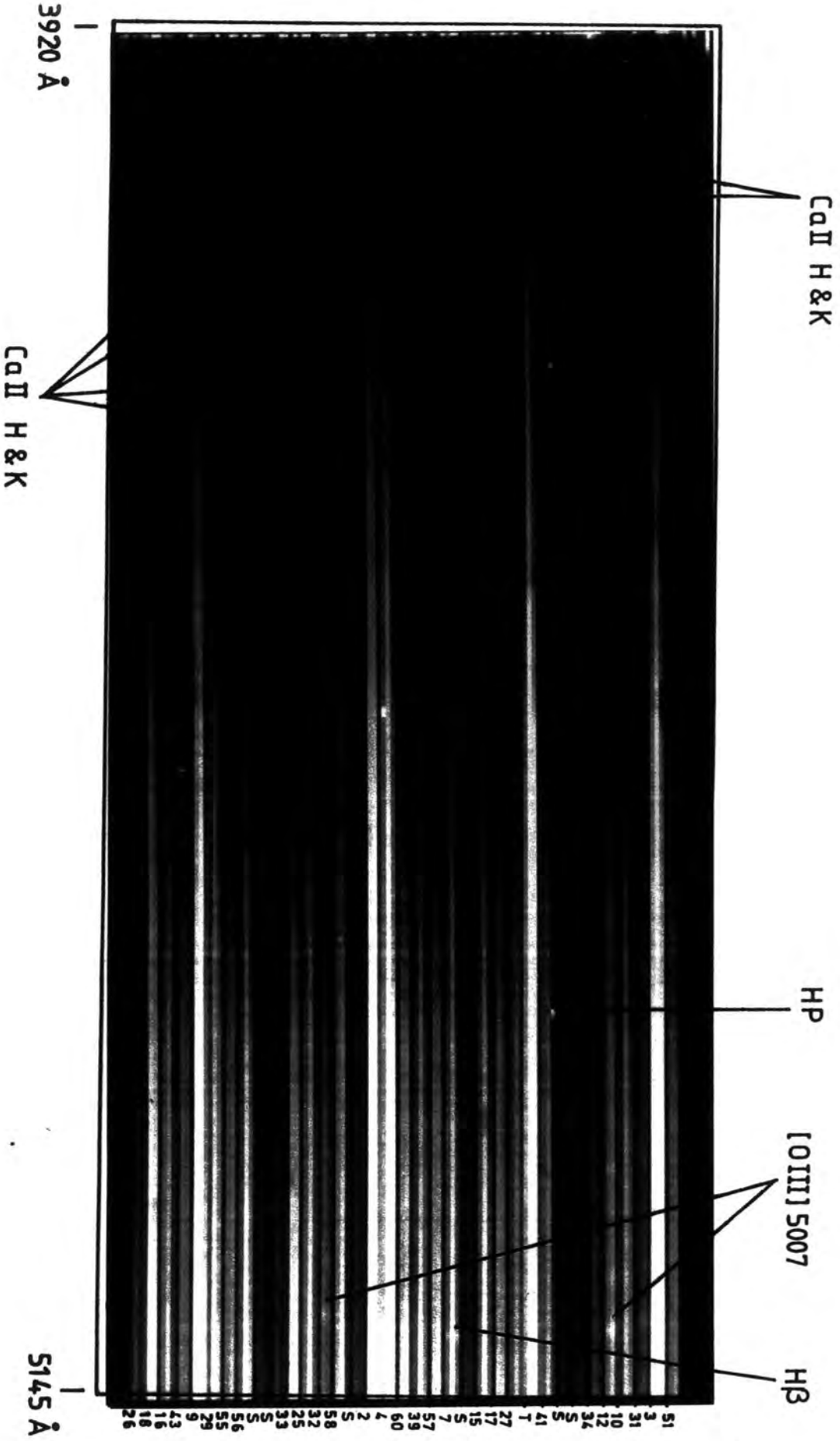
3920 Å

5145 Å

CaII H & K

CaII H & K

Hβ

[OIII] 5007

Hβ
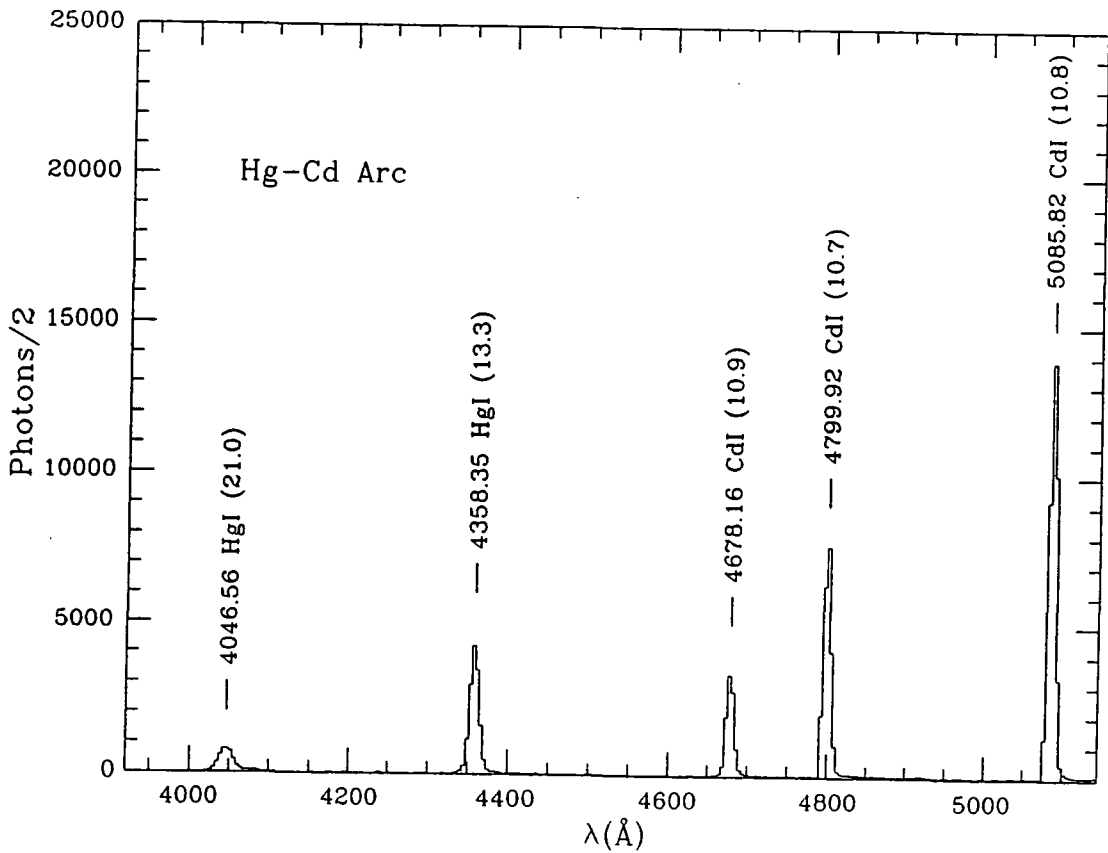
Figure 6.4. The Mercury-Cadmium arc spectrum. This shows 3x15s exposures combined into one spectrum. Wavelengths for the emission lines come from the MIT wavelength tables (Harrison 1939). The measured FWHM for each of the lines (based on a Gaussian fit) is indicated in brackets.

polynomial fits for each fibre were then used to rebin the spectra in the filtered data frame on a linear wavelength scale.

Frames of the twilight sky were then used to estimate the relative transmission of each fibre. Prior to summing the counts in each fibre spectrum cosmic ray events were removed by median filtering the individual frames using BCLEAN in FIGARO. The spectra in the cleaned data frame were then renormalised to take out the fibre-to-fibre variation (which lay at ~12% level).

For the sky-subtraction, the six sky fibres on the data frame were averaged and the result subtracted from each galaxy spectrum. The mean sky observed in the 864 field is shown in Figure 6.5 and it can be seen that there are no very strong emission lines within the observed wavelength range.

The resullting 28 filtered, wavelength-calibrated and sky-subtracted galaxy spectra were then used to estimate redshift velocities. This was achieved by two means; firstly by fitting identifiable, high signal-to-noise emission lines with Gaussian profiles using GAUSS in FIGARO (the redshift velocity being given by $v = c(\lambda - \lambda_0)/\lambda_0$ where λ and λ_0 are the peak wavelengths of the feature in the observed and rest frames, respectively and c is the velocity of light) and, secondly, by obtaining absorption redshifts via the cross-correlation methods of Tonry and Davis (1979) as implemented in the DUSDERS software package (Inglis 1985). Briefly this latter method involved the following. Prior to carrying out this procedure galaxy spectra were inspected for any remaining cosmic ray events and these were then removed together with the emission lines. The spectra were then continuum subtracted and rebinned into 256 logarithmic wavelength channels and then Fourier filtered to remove high frequency noise and low frequency distortions introduced by continuum subtraction. The galaxy spectra were then individually cross-correlated against the 19 available templates (see Table 6.3 in Section 6.4 below) and the highest peak searched for in each of the cross-correlation spectra. Thus with a relative shift of v_R kms^{-1} with respect to a template with a velocity of v_T kms^{-1} the redshift velocity is

$$v = (v_R + v_T) + (v_R v_T)/c \quad \text{kms}^{-1} \tag{6-3}$$

where all measured velocities are corrected to a heliocentric co-ordinate system.
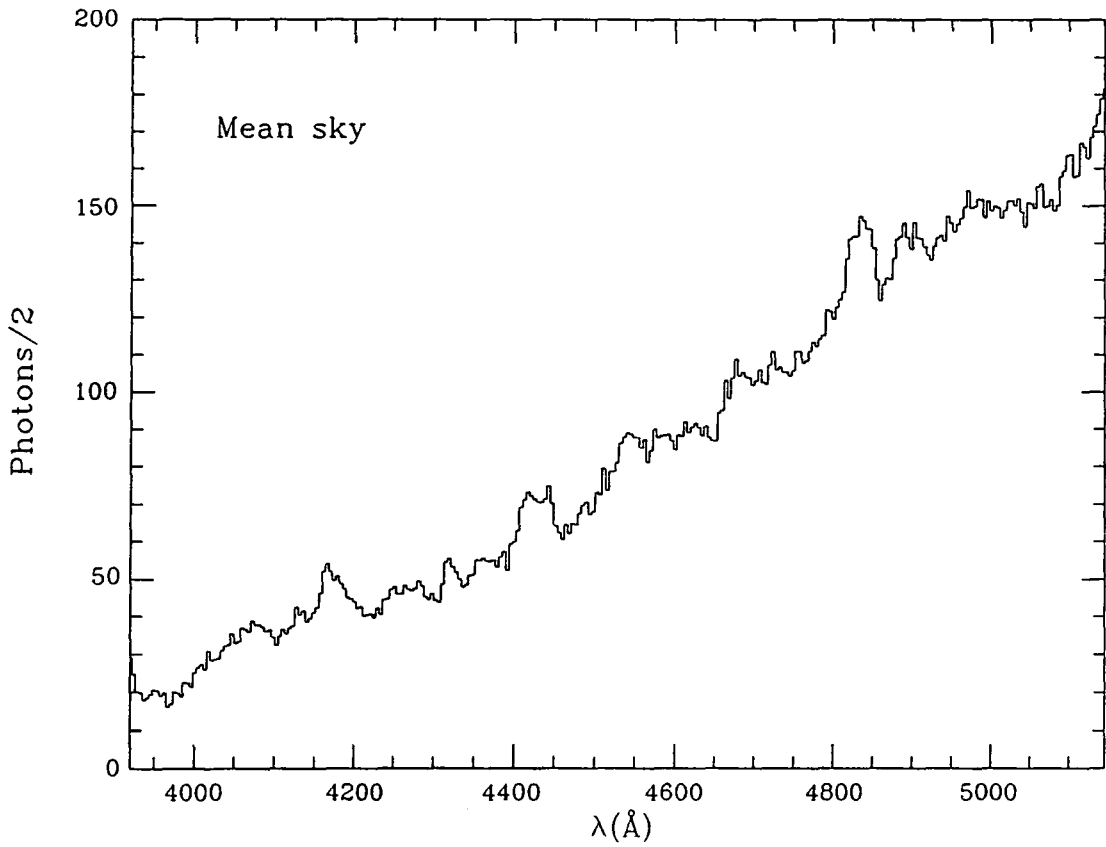
Figure 6.5. The mean sky spectrum observed in the 13h40+00 field. This spectrum is a mean over the six sky spectra seen in the median filtered image in Figure 6.3. Note the lack of any prominent emission features.

The templates (see Table 6.3 below), chosen to give a wide range of possible spectral types with which to match the galaxy spectra, were initially cross-correlated against each other to provide an internally consistent set of redshift velocities. The zero-point for these assigned velocities was then set by requiring that the mean was equal to the mean of the velocities quoted in the original catalogues.

6.4 Results

This section describes the results of re-observing the 864 field of Peterson et al. (1986) with the UKST/FLAIR instrument and the tests made on the accuracy and completeness of the redshift information gathered. Also described are the preliminary observations of SERC fields 862 and 865 which form part of the new 9 field Schmidt survey discussed in Section 6.2 above. These data are used to show that the new modifications to FLAIR now make the UKST/FLAIR set-up capable of performing large-scale redshift surveys.

Systematic and random errors in the estimated redshift velocities can be induced at various places in the data reduction, particularly in the wavelength calibration procedure. With no night-sky lines to make a simple check of this calibration (by comparing their measured wavelengths with their rest values) an alternative high signal-to-noise 'rest' spectrum had to be sought with identifiable and measurable spectral features. The solar template (see Table 6.3 below) obtained from a frame of reflected sunlight provided such a spectrum and so measuring the wavelengths of 4 prominent absorption lines (again using GAUSS in FIGARO) and comparing these with their rest values, an rms of $\pm34\text{kms}^{-1}$ was obtained for the corresponding velocity differences around a mean of -6kms^{-1} indicating that there may not be any serious problems with the calibration of the wavelength scale as anticipated (see Section 6.2 above).

A further test of the zero-point for the redshift velocity scale and possible random errors in the velocity measurements came from differences between the published heliocentric velocities for the templates and the velocities measured by FLAIR. In Table 6.3 the results of inter-cross-correlating the template spectra to obtain a consistent set of

Table 6.3 Details of the template objects.

(1) Name	(2) Field	(3) m_B	(4) Type	(5) V_C kms^{-1}	(6) $\sigma(V_C)$ kms^{-1}	(7) Source	(8) V_F kms^{-1}	(9) r_F	(10) ΔV kms^{-1}
NGC5258	864	13.7	Sa	6793	16	AARS	6825	4.5	32
NGC5329	864	14.4	E	7109	25	CfA	7131	9.2	22
	865						7081	8.5	-28
GNA003	864	14.6	Sab	3782	17	AARS	3865	8.4	83
GNA009	864	15.7	S0	14380	18	AARS	14321	6.8	-59
NGC4753	862	10.9	S0(P)	1288	(50)	RSA	1139	9.6	-149
NGC4772	862	(12.4)	Sa	1042	10	RSA	1159	9.6	117
NGC4996	862	14.4	S0/a	5488	26	CfA	5447	8.6	-41
NGC4845	862	12.3	Sab	1232	20	CfA	1267	9.0	35
NGC5713	867	12.0	Sbc(P)	1883	6	RSA	1919	4.2	36
NGC5746	867	11.8	Sb	1724	10	CfA	1808	9.7	84
A2058-28	464			11505	107	SRC	11804	7.6	299
MCG05-50-02	464			5953		FJ	5905	7.1	-48
E402-IG10	402			5330		FJ	5370	7.3	40
E402-G26	402			2796		FJ	2749	6.8	-47
NGC7391	891	13.7	E	3085	26	CfA	2851	8.9	-234
NGC7371	747	12.8	Sa	2685	15	RSA	2496	9.0	-189
HD215110*	891	(8.0)$_V$	dG4	-9		SRV	15	8.4	24
Sun*			dG2	0			-6	6.0	-6

Notes:

*Stars; ( )$_V$ indicates visual magnitude.
()Numbers in brackets are approximate.

References:

AARS. The Anglo-Australian Redshift Survey. Peterson, B.A., Ellis, R.S., Efstathiou, G., Shanks, T., Bean, A.J., Fong, R., & Zen-Long, Z., 1986. *Mon. Not. R. astr. Soc.*, 221, 233.

CfA. The Center for Astrophysics Redshift Survey. Huchra, J., Davis, M., Latham, D., & Tonry, J., 1983. *Astrophys. J. Suppl.*, 52, 89.

RSA. *A Revised Shapley-Ames Catalogue of Bright Galaxies*. Sandage, A., & Tammann, G.A., 1987. Carnegie Institution of Washington Publication 635.

SRC. *Second Reference Catalogue of Bright Galaxies*. de Vaucouleurs, G., de Vaucouleurs, A., & Corwin, H.G., 1976. University of Texas Press, Austin.

FJ. Fairall, A.P., & Jones, A., 1988. *Publ. Dept. Astr. Univ. Cape Town*, No. 10.

SRV. *General Catalogue of Stellar Radial Velocities*. Wilson, R.E., 1963. Carnegie Institution of Washington Publication 601.

The columns are as follows; (1) object identification, (2) UKST/SERC field of observation, (3) apparent blue magnitude (as quoted in original reference; in the RSA this is B_T), (4) morphological (galaxies) or spectral (stars) type, (5) catalogue heliocentric velocity, (6) quoted error on V_C, (7) catalogue identification, (8) heliocentric absorption velocity from FLAIR, (9) Tonry and Davis r-factor associated with V_F and (10) the difference $V_F - V_C$.

measured FLAIR velocities are presented (column (8)) together with the published source material (column (5)). The mean of the differences between the measured and published velocities (column (10)) is -2kms^{-1} with a scatter of ±117 kms^{-1} and this small offset confirms the zero-point of the overall velocity scale (no zero-point correction has been adopted for the FLAIR velocities in column (8)). Despite the high signal-to-noise of the templates, the observed scatter about the mean is quite large and, although part of this error may come from the low spectroscopic resolution of the observations (11Å FWHM corresponds to 730kms^{-1} at λ≈4500Å), it is suggested below that there may also be some contribution to the dispersion from the catalogue velocities (e.g. A2058-28).

Observations of the 28 target galaxies from the 864 field of Peterson et al. (1986) are now considered and in Figure 6.6 (a) to (d) examples of the UKST/FLAIR spectra are shown for faint (b$_J$>16^m.6) objects. The most prominent absorption features are marked and in most cases show high signal-to-noise. In Table 6.4 the estimated UKST/FLAIR absorption (column (4)) and emission (column (6)) velocities for the 28 galaxies are shown together with an adopted velocity for each object (column (8)). The method of obtaining the adopted velocity depended upon the Tonry and Davis (1979) r-factor of the measured absorption velocity (both the r-factor and velocity, in this case, being averaged over, generally, the largest number of templates that gave a consistent velocity for the object to within ±500kms^{-1} of the mean). For galaxies with high r values (r>2.5) the absorption velocity was adopted as the final UKST/FLAIR velocity whilst those with low r values (r≤2.5) the emission-line velocity was taken, if available. In the remaining three cases (GNA010, GNA016, and GNA055) where the cross-correlation procedure gave r-factors of ≤2.5, averaged over a reasonable number of templates, and the galaxies showed no emission lines, the spectra were inspected visually (Figure 6.6 (e), (f) and (g)) to check the cross-correlation result and the absorption velocity was subsequently adopted (this visual inspection was further carried out on all the spectra to confirm the final adopted velocities). Finally, there were 6 galaxies, which were generally of late morphological type, that gave mostly low cross-correlation r-factors, and whose spectra showed neither significant emission or absorption features; no velocity could be claimed for these galaxies.

Column (9) of Table 6.4 gives the original estimates of the redshift

Figure 6.6. The observed of galaxies in the 13h40+00 field median filtered over 4x3000s exposures (see Figure 6.3). The first four figures, (a) to (d), demonstrate the high performance of FLAIR for galaxies near the limiting magnitude of $m(b_J)=16^m.76$. These spectra also show the variations for early and late-type galaxies. The spectra in (e), (f) and (g) are for the galaxies that showed low cross-correlation significance ($r<2.5$) and no significant emission lines (see text and Table 6.4). In all cases absorption and emission features with high signal-to-noise are marked.

(a) GNA056 (S0) m_{b_j} = 16.66 V_{FLAIR} = 23053 kms^{-1}

(b) GNA057 (S0) m_{b_j} = 16.70 V_{FLAIR} = 26044 kms^{-1}

(c) GNA051 (Sbc) m_{b_j} = 16.76 V_{FLAIR} = 25149 kms^{-1}

(d) GNA032 (Scd) m_{b_j} = 16.64 V_{FLAIR} = 3763 kms^{-1}

(e) GNA010 (Sb) m_{b_j} = 15.59 V_{FLAIR} = 18107 kms^{-1}

(f) GNA016 (Sb) m_{b_j} = 16.1 V_{FLAIR} = 21603 kms^{-1}

(g) GNA055 (S0) m_{b_j} = 16.69 V_{FLAIR} = 26722 kms^{-1}
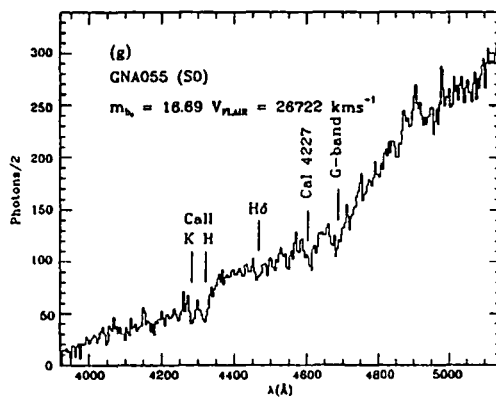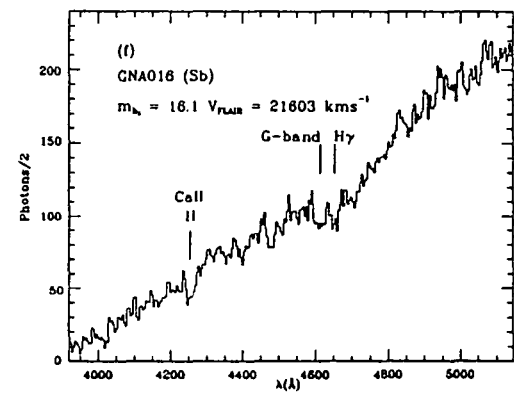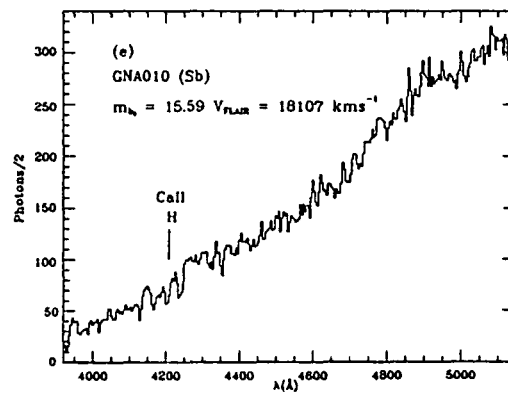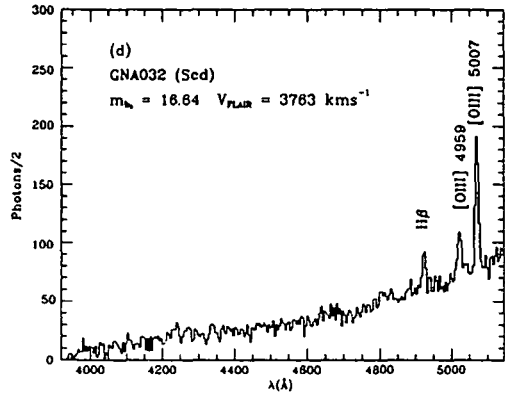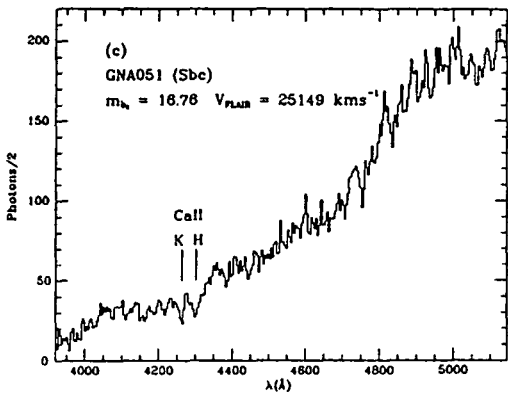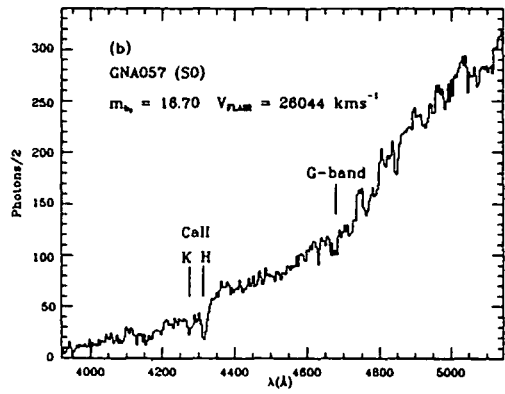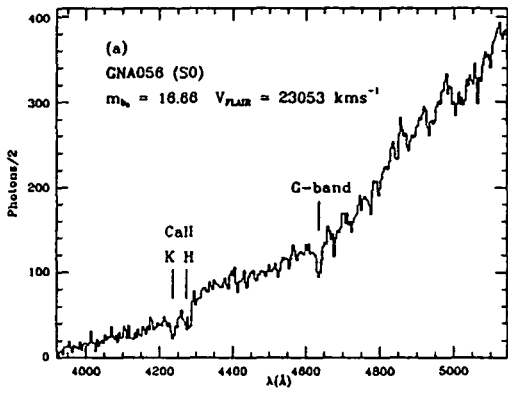
Table 6.4 FLAIR observations of galaxies in the 13h40+00 field.

(1) GNA	(2) $m^*_{b_J}$	(3) Type	(4) V^a_F kms^{-1}	(5) r_F	(6) V^e_F kms^{-1}	(7) N^e	(8) V_F kms^{-1}	(9) V_{ARRS} kms^{-1}	(10) ΔV kms^{-1}
2	13.32	Sa	6825	4.5	6693	1	6825	6793	32
3	14.27	Sab	3865	8.4			3865	3782	83
4	15.15	Sbc	11981	2.8	12192	1	11981	12106	-125
9	15.38	S0	14321	6.8			14321	14380	-59
7	15.55	Sb	13816	2.4	14095	1	14095	14195	-100
10	15.59	Sb	18107	†2.0			18107	17859	248
15	15.84	S0	11836	4.2			11836	11916	-80
12	15.89	Sc			4396	3(23)	4396	4596	-200
16	16.10	Sb	21603	†2.1			21603	21763	-160
18	16.13	S0	6841	6.1			6841	6731	110
17	16.18	Sbc	14170	4.1			14170	14246	-76
29	16.30	S0	8008	4.9	8026	1	8008	7791	217
25	16.39	Sa						21399	
33	16.44	S0	26825	3.7			26825	26563	262
27	16.44	Sc						18477	
26	16.52	Sc						27506	
39	16.53	Sb	21948	2.9			21948	22025	-77
31	16.54	Sa			3815	3(40)	3815	3810	5
34	16.55	Sb						17305	
41	16.57	Sb						14351	
32	16.64	Scd			3763	3(16)	3763	3674	89
58	16.65	S(P)	21612	2.3	21319	1	21319	21559	-240
56	16.66	S0	23053	3.9			23053	22944	109
55	16.69	S0	26722	†2.3			26722	26563	159
57	16.70	S0	26044	3.8			26044	26015	29
43	16.71	Scd						27099	
60	16.72	S0	21925	3.2			21925	22015	-90
51	16.76	Sbc	25149	2.6			25149	25254	-105

Notes:
†See Figure 6.6 (e,f,g).

The columns are as follows; (1) Peterson et al. galaxy identification, (2) apparent total blue magnitude, (3) morphological type, (4) absorption velocity from FLAIR, (5) Tonry and Davis r-factor associated with V^a_F, (6) emission-line velocity from FLAIR, (7) number of observed emission lines and the line-to-line error (in brackets), (8) the adopted FLAIR velocity, (9) the velocity from Peterson et al. and (10) the difference $V_F - V_{AARS}$.

velocities for these 28 galaxies from Peterson et al. (1986) and in column (10) the difference between these and the adopted FLAIR velocities are shown. The mean and rms dispersion of these values are

$$V_{FLAIR} - V_{AARS} = 1\pm144 \text{ kms}^{-1} \qquad (6\text{-}4)$$

On comparing just the absorption-line velocities, the mean and dispersion are

$$V_{FLAIR} - V_{AARS} = 8\pm160 \text{ kms}^{-1} \qquad (19 \text{ galaxies}) \qquad (6\text{-}5)$$

and this agrees well with the values for the emission-line galaxies

$$V_{FLAIR} - V_{AARS} = -28\pm161 \text{ kms}^{-1} \qquad (8 \text{ galaxies}) \qquad (6\text{-}6)$$

Thus this seems to show that the original estimate of error for the FLAIR velocities of between 150 and 200 kms^{-1} was justified (given that there is a much smaller uncertainty on the Peterson et al. redshift values).

A further check on the accuracy of the absorption-line velocities was obtained by calibrating the Tonry and Davis (1979) r-factor using the method of Bean (1983, see also Peterson et al. 1986, Metcalfe et al. 1989 and Section 4.3.3 of Chapter 4). As discussed in Chapter 4 the one-sigma error δv_z on a measurement of the redshift velocity via cross-correlation is related, theoretically, to the r-factor (the ratio of the height of the principal peak in the cross-correlation spectrum to the average height of the peaks) by equation 4-3. By degrading a typical template spectrum by adding Poisson noise to each pixel in proportion to the square root of the observed count, the distribution of errors δv_z at a given r can be determined by cross-correlating many degraded spectra (at various signal-to-noise levels) with the original template. The result of this procedure for the template NGC5329 is shown in Figure 6.7. The dashed lines indicate a fit of equation 4-3 to the 1σ error giving

$$c = 789 \text{ kms}^{-1} \qquad (6\text{-}7)$$

Thus, at the average value of r=7.9 for the template galaxies (based on the inter-template cross-correlations, see Table 6.3, column (9)) this procedure predicts an rms error of ±89kms-1 as compared to the ±117 kms-1 error found above from direct comparisons with the published catalogue

174

ccf
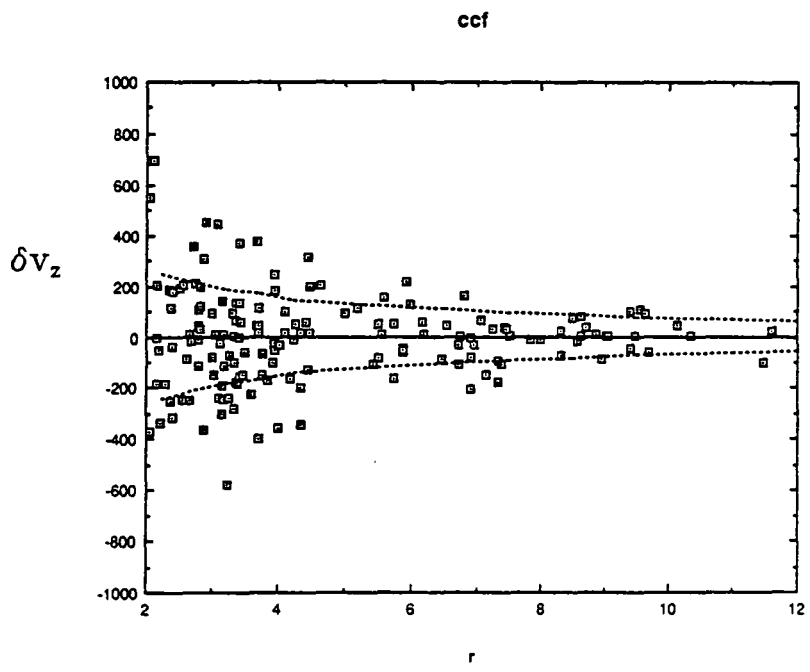
Figure 6.7. Calibration of the Tonry and Davis (1979) r-factor for the FLAIR absorption-line redshifts. The dashed lines represent 1-sigma devaitions in δv_z.

velocities. Some of this difference between the two estimates may arise from residual errors associated with the catalogue redshifts. At the average cross-correlation value of r=3.8 for the 864 galaxies, the predicted error is ±164 kms-1 in reasonable agreement with the ±152 kms-1 of equation 6-6 inferred from the comparison with the Peterson et al. data, assuming an error of ±50 kms-1 for their previous work. Thus this procedure confirms that galaxy velocities to an accuracy of ±150kms-1 rms are now available from the UKST data.

Since redshift information, at this accuracy, was obtained for 22 out of 28 of the galaxies observed in the 864 field, the corresponding completeness is ~80%.As discussed above (Section 6.2), since the spectra of the remaining 6 generally late-type galaxies exhibit only very weak features (in spite of having reasonable signal-to-noise) the best chance of obtaining redshifts for such objects may be by taking short exposure observations with the red blazed grating to try to detect features such as the redshifted emission lines (e.g. $H\beta$(4861), [O III] (4959, 5007), $H\alpha$ (6563) and N II (6584)) that frequently occur in such galaxies.

Finally, in Tables 6.5 and 6.6 are presented some preliminary results for the nine field redshift survey for fields 862 and 865, respectively. The redshift completeness rate in these two fields was 85% and 89%, respectively, to a limit of $b_J \approx 16^m.8$ with an average r-factor of r=4.0 and r=4.3. Since the observational set-up was virtually the same in all the UKST observing runs for this survey equations 4-3 and 6-7 imply that the predicted errors for the velocities in these fields is ±158 and ±149 kms^{-1} rms, respectively, and this further indicates that the UKST/FLAIR instrument is now clearly capable of performing a galaxy redshift survey to $b_J \approx 16^m.8$ over an extended region of the southern sky.

Table 6.5 FLAIR observations of galaxies in the UKST/SERC field 862.

(1) No.	(2) RA h	m	s	Dec °	'	"	(3) $m_{b_J}^*$	(4) V_F^a kms^{-1}	(5) r_F	(6) V_F^e kms^{-1}	(7) N^e	(8) V_F kms^{-1}
G1#	12	55	27.8	1	50	45	11.71	1267	9.0	1114	3(14)	1267
G7	12	54	37.8	-1	26	13	13.91	3185	4.4	2898	2(10)	3185
G13	13	7	7.0	-0	46	56	14.71	7798	4.5			7798
G19	12	53	24.3	-1	4	39	15.29			3039	3(17)	3039
G25	12	58	20.3	-1	4	39	15.43	6950	3.9	6985	2(42)	6950
G31	12	56	30.4	-2	52	36	15.68	14406	3.9			14406
G37	12	52	42.8	0	31	3	15.83	14210	6.3			14210
G43	13	5	29.7	1	13	35	15.96	12643	3.8			12643
G49	13	10	22.7	1	12	21	16.09	14571	3.1			14571
G55	12	51	42.1	-1	45	51	16.18					
G61	12	50	24.7	-2	12	29	16.26					
G67	13	9	35.0	0	1	33	16.32	12392	2.3			12392
G73	12	58	7.1	1	20	17	16.36	24646	3.2			24646
G79	12	58	26.4	-1	42	33	16.40			1521	3(21)	1521
G85	12	50	6.1	-2	27	54	16.43					
G91	13	9	2.6	-0	13	4	16.47	26959	2.8			26959
G97	13	8	56.3	0	24	52	16.49	19219	6.0			19219
G103	12	51	43.5	-2	19	7	16.54	14322	3.0	14237	1	14322
G109	13	7	9.5	0	2	28	16.59	28678	3.8			28678
G115	12	59	9.7	1	7	42	16.62	24827	2.2			24827
G121	12	56	4.0	-1	18	19	16.66	25955	4.4			25955
G127	12	54	20.0	-1	32	28	16.70					
G133	12	56	47.5	-1	44	37	16.73	25407	2.9			25407
G139	13	8	0.0	-0	14	17	16.75	19202	3.3			19202
G145	12	59	58.8	0	36	49	16.78	20500	3.9			20500
G151	12	53	47.5	-2	31	6	16.81	21394	2.8			21394

Notes:

#NGC4845 (see Table 6.3)

The columns are as follows; (1) galaxy identification, (2) 1950 equatorial coordinates, (3) apparent total blue magnitude, (4) absorption velocity from FLAIR, (5) Tonry and Davis r-factor associated with V_F^a, (6) emission-line velocity from FLAIR, (7) number of observed emission lines and the line-to-line error (in brackets), (8) the adopted FLAIR velocity.

Table 6.6 FLAIR observations of galaxies in the UKST/SERC field 865.

(1) No.	(2) RA h	m	s	Dec °	'	"	(3) $m^*_{b_J}$	(4) V^a_F kms^{-1}	(5) r_F	(6) V^e_F kms^{-1}	(7) N^e	(8) V_F kms^{-1}
G1#	13	50	19.9	-0	52	7	12.18	1648	4.2			1648
G7	14	6	8.9	-0	55	31	14.19	1426	4.5			1426
G13	14	2	17.8	-0	24	11	14.77	7232	9.9			7232
G19	13	55	33.1	-0	8	58	15.02	9039	3.0	8848	1	9039
G25	13	50	16.0	-2	21	23	15.29	22953	2.4			22953
G31	14	6	6.6	-2	45	59	15.40	8889	2.8	8775	1	8889
G37	13	59	31.7	-1	9	22	15.48	7389	9.4			7389
G43	13	57	46.9	-2	4	29	15.57	9214	3.7			9214
G49	13	56	27.8	0	29	1	15.77	9899	5.2			9899
G55	13	49	55.4	2	11	31	15.82	9972	4.9			9972
G61	14	2	51.1	-0	34	23	15.89	14713	3.6			14713
G67	13	50	10.6	0	22	34	15.99	4781	2.9	4614	4(28)	4781
G73	14	3	1.9	1	47	24	16.09	12890	7.0			12890
G79	13	59	11.9	1	56	52	16.18	25937	2.4			25937
G85	14	10	38.1	2	0	17	16.22	14489	3.6			14489
G91	14	4	39.0	-2	29	24	16.35	16727	3.7			16727
G97	13	55	38.5	-1	8	24	16.40			7613	1	7613
G103	13	50	20.7	-1	41	32	16.47					
G109	14	2	6.2	-2	4	44	16.56	20217	2.7			20217
G115	13	55	53.8	-1	26	44	16.58	14066	6.5			14066
G121	13	58	55.0	2	12	50	16.60			7464	2(69)	7464
G127	13	54	52.6	-2	43	17	16.63	8007	3.0			8007
G133	14	3	46.9	-1	48	7	16.66	16373	2.6			16373
G139	13	56	9.2	-2	34	7	16.69	7012	5.3			7012
G145	13	51	58.9	1	7	50	16.74					
G151	14	2	35.8	-1	28	49	16.76					
G157	14	10	2.2	-0	48	10	16.79	16333	1.8			16333

Notes:

#NGC5334, an Sc galaxy with a measured velocity of $V = 1383 kms^{-1}$ from 21cm radio observations (Fisher and Tully 1981).

The columns are as follows; (1) galaxy identification, (2) 1950 equatorial coordinates, (3) apparent total blue magnitude, (4) absorption velocity from FLAIR, (5) Tonry and Davis r-factor associated with V^a_F, (6) emission-line velocity from FLAIR, (7) number of observed emission lines and the line-to-line error (in brackets), (8) the adopted FLAIR velocity.

6.5 Future developements

In the previous section it was shown that using the current multi-object UKST/FLAIR spectrograph redshifts could be attained (at an accuracy of ~150kms^{-1} rms and at a rate of 14 objects per hour) for 80 to 90% of galaxies in a magnitude limited catalogue complete to b_J=16^m.8. As well as completing and analysing the 9 field redshift survey of ~250 galaxies, there are plans to extend these observations to cover the 60 plate contiguous area (at b_J<16^m.8) of the ROE/Durham Southern Galaxy Catalogue around the SGP that is currently being completed (Collins et al. 1988). Eventually the hope is to spectroscopically map the entire area of the south galactic hemisphere to this depth using a complete catalogue similar to the APM Galaxy Survey.

In preparation for the requirements of such surveys several developments in the present UKST/FLAIR system are now under-way. To improve the rate of collection of spectra a dual-CCD system has recently been introduced at the UKST (Watson et al. 1990). This uses the existing technology of FLAIR but doubles the number of fibres available by having two bundles of 35, 100μm fibres, two identical spectrographs and two blue sensitive GEC CCDs; the read-out of the chips being controlled by the same computer hardware. Initial tests of this system in July/August of 1989 have proved successful and this system will provide the initial data for the 60 field redshift survey.

More general improvements to the system are included in the FLAIR II proposal. This includes an improved blue (4000Å) throughput and a higher instrumental resolution spectrograph (FISCH, Gray and Watson 1990) and more automated methods of fibre positioning and loading the fibre plate-holder into the telescope. The new spectrograph will have little of the defocussing of the current Pentax lens system and will be able, initially, to image ~70 of the 100μm fibres (although with improved, larger area detectors this could be increased to well over 100). The current FLAIR plate-holder was designed with little modification to the telescope itself and so the loading of the plate-holder and the slow manual set-up of the positions of the fibres on the copy plates represents a considerable amount of work for each observation. With new modifications to the telescope and plate-holder, and an automated fibre positioner (based on a TV alignment system) it is hoped that the 'turn-around time' for the observation of fields can be reduced to several

hours. Thus the aim is to be able to make the observations of ~100 objects a matter of routine.

Such improvements are now under way, and so it now seems possible that a large-map of the galaxy distrubution (sampled at a high rate of greater than 1-in-3) to a competitively deep depth of z<0.1 over an area of ~0.5str can now be produced. With such a large contiguous volume survey (the volume of such a survey is ~20 times the volume of the original CfA $m_B < 15^m.5$ slice of de Lapparent et al. 1986a), it would be possible to analyse the distribution of various currently 'observed' structures (such as 'voids', 'walls', 'filaments', clusters etc.) as well as carrying out similar statistical analyses to the ones described in this thesis. This will eventually lead to a considerable improvement of our knowledge of large-scale structure and our understanding of what models best describe their evolution.

Chapter 7

Conclusions

The main aim of this thesis was to provide some constraints on the likely form of matter perturbations in the Universe using the dynamical and clustering information provided by systematic redshift surveys of galaxies. In respect of this aim the following conclusions about the matter distribution were drawn from a study of the ~700 galaxies in the Durham/SAAO, Parker et al. and Durham/AAT redshift surveys:-

1) From an analysis of the 3-d spatial distribution of these galaxies in Chapter 3 (Section 3.2.1), it appeared that these volumes have not under-sampled specific 'large-scale' structures that have been claimed are visible in the general galaxy distribution (e.g. large 'wall-like' structures, Abell type clusters etc).

2) Using luminosity function estimators that attempt to measure the luminosity distribution in a way which is independent of the galaxy clustering in a sample, the new Durham/SAAO and Parker et al. surveys gave, respectively, (Chapter 3, Section 3.2.2)

$$M^* = -19.9 \pm 0.15 \quad \text{and} \quad M^* = -20.0 \pm 0.24 \quad (\alpha = -1) \quad (7\text{-}1)$$

for the Schecter (1976) parameter M^* (with $\alpha = -1$ and $H_0 = 100 \text{kms}^{-1} \text{Mpc}^{-1}$) over the range $-22 \leq M(b_J) \leq -17.4$ and this is in good agreement with

$$M^* = -20.18 \pm 0.20 \quad (\alpha = -1) \quad (7\text{-}2)$$

obtained for the Durham/AAT Survey. Overall this gives

$$M^* = -20.00 \pm 0.11 \quad (\alpha = -1) \quad (7\text{-}3)$$

for these three samples which is somewhat brighter than other catalogues.

3) Using the results of 2) to predict the mean counts of galaxies as a function of redshift it was shown (Chapter 3, Section 3.2.3) from the observed

counts that these three samples were fairly homogeneous on scales $\geq 50h^{-1}$ Mpc. On the other hand variations between northern and southern Galactic hemisphere halves showed some deviation in their behaviour.

4) Similar models to 3) applied to the differential counts as function of apparent magnitude (Chapter 3, Section 3.2.3) suggested that there was some trend (confirmed by deeper galaxy counts) that the observed slope of log $\Delta N(m)$ versus m is steeper than a simple no-evolution model at $m(b_J) \approx 17^m$. This trend has, as yet, not been fully explained; if it is real (i.e. it is not an artefact of the observing procedure), it either implies evolution at relatively bright ($\sim 17^m$) magnitudes or large-scale clustering on scales of $\sim 300h^{-1}$ Mpc, however the latter (see Chapter 5, Section 5.2.2) hypothesis seems unlikely on the basis of the observed two-point correlation function.

5) The small-scale ($\sigma \leq 1h^{-1}$ Mpc) projected correlation functions measured in the new Durham/SAAO and Parker et al. surveys gave values of, respectively, (Chapter 4, Section 4.3.1)

$$r_o = (5.8 \pm 0.6)h^{-1} \text{ Mpc} \quad \text{and} \quad r_o = (2.6 \pm 0.7)h^{-1} \text{ Mpc} \quad (7\text{-}4)$$

for the two-point clustering length ($\gamma = 1.8$) and (Section 4.1.2)

$$Q = 0.48 \pm 0.1 \quad (7\text{-}5)$$

for the Durham/SAAO three-point amplitude (although it was suggested that the latter was perhaps a somewhat larger $Q = 0.75 \pm 0.14$). These are in reasonable statistical agreement with $r_o = (4.5 \pm 0.4)h^{-1}$ Mpc (Section 4.3.1) and $Q = 0.60 \pm 0.06$ (Section 4.1.2) from the Durham/AAT Survey and in good general accord with the values from other redshift catalogues (Sections 4.3.1 and 4.3.2). The overall values for r_o and Q in these 3 samples at this scale is thus (Section 4.4)

$$r_o = (4.5 \pm 0.3)h^{-1} \text{ Mpc} \quad \text{and} \quad Q = 0.58 \ (0.62) \pm 0.05 \quad (7\text{-}6)$$

(the value in brackets for Q incorporating the larger value of Q for the Durham/SAAO sample).

6) The range of small-scale ($\sigma \leq 1h^{-1}$ Mpc) line-of-sight rms peculiar motions exhibited by these catalogues is larger than has previously been

anticipated by Bean et al. (1983). For the new surveys (Chapter 4, Section 4.3.3)

$$\langle \omega^2 \rangle^{1/2} = (600 \pm 140) \text{kms}^{-1} \quad \text{and} \quad \langle \omega^2 \rangle^{1/2} = (0 \pm 240) \text{kms}^{-1} \quad (7\text{-}7)$$

for the Durham/SAAO and Parker et al. samples, respectively, as compared to

$$\langle \omega^2 \rangle^{1/2} = (190 \pm 90) \text{kms}^{-1} \quad (7\text{-}8)$$

for the Durham/AAT Survey. The large value for the peculiar motion in the Durham/SAAO Survey is not believed to be a result of excessive redshift measurement error or dominance by clusters observed in the distribution. Such a result also seems to be confirmed by the visual appearance of the redshift distributions (Chapter 3, Section 3.2.1). Overall, the rms peculiar velocity is (Section 4.3.3, Chapter 4)

$$\langle \omega^2 \rangle^{1/2} = (290 \pm 70) \text{kms}^{-1} \quad (7\text{-}9)$$

which in spite of the larger errors measured, is in good agreement with the observations of such motions in other samples.

7) Using the Cosmic Virial Theorem (Chapter 2, Section 2.2.2.1) of Peebles (1976a) an estimate of the mean mass density parameter Ω_0 was obtained assuming that galaxies trace the mass distribution. For the Durham/SAAO Survey, using the results presented in 5) and 6) above

$$\Omega_0 = 0.6 \, (0.4) \pm 0.2 \quad (7\text{-}10)$$

(the value in brackets again incorporating the higher value of Q) whereas for the Durham/AAT survey

$$\Omega_0 = 0.1 \pm 0.1 \quad (7\text{-}11)$$

Here the larger errors in $\langle \omega^2 \rangle^{1/2}$ carry through to these estimates of Ω_0. The best estimate for all 3 catalogues is

$$\Omega_0 = 0.18 \pm 0.09 \quad (7\text{-}12)$$

which confirms that $\Omega_o=1$ models are excluded unless galaxies are biassed tracers of the mass distribution with bias parameter

$$b = 2.4\pm0.6 \qquad (7\text{-}13)$$

8) Measurements of the direction-averaged redshift two-point correlation function $\xi_s(s)$ on scales $s<1h^{-1}$ Mpc indicate (Chapter 5, Section 5.1.1) that the above estimated parameters for r_o and $\langle\omega^2\rangle^{1/2}$ (points 5 and 6) are a good representation of $\xi_s(s)$ in these surveys at these separations when compared to the data using the model in equation 2-34 (Chapter 2, Section 2.1.2.2). At larger scales between $2\leq s\leq 7$ h^{-1} Mpc such models significantly underestimate the observed $\xi_s(s)$ with

$$r_o = (7.1\pm0.8)h^{-1} \text{ Mpc} \qquad \text{Durham/SAAO}$$

$$r_o = (7.1\pm0.8) \text{ } h^{-1} \text{ Mpc} \qquad \text{Durham/AAT} \qquad (7\text{-}14)$$

$$r_o = (4.4\pm1.1)h^{-1} \text{ Mpc} \qquad \text{Parker et al.}$$

being appropriate for this region in these samples. It is suggested that such an enhancement is not a result of random peculiar motions in these samples. The overall result of

$$r_o = (6.6\pm0.5)h^{-1} \text{ Mpc} \qquad (7\text{-}15)$$

is significantly different from $r_o=4.5h^{-1}$ Mpc by ~4 s.d. In an overview of the estimates of $\xi_s(s)$ in this range of separation from other brighter magnitude limit surveys it was concluded that the evidence for this 'shoulder' feature in $\xi_s(s)$ was encouraging but the uncertainties were measured to be larger than indicated in equation 7-15. However, it was argued that, rather than this larger error being due to the influence of large-scale (~50 h^{-1} Mpc) mean clustering, these fluctuations may be caused by other sources of error (for example, magnitudes, selection functions and weighting schemes). This is supported to some extent by the close agreement between the shallow and deep (z<0.1) sample estimates of the small-scale ($\leq 1h^{-1}$ Mpc) clustering and peculiar motions (Chapter 4, Section 4.3)

9) On the basis that the samples in these surveys are fair representations of the general clustering distribution (see points 3 and 4 above) and that other sources of error (for example, number density

fluctuations) in the estimation of $\xi_s(s)$ in the region $2 \leq s \leq 7h^{-1}$ Mpc are small, the likely implication of the shoulder in $\xi_s(s)$ was discussed (Chapter 5, Section 5.1.3). It was suggested that such an amplification of $\xi(r)$ could only be caused by infall if $\Omega_o \approx 1$ and this is in direct contradiction to 7) above unless the galaxies were biassed by a factor of order given in equation 7-13. In such case this would again seem to make the amplification of $\xi(r)$ too small. This suggests that the shoulder is then a real spatial feature in $\xi(r)$. On this basis a simple three power law model for $\xi(r)$ was suggested and the integrals J_2 and J_3 gave

$$J_2 = 146h^{-2} \text{ Mpc}^2 \qquad J_3 = 291h^{-3} \text{ Mpc}^3 \qquad (7\text{-}16)$$

at $r \approx 10h^{-1}$ Mpc.

10) At larger scales ($\geq 10h^{-1}$ Mpc) the within-field $\xi_s(s)$ in the Durham/SAAO Survey displays a break from the power law in the region $2 \leq s \leq 7h^{-1}$ Mpc at $\sim 9h^{-1}$ Mpc and decreases rapidly to zero by $\sim 10h^{-1}$ Mpc. At $s \geq 10h^{-1}$ Mpc $\xi_s(s)$ in this sample is consistent, statistically, with $\xi(r)=0$ at scales of up to 100 h^{-1} Mpc. Although similar behaviour was seen in the Durham/AAT sample some of the peak-trough-peak structure was quite well repeated in both samples. The interfield correlation function estimate appeared somewhat different from the within-field estimates but again was statistically consistent with $\xi(r)=0$ at these scales. The overall conclusion from all 3 samples is that $\xi_s(s)$ breaks to smaller values at $\sim 7h^{-1}$ Mpc and is consistent with $\xi(r)=0$ at all separations from 10 up to 100 h^{-1} Mpc at the 1σ (0.1 to 0.05 in ξ, respectively) confidence level assuming that a fair sample of the clustering has been obtained. Similarly large-scale clustering of the form $|\xi(r)| \geq 0.2$ can be rejected at between 2 (at $10h^{-1}$ Mpc) and 4 (at $100h^{-1}$ Mpc) standard deviations over this scale range.

11) In a detailed comparison of the results from 10) with other measures of large-scale ($\geq 10h^{-1}$ Mpc) structure (Chapter 5, Section 5.2.2) there was tentative evidence that $\xi(r)$ continued like $\xi(r) \approx (7/r)^{1.8}$ to ~ 50 h^{-1} Mpc (from the rich Abell clusters) and some fairly strong evidence that $\xi(r)$ was such a power law to at least $20h^{-1}$ Mpc (from the QDOT IRAS, CfA ($m_B < 15^m.5$) and APM galaxy catalogues). Other measures appear to agree with the conclusions of 10) above (from the QSO's and the Quadrupole and Dipole moments in the Microwave Background).

12) On the basis of more large-scale structure to $\sim 20h^{-1}$ Mpc as indicated in 11) the ~ 2.5 to 2.8 s.d. significance of the break from $\xi(r)=(6.6/r)^{1.8}$ in the overall correlation function from the combined 17^m samples was questioned. Based on the shape and independence of the fields in these samples it was argued that the errors in $\xi_s(s)$ will not increase dramatically as a result of the larger correlations claimed and so there is still evidence that the break in these samples occurs at $\sim 7\ h^{-1}$ Mpc.

13) Confronting the observations of 1) to 12) with models for the dynamical evolution of the mass distribution (Chapter 5, Section 5.3) it was seen that the explosive scenarios, and growth of structure from adiabatic perturbations with baryons or neutrinos could provide a variety of scale lengths in the mass distribution. In this respect possibilities for the observed features seen in $\xi(r)$ (points 9 and 10 above) were hinted at. The CDM model, while not providing exact duplication of the observed data gave $\xi(r)\approx 0$ at $r\gtrsim 10h^{-1}$ Mpc, consistent with the observations in these samples.

14) Finally, the multi-object spectrographic instrument, FLAIR, on the UKST was demonstrated (in Chapter 6) to be capable of performing large angular scale redshift surveys to a limit of $b_J\approx 17^m$ with an rms accuracy of $\sim 150 kms^{-1}$ in velocity and with a completeness rate of 80-90%. This will pave the way for future large area coverage redshift surveys in the southern Galactic hemisphere.

Appendix

Combining measurements of a quantity with a normal distribution of errors

If independent measurements of a quantity x (x_1, x_2,...etc) are made such that the distribution of errors on x (with rms widths σ_1, σ_2,...etc) are normally (i.e. Gaussian) distributed and drawn from the same normal parent distribution, then the best overall mean value of x is given by (see, for example, Barford 1967)

$$\langle x \rangle = \sigma^2[(x_1/\sigma_1^2) + (x_2/\sigma_2^2) + ...)] \qquad \text{(A-1)}$$

where the variance of the resulting normal distribution of $\langle x \rangle$ is

$$\sigma^2 = 1/[(1/\sigma_1^2) + (1/\sigma_2^2) + ...] \qquad \text{(A-2)}$$

Such measurements of x are therefore combined by weighting the individual estimates according to the inverse square of their 1-sigma errors.

References

Abell, G.O., 1958. <u>Astrophys. J. Suppl. Ser.</u>, **3**, 211.

Bahcall, N.A., Henrikson, M.J., Smith, T.E., 1990. <u>Astrophys. J. Lett.</u>, preprint.

Bahcall, N.A. & Soneira, R.M. 1983. <u>Astrophys. J.</u>, **270**, 20.

Bahcall, N.A., Soneira, R.M. & Burgett, W.S., 1986. <u>Astrophys. J.</u>, **311**, 15.

Barford, N.C., 1967. <u>Experimental Measurements: Precision, Error and Truth.</u> Addison-Wesley.

Barnes, J.E., 1987. In: <u>Nearly Normal Galaxies, Proc. Eighth Santa Cruz Summer Workshop</u>, ed. Faber, S.M., Springer-Verlag, New York.

Bean, A.J., 1983. <u>PhD Thesis</u>, University of Durham.

Bean, A.J., Efstathiou, G., Ellis, R.S., Peterson, B.A. & Shanks, T., 1983. <u>Mon. Not. R. astr. Soc.</u>, **205**, 605.

Bhavsar, S.P., & Ling, E.N., 1988. <u>Astrophys. J.</u>, **331**, L63.

Binggeli, B., Sandage, A., & Tammann, G.A., 1988. <u>Ann. Rev. Astr. Astrophys.</u>, **26**, 509.

Broadhust, T.J., 1988. <u>PhD thesis</u>, University of Durham.

Broadhurst, T.J., Ellis, R.S., & Shanks, T., 1988. <u>Mon. Not. R. astr. Soc.</u>, **235**, 827.

Broadhurst, T.J., Ellis, R.S., Koo, D.C. & Szalay, A.S. 1990. <u>Nature</u>, **343**, 727.

Burstein, D., Davies, R.L., Dressler,A., Faber, S.M., Lynden-Bell, D., Terlevich, R. & Wegner, G., 1986. In: <u>Galaxy Distances and Deviations from the Hubble Flow</u>, eds. Madore, B.F. & Tully, R.B., Reidel, Dordrecht.

Chester, T., Beichmann, C., Conrow, T.,1987. <u>Revised IRAS Explanatory Supplement</u>, Ch.12.

Collins, C.A., Heydon-Dumbleton, N.H., MacGillivray, H.T., 1988a. <u>Mon. Not. R. astr. Soc.</u>, **236**, 7p.

Collins, C.A., Heydon-Dumbleton, N.H., MacGillivray, H.T. & Shanks, T., 1988b. In: <u>Large-scale structures in the Universe, IAU Symposium No. 130</u>, p125, eds. Audouze, J. et al., Reidel, Dordrecht.

Couch, W.J. & Newell, E.B., 1980. <u>Publ. astr. Soc. Pacific</u>, **92**, 746.

Cullum, M., Deiries, S., D' Odorico, S. & Reiβ, R., 1985. <u>Astr. & Astrophysics</u>, **153**, L1.

da Costa, L.N., Pellegrini, P.S., Sargent, W.L.W., Tonry, J., Davis, M., Meiksin, A., Latham, D.W., Menzies, J.W. & Coulson, I.A., 1988. <u>Astrophys. J.</u>, **327**, 544.

Davis, M., 1986. In: Inner Space/Outer Space, p173, eds. Kolb, E.W., Turner, M.S., Lindley, D., Olive, K. & Seckel, D., Chicago University Press, Chicago.

Davis, M., 1987. In: Proc. Thirteenth Texas Symp. on Relativistic Astrophysics, p289, ed. Ulmer, M.P., World Scientific, Singapore.

Davis, M., Efstathiou, G., Frenk, C.S. & White, S.D.M., 1985. Astrophys. J., 292, 371.

Davis, M. & Geller, M.J., 1976. Astrophys. J., 208, 13.

Davis, M., Groth, E.J. & Peebles, P.J.E., 1977. Astrophys. J., 212, L107.

Davis, M. & Huchra, J., 1982. Astrophys. J., 254, 437.

Davis, M., Huchra, J., Latham, D.W. & Tonry, J., 1981. Astrophys. J., 253, 423.

Davis, M., Meiksin, A., Strauss, A., da Costa, N.L. & Yahil, A., 1988. Astrophys. J., 333, L9.

Davis, M. & Peebles, P.J.E., 1983. Astrophys. J., 267, 465.

Dawe, J.A. & Watson, F.G., 1984. In: Astronomy with Schmidt-type Telescopes, p181, ed. Capaccioli, M., Reidel, Dordrecht.

de Lapparent, V., Geller, M.J. & Huchra, J.P., 1986a. Astrophys. J., 302, L1.

de Lapparent, V., Geller, M.J. & Huchra, J.P., 1987. In : Proc. Thirteenth Texas Symp. on Relativistic Astrophysics, p281, ed. Ulmer, M.P., World Scientific, Singapore.

de Lapparent, V., Geller, M.J., & Huchra, J.P., 1988. Astrophys. J., 332, 44.

de Lapparent, V., Kurtz, M.J. & Geller, M.J., 1986b. Astrophys. J., 304, 585.

Deiries, S., 1986. In: The Optimisation of the Use of CCD Detectors in Astronomy, p73, June 17-19, eds. Baluteau, J.P. & D' Odorico, S., Pub. ESO.

Dekel, A. & Rees, M.J., 1987. Nature, 326, 455.

Dressler, A., 1980. Astrophys. J., 236, 351.

Dressler, A., 1984. Astrophys.J., 281, 512.

Dressler, A., Faber, S.M., Burstein, D., Davies, R.L., Lyden-Bell, D., Terlevich, R.J. & Wegner, G., 1987. Astrophys. J., 313, L37.

Efstathiou, G., 1988. In: Comets to Cosmology, Proceedings of the Third IRAS Conference, p312, ed. Lawrence, A., Springer-Verlag, Berlin.

Efstathiou, G. & Eastwood, J.W., 1981. Mon. Not. R. astr. Soc., 194, 503.

Efstathiou, G., Ellis, R.S. & Peterson, B.A., 1988. Mon. Not. R. astr. Soc., 232, 431.

Efstathiou, G., & Jedrzejewski, 1984. Adv. Space. Res., 3, 379.

Efstathiou, G., Kaiser, N., Saunders, W., Lawrence, A., Rowan-Robinson, M., Ellis, R.S. & Frenk, C.S., 1990. <u>Mon. Not. R. astr. Soc.</u>, **247**, 10P.

Einasto, J., Joeveer, M., & Saar, E., 1980. <u>Mon. Not. R. astr. Soc.</u>, **193**, 353.

Ellis, R.S., 1987. In: <u>Observational Cosmology, Proc. IAU Symp. No. 124</u>, eds. Hewitt, A., Burbidge, G.R. & Fong, L.Z., Reidel, Dordrecht.

Faber, S.M. & Gallagher, J.S., 1979. <u>Ann. Rev. Astron. Astrophys.</u>, **17**, 135.

Fall, S.M., 1979. <u>Rev. Mod. Phys.</u>, **51**, 21.

Fall, S.M. & Tremaine, S., 1977. <u>Astrophys.J.</u>, **216**, 682.

Felten, J.E., 1977. <u>Astr. J.</u>, **82**, 861.

Felten, J., 1985. <u>Comments Astrophys.</u>, **11**, 53.

Fixsen, D.J., Cheng, E.S. & Wilkinson, D.T., 1983. <u>Phys. Rev. Lett.</u>, **50**, 620.

Geller, M.J., de Lapparent, V., & Kurtz, M.J., 1984. <u>Astrophys. J.</u>, **287**, L55.

Gray, P.M., 1983. <u>Proc. S.P.I.E.</u>, **445**, 57.

Gray, P.M. & Watson, F.G., 1990. Preprint.

Groth, E.J. & Peebles, P.J.E., 1977. <u>Astrophys.J.</u>, **217**, 385.

Groth, E.J. & Peebles, P.J.E., 1986a, <u>Astrophys. J.</u>, **310**, 499.

Groth, E.J. & Peebles, P.J.E., 1986b, <u>Astrophys. J.</u>, **310**, 507.

Guth, A.H., 1984. In: <u>Eleventh Texas Symp. on Relativistic Astrophysics</u>, ed. Evans, D.S., p1, <u>Ann. N.Y. Acad. Sci.</u>, New York.

Guth, A.H., 1986. In: <u>Outer Space/Inner Space</u>, p287, eds. Kolb, E.W., Turner, M.S., Lindley, D., Olive, K. & Seckel, D., Chicago University Press, Chicago.

Hacking, P., Condon, J.J. & Houck, J.R., 1987. <u>Astrophys. J.</u>, **316**, L15.

Hamilton, A.J.S., 1988. <u>Astrophys. J.</u>, **331**, L59.

Harrison, E.R., 1970. <u>Phys. Rev. D.</u>, **1**, 2726.

Harrison, G.R., 1939. <u>The MIT Wavelength Tables</u>, Publications of the MIT Technology Press.

Haynes, M.P. & Giovanelli, R., 1988. In: <u>Large-Scale Motions in the Universe</u>, A Vatican Study Week, p31, eds. Rubin, C.R. & Coyne, G.V., Princeton University Press.

Hewett, P.C., 1982. <u>Mon. Not. R. astr. Soc.</u>, **201**, 867.

Heydon-Dumbleton, N.H., Collins, C.A. & MacGillivray, H.T., 1989. <u>Mon. Not. R. astr. Soc.</u>, **238**, 379.

Huchra, J., Davis, M., Latham, D. & Tonry, J., 1983. <u>Astrophys. J. Suppl.</u>, **52**, 89.

Huchra, J. & Geller, M.J., 1982. <u>Astrophys. J.</u>, **257**, 423.

Huchra, J., Geller, M., de Lapparent, V. & Burg, V., 1988. In: <u>Large-Scale Structures in the Universe</u>, <u>IAU Symposium No. 130</u>, p105, eds. Audouze, J. et al., Reidel, Dordrecht.

Inglis,I., 1985. <u>PhD thesis</u>, University of Durham.

Jones, B.J.T., Martínez, V.J., Saar, E. & Einasto, J., 1988. <u>Astrophys. J.</u>, 332, L1.

Kaiser, N., 1984. <u>Astrophys. J.</u>, 284, L9.

Kaiser, N., 1986a. <u>Mon. Not. R. astr. Soc.</u>, 219, 785.

Kaiser, N., 1986b. In: <u>Outer Space/Inner Space</u>, p 258, eds. Kolb, E.W., Turner, M.S., Lindley, D., Olive, K. & Seckel, D., Chicago University Press, Chicago.

Kaiser, N., 1987. <u>Mon. Not. R. astr. Soc.</u>, 227, 1.

Kaiser, N. & Silk, J., 1986. <u>Nature</u>, 324, 529.

Kent, S.M. & Gunn, J.E., 1982. <u>Astr. J.</u>, 87, 945.

Kibblewhite, E.J., Bridgeland, M.T., Bunclark, P. & Irwin, M.J., 1984. In: <u>Astronomical Microdensitometry Conference, NASA Conf. Pub.</u>, 2317, 277.

Kirshner, R.P., Oemler, A. & Schechter, P.L., 1978. <u>Astr. J.</u>, 83,1549.

Kirshner, R.P., Oemler, A. & Schechter, P.L. 1979. <u>Astr. J.</u>, 84, 7.

Kirshner, R.P., Oemler, A., Schechter, P.L. & Schectman, S.A., 1981. <u>Astrophys. J.</u>, 248, L57.

Kirshner, R.P., Oemler, A., Schechter, P.L. & Schectman, S.A., 1983. <u>Astr. J.</u>, 88, 1285.

Kirshner, R.P., Oemler, A., Schechter, P.L. & Schectman, S.A., 1987. <u>Astrophys. J.</u>, 314, 493.

Klypin, A.A. & Kopylov, A.I., 1983. <u>Soviet Astr. Letters</u>, 9, 41.

Lauberts, A., 1982. <u>The ESO/Uppsala Survey of the ESO(B) Atlas</u>, Munchen, European Southern Observatory.

Lilje, P.B. & Efstathiou, G., 1989. <u>Mon. Not. R. astr. Soc.</u>, 236, 851.

Limber, D.N., 1953, <u>Astrophys. J.</u>, 117, 134.

Loveday, J., 1989. <u>PhD thesis</u>, University of Cambridge.

Lubin, P.M., Villela, T., Epstein, G.L. & Smoot, G.F., 1985. <u>Astrophys. J.</u> 298, L1.

Lucey, J.R. 1983. <u>Mon. Not. R. astr. Soc.</u>, 204, 33.

Lucey, J.R., Currie, M.J. & Dickens, R.J., 1986. <u>Mon. Not. R. astr. Soc.</u>, 222, 427.

Lynden-Bell, D., 1971. <u>Mon. Not. R. astr. Soc.</u>, 155, 95.

Lynden-Bell, D., 1987. <u>Q. Jl. R. astr. Soc.</u>, 28, 187.

Lyubimov, V.A., Novikov, E.G., Nozik, V.Z., Tretyakov, E.F. & Kozik, V.F., 1980. Phys. Lett. , 94B, 266.

MacGillivray, H.T. & Stobie, R.S., 1984. Vistas Astr., 27, 433.

Maddox, S.J., Efstathiou, G. & Loveday, J., 1988. In: Large-scale Structures in the Universe, IAU Symposium No. 130, p151, eds. Audouze, J. et al., Reidel, Dordrecht.

Maddox, S.J., Efstathiou, G., Sutherland, W.J. & Loveday, J., 1990a. Mon. Not. R. astr. Soc., 242, 43p.

Maddox, S.J., Sutherland, W.J., Efstathiou, G. & Loveday, J., 1990b. Mon. Not. R. astr. Soc., 243, 692.

Maddox, S.J., Efstathiou, G. & Sutherland, W.J., 1990c. Mon. Not. R. astr. Soc., 246, 433.

Maddox, S.J., Sutherland, W.J., Efstathiou, G., Loveday, J. & Peterson, B.A, 1990d. Mon. Not. R. astr. Soc., 247, 1p

Marshall, F.E., Boldt, E.A., Holt, S.S., Miller, R., Mushotzky, R.F., Rose, L.A., Rothschild, R. & Serlemitsos, P.J., 1980, Astrophys. J., 235, 4.

Mészáros, P.,1974. Astron. Astrophys., 37, 225.

Mészáros, A. & Mészáros, P., 1988. In: Large-Scale Structures in the Universe, IAU Symposium No. 130, p203, eds. Audouze, J. et al., Reidel, Dordrecht.

Metcalfe, N., Fong, R. & Shanks, T., 1990a. In preparation.

Metcalfe, N., Shanks, T., Fong, R., & Jones, L.R., 1990b. Mon. Not. R. astr Soc., submitted.

Metcalfe, N., Fong, R., Shanks, T. & Kilkenny, D., 1989. Mon. Not. R. astr. Soc., 236, 207 (the Durham/SAAO Survey).

Nolthenius, R. & White, S.D.M., 1987. Mon. Not. R. astr. Soc., 235, 505.

Oates, A.P., 1990. Proc. S.P.I.E., preprint.

Olive, K.A., Schramm, D.N., Steigman, G., Turner, M.S. & Yang, J., 1981. Astrophys. J., 246, 557.

Oort, J.H., 1983. Ann. Rev. Astron. Astrophys., 21, 373.

Ostriker, J.P., 1988. In: Large-Scale Structures in the Universe, IAU Symposium No. 130, p321, eds. Audouze, J. et al., Reidel, Dordrecht..

Ostriker, J.P. & Cowie, L.L., 1981. Astrophys.J., 243, L127

Ostriker, J.P. & Thompson, C., 1987. Astrophys. J. 323, L97.

Ostriker, J.P., Thompson, C. & Witten, E., 1986. Phys. Letters B., 280, 231.

Parker, Q.A., MacGillivray, H.T., Hill, P.W. & Dodd, R.J., 1986. Mon. Not. R. astr. Soc., 220, 901.

Parker, Q.A., & Watson, F.G., 1990. Astr. Astrophys. Suppl., 84,455.

Parry, I.R. & Gray, P.M., 1986. Proc. S.P.I.E., 627,118.

Peebles, P.J.E., 1973. Astrophys. J., 185, 413.

Peebles, P.J.E., 1974. Astrophys. J., 189, L51.

Peebles, P.J.E., 1976a. Astrophys. Space Sci., 45, 3.

Peebles, P.J.E., 1976b. Astrophys. J. 205, L109.

Peebles, P.J.E., 1979. Astr. J., 84, 730.

Peebles, P.J.E., 1980. The Large-Scale Structure of the Universe, Princeton University Press.

Peebles, P.J.E., 1981a. In: Proc. Tenth Texas Symp. on Relativistic Astrophysics, eds. Ramaty, R. & Jones, F.C., Ann. N.Y. Acad. Sci., 375, 157.

Peebles, P.J.E., 1981b. Astrophys. J., 243, L119.

Peebles, P.J.E., 1981c. Astrophys. J., 248, 885.

Peebles, P.J.E., 1987, Nature, 327, 210.

Peebles, P.J.E., 1989. 'Galaxy Correlation Functions; Comments on Recent Developments', preprint.

Peebles, P.J.E. & Groth, E.J., 1975. Astrophys. J., 196, 1.

Peebles, P.J.E. & Hauser, M.G., 1974. Astrophys.J. Suppl. Ser., 28, 19.

Penzias, A.A. & Wilson, R.W., 1965. Astrophys. J., 142, 419.

Peterson, B.A., Ellis, R.S., Efstathiou, G., Shanks, T., Bean, A.J., Fong, R. & Zen-Long, Z., 1986. Mon. Not. R. astr. Soc., 221, 233 (the Durham/AAT Survey).

Phillips, S. & Shanks, T., 1987. Mon. Not. R. astr. Soc., 229, 621.

Pierre, M., Shaver, P.A., Iovino, A., 1988. Astron. Astrophys, 197, L3

Politzer, H.D. & Wise, M.B., 1984. Astrophys. J., 285, L1.

Press, W.H., & Schechter, P.L., 1974. Astrophys. J., 187, 425.

Rees, M.J. 1980. In: Objects at High Redshift, IAU Symposium No. 92, p207, eds. Abell, G.O. & Peebles, P.J.E., Reidel, Dordrecht.

Reines, F., Sobel, H. & Pasierb, E., 1980. Phys. Rev. Lett., 45, 1307.

Rood, H.J., 1982. Astrophys. J. Suppl., 49, 111.

Rowan-Robinson, M., Lawrence, A., Saunders, W., Crawford, J., Ellis, R., Frenk, C.S., Parry, I., Xiaoyang, X., Allington-Smith, J., Efstathiou, G. & Kaiser, N., 1990. Mon. Not. R. astr. Soc., in press.

Sachs, R.K. & Wolfe, A.M., 1967. Astrophys. J., 147, 73.

Sandage, A., & Tammann, G.A., 1987. Carnegie Instit. of Washington Publ., 635.

Sandage, A., Tammann, G.A., & Yahill, A., 1979. Astrophys. J., 232, 352.

Schechter, P.L., 1976. Astrophys. J., 203, 297.

Seldner, M., & Peebles, P.J.E., 1977. Astrophys. J., 215, 703.

Seldner, M., Siebers, B., Groth, E.J., & Peebles, P.J.E., 1977. Astr. J., 82, 249.

Shafer, R.A. & Fabian, A.C., 1983. In: Early Evolution of the Universe and its Present Structure, IAU Symposium No. 104, ed. Abell, G. & Chincarini, G., Dordrecht, Reidel.

Shane, C.D. & Wirtanen, C.A., 1967. Pub. Lick Obs., 22, pt 1.

Shanks, T., 1985. Vistas Astr., 28, 595.

Shanks, T., 1988. In: The Epoch of Galaxy Formation, Durham, July, 1988.

Shanks, T., 1990. In: Galactic and Extragalactic Background Radiation, Proc. IAU Symp. No. 139, eds. Bowyer, S. & Leinert, C., Kluwer, Dordrecht.

Shanks, T., Bean, A.J., Efstathiou, G., Ellis, R.S., Fong, R. & Peterson, B.A., 1983. Astrophys. J., 274, 529.

Shanks, T., Fong, R., Boyle, B.J. & Peterson, B.A., 1987. Mon. Not. R. astr. Soc., 227, 739.

Shanks, T., Hale-Sutton, D., & Boyle, B.J., 1988. In: Large-Scale Structures in the Universe, IAU Symposium No. 130, p371, eds. Audouze, J. et al., Reidel, Dordrecht.

Shanks, T., Stevenson, P.R.F., Fong, R., & MacGillivray, H.T., 1984. Mon. Not. R. astr. Soc., 206, 767.

Shapley, H., & Ames, A., 1932. Harvard Annals. 88, pt 11.

Sharp, N.A., 1979. Astron. Astrophys., 74, 308.

Silk, J., 1967. Nature, 215, 1155.

Soneira, R.M., & Peebles, P.J.E., 1978. Astr. J., 83, 845.

Stevenson, P.R.F., Shanks, T., Fong, R. & MacGillivray, H.T., 1985. Mon. Not. R. astr. Soc., 213, 953.

Strauss, M.A. & Davis, M., 1988. In: Large-Scale Structures in the Universe, IAU Symposium No. 130, p191, eds. Audouze, J. et al., Reidel, Dordrecht.

Strukov, I.A., Skulachev, D.P. & Klypin, A.A., 1988. In: Large-Scale Structures in the Universe, IAU Symposium No. 130, p27, eds. Audouze, J. et al., Reidel, Dordrecht..

Sutherland, W.J., 1988. In: Large-Scale Structures in the Universe, IAU Symposium No. 130, p538, eds. Audouze, J. et al., Reidel, Dordrecht.

Tonry, J. & Davis, M., 1979. Astr. J., 84, 1511.

Turner, E.L., 1976. Astrophys. J., 208, 20.

Turner, E.L., 1979. Astrophys. J., 231, 645.

Uson, J.M. & Wilkinson, D.T., 1984. Astrophys.J. 277, L1.

Vishniac, E.T. & Ostriker, J.P., 1986. Soc. Ital. Fis., 1, 157.

Wagoner, R.V., 1973. Astrophys. J., 179, 343.

Watson, F.G., 1986. Proc. S.P.I.E., 627,787.

Watson, F.G., 1988. In: Fibre Optics in Astronomy, ed. Barden, S.C., A.S.P. Conf. Series, 3, 125.

Watson, F.G., Oates, A.P., Shanks, T., & Hale-Sutton, D., 1990. In preparation.

Weinberg, S., 1979. Phys. Rev. Letters, 42, 850.

White, S.D.M., 1979. Mon. Not. R. astr. Soc., 186,145.

White, S.D.M., Frenk, C.S. & Davis, M., 1983. Astrophys. J. 274, L1.

White, S.D.M., Frenk, C.S., Davis, M. and Efstathiou, G., 1987. Astrophys. J., 313, 505.

Wilkinson, D.T., 1988. In: Large-Scale Structures in the Universe, IAU Symposium No. 130, p7, eds. Audouze, J. et al., Reidel, Dordrecht.

Yang, J., Turner, M.S., Steigman, G., Schramm, D.N. & Olive, K.A., 1984. Astrophys. J., 281, 493.

Yee, H.K.C. & Green, R.F., 1984. Astrophys. J., 280, 79.

Zabludoff, A.I., Huchra, J.P. & Geller, M.J., 1990. Astrophys. J. Suppl. Ser., 74,1.

Zel'dovich, Ya.B., 1972. Mon. Not. R. astr. Soc., 160, 1p.

Zwicky, F., Herzog, E., Wild, P., Karpowicz, M. & Kowal, C.T., 1961-1968. Catalogue of Galaxies and Clusters of Galaxies, California Institute of Technology, Pasadena.